Quantitative cerebral metabolic imaging using sodium and phosphorus nuclear magnetic resonance at 7 Tesla

Renata Porciuncula Baptista

université
PARIS-SACLAY

Quantitative Cerebral Metabolic Imaging using Sodium and Phosphorus Nuclear Magnetic Resonance at 7 Tesla

Imagerie métabolique cérébrale quantitative par résonance magnétique nucléaire du sodium et du phosphore à 7 Tesla

Thèse de doctorat de l'Université Paris-Saclay

École doctorale n°575,Electrical, optical, bio : physics and engineering (EOBE)
Spécialité de doctorat: Imagerie et Physique Médicale
Graduate School : Sciences de l'Ingénierie et des Systèmes, Référent : Faculté des sciences d'Orsay

Thèse préparée dans l'unité de recherche : **BAOBAB**, (**Université Paris-Saclay, CNRS, CEA**), sous la direction du **Fawzi BOUMEZBEUR**, directeur de recherche et le co-encadrement du **Cécile RABRAIT-LERMAN**, ingénieure de recherche.

Thèse soutenue à Paris-Saclay, le 17 octobre 2022, par

Renata PORCIUNCULA BAPTISTA

Composition du jury

Jean-Marie BONNY Directeur de recherche, INRAE - AgroResonance	Président
Guillaume MADELIN Maître de conférences, HDR, New York University	Rapporteur & Examinateur
Lijing XIN Chargée de recherche, HDR, EPFL - CIBM	Rapporteur & Examinatrice
Julien VALETTE Directeur de recherche, HDR, CEA - MIRCen	Examinateur
Wafaa ZAARAOUI Chargée de recherche, CNRS UMR 7339 - CRMBM	Examinatrice
Fawzi BOUMEZBEUR Directeur de recherche, HDR, CEA - NeuroSpin	Directeur de thèse

THESE DE DOCTORAT
NNT : 2022UPAST123

université PARIS-SACLAY

ÉCOLE DOCTORALE
Physique et ingénierie : Electrons, Photons, Sciences du vivant (EOBE)

Titre: Imagerie métabolique cérébrale quantitative par résonance magnétique nucléaire du sodium et du phosphore à 7 Tesla
Mots clés: Imagerie médicale, Imagerie par résonance magnétique, Cerveau, Physiologie, Metabolisme

Résumé: L'imagerie par résonance magnétique (IRM) permet l'étude non-invasive du métabolisme des tissus. Cette thèse porte sur le développement de méthodes innovantes pour l'IRM métabolique cérébrale des noyaux sodium (^{23}Na) et phosphore (^{31}P) à ultra-haut champ magnétique (UHF). Ces noyaux sont particulièrement intéressants car ils sont liés aux activités métaboliques. En raison de divers défauts cellulaires ou d'anomalies mitochondriales, les cellules du cerveau peuvent ne pas répondre aux besoins énergétiques, ce qui peut causer un dysfonctionnement du cerveau et une neurodégénérescence. L'objectif est donc de proposer les imageries quantitatives du ^{31}P (et de ses métabolites) et du ^{23}Na à UHF en tant qu'outils pour l'étude de la progression des maladies neurodégénératives. Parmi les techniques disponibles pour sonder le métabolisme énergétique de manière non-invasive, la spectroscopie RMN (SRM) in vivo du ^{31}P est l'une des plus prometteuses pour la recherche clinique. Bien que la ^{31}P-SRM a été appliquée avec succès pour l'étude de syndromes métaboliques au niveau des muscles, son application au domaine de la neuroénergétique a souvent été limitée par les concentrations relativement faibles d'ATP et de PCr dans le cerveau. Récemment, la ^{31}P-SRM a bénéficié de l'arrivée des scanners IRM cliniques à UHF favorisant le développement d'approches d'imagerie spectroscopique (MRSI). Cependant, la pertinence clinique de ces approches MRSI pour l'étude des maladies neurodégénératives est limitée par les temps d'acquisition (TA) long notamment en ^{31}P-MRSI 3D du cerveau entier. Nous avons donc proposé une approche d'IRM ^{31}P sélective en fréquence plus rapide focalisée sur l'imagerie de deux (ou plus) métabolites phosphorylés typiquement la PCr et l'ATP. Par l'ajout d'un module de saturation sélective du γ-ATP, nous avons évalué un protocole permettant d'estimer simultanément dans divers régions corticales les concentrations absolue d'ATP et de PCr ainsi que le flux à travers la créatine kinase (V_{CK}). Pour ce faire, nous avons développé une correction des inhomogénéités du champ radiofréquence B_1^+. Nous avons calculé une carte moyenne de l'angle de bascule (FA) sur la base d'acquisitions chez une cohorte indépendante de 6 volontaires sains. Nous avons ainsi pu estimer et prendre en compte les FA d'excitation et de saturation effectifs dans notre quantification des concentrations en ATP et PCr et de V_{CK}. Nous avons également développé une variante de ce protocole pour étudier le rapport PME/PDE dans le cadre d'une collaboration clinique avec le CHU de Poitiers. La concentration totale en sodium tissulaire (TSC) a démontrée à travers plusieurs études sa pertinence en tant que biomarqueur de viabilité cellulaire en particulier dans les maladies d'Alzheimer ou la sclérose en plaques. Les études actuelles utilisent des séquences à temps d'écho ultra-court combinées à des trajectoires déterministes non-Cartésiennes à travers l'espace **k**. Néanmoins, le TA reste relativement long, même à UHF, en raison de la sensibilité intrinsèque et des concentrations modérées du ^{23}Na. Les trajectoires déterministes n'exploitent pas au mieux la parcimonie de l'espace **k** en raison de leurs motifs géométriques. Par conséquent, nous avons proposé d'évaluer une approche stochastique d'encodage de l'espace **k**, SPARKLING, dans le contexte de l'IRM ^{23}Na cérébrale sous-échantillonnée. Dans des régimes favorables (dépendant du rapport signal/bruit et de la taille des images) que nous avons déterminés à travers une étude théorique basée sur un outil de simulation dédié, cette approche permet de réduire drastiquement les TA tout en préservant les détails anatomiques et le caractère quantitatif des cartes de TSC, surpassant les trajectoires 3D non-Cartésiennes couramment utilisées (TPI et Radial). Nous avons notamment validé in vitro et in vivo l'approche SPARKLING dans certains de ces scénarios, observant une qualité d'image similaire à celle de la TPI en dépit d'un TA moindre.

Title: Quantitative Cerebral Metabolic Imaging using Sodium and Phosphorus Nuclear Magnetic Resonance at 7 Tesla
Keywords: Medical imaging, Magnetic resonance imaging, Brain, Physiology, Metabolism

Abstract: Magnetic resonance imaging (MRI) allows for the non-invasive study of metabolism in soft tissues. This thesis consists in the development of innovative methods for metabolic cerebral imaging using sodium (^{23}Na) and phosphorus (^{31}P) MRI at ultra-high magnetic field (UHF). These nuclei are of interest because of the central roles of their electrolytes and metabolites in cell physiology and biochemistry. Due to various cellular defects or mitochondrial abnormalities, brain cells can fail to meet energy requirements, which can lead to brain dysfunction and neurodegeneration. The idea is therefore to detect and evaluate the evolution of neurodegenerative diseases using these nuclei and their electrolytes/metabolites as biomarkers of disease progression. Among the different techniques that can be used to probe energy metabolism non-invasively, in vivo ^{31}P magnetic resonance spectroscopy (MRS) is one of the most promising for clinical research. While in vivo ^{31}P-MRS has been successfully applied to study metabolic syndromes of the musculoskeletal system, its application to the study of neuroenergetics has often been limited by the relatively low concentrations of ATP and PCr in the brain. Recently, ^{31}P-MRS has benefited from the advent of UHF clinical MRI scanners promoting the development of various ^{31}P magnetic resonance spectroscopic imaging (^{31}P-MRSI) approaches. However, the clinical relevance of these ^{31}P-MRSI approaches for the study of neurodegenerative diseases remain limited due to their long acquisition time (AT). Thus we have proposed a rapid frequency-selective 3D 31P-MRI sequence capable of measuring two (or more) phosphorylated metabolites typically Adenosine Triphosphate (ATP) and Phosphocreatine (PCr). By adding a module for the selective saturation of γ-ATP, a saturation transfer 31P-MRI protocol is proposed to estimate simultaneously in several cortical areas the concentrations of PCr, ATP and the flux through the creatine kinase (V_{CK}). To account for the radiofrequency field (B_1^+) inhomogeneities in our quantification pipeline, we generated a B_1^+ template map from data acquired on an independent cohort of 6 healthy volunteers. This B1+ template map was then used to estimate the effective excitation and saturation flip angles in the quantification/modelling of our 3D ST ^{31}P MRI data. We also developed a variant of this sequence and protocol to study the PME/PDE ratio in the context of our collaboration with the University Hospital of Poitiers. Total tissue sodium concentration (TSC) has been confirmed through several studies as a relevant biomarker of cell viability and metabolic imbalance, particularly in neurological diseases such as Alzheimer's disease and multiple sclerosis. Most of these studies have used ultra-short echo time sequences combined with non-Cartesian deterministic k-space trajectories such as TPI, radial or FLORET. Nevertheless, the TA remains relatively long, even at UHF, due to the moderate intrinsic sensitivity and concentration of sodium. Deterministic trajectories do not exploit the inherent parsimony of k-space to the fullest extent due to their geometric patterns. Therefore, we hypothesized that ^{23}Na MRI could benefit from stochastic compressed sensing (CS) approaches such as SPARKLING that could lead to shorter TA while preserving good image quality. Determining the scenarios of interest is not trivial because CS performance depends on the signal-to-noise ratio and image size. Our contribution consisted in conducting first a theoretical study to find regimes in which the 3D SPARKLING approach outperforms the non-Cartesian 3D trajectories commonly used today using a dedicated brain ^{23}Na MRI data simulation tool. The CS SPARKLING approach was then applied in vitro and in vivo for validation, demonstrating that in those scenario, it can outperform TPI by preserving image quality with a significantly reduced TA.

THESIS

Quantitative Cerebral Metabolic Imaging using Sodium and Phosphorus Nuclear Magnetic Resonance at 7 Tesla

by

Renata Porciuncula Baptista

Submitted in partial fulfilment of the requirements for the degree of
Doctor of Philosophy at Université Paris-Saclay,
under the supervision of

Dr Cécile Rabrait-Lerman
CEA NeuroSpin
Université Paris-Saclay

Dr Fawzi Boumezbeur
CEA NeuroSpin
Université Paris-Saclay

October 2022

You have to act as if it were possible to radically transform the world.
And you have to do it all the time.

Angela Y. Davis

Acknowledgements

After uncountable hours working from my living room – after all, this was a COVID thesis, this Ph.D. has come to an end. A journey would certainly not be possible without the collaboration of excellent researchers and their teams, for whom I express my deepest gratitude!

First, I would like to thank my advisors, Cécile Lerman and Fawzi Boumezbeur, for taking me in for an internship at NeuroSpin during my master's and offering me to stay for a Ph.D. Also, I thank them for the support, freedom, and trust they put in me throughout this project.

I am grateful to Alexandre Vignaud, who went out of his way and spent countless hours discussing, offering advice, and guiding me throughout this journey. Also, for good book tips!

Also, I thank Philippe Ciuciu for wanting to expand SPARKLING to X-MRI and for being available to answer any questions I had. I could not thank our collaborators of the SPARKLING project enough: Marc La Pert, Remy Guillevin, and, especially, Mathieu Naudin, for his patience and contributions. Indeed, this thesis would be a contribution of smaller value without your help.

I also want to thank the METRIC team, especially Franck Mauconduit, for his help with sequence programming and Alexis Amadon for valuable scientific discussions about B_1^+ correction. As well as my fellow Ph.D. teammates for the support on many occasions. Zaineb Amor for being a good friend and helping me out many times. hMy many thanks to Bruno Meneses, who taught me more about MR physics than any book while being a great friend even after leaving the laboratory for new adventures.

I have been a teacher assistant at the Computer Science department at Paris-Saclay University for the last three years. I am grateful for this experience and Laurent Rosaz for the opportunity. Also, I found a warm atmosphere and support outside of my teaching assistant duties. I would like to thank Nicole Bidoit, Emmanuel Waller, Olivia Carter and Sylvie Delaët. It was a pleasure to share this experience with you.

I am a good follower of Paulo Freire's philosophy, and an admirer of his quote, " Whoever teaches learns in the act of teaching, and whoever learns teaches in the act of learning." I also need to thank my students who help me become a better teacher and for

allowing me to be a part of their learning process. I am glad to be a small part of their journey and pleased for the moments of curiosity filled with mutual respect we shared in the classroom.

I also would like to thank the mentorship program for women in science organized by Paris-Saclay University which I had the pleasure of participating. This incredible committee organized several events and essential discussions about the challenges faced by young women in science - in academia or in the industrial workforce, which unfortunately remains current. Thank Celine Hudelot, for being my mentor, for sharing advice, and for introducing me to part of your network.

The European Society of Magnetic Resonance in Medicine also organized a mentorship program I enjoy participating in. I was matched with one of the most outstanding MR scientists of the moment, who always had great advice to share. Thank you to my mentor Pr Andrew Webb.

None of the scientific production at NeuroSpin would be possible without the hard work of Maryline Hevin, Nathalie Blancho, and Julie Corgeron. I am also grateful to UNIACT team, particularly the radiographers, for being the best companies for manipulations one could ask for. My infinite gratitude toward Chantal Ginesty and Valerie Berland for the support; NeuroSpin is a better place with you in it. A special thanks to the nurses and physicians without whom no clinical research would be possible.

It is not only of "scientific interactions" that a Ph.D. is done. A "COVID" Ph.D. especially needed good times outside of work. In this note, I would like to thank my friends who followed me from nearby Vinicius for movie nights, biking trips, and delicious meals. Isadora and Shailu for those barbecues on the lake and games that helped to keep my sanity. Lena, Dandara, Dayanne, and Eloise, for nights out, museums, and concerts, enjoy the best Paris offers. And for all of you who were always there for me to cheer me up and had the ungrateful job of hearing me complaining when things got hard.

I would like to thank long-life friends who have been by my side for more than ten years. Even when we had an ocean of distance, I knew I could always count on Nayara M., Luiz, Nayara E., Julia, Yuri, Krishynan, and Felipe. With a special thanks to Rebeca and Pedro, my artistic friends, who, more than moral support, provided me with illustrations throughout my thesis and conferences.

To Ana and Geoffroy for being amazing friends, welcoming me into their family, and supporting me for all those years. I am fortunate to have you two in my life!

To my parents, Nazareth and Renato, and my sister, Ana Terra, for everything. For their support and respect for my choices. I recognize everything you have given up so that I could be here today, and I am very grateful.

Finally, I would like to thank all the volunteers, patients, and their families for donating their time and making clinical research possible. I also want to thank the Brazilian people for investing in my formation until my master in France. Also, I would like to thank the French people for financing this public and independent project. This work is a small

attempt to repay the investment and trust deposited in me.

* * *
* *
*

Contents

List of Figures

List of Tables

Symbols Used

Symbol	Constant name	Value
k_b	Boltzmann constant	$1.381 \times 10^{-23}\,\mathrm{J \cdot K^{-1}}$
$\hbar$	Planck constant (reduced)	$1.055 \times 10^{-34}\,\mathrm{J \cdot s}$

Symbol	Description	Unit
[A]	concentration of metabolite A	mmol/L
$\mathrm{B_0}$	static main field	$\mathrm{kg \cdot s^{-2} \cdot A^{-1}}$ (T)
$\mathrm{B_1^+}$	coil transmission field	T
$\mathrm{B_1^-}$	coil reception field	T
BW	radiofrequency bandwidth	$\mathrm{s^{-1}}$ (Hz)
E	electric field	$\mathrm{V \cdot m^{-1}}$
f	temporal frequency	$\mathrm{s^{-1}}$ (Hz)
f_0	Larmor temporal frequency	$\mathrm{s^{-1}}$ (Hz)
G	spatial static field gradients	$\mathrm{T \cdot m^{-1}}$
k	spatial frequency	$\mathrm{m^{-1}}$
M	macroscopic magnetisation	$\mathrm{A \cdot m^{-1}}$
$\mathrm{M_o}$	macroscopic equilibrium magnetisation	$\mathrm{A \cdot m^{-1}}$
$\mathrm{T_1}$	spin-lattice relaxation time	s
$\mathrm{T_2}$	spin-spin relaxation time	s
$\mathrm{T_2^*}$	effective spin-spin relaxation time	s
α	magnetisation nutation angle (flip angle)	degree (°), rad
α_E	Ernst flip angle	degree (°), rad
γ	gyromagnetic ratio	$\mathrm{rad \cdot s^{-1} \cdot T^{-1}}$
δ	chemical shift	ppm
$\delta \mathrm{B_0}$	static field inhomogeneity	T
Δf_0	offset from carrier frequency	$\mathrm{s^{-1}}$ (Hz)
$\Delta\omega$	offset from carrier angular frequency	$\mathrm{rad \cdot s^{-1}}$
ω_0	Larmor angular frequency	$\mathrm{rad \cdot s^{-1}}$

ρ	sample density	
χ	magnetic susceptibility	—

Mathematical notations

The imaginary unit is expressed by $\imath$, such that $\imath^2 = -1$.
Italic bold letters denote vectors, *e.g.* $\boldsymbol{v}$.
Upper-case bold letters denote matrices, *e.g.* $\mathbf{M}$.
Vector or matrix transpose is represented by an exponent T following the object, *e.g.* $\boldsymbol{v}^{\mathrm{T}}$.

General Introduction

In the early 1980's, magnetic resonance imaging (MRI) was introduced into clinical use. Thanks to its innocuous and non-invasive character, this imaging technique has become increasingly popular. The hydrogen nucleus (a single proton) is used for imaging because of its abundance in water and fat. Since then, proton (1H) MRI has allowed health professionals and researchers to exploit its different contrasts and diversify its fields of application.

At its core, an MRI scanner consists of a huge magnet that generates an intense static magnetic field (B_0). Over the years, technological developments increased this B_0 from less than 0.1 Tesla (T) to 11.7 T for humans [Quettier 2020, Allard 2022] and 21 T for rodents [Schepkin 2010]. As the NMR signal's Signal-To-Noise ratio (SNR) is thought to be proportional to the power 1.65 of the B_0 magnetic field [Pohmann 2016], the subsequent increase in SNR allows for higher spatial resolutions proton MRI with nominal resolution up to 0.2 mm isotropic for human brain imaging [Stucht 2015].

Thanks to the recent advent of 7T clinical MRI scanners and the availability of sub-millimeter anatomical brain images, physicians can diagnose and follow up more precisely on focal epilepsy lesions, which were barely visible at weaker magnetic fields [Feldman 2019, Opheim 2021]. Besides anatomical data, proton MRI can provide other cognitive information. For instance, functional MRI (fMRI) has helped the development of Neurosciences, allowing for a better, more objective understanding of how the brain works. As for most proton MRI modalities, thanks to B_0 increase, fMRI has gained sensibility and specificity [Beisteiner 2011, Worthoff 2019].

Non-proton MRI, also named X-nuclei MRI (X-MRI), brings a whole new information set. Sodium-23 (^{23}Na) and Phosphorus-31 (^{31}P) MRI, in particular, have the potential to assess cell metabolism and energy metabolism as the activity of the sodium-potassium pump (Na^+K^+-ATPase) is critical for maintaining cellular homeostasis, especially in neurons. If the cell membrane is damaged or there is an acute or chronic deficit in energy metabolism, this can lead to cell malfunction and, eventually, cell death [Mccarthy 2015].

Several studies have demonstrated the relevance of X-MRI to investigating neurodegenerative diseases such as Alzheimer's disease [Haeger 2021], disease Parkinson's, [Grimaldi 2021] and Multiple Sclerosis [Eisele 2019, Huhn 2019]. However, X-MRI presents its

challenges, mainly due to the relatively low intrinsic sensitivities of those exotic nuclei compared to the proton and the much lower *in vivo* concentrations of those chemical species in living times compared to water. This results in a thousandfold less signal when compared to proton MRI depending on the applications. Longer acquisitions times are needed to obtain useful image quality. Researchers must reach specific compromises in terms of spatial and temporal resolutions to tackle this issue while maintaining satisfactory detection thresholds. In this battle, continuous software and hardware developments are crucial to push forward the field and realize the promises of metabolic imaging using X-MRI.

NeuroSpin is a department of the CEA (Commissariat à l'Energie Atomique et aux Energies Alternatives - French Alternative Energies and Atomic Energy Commission). It is a research center dedicated to developing neuroimaging using MRI at ultra-high magnetic fields. It is equipped with three preclinical MRI scanners (7T, 11.7T, and 17T) and three clinical MRI scanners at 3T, 7T, and 11.7T (figure GI.1), the latest being the largest and strongest MRI scanner in the World (GI.2). There could not be a better place to develop X-nuclei MRI and its applications than NeuroSpin.

Figure GI.1 – Iseult 11.7T MRI Scanner : ©F.Rhodes – CEA

Even though many studies have been established to study possible biomarkers on the brain using ^{23}Na [Thulborn 2018] and ^{31}P MRI and MRS [Cadoux-Hudson 1989, Wang 2017b]. Due to lower nuclear sensitivity, lower concentrations when compared to ^{1}H MRI, acquisition time is still a limitation on the use of this application. This Ph.D. thesis aims to achieve methodological developments on ^{23}Na MRI and ^{31}P MRI to take a step closer to using ^{23}Na and ^{31}P MRI in neurodegenerative clinical research by accelerating

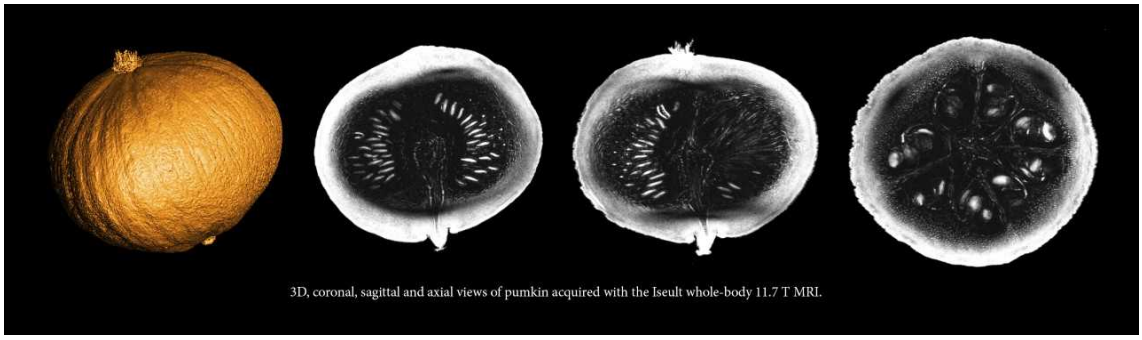

Figure GI.2 – Pumpkin images. From [Allard 2022]

X-MRI acquisitions. So, in the future, medical professionals could incorporate those techniques into their clinical routine and, therefore, be able to access cell metabolism and better understand neurodegenerative diseases.

Thesis objectives

So the goal of this thesis is to develop methods for cerebral metabolic imaging to investigate neurodegenerative diseases. Specifically, we aim to:

- ^{31}P MRI: Develop a clinical protocol able to quantify V_{ck} in the brain:
  - Estimate the absolute concentrations of high-energy phosphates: ATP and PCr;
  - Estimate the forward kinetic constant of the creatine kinase reaction.
- ^{23}Na MRI: Study the potential of 3D SPARKLING, an optimized **k**-space sampling scheme for undersampled sodium MRI:
  - Determine the optimal scenario in terms of spatial resolution and SNR for SPARKLING at 7T;
  - Study its ability to accelerate acquisition while preserving image quality when compared to state-of-art techniques such as TPI;
  - Quantify the impact of acceleration on quantification of total sodium concentration.

These developments should then be applied in clinical studies through collaborations.

The following two parts are dedicated to each of those sets of objectives: part II for phosphorus MRI development and part III for sodium MRI development, respectively.

Thesis Overview

This thesis consists of three parts. Part I describes some basic concepts essential to understanding this manuscript. The second one presents the work developed on ^{31}P, and

the third represents the work developed on ^{23}Na MRI. Together they described the past three years and the new research possibilities the contribution proposed here opens.

In detail, the first chapter 1 briefly describes the NMR phenomenon, the techniques behind MRI acquisitions are made as well how images are acquired and reconstructed in **k**-space. The chapter 2 presents the state-of-the-art of X-nuclei MRI, especially ^{23}Na and ^{31}P MRI, which were the focus of this thesis showing its motivation and challenges and how literature tackles this problem nowadays.

In Part II, we focus on ^{31}P MRI and propose a different way other than classical MRS approaches to assess flux through creatine kinase. The medical motivation is that we believe this could be a better imaging tool for the search of biomarkerers in neurodegenerative diseases. Currently, techniques have limited use in brain regions due to long spectroscopy acquisition. The part II presents our contribution for ^{31}P MRI and 3D flux estimation, developing a multiplex frequency selection sequence and protocol, and modeling applied along with a post-processing pipeline. We also show results acquired *in vitro* and *in vivo*.

The part III presents our contribution to ^{23}Na MRI and faster acquisitions. The protocol [Haeger 2021] takes around 30 minutes to image tissue sodium concentration at a spatial resolution of 3 mm isotropic. While this was possible in our clinical research protocol, using it in a clinical routine seems far from reality. Our contribution consisted of developing a simulation to evaluate the scenario of interest and parameters trajectories optimization. Finally, we show the results obtained *in vitro* and *in vivo* at 7T. This development multiplies clinical research possibilities, thanks to the reduction of time acquisition.

* * *
* *
*

Part I

Fundamentals and State-of-the-art

Chapter 1

Principles of X-nuclei NMR

Chapter Outline

The goal of this chapter is to summarize important concepts necessary to understanding this manuscript. Here, we briefly summarize basic concepts of nuclear magnetic resonance (NMR) phenomenon, pulse sequences, image acquisition and reconstruction.

For further information, the reader may referred to MR handbooks [Bernstein 2004, de Graaf 2007].

1.1 NMR phenomenon

MRI is possible thanks to the Nuclear Magnetic Resonance (NMR) phenomenon. I. Rabi first described this physical phenomenon in 1938 [Rabi 1938], which won him the Nobel Prize in Physics in 1944. This phenomenon will be explained in this section.

All atomic and subatomic particles possess an intrinsic property called spin. The NMR phenomenon can be observed in any atomic nucleus with a non-zero spin. This is typically the case for atoms with an odd number of protons, neutrons, or both. A spin can be defined by quantum mechanics' quantized number I (half-integer). In the absence of a magnetic field, the moment of spins cancels each other such that the atom's nucleus has no overall momentum. Each nucleus with a non-zero spin has a magnetic moment μ, which is defined as:

$$\mu = \gamma I \tag{1.1}$$

Where γ is the gyromagnetic ratio specific to the considered nucleus (Table 1.1), the proton, i.e., the nucleus of the hydrogen atom, is the most commonly used nucleus in NMR and MRI. Many other nuclei of interest for chemistry and biomedical research can be studied using NMR, as summarized in (Table 1.1).

Table 1.1 – The gyromagnetic ratios for several common nuclei

Nuclei	Spin (I)	Gyromagetic Ratio γ (MHz/T)	Natural Abundance (%)
^{1}H	1/2	42.576	99.9985
^{13}C	1/2	10.705	1.07
^{31}P	1/2	17.235	100
^{27}Al	5/2	11.103	100
^{23}Na	3/2	11.262	100
^{7}Li	3/2	16.546	92.41
^{29}Si	1/2	-8.465	4.68
^{17}O	5/2	5.772	0.038
^{15}N	1/2	-4.361	0.368

To give the reader an idea of the relative sensitivity of ^{23}Na applications, one must consider that in the healthy brain, sodium concentration is about 40 mM. While water abundance in human body is 88 M [Brown 2014]. This can lead to an signal-to-noise ratio (SNR) for ^{23}Na MRI of about 5500 fold less when compared to ^{1}H MRI [Ladd 2018]. Regarding ^{31}P, Phosphocreatine (PCr) concentration in an adult human brain [Buchli 1994], is in the order of 3.4 mM, which can lead to a large SNR deficit of up to 42000 fold less when compared to ^{1}H MRI, which is imaging the signal of water.

1.1.1 Precession

In the absence of a static magnetic field ($\vec{B_0}$), each nuclear magnetic moment is oriented randomly. However, once a $\vec{B_0}$ is applied, the spins will precess around $\vec{B_0}$ by aligning their rotation vector parallel or antiparallel to $\vec{B_0}$, leading to two different low or high energy states (for I=1/2).

The frequency of this precession is called Larmor angular frequency, and it is defined as:

$$w_o = \gamma B_0 \tag{1.2}$$

for the ordinary Larmor frequency (in Hz): $f_0 = \frac{w_0}{2\pi}$.

Depending on the intensity of the $\vec{B_0}$ field, the nucleus of interest, and the sample temperature, an average macroscopic magnetization $\vec{M_0}$ appears. The distribution of spins in the high or low-energy states follows the Maxwell-Boltzmann statistic. This average macroscopic magnetization is referred to as net magnetization. It can be observed from a large sample as derived from the Boltzmann statistics (for $kT \gg \gamma\hbar B_0$):

$$\vec{M_0} = \frac{\rho\gamma^2 h^2}{16\pi^2 kT}\vec{B_0}, \tag{1.3}$$

Where ρ is the number of nuclei per unit volume, also known as spin density, k is the Boltzmann constant, T is the temperature (in Kelvin), and h is the Plank's constant. At this thermodynamic equilibrium state, the net magnetization vector $\vec{M}$ is equal to $\vec{M_0}$ aligned along the static field $\vec{B_0}$. One can notice that the $\vec{M}$ depends on the intensity of $\vec{B_0}$, hence the benefit of working at ever more intense magnetic fields. Another way to increase the magnetization is to decrease the temperature. Albeit this is not possible *in vivo*, the principle of hyperpolarization is based on that fact. The high level of polarization (nearly all the electrons are aligned in the same direction) can be transfered to ^{13}C-labeled probes, which increases their MRI signal. Details of this approach can be found in Wang [Wang 2019].

1.1.2 Excitation

NMR signal can not be observed when $\vec{M}$ is aligned with $\vec{B_0}$. To detect this magnetization M, a secondary radiofrequency (RF) field $\vec{B_1}$ is used to flip $\vec{M}$ onto the transversal plane with regards to the orientation of $\vec{B_0}$. Initially, $\vec{M}$ is aligned with $\vec{B_0}$, and when $\vec{B_1}$ is applied, $\vec{M}$ will be tipped out of alignment. This $\vec{B_1}$ field, oscillating at frequency w_{rf} is transmitted through an RF coil [Hernandez 2020].

To resonate with the spins, the B_1 field oscillates at the Larmor frequency ($w_{rf} = w_0$). We will describe this system on the rotation frame of reference, where the rotation speed is set at the Larmor frequency. The magnetization now can be decomposed as:

$$\vec{M} = \begin{bmatrix} Mx \\ My \\ Mz \end{bmatrix} \text{ and } \vec{M}_{xy} = \begin{bmatrix} Mx \\ My \\ 0 \end{bmatrix} \tag{1.4}$$

when the $\vec{M}_{xy}$ is the transverse magnetization and $\vec{M}_z$ is called the longitudinal magnetization.

The nutation angle α, also known as flip angle (FA), is:

$$\alpha = \arccos\left(\frac{Mz}{||\vec{M}||}\right) \text{ for } 0 \leq \alpha \leq \pi$$
$$\alpha = \arcsin\left(\frac{||\vec{M}_{xy}||}{||\vec{M}||}\right) \text{ if } 0 \leq \alpha \leq \pi/2$$

The longer and more intense $\vec{B_1}$ is, the larger the FA that the net magnetization $\vec{M}$ experiences. When one does not consider $\vec{B_0}$ inhomogeneities in the sample (on-resonance), the relationship between the radiofrequency pulse $B_1(t)$ and α can be defined as:

$$\alpha = \gamma \int B_1(t)dt \tag{1.5}$$

If the pulse envelope is rectangular (the amplitude of $B_1(t)$ is a constant), the flip angle is:

$$\alpha = \gamma T B_1^+ \tag{1.6}$$

where T is the duration of the pulse and B_1^+ is the intensity of the transmission B_1. Let us define the transmit field generated by an RF coil as the B_1 field in the positively rotating frame of reference B_1^+, which can be defined in terms of x and y components of B_1 field in the laboratory frame of reference:

$$\mathrm{B}_1^+ = \frac{B_{1x} + iB_{iy}}{2} \tag{1.7}$$

B_1^+ is assumed to be rotating in the same direction as nuclear precession.

1.1.3 Relaxation

Following RF excitation, the longitudinal magnetization $\vec{M}$ is restored through relaxation processes characterized by two relaxation times: T_1 for the longitudinal magnetization $\mathbf{M}_z$ and T_2 for the transverse magnetization $\mathbf{M}_{xy}$. In the rotating frame of reference at angular frequency ω_0, the relaxation of the magnetization is modeled by the Bloch equations:

$$\frac{d\mathbf{M}_{xy}}{dt} = -\frac{\mathbf{M}_{xy}}{T_2} \tag{1.8}$$
$$\frac{d\mathbf{M}_z}{dt} = \frac{\mathbf{M}_0 - \mathbf{M}_z}{T_1} \tag{1.9}$$

The rotation of $\mathbf{M}_{xy}$ in the transverse plane induces an electromotive force (emf) through a reception coil that is often the same one used to excite the spins. This emf can be detected, and this signal is called the free induction decay (FID) [Hahn 1950] (Figure 1.1):

In MRI, the relaxation phenomenon brings information about the nuclei environment, and these relaxation times are responsible for different images contrasts:

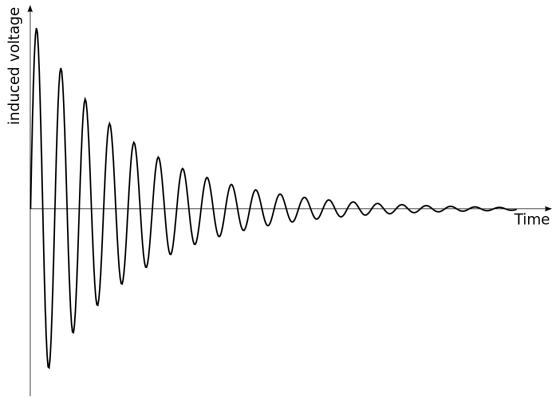

Figure 1.1 – Free induction decay

- T_1 weighted images: In complex biological environments such as tissues, molecules (and therefore their constituent atoms) tend to possess slow to intermediate correlation times, leading to shorter longitudinal (and transverse) relaxation times. Consequently, steady-state magnetization is larger where the T_1 is shorter, leading to brighter pixel intensities on T_1 weighted images. In opposition, free water has slower longitudinal relaxation times and lower pixel intensities (even dark pixels if the inversion time is set right).

- T_2 weighted images: T_2 is defined as the characteristic time governing the decay of the macroscopic magnetization in the transverse plane. This arises from the loss of phase coherence between magnetic moments intrinsically due to energy transfers at the atomic or molecular levels between spins ("spin-spin" interactions). The T_2 decay or amount of dephasing the spin population experience depends on multiple factors. As for T_1 times, T_2 values for a considered molecule/atom differ between tissues according to their correlation time, the longer the correlation time the shorter the intrinsic T_2.

- T_2^* weighted images: in any actual NMR experiment, the transverse magnetization decays much faster than can be predicted from its intrinsic T_2 value. This effective decay is characterized by the T_2^* relaxation time. This faster T_2^* decay results essentially from the additional loss of phase coherence brought by the B_0 static magnetic field inhomogeneities at the microscopic and macroscopic levels. These inhomogeneities might be the after-effect of natural deformities in the actual magnet or vulnerability prompted by field distortions created by the tissue or different materials set close to or within the sample/subject. The effects of those $\vec{B_0}$ changes can be recovered when using spin-echo sequences such as Rapid Acquisition with Relaxation Enhancement (RARE). For more details, one can refer to [Hennig 1986].

The term T_2^* can be defined:

$$\frac{1}{T_2^*} = \frac{1}{T_2} + \gamma \Delta B_0$$

where ΔB_0 represents the variation of the effective B_0 field across the considered pixel or voxel.

On spin-echo (SE) imaging, the TR and the TE are used to control image contrast and the "weighting" of the MR image. By varying the relationship between TR and TE, we obtain the different contrast:

- short TR and short TE: T_1 weighted images
- long TR and long TE: T_2 weighted images or, possibly, T_2 * weighted images
- long TR and short TE: Proton density weighted images

We say TE is short when compared to T_2 and the ratio $TE/T_2 \to 0$. When TR is long compared to T_1, the T_1-weighting term $e^{-TR/T_1} \to 0$.

Chemical Shift

In addition to the external static magnetic field B_0, nuclei experience an induced local magnetic field originating from their immediate electronic cloud. As a consequence, the total magnetic field experienced by the nuclei is different depending on their electronic orbitals (remember that electrons themselves have a magnetic moment). The electronic cloud (or probability distribution) around a given nucleus (^{1}H, ^{13}C, ^{15}N, etc.) depends on the molecule it belongs to and its possible conformations/geometry (bond partners, bond lengths, angles between bonds, etc...). Thus, nuclei in a molecule resonate at slightly different resonance frequencies due to the "shielding effect" of their electronic cloud. One can define a "shielding" constant σ:

In nuclear magnetic resonance spectroscopy (MRS), the chemical shift (expressed in ppm) is defined as the relative resonance frequency of a single or a group of equivalent nuclear spins typically from a specific molecular moiety with respect to a reference chemical compound (e.g. TMS: tetra-methyl silane in ^{1}H MRS) used as a standard of chemical shift ($\delta_r ef$ = 0 ppm): $\delta = (\hat{-}\hat{}\mathbf{ref})/\mathbf{ref}$

The chemical shift values are independent of the intensity of the B_0 field. Therefore, for any given molecule, the set of chemical shift values (with the corresponding peak intensities) serves as a "signature" of the molecule in question.

1.2 From FID to image

1.2.1 Excitation: selective and non-selective

The main characteristics of a $\vec{B_1}$ RF pulse are its waveform (amplitude and frequency/phase modulation), duration, bandwidth, and effective/targeted flip angle. Short and intense pulses, rectangles, also known as hard pulses, are most used to achieve uniform spin excitation across a given frequency range [de Graaf 2007]. When a particular type of spectral selectivity is needed, other pulses are preferable, such as gaussian and sinc pulses. This is because the spectral selectivity profile is given by the Fourier transform (FT) of the

considered pulse. In the case of the hard pulse, the sinc form of its FT leads to offresonance excitation (Figure 1.2).

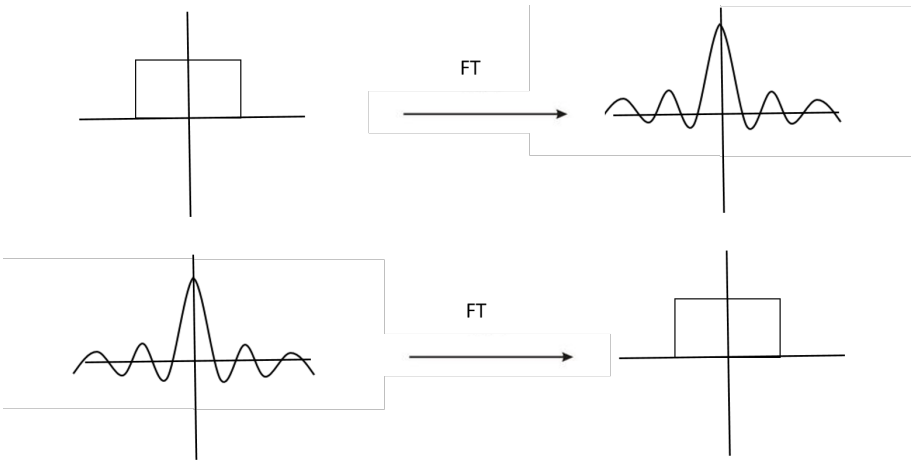

Figure 1.2 – A rectangle's Fourier transform (FT) is a sinc pulse and vice versa. The inverse FT converts the curve back to square on the left

.

Better selectivity profiles can be obtained with more sophisticated pulses such as Shinnar-Le Roux (SLR) [Pauly 1991a]. Sinc pulses are still primarily used for easy implementation, especially for small flip angles [de Graaf 2007]. Similar pulses can be used for inversion and refocusing.

Spatially Selective Excitation

In some applications, spatially selective excitation is required. In theory, a perfectly rectangular profile in the frequency/space domain can be obtained with an infinite sinc pulse in the time domain combined with the appropriate selection gradient. However, this is impossible in practice due to the limited T_2 and T_2^* times. Therefore truncation of the RF pulse profile is needed.

During the application of spatially selective RF pulses, a gradient pulse $\mathbf{G} = [G_x G_y G_z]^T$ must be applied to achieve the expected spatial selectivity (position, orientation, slice thickness). This gradient modifies the static field at any given point $\mathbf{r}$ in the coordinates system (x,y,z). The total static magnetic field is then:

$$B(\mathbf{r}) = B_0 + \mathbf{rG} \tag{1.10}$$

The resonance condition is then modified to:

$$w(\mathbf{r}) = \gamma B_0 + \gamma \mathbf{rG} - \omega_{rf} \tag{1.11}$$

where ω_{rf} is the angular frequency of the radio-frequency pulse.

This means that the Larmor resonance frequency now depends on the position r. Therefore, there will be coordinates for which the RF excitation pulse is on-resonance and others for which it will be off-resonance, determining the achieved slice selection profile. In

particular, the slice thickness is determined by the gradient strength and the bandwidth of the RF pulse.

With the introduction of these static field gradients, there is now a linear relationship between the off-resonance term $\Delta\omega$ and location $\mathbf{r}$. In particular, when neglecting B_0 inhomogeneity, and when matching ω_{rf} with ω_0, the equation 1.11 simplifies to:

$$w(\mathbf{r}) = \gamma \mathbf{r}\mathbf{G} \tag{1.12}$$

As pictured in the figure 1.3, a single gradient G_Z is applied in the Z direction: we can write $\omega(Z) = \gamma G_Z Z$. In order to selectively excite a slice of thickness W positioned at $Z = 0$, one must apply a pulse of bandwidth $BW = \Delta\omega(W/2) - \Delta\omega(-W/2) = \gamma G_Z W$ at the Larmor frequency ω_0.

A rectangular spectral response is achieved with a pulse of sinc temporal envelope (in practice, a sinc pulse truncated after a few zero-crossings), with the main lobe of duration $2/\mathrm{BW} = 2/\gamma G_Z W$. More generally, in the equation 1.11, the same pulse envelope can be used to excite any slice centered around Z_C by adjusting ω_{rf} accordingly:

$$\omega_{rf,C} = \omega_0 + \gamma G_Z Z_C \tag{1.13}$$

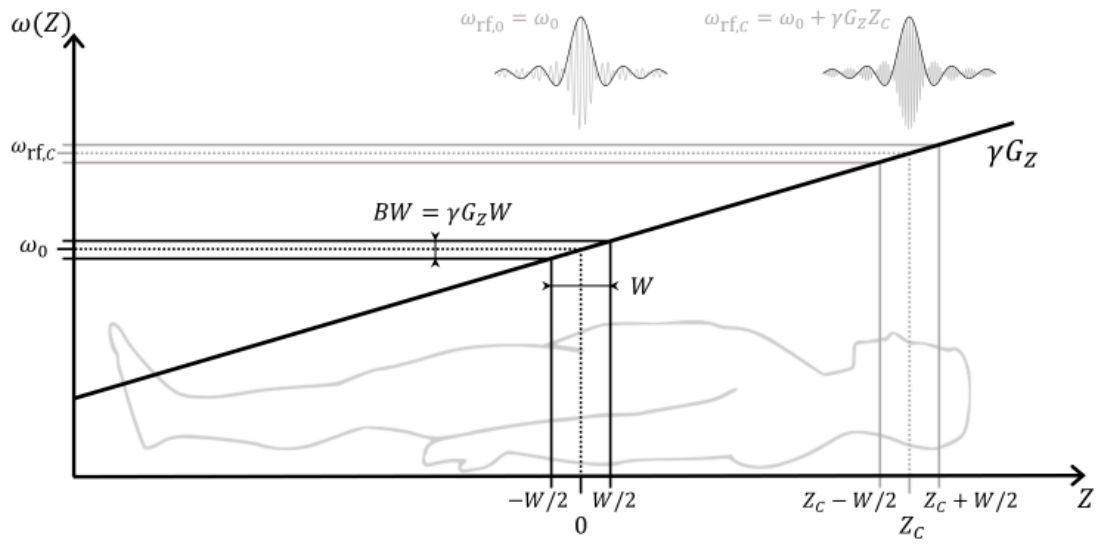

Figure 1.3 – Illustration of spatial selection of a transversal slice by coupling a linear static field gradient G_Z along Z and a spectrally selective pulse with a sinc envelope. A slice of thickness W around the isocentre (left, in black) is selected by applying a pulse whose carrier frequency ω_{rf} matches ω_0 and whose envelope corresponds to a bandwidth BW = γG_ZW. From [Tomi-Tricot 2018].

For 3D images, non spatially selective excitation is often applied. No gradient is needed during the RF excitation. Typically, to avoid non-excitation due to ΔB_0 broad pulses in frequency spectra are used like the rectangle pulses. In this case, $\alpha = \gamma \mathrm{B}_1^+ T$, where T represents the duration of the RF pulse. In this thesis, we are often interested in 3D non-selective excitation because they provide the higher SNR possible.

Spectrally selective excitation

The primary magnetic field $\vec{B_0}$ is shielded by electrons, reducing the net magnetic field experienced by nuclei. Consequently, various intra-molecular and inter-molecular circumstances (e.g., atoms in different molecules or ionic/electronic interactions within and between molecules) lead to slightly different Larmor frequencies due to this shielding. Chemical shifts are quantified by a dimensionless metric δ which describes the relative difference in the frequency with a "reference" Larmor frequency (expressed in ppm):

$$f = \frac{\gamma}{2\pi} B_0(1 - \delta) \tag{1.14}$$

Spectrally selective RF pulses selectively excite the spins of particular chemical species (typically fat or water protons in conventional MRI). ^{31}P spectra also have several metabolites of interest (figure 1.4). To observe a specific metabolite, one must set the frequency of their B_1 RF field to match the resonance frequency of this metabolite. To obtain a good selectivity, a narrow frequency bandwidth pulse is needed. As shorter bandwidths are linked to longer RF pulses, spectral selectivity requires longer RF pulses and leads to larger T_2*-weighting and loss of signal. Gaussian pulses offer a good compromise. Alternatively, one can use Hermitian or sinc pulses. More sophisticated solutions are numerically optimized pulses such as the Shinnar-Le-Roux (SLR) [Pauly 1991b] or even asymmetric RF pulses [Starcuk 1993].

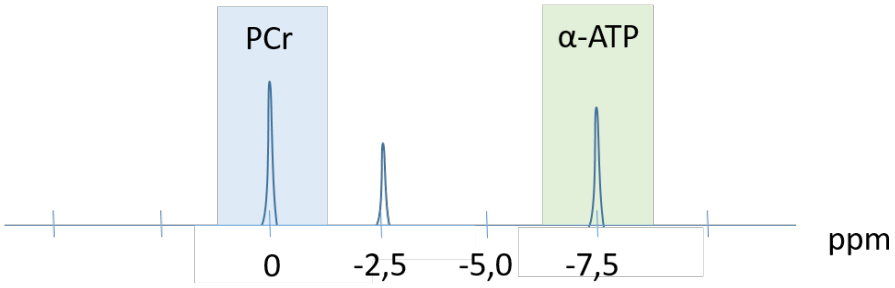

Figure 1.4 – Schema of simplified spectra of ^{31}P at 7T in the human brain. PCr stands for phosphocreatine, α-ATP stands for the α (first phosphate group) resonance of adenosine triphosphate.

1.2.2 Spatial encoding

By default, the FID only gives spectral information about the sample without any spatial specific information. To do so, magnetic field gradients are used to encode this spatial information. This is the basis of MRI. Paul Lauterbur and Mansfield first discovered this [LAUTERBUR 1973]. Lauterbur applied magnetic field gradients rotated successively by 45°, and he was able to obtain four different one-dimensional projections of an object via its NMR signal.

The Larmor frequency is proportional to the static field intensity; by adding time-varying gradient pulses to $\vec{B_0}$, the precession frequencies (or phases) of spins would vary

spatially. These different frequencies (or phases) can be separated and inform us about the spatial distribution of these spins in the object:

$$\omega(x) = \gamma B(x)$$

- frequency encoding, a unique precession frequency to each spin at a distinct spatial location, linearly depending on spatial location. This technique can be applied in any physical direction during the signal readout.

$$\omega(x) = \gamma(B_0 + G_x(t))$$

- phase encoding consists in applying a gradient lobe with linearly incremented intensities while the magnetization is in the transverse plane (before signal readout). For Cartesian 3D MRI, phase encoding is usually applied orthogonally to the slice and frequency encoding directions. For a y phase-encoding gradient G_y:

$$\varphi(x) = \gamma \int G_y(t)dt$$

1.2.3 RF Coils

Radiofrequency coils come in all shapes and sizes. There does not exist a single coil design optimal for all MRI applications.

The "birdcage" volume was MRI's first popular coil configuration [Bernstein 2004] (Figure 1.5).

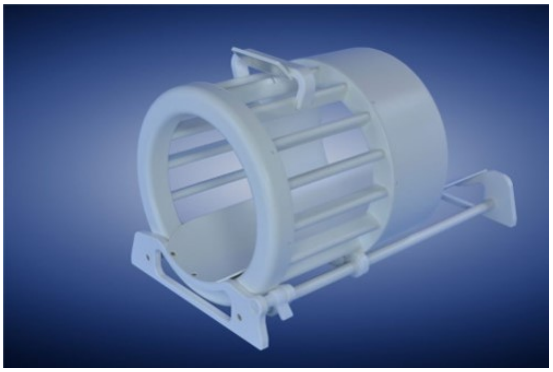

Figure 1.5 – Dual Tuned ^{31}P-^{1}H Quadrature Head Coil for 7 T using birdcage coil design from rapid biomedical.

Figure 1.6 – Helmet Head coil for 7T with one channel in transmission and 32 channels reception from Nova.

Ideally, a transmit coil generates a uniform RF field for a homogeneous excitation throughout the brain. It is defined by its transmission profile (B_1^+). Another critical property is its transmission efficiency, i.e., the power needed to generate a unit of Rf field (usually expressed in W/µT).

The primary property of a good reception coil is its sensitivity to the organ of interest. Typically, the smaller the coil, the more sensitive it should be. However, the reception coil or array of coils must also cover the whole organ of interest with minimal sensitivity bias

throughout. Consequently, a trade-off needs to be found. The sensitivity is defined by its reception profile (B_1^-).

Birdcage design privileges a homogeneous B_1^+ field. However, their sensitivity is compromised due to their large size and often poor filing factor (ratio of the volume occupied in the coil and total volume) [de Graaf 2007]. Surface coils are more sensitive, but their B_1^+ is highly inhomogeneous.

Typically, a birdcage is desirable for transmission and a surface coil for reception. Some commercial coils use the birdcage design for both transmission and reception. For a single coil in transmission and reception, and at low frequency, $B_1^+ B_1^- = 1$. This idea of reciprocity provides a handy approach for estimating the reception sensitivity from the transmitted RF field pattern in NMR spectroscopy and MRI. Hoult et al. were the first to describe the reciprocity principle for NMR. [Hoult 2000].

While complex, more efficient/sensitive designs exist. One such design is the helmet coil which consists of an array of reception loops positioned close to the head in the shape of a helmet. This design increases the SNR obtained, but as a trade-off, B_1^+ maps are inhomogeneous and need to be accounted for in the image reconstruction pipeline.

Power deposition

The transmit coil emits energy (via the E and H fields) that is dissipated in the brain/body as heat. With higher static magnetic fields, this energy increases quadratically, leading to potential heating hazards.

To address this problem (for MRI and another electromagnetic devices such as cell-phones), authorities elaborated norms/guidelines to dictate the limits acceptable for specific absorption rate (SAR). It is defined by:

$$\mathrm{SAR} = \frac{1}{V} \int_{\mathrm{sample}} \frac{\sigma(\mathbf{r}) |\mathbf{E}(\mathbf{r})|^2}{\rho(\mathbf{r})} d\mathbf{r} \tag{1.15}$$

where σ is the sample electrical conductivity, E is the root mean square of the electric field, ρ is the sample density, and V is the sample volume. The human body can tolerate up to a few watts per kilogram of tissue before its temperature increases. SAR constraints directly impact the design of high-energy pulses such as adiabatic pulses, limiting their clinical applications at UHF. Pulse optimization methods exist to lower the energy of such pulses under SAR/B_1^+ constraints as bandwidth-modulated adiabatic selective saturation and inversion (BASSI) [Warnking 2004]. BASSI pulses are derived from an analytical calibration equation that allows the determination of the precise amplitude to achieve any effective flip angle. However, pulse optimizations are out of the skope of this thesis.

1.3 MRI pulse sequences

This section describes the sequences used in this Ph.D. thesis. The application of RF pulses and gradients waveforms in a timely manner define an MRI pulse sequence. The initial combination of these two elements is usually repeated within loops to acquire all the

intended slices/weightings or dimensions of **k**-space incrementally. We focused on ^{23}Na and ^{31}P 3D MRI in this work. In those 3D MRI sequences, **k**-space encoding is realized using non-Cartesian frequency encoding along so-called "Spokes," i.e., predetermined sequences of points acquired in the k-space during each TR. In those sequences, the time between the middle of the RF excitation pulse (when the nutation occurs) and the acquisition of the first point (usually at the center of **k**-space) is called the echo-time (TE). In contrast, the delay between two consecutive excitations is called the repetition time (TR). The TR, TE, and FA values determine the (T_1/T_2^*) contrast obtained in the MR image.

1.3.1 Gradient-recalled-Echo

The most generic MRI sequence is the cartesian gradient-recalled-echo (GRE) sequence.

The diagram of this sequence for a 3D non-selective non-cartesian acquisition is shown in the figure 1.7. This sequence consists of a nutation of α followed by applying frequency encoding gradients in XYZ during readout. By relying solely on frequency encoding, this sequence avoids slice selection gradients during RF excitation and phase encoding gradients just before readout saving time and allowing short or ultra-short TE.

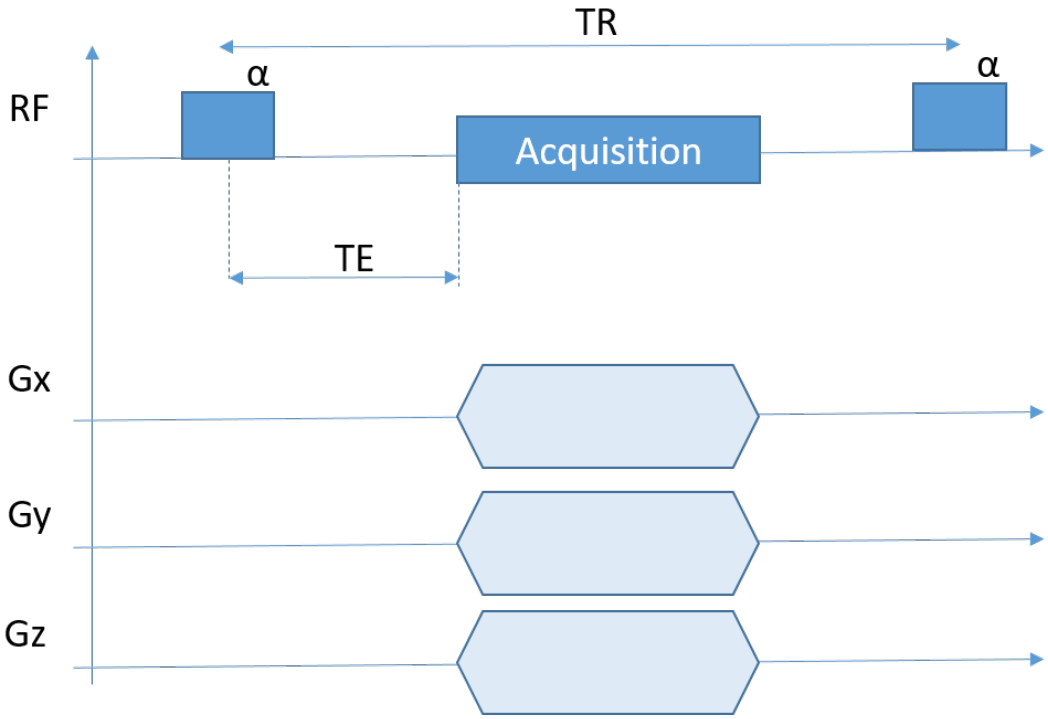

Figure 1.7 – GRE sequence for 3D non-selective imaging for cartesian sampling.

The main problem of this sequence is that it assumes $TR >> T_1$ to guarantee fully longitudinal magnetization before the next RF pulse. In reality, this rarely happens because it would lead to ineffective and long acquisition times.

1.3.2 Spoiled Gradient-recalled-Echo

To shorten TR while avoiding unwanted coherence pathways, a technique called "spoiling" is applied. Two types of spoiling are used: Gradient Spoiling and RF-Spoiling.

RF Spoiling consists in incremental a phase-cycling pattern on the RF pulses. The design applied in this work is [Zur 1991]:

$$\begin{cases} \theta_0 & = \theta_{inc} \\ \theta_n & = \theta_{n-1} + n\theta_{inc} \end{cases}$$

where $\theta_{inc} = 119°$.

The gradients are counterbalanced by a spoiling gradient applied at intensity strong enough at the end of each cycle. The purpose of these gradients is to scramble the phase and destroy the chance of unwanted coherence. Without the spoiling, the resonant offset will vary from cycle to cycle (because the phase encoding steps change). Therefore, the phase encoding information from one cycle can "spill over" to the next cycle, creating unwanted stimulus echoes and flash bands in the image.

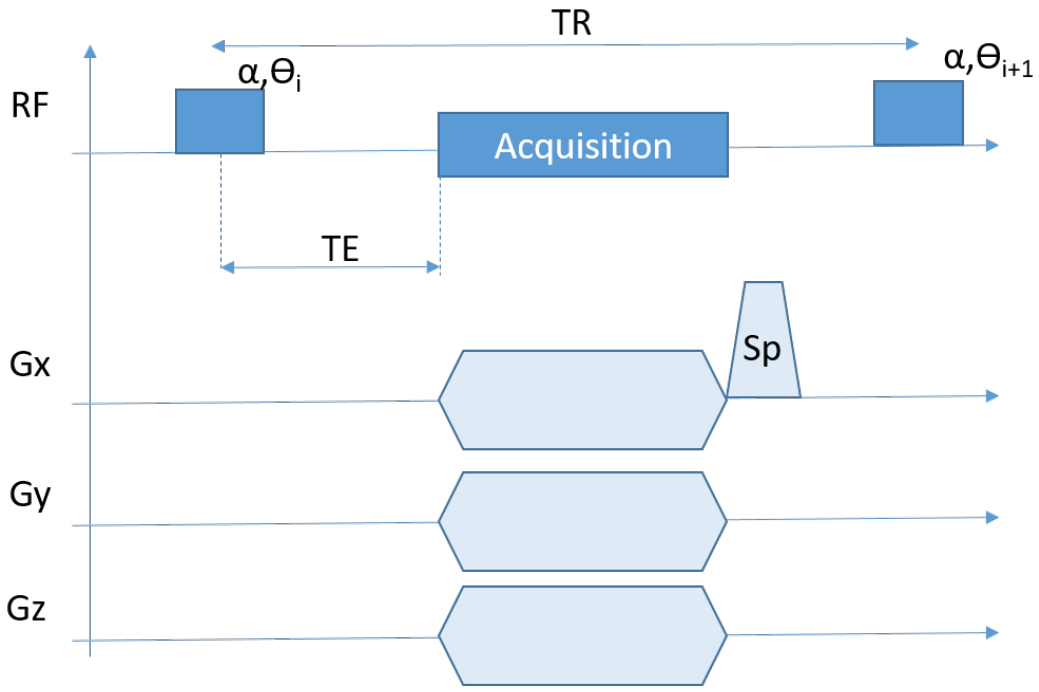

Figure 1.8 – SPGRE sequence for 3D non-selective- imaging.

Assuming a perfect spoiling and that a steady-state is obtained, then the signal equation of this sequence is [Ernst 1966]:

$$S(t) = k\mathrm{SD}\sin\alpha\left(1 - \frac{1 - E_1}{1 - E_1\cos\alpha}\right)E_2^* \tag{1.16}$$

with $E_1 = \exp\left(\frac{TR}{T_1}\right)$ and $E_2^* = \exp\left(\frac{TR}{T_2^*}\right)$ where k is a constant and SD is the spin density. From this equation, we can obtain that for a given (T_1, TR), the MRI signal is

maximized for $\alpha = \alpha_E$, called the Ernst angle:

$$\alpha_E = \arccos(E_1). \tag{1.17}$$

This sequence allows for a fast acquisition by controlling α for a given TR. A short TR is often expected to avoid dead times. This sequence will be the base for all sequences developed in this thesis. The shape of readout gradients will change depending on the non-cartesian sampling scheme chosen.

1.3.3 Ultra short echo time sequences

In MR experiments, the transversal magnetization decays with T_2^*. Standard MR sequences offer echo times in the range of a few milliseconds for spin-echo sequences and down to 1 ms for gradient-echo sequences. Signals arising from tissues with a very short T_2, well below 1 ms, are therefore not visible using standard sequences, as the signal has already decayed by the time of acquisition.

If the $TE << T_2^*$, typically a fraction of an ms, this sequence qualifies as a ultra-short echo time (UTE) sequence, and the T_2^*-weighting is negligible. To minimize this TE delay, slice selection gradients are turned off, and the acquisition starts as soon as possible after the RF excitation. Typically, it takes about 10-50 μs of dead time between transmit and receive is limited by post-transmit attenuation of the coil with stored RF energy and reconditioning of the receive coil prior to acquisition. Since the aim is to start the acquisition immediately, there is no time for phase encoding or phase relaxation read gradient [Robson 2003], so a non-Cartesian spoke from the center to the rim of the **k**-space is required. Classically in UTE MRI, **k**-space is sampled radially, but helical sampling is also used for sampling with slightly longer signal lifetimes [Du 2008]. A center-out sampling pattern is desirable because it minimizes T_2^*-weighting and ensures that the maximum signal is obtained at the center of **k**-space.

The following section will explore **k**-space sampling patterns used in those UTE MRI sequences.

1.4 K-space sampling

1.4.1 K-space

The MRI signal at the end of the receive chain can be written as follows:

$$S(t) = \int_{V_s} \rho(\mathbf{r}) \exp^{r\Phi(r,t)} d\mathbf{r} \tag{1.18}$$

where $\rho(\mathbf{r})$ is the effective spin density, the V_s the volume sampled, and the accumulated phase in radians is:

$$\mathbf{\Phi}(\mathbf{r}, t) = \gamma \int_0^t \mathbf{r}\mathbf{G}(\tau) d\tau \tag{1.19}$$

A function $\mathbf{k}(t)$ defined in what is called **k**-space, also known as the spatial frequency domain, is a grid of raw MRI data, where the vector $\mathbf{k}= k_x, k_y, k_z$ represents each coordinate [Ljunggren 1983, Twieg 1983].

$$\mathbf{k}(t) = \gamma \int_0^t \mathbf{G}(\tau) d\tau \tag{1.20}$$

Now the equation 1.18 can be rewritten as:

$$S(t) = \int_{V_s} \rho(\mathbf{r}) \exp^{-i\mathbf{k}(t)\mathbf{r}} \, d\mathbf{r} \tag{1.21}$$

The signal in each **k**-space point contains spatial frequency and phase information about every pixel in the final image, and the overall set of k-space points corresponds to a sampling of the spatial Fourier transform of the spin density function (to which one could eventually add the different weightings and eventual bias). **K**-space is the Fourier transform of the MR image measured (Figure 1.9). The low spatial frequencies near the center of **k**-space contain most of the overall signal in the image, while the high spatial frequencies contain finer contrasts/details.

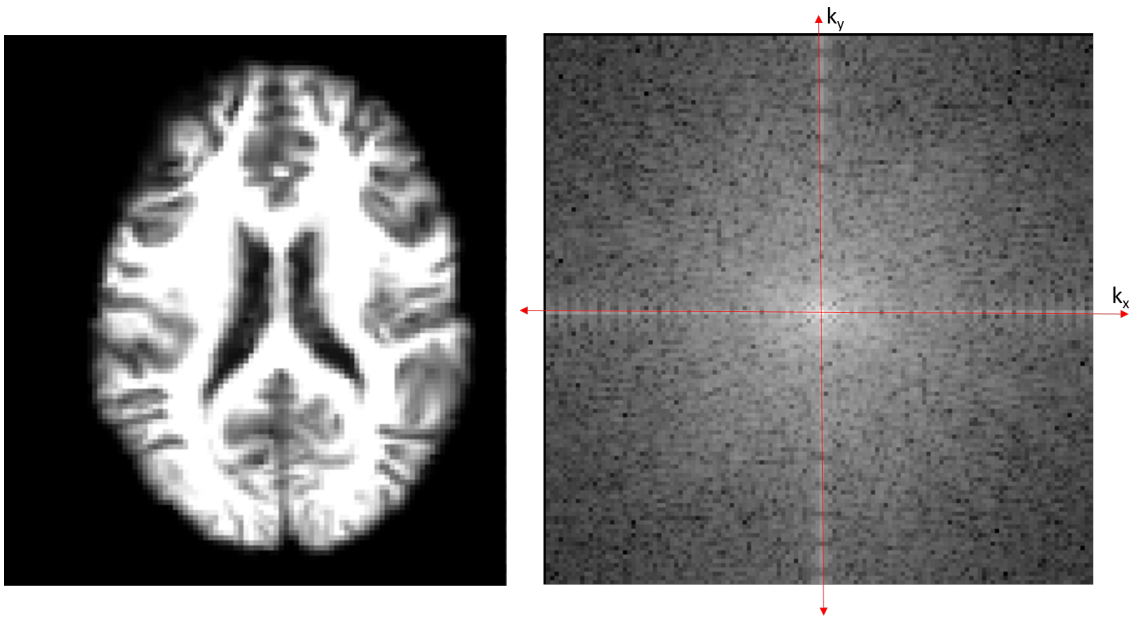

Figure 1.9 – Central slice of MP-RAGE at 2 mm isotropic and its corresponding Magnitude of Fourier Transform.

Nyquist-Shannon Theorem

The Nyquist-Shannon theorem is announced as follows [Shannon 1949]:

> **Theorem 1.** If a function $x(t)$ contains no frequencies higher than B (Hz), it is entirely determined by giving its ordinates at a series of points spaced $1/(2B)$ seconds apart.

This means the digital sampling rate must be at least twice the highest frequency within that signal to measure a signal correctly. B stands for bandwidth.

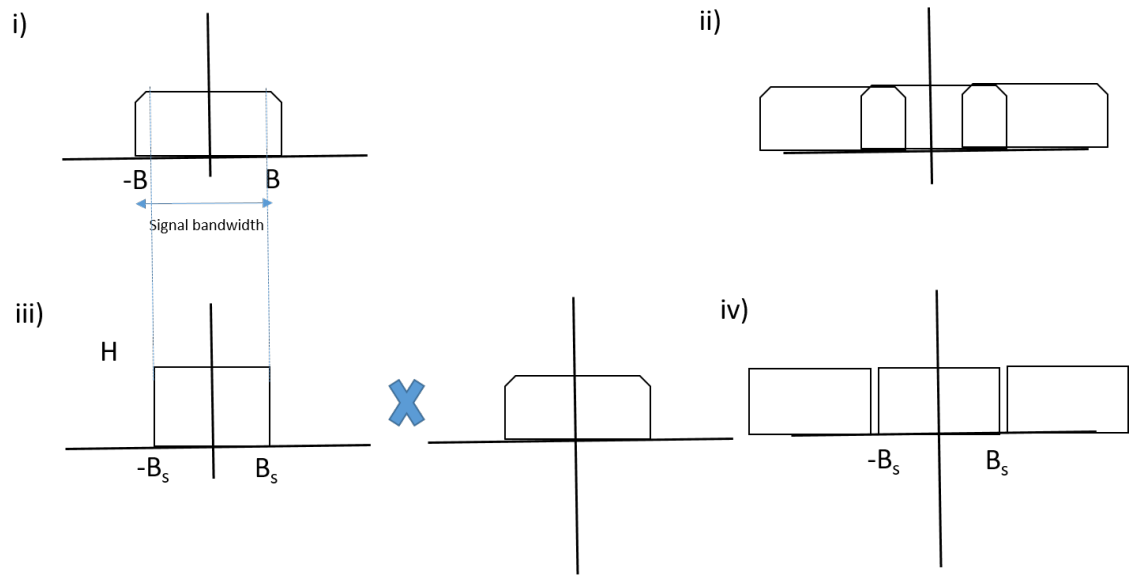

Figure 1.10 – Fourier transform of a time-domain signal (i) before sampling and (ii) after discrete sampling at frequency f_s. The frequency domain replication interval is $f_s = 1/\delta$t. Because $f_s <$ 2B, the replicates overlap resulting in aliasing. (iii) Fourier transform of the signal in (ii) after windowing with a low-pass filter H of cut-off frequency $B_s <$ B. (iv) Resulting Fourier transform of (iii) after discrete sampling at frequency f_s

For 3-D cartesian trajectories, the Nyquist-Shannon condition can be simply described as $N_s \geq (k_{max}L)^2$ where $k_{max} = \dfrac{1}{2 * \Delta x}$, where Δx stands for the target resolution. For 3-D radial trajectories, the Nyquist-Shannon condition is defined as : $N_s \geq 4\pi(k_{max}L)^2$.

Point spread function

A valuable criterion to evaluate/compare k-space sampling schemes is the point spread function (PSF), which is defined as the modulus of the Fourier transform of the sampling pattern viewed as a set of Dirac impulses:

$$PSF(\mathbf{r}) = \int e^{i\mathbf{k}(t)\mathbf{r}} dt \tag{1.22}$$

If the object observed was a Dirac impulse, PSF is the image reconstructed. A more general term for the PSF is a system's impulse response. The perfect PSF, meaning a system that does not induce a loss of spatial information via signal bleeding, would also be a Dirac impulse. The degree of blurring of the point-like object is a measure of the quality of an imaging system.

1.4.2 Methods of filling k-space

The most common way of acquisition used nowadays is the Cartesian sampling scheme. It consists in filling **k**-space row by row. The advantage of this method is that it is easier to

acquire and is the most efficient way of respecting the Nyquist-Shannon criteria. Cartesian acquisitions also allow for easier/faster reconstructions via the direct application of FFT techniques (for more details, the reader may refer to section 1.5). In the figure 1.11, we can see examples of common 2D cartesian and non-cartesian trajectories.

However, a non-Cartesian sampling scheme offers significant advantages in acquisition time, efficient use of MRI hardware, and reduction in sensitivity to motion and flow. Cartesian acquisition schemes are not appropriate for UTE MRI and thus not often used to acquire X-nuclei MRI data [Konstandin 2014]. This is because many of these nuclei have short relaxation times, which makes it more interesting to use center-out spokes. Moreover, they allow the physicist to focus on low spatial frequencies where most of the rare MR signal is.

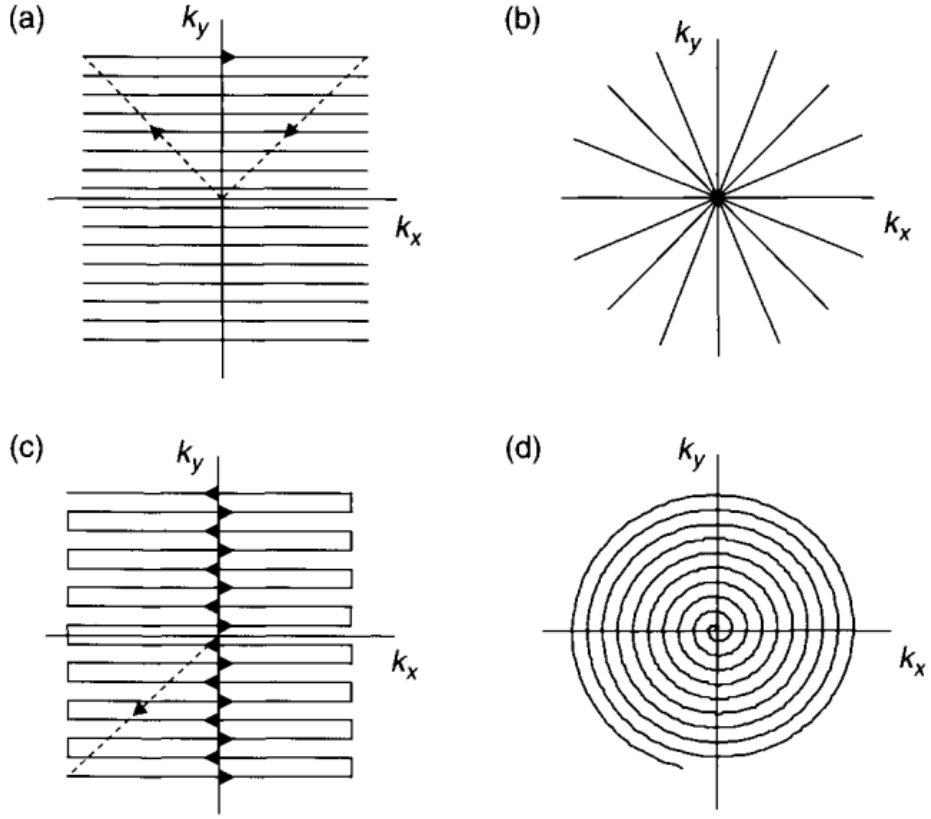

Figure 1.11 – **K**-space trajectories for some commonly used trajectories (a) standard Cartesian, (b) radial, (c) echo-planar imaging, and (d) spiral from UTE sequences. From [Bernstein 2004].

In general, for any MRI protocol, SNR varies according to this equation:

$$\mathrm{SNR} \propto \mathrm{SD} B_0^{\beta} f_{coil}(B_1^-) \Delta V f_{seq}(TR, TE, \alpha) \sqrt{N_{shots} T_{obs} N_{avg}}, \tag{1.23}$$

where SD is the spin density, B_0 is the main magnetic field with a power β about 2 [Le Ster 2022], f_{coil} is a sensitivity function linked to the B_1^- sensitivity profiles of

the receiver coil elements, ΔV is the voxel volume, f_{seq} the signal equation depending on the sequence used and its core parameters, N_{shot} number of shots/spokes, T_{obs} the observation/acquisition time per TR and N_{avg} the number of average.

It is known that SNR is the bottleneck for X-MRI applications, and the equation 1.23illustrates the trade-off that needs to be found.

While some X-MRI applications have used 2D radial [Song 2004, Chandarana 2011] or stack of spiral trajectories the [Irarrazabal 1995, Thedens 1999], 3D acquisition is often more advantageous in term of SNR per unit of time. Indeed, for full 3D MRI acquisitions, signal originates from the whole sample. Moreover, the TR for 3D MRI acquisitions can usually be shorten further than for 2D multislice MRI acquisitions, which is advantageous for nuclei with short T_1 relaxation times. Yet, since the whole 3D **k**-space must be filled – which takes time – before reconstructing, 3D imaging is more sensitive to patient motion. Any spatial information damaged during acquisition impacts the quality of all pictures in the volume. In 2D imaging, however, each slice is reconstructed individually. Thus motion during the acquisition of one slice has no bearing on the remainder of the FOV. However, as we work at relatively low spatial resolution in X-MRI, this limitation is less critical.

We can divide strategies of sampling of **k**-space into two types: parametric and optimization-based trajectories. The two types are described below.

3D Non-cartesian parametric trajectories

Parametric trajectories are the trajectories for which a set of equations defines the gradient waveforms. They are easy to compute and therefore adaptable on the MRI console for different parameters. For the non-Cartesian **k**-space sampling scheme currently used, we can cite radial, density-adapted three-dimensional radial projection reconstruction pulse sequence (DA-3DPR) [Nagel 2009], Twisted Projection Imaging (TPI) [Boada 1997] or Fermat-looped orthogonally-encoded trajectories (FLORET) [Robison 2017]. Some of those are illustrated in the figure 1.12.

Due to their deterministic nature, the inherent sparsity of **k**-space is not fully exploited by those parametric trajectories. Even though undersampling for those radial or TPI trajectories affect notably the quality of the PSF, proper reconstruction techniques (density compensation, regridding algorithms, iterative reconstruction ...) can lead to satisfactory results [Hoge 1997, Block 2007, Stobbe 2008, Zeng 2013].

3D Non-cartesians non-parametric trajectories

Non-parametric trajectories, also known as optimization-based trajectories, offer better exploitation of **k**-space. Several attempts have been made in proton MRI to improve the sampling scheme [Kumar Anand 2008, Mir 2004, Dale 2004]. The idea is the base of compressed sensing techniques: (i) global variable density sampling but (ii) locally uniform coverage of **k**-space [Lustig 2007].

A promising CS technique that will be exploited in this thesis is SPARKLING [Lazarus 2019, Chaithya G R 2022]. SPARKLING stands for Spreading Projection Algorithm

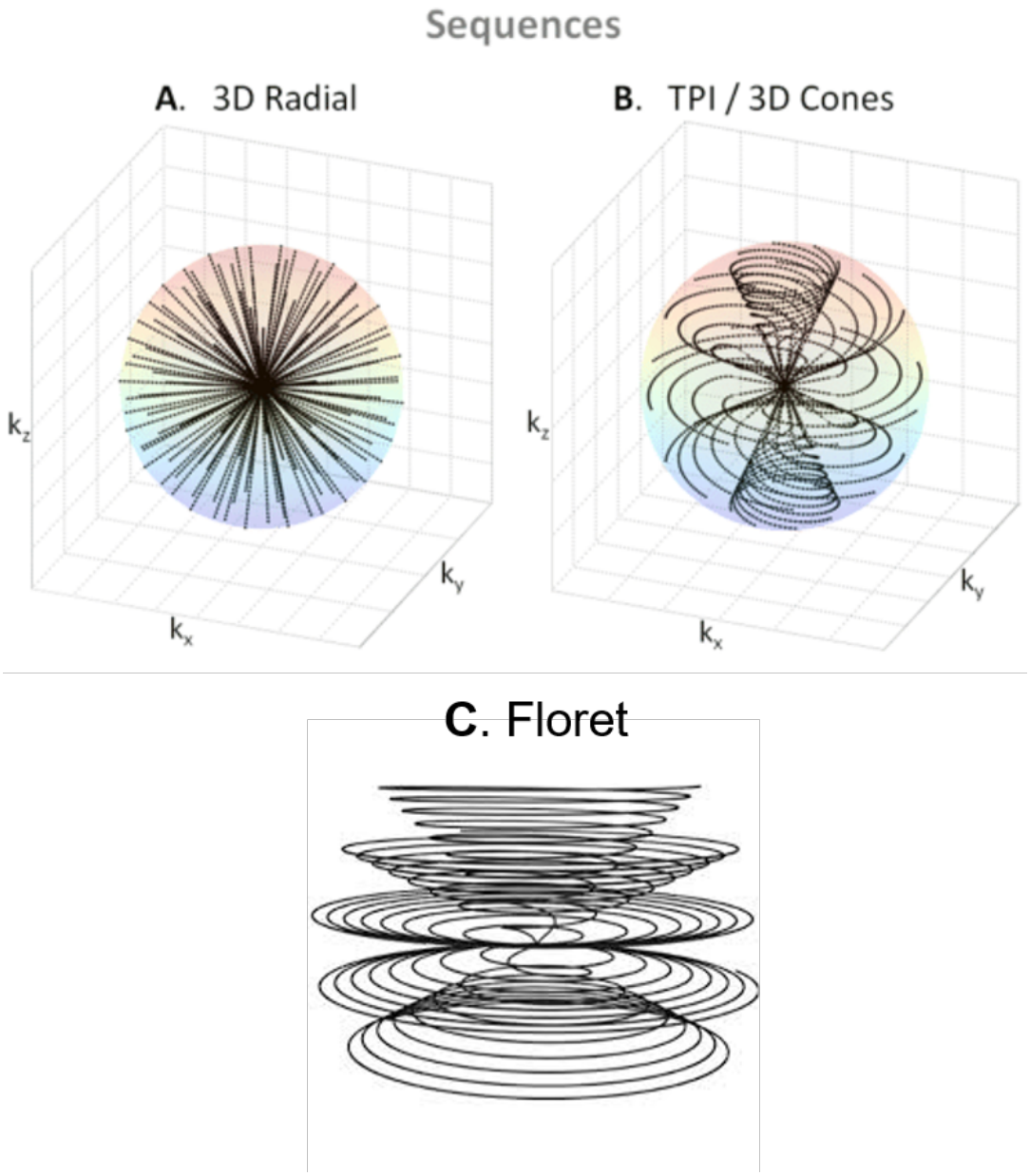

Figure 1.12 – **K**-space trajectories from UTE sequences. A. 3D radial. B. Twisted projection imaging (TPI) or 3D cones types of sequences. From [Madelin 2012]. C. Floret.

for Rapid K-space samplING developed at NeuroSpin by Philippe Ciuciu and colleagues. SPARKLING is an optimization-driven method that has been recently introduced for accelerated 2D $T_2^* - w$ MRI using compressed sensing. It has then been extended to address 3D imaging using either stacks of 2D sampling patterns or a local 3D strategy that optimizes a single sampling trajectory at a time. SPARKLING has the advantage of performs variable density sampling (VDS) along a prescribed target density while maximizing sampling efficiency and meeting the gradient-based hardware constraints.

The trajectory $\hat{\mathbf{K}}$ is optimized as:

$$\hat{\mathbf{K}} = \arg\min_{\mathbf{K}} F_p(\mathbf{K}) = F_p^a(\mathbf{K}) - F_p^r(\mathbf{K}) \tag{1.24}$$

where $F_p^a(\mathbf{K})$ is the attraction term enforcing the sampling pattern $\mathbf{K}$ and $F_p^r(\mathbf{K})$ the repulsion term.

$$F_p^r(\mathbf{K}) = \frac{1}{2p^2} \sum ||\mathbf{K}[i] - \mathbf{K}[j]||_2 \tag{1.25}$$

1.4.3 Evaluation of trajectories

In theory, to compare different trajectories, we need to keep in mind:

- SNR performance is the same for K-space sampling density with the same uniformity. When sections of **k**-space are sampled more densely than other parts, the SNR performance is worse than when all parts are sampled equally densely.
- The point spread function's width is influenced by the trajectory (PSF). The PSF broadening determines the effective resolution of the reconstructed image.
- T_2^* relaxation during readout acts like a low-pass filter, creating image blurring and lowering the effective spatial resolution. The magnitude of this effect is determined by the readout length and relaxation properties of our nucleus of interest.

In practice, trajectory design is limited by maximum gradient strength, slew rates, and duty cycle. The following section will explore how we reconstruct images acquired using different **k**-space sampling schemes.

1.5 Reconstruction techniques

1.5.1 Fourier reconstruction

For MRI data acquired using a cartesian sampling pattern, reconstruction is straightforward. The signal can be obtained by applying the Fourier Transform (FT). The discrete Fourier transformation (DFT) for a signal s of N samples is defined as:

$$S(k) = \sum_{n=0}^{N-1} s(n) \mathrm{e}^{-2\mathrm{i}\pi k \frac{n}{N}} \qquad \text{pour} \qquad 0 \leqslant k$$

Several algorithms have been developed to compute the Fourier Transform of multidimensional data in the complexity of $O(N \log N)$ where N is the size of the data. One of the most famous is the Cooley–Tukey algorithm [Gentleman 1966].

To take advantage of those algorithms, a zero-filling step is typically necessary to set the size of the grid signal at a power of 2. This increases reconstruction time. To avoid

Gibbs ring artifacts, a filter in the form of a window is also applied before reconstruction to reinforce Nyquist criteria by mitigating high frequencies.

For data acquired according to a non-Cartesian k-space sampling scheme, we mainly have two ways of reconstructing the image: gridding [Schomberg 1995] and iterative techniques [Yang 2009]. The first one is the current standard, which has the advantage of being fast to compute. The latter is known for increased accuracy, the possibility to account for off-resonance effects, and the ease with which a priori knowledge and image models can be exploited.

1.5.2 Gridding techniques

The FFTs algorithms are faster for uniformly sampled rectilinear k-space trajectories. To avoid using slower adaptations, gridding is used. This technique uses a convolution in **k**-space to convert the input data to a uniform rectilinear data set. The choice of the convolution function impacts reconstruction duration and interpolation accuracy. The Kaiser-Bessel function is the most common using kernel.

For trajectories like TPI, radial, or other "center out" spokes, where the center of the k-space is sampled multiple times, a data needs to be weighting accordingly. Image reconstruction without compensation for the density variation can result in a severely degraded point spread function. Determination of the density compensation term has been an active topic for investigation with analytical and numerical approaches. Some studies have been made to optimize the density compensation function for parametric trajectories. For more complex trajectories, iterative methods of defining density compensation can be used [Pipe 1999].

The nonuniform Fourier transform

The algorithm of non-uniform Discrete Fourier Transform (DFT) of Dutt and Rokhlin [DUTT 1993] has been extended to 2D and is defined as:

$$W_k = \sum_{n=0}^{N-1} x(k_t) \exp^{(-2i\pi k.n/N)} \tag{1.26}$$

where $x(k_t)$ is the value of the samples at location **k** at instant t. This method is more accurate than the Kaiser-Bassel regridding and requires similar computation time [Sarty 2001]. However, Kaiser-Bessel methods are still more used in the literature because of their convenience [Jackson 1991, Fessler 2007].

The kernel $K(u)$ Kaiser-Bessel is defined by:

$$K(u) = \frac{1}{W} I_0 \left(\beta(1_2 \frac{u}{W}) \right)^2 \tag{1.27}$$

with I_0 being the zero-order Bessel function of the first kind, W the width of the kernel, and β is defined according to [Beatty 2005]:

$$\beta = \pi\sqrt{\frac{W^2}{a^2}((a-0.5)^2 - 0.8)} \tag{1.28}$$

with a being an over-sampling factor.

1.5.3 Iterative techniques

These techniques approach the image reconstruction process as solving an inverse problem and iteratively trying to optimize a given cost function by refining an image model. Its non-Cartesian Fourier samples match the measured data. MRI image is known to be sparse, some applications are sparse in the pixel domain like angiograms while others more complicated images have a sparse representation in some transform domain–for example, in terms of spatial finite-differences or their wavelet coefficients [Lustig 2007]. Evaluating the non-uniform Fourier transform of the image model is the main bottleneck for such algorithms. Many researchers use the non-uniform FFT (NUFFT) approximation to accelerate iterative algorithms.

We consider a discrete image and define $\mathbf{x}$ and $\mathbf{y}$ the observed signal, $\mathbf{E}$ the encoding matrix that describes the principles of the physics of MRI. The model is then defined as follows:

$$\mathbf{y} = \mathbf{E}\mathbf{x} \tag{1.29}$$

We assume that a sparse representation can describe the signal in this context.

In this case, we adopt the discrete wavelet transform (DWT). The DWT being represented by the matrix $\mathbf{W}$, we define $\mathbf{M} = \mathbf{E}\mathbf{W}$. Therefore, we now have the following problem to solve:

$$\mathbf{y} = \mathbf{M}\omega \tag{1.30}$$

where $\omega = \mathbf{W}^{-1}x$.

Now, we are looking for an optimal solution ω^* that will minimize the two terms of the cost function. They represent respectively data fidelity $F(b)$ and a regularization term $R(\omega)$ that is added due to the ill-conditioned nature of the matrix $\mathbf{E}$ due to sub-sampling. This is why inverting the matrix $\mathbf{E}$ is impossible. To tackle this problem, one needs to define a regularization term. Thus, the optimization problem can be defined as:

$$\omega^* = \arg\min_{\omega} F(\mathbf{y} - \mathbf{M}\omega) + \lambda R(\omega) \tag{1.31}$$

where lambda (λ) is a regularization parameter balancing the two constraints, in the context of MRI, the quadratic norm is often used because $\mathbf{b}$, the noise, is assumed to be a Gaussian process.

$$F(b) = ||b||^2 \tag{1.32}$$

In this case, we reinforce the prior information of sparsity known from MRI signals. Different functions and norms $||\cdot||$ can be used. Here we will adopt this model. The final problem we will solve is then:

$$\omega^* = \arg\min_{\omega} \frac{1}{2}||\mathbf{y} - \mathbf{M}\omega||_2^2 + \lambda||(\omega)||_1 \tag{1.33}$$

Other norms have been exploited as total variation (TV) norm defined in 1992 [Rudin 1992]:

$$V(y) = \sum_{i,j} \sqrt{|y_{i+1,j} - y_{i,j}|^2 + |y_{i,j+1} - y_{i,j}|^2} \tag{1.34}$$

To solve this problem, several options are available like fast iterative shrinkage-thresholding algorithm (FISTA) and proximal optimized gradient method (POGM) [Lin 2019]. As the POGM algorithm is the best algorithm to apply to a synthesis formulation of the MRI reconstruction problem in a recent benchmark study [Fessler 2020], we adopted the POGM algorithm whenever needed in this thesis.

Reconstruction quality can be measured using different metrics. A standard option is the structural similarity index measure (SSIM) [Wang 2004]. It is a metric that has demonstrated good agreement with human observers in reference image tasks. This metric analyzes the viewing distance, edge information between the reference and the test images, changed and preserved edges, textures, and structural similarity of the images. SSIM is defined as:

$$\text{SSIM}(x, y) = \frac{(2\mu_x\mu_y + c_1)(2\sigma_{xy} + c_2)}{(\mu_x^2 + \mu_y^2 + c_1)(\sigma_x^2 + \sigma_y^2 + c_2)} \tag{1.35}$$

where μ_x is the average of x, μ_y is the average of y, σ_x^2 is the variance of x, σ_y^2 is the variance of y, $c_1 = (k_1 L)^2$, $c_2 = (k_2 L)^2$ are variable to stabilize the denominate is very small. L is the dynamic values of the pixels. k_1=0.01 and k_2=0.003 by default.

However, SSIM is not robust to blurring, which limits its use [Renieblas 2017].

Once the image is reconstructed, an important step in studying cerebral metabolism is quantification, which is the focus of the next section.

1.6 Quantification

1.6.1 Tissue concentration

The estimation of a tissue concentration for an electrolyte or a metabolite of interest is often the goal of X-nuclei MRI applications. There are different techniques to obtain those values. Usually, reference signals obtained from internal or external sources with known (or assumed) concentrations calibrate the spin concentration per unit of signal. When several

of these references are available, concentrations are estimated using linear regression of the signal intensities of those references to their known concentrations.

Examples of references are given below [Tofts 1988,Kreis 1993,Ernst 1993,Dhamala 2019]:

- tissue-mimicking phantoms in the same FOV as the subject;
- tissue-mimicking phantom with comparable load to the subject;
- an organ/compartment within the patient with a stable/known concentration;
- another metabolite or groups of metabolites with a stable/known concentration;
- virtual reference methods;

External referencing

The first approach is called the external referencing method. In principles, tissue-mimicking phantoms are prepared with known/measured concentrations and T_1 and T_2 relaxation times if possible in the range of the values expected *in vivo*. At least one such phantom is necessary. To improve the quantification, more phantoms are recommended.

Another type of external referencing is what is called the virtual reference method. Electronic REference To access In vivo Concentrations (ERETIC) [Barantin 1997] is an example of these methods. It uses a synthetic signal generated by an external RF source. This source generates a stable and robust electronic quantitative reference signal. The ERETIC method uses RF pulses synthesized during acquisition to generate the signal, eliminating the need to add chemicals to the sample. Therefore, there are no concerns about toxicity, chemical activity, binding, or visibility. The experimenter can easily change the frequency, line width, and amplitude of the ERETIC signal, and the shape of the line does not depend on the uniformity of B0. In addition, the line width is freely selectable, so there are no relaxation time considerations when using ERETIC. When the spectrometer is appropriately configured, the RF coil load caused by the sample reduces the ERETIC signal by the same amount as the metabolite signal from the sample, as expected by the quantitative reference [Ziarelli 2006]. Yet, such a solution requires the development of a custom pulse sequence and modifying the system configuration, which is seldom possible (figure 1.13).

The ERETIC method is used in spectroscopy techniques. For MRI, a new method was developed called Virtual Phantom Magnetic Resonance Imaging (ViP MRI) [Saint-Jalmes 2014, Salvati 2016]. The aim is to generate reference signals on MR images using external radiofrequency signals. The idea is to design various numerical phantoms with a given fat fraction, T_2^*, and a field map. Then, the **k**-space of these numerical phantoms is converted into RF signals by a waveform generator to generate virtual phantoms. Finally, the RF signal is transmitted to the MR scanner bore by a dedicated RF coil.

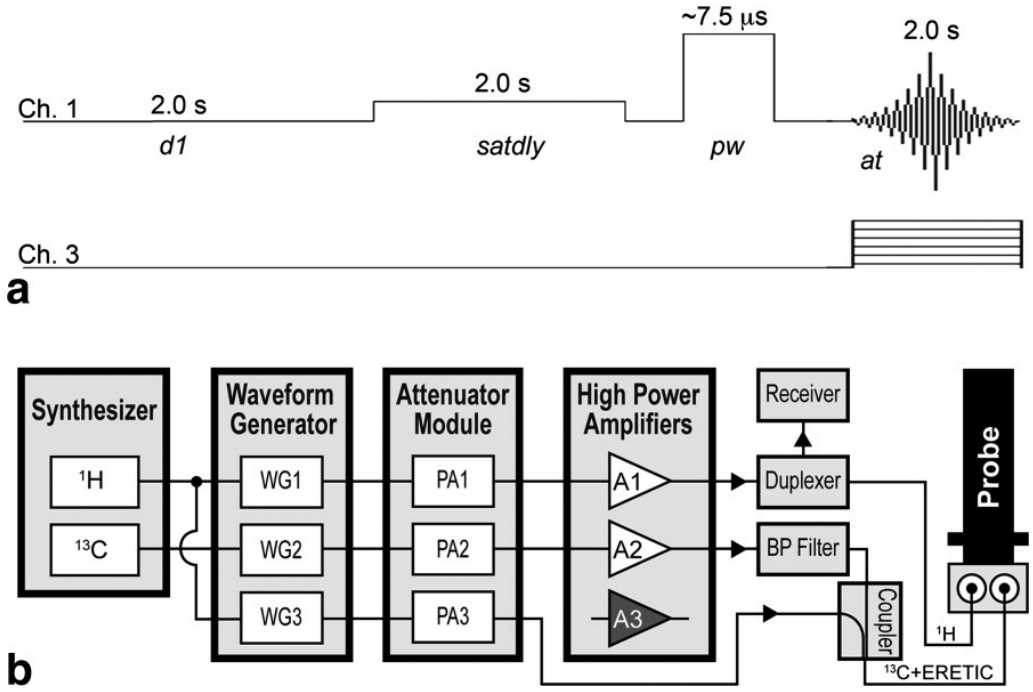

Figure 1.13 – (a) Pulse sequence diagram of the ERETIC sequence and (b) system diagram of the Varian INOVA console highlighting the modifications required for generating an ERETIC signal at the 1H frequency. The output of the ^{1}H synthesizer was shared between the waveform generators (WG) for channels 1 and 3. The ERETIC signal was taken directly from the output of the Programmable Attenuator (PA) module, combined with the output from channel 2 using a directional coupler, and transmitted through the X channel of the nanoprobe. The transmission of the ERETIC waveform and the data acquisition were synchronized in the pulse sequence. (d1, relaxation delay; satdly, presaturation delay; pw, pulse width; acquisition time; BP, bandpass.. From [Albers 2009].

Phantom replacement

When a single large phantom is used as an external reference of concentration, it is referred to as the phantom replacement method. In this case, the phantom (with comparable dielectric constant) and the subjects must be measured using identical parameters and positioned similarly relative to the coil to ensure equivalent coil loading and directly similar signals. Identical B_1^+ and B_1^- fields can only be supposed in those circumstances. In practice, co-registration and, in some situations, additional B_1^+ and B_1^- correction steps are needed.

Internal reference

The second approach is referred to as the internal referencing method. In the case of an organ/compartment of reference, it should be considered carefully as between patients or experiments, variations exist. For ^{23}Na MRI, the sodium concentration in the cerebrospinal fluid (CSF) compartment [Insko 2002, Romanzetti 2014] or blood [Pabst 2001] is often used as an internal reference of concentration ([Na]≈140 mmol/L). In the case of an internal signal/metabolite of reference, it can also be problematic since one must assume a fixed

and stable concentration which is not necessarily true for patients but is quite practical, especially for data acquired in healthy volunteers. In ^{31}P MRI/MRS, the ATP or PCr signals have been used as an internal reference of concentrations ([ATP]≈3 mmol/L in the brain or [PCr]≈33 mmol/L in the muscle).

1.6.2 Partial volume effect

MRI is inherently affected by the partial volume effect. This term means that the measured intensity of concentration is inaccurate due to the relatively low image resolution and the limited tissue sampling. The low resolution causes a blurring of the image so that signal/concentrations are spread to the surrounding pixels, as illustrated below (Figure 1.14).

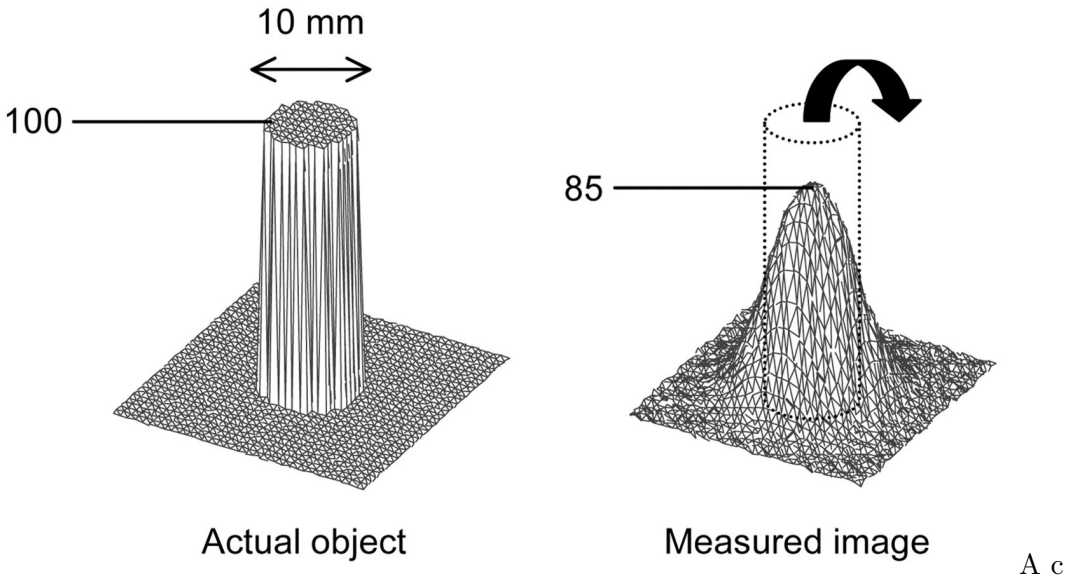

A c

Figure 1.14 – Circular source (diameter of 10 mm) of uniform activity (100 arbitrary units) in the intensity of voxel measured image in which part of a signal emanating from the source is seen outside the actual source. The maximum intensity in the measured image is reduced to 85. From [Soret 2007].

This effect is called spill out. Quantification accuracy can be improved by increasing spatial resolution (when possible) and using partial volume corrections techniques [Niesporek 2015]. Partial volume correction methods can use a priori knowledge anatomically to correct the impact of neighboring voxels. For instance, the Müller-Gärtner (MG) method, [Müller-Gärtner 1992] which has been developed for PET imaging, assumes that white matter uptake is homogeneous (Code available at https://github.com/UCL/PETPVC). All brain pixels are classified as white matter or grey matter and sorted into respective segments. Based on these segments and the assumed MRI resolution, the spill out from WM to GM can be estimated and subtracted. Similarly, the spill-out from GM to the surroundings can be assessed and compensated for. The result is a grey matter image with corrected activity values in all pixels.

In this chapter, we presented the necessary concepts to understand this thesis. Now, we can explore the state-of-art techniques and the quantification of the electrolytes and metabolites we are interested in.

* * *
* *
*

Chapter 2

X-nuclei MR imaging of the human brain

Chapter Outline

After explaining in chapter one the basic principles of MRI needed to comprehend the work done during this thesis, here we will discussed the rationale that motivate this work on metabolic imaging using x-nuclei MRI and its state-of-the-art. Proton imaging allows the generation of different contrast between anatomically distinct soft tissues. However, as shown in the table 1.1, the proton is not the only nuclei with a nonzero spin quantum. This means that other nuclei can generate NMR signals. Here, we present the different metabolites and ions of interest, as well as the creatine kinase activity, which have been studied as possible biomarkers for Neurology or Psychiatry. We also present the challenges related to sodium MRI and phosphorus MRI/MRS.

2.1 Cerebral metabolism: who plays an important role?

The human brain represents 2% - 3% of the human weight, but it is responsible for consuming 20% - 30% of the energy metabolized in the whole body [Clarke 1999]. The principal actors of cerebral metabolism are metabolites; without being exhaustive here, we will present some of the metabolites that drive cerebral metabolism.

2.1.1 Glucose

The human body has different sources of energy. However, the brain's principal energetic source is glucose, and its concentration is around 5 mM (1g/L) in the bloodstream and about 1-2 mM in the human brain. Glucose is not synthesized in the brain. The human body does not produce glucose. Only vegetables produce glucose as a result of photosynthesis reaction. Therefore, humans need to acquire glucose from their diet. Glucose can be found in different aliments, but the principal source is plants such as potatoes or cereals (i.e., wheat, corn).

After ingestion, the human body will degrade the chain of carbohydrates through digestion. The result of this process is monosaccharides. Amongst them, we found glucose. Glucose goes through the blood-brain barrier after circulating in the brain vascular system. It is then taken up by glial cells (astrocytes) and neurons. Two main pathways are available to produce ATP according to oxygen availability.

When no oxygen is available, anaerobic glycolysis is the principal reaction. In both cases, glucose is degraded in two pyruvate molecules, generating four ATP molecules and 2 reduced equivalents of $NaDH^+$ per glucose unit. If oxygen is lacking, pyruvate is converted into lactate via the lactate dehydrogenase enzyme. When oxygen is available, glucose's complete oxidation occurs via the Krebs cycle (called the citric acid or tricarboxylic acid - TCA - cycle). One can find details of this reaction in the figure 2.1). Through glycolysis, the TCA cycle, and the oxidative phosphorylation chain, which is coupled, 30 to 38 molecules of ATP are produced per glucose unit.

Notably, lactate molecules produced via anaerobic glycolysis accumulate in tissue until oxygen is available or drained to other organs for further oxidation or conversion back to glucose (gluconeogenesis).

2.1.2 PME and PDE

Phosphomonoesters and phosphodiesters are needed as building blocks for synthesizing Phospholipidic cellular membranes, especially those found in neurons. The NMR peaks attributed to PME contain resonances from phosphoethanolamine (PE) and phosphocholine (PC), both metabolites of the membrane synthesis pathways (such as the Kennedy pathway), as well as negligible contamination from carbohydrate metabolism intermediates such as fructose-6-phosphate or glucose-6-phosphate. The PDE signal contains mainly contributions from glycerophosphoethanolamine (GPE) and glycerophosphocholine (GPC). Both metabolites are also involved in membrane metabolism but have instead been linked

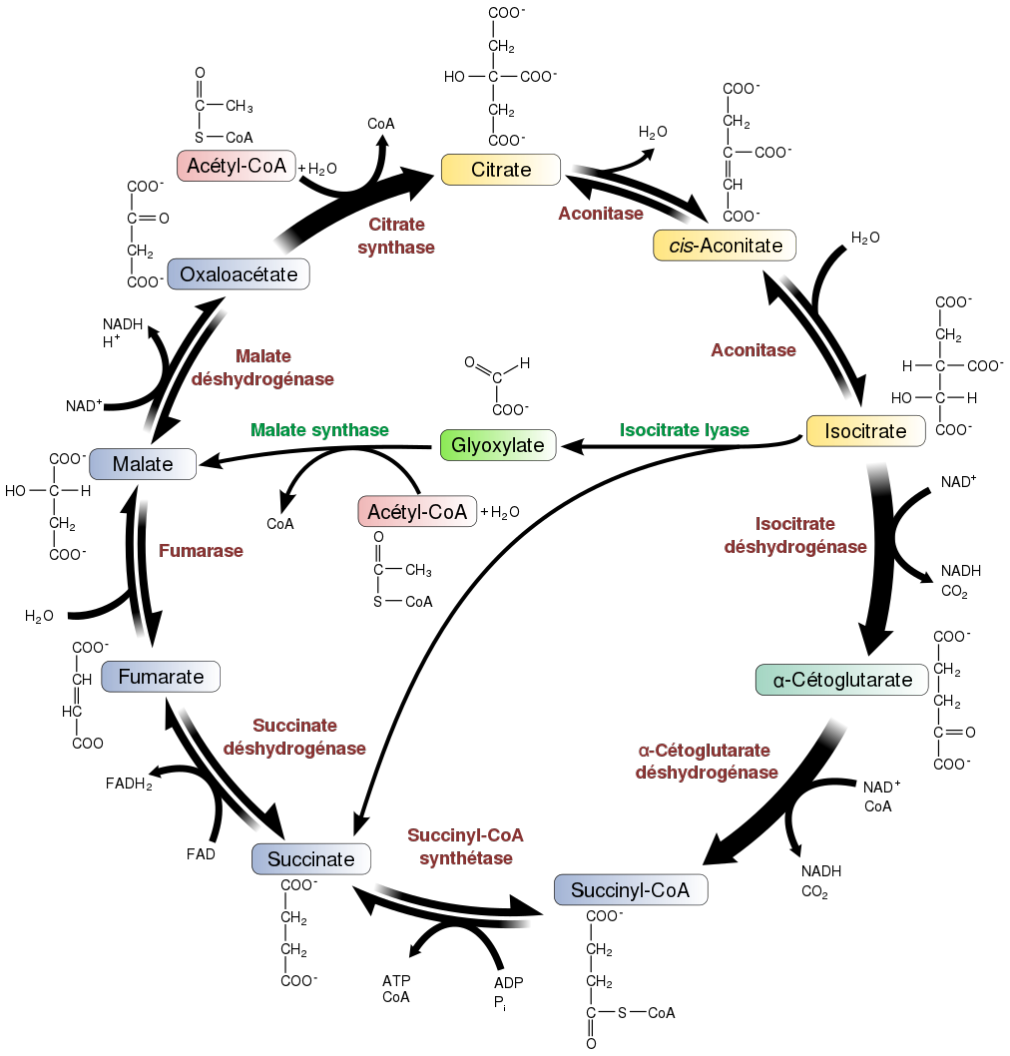

Figure 2.1 – The Krebs cycle: this instructional diagram of the citric acid or tricarboxylic acid or Krebs cycle shows the different chemical steps and reactions leading to the oxidation of acetyl-coA, which is mainly produced from glycolysis. From Agrotman, vector version: Flappiefh, CC BY-SA 3.0 Wikimedia Commonsm

to phospholipids degradation pathways. For instance, PME decreases while PDE increases during the first 2-3 years of life [Clarke 2018]. At birth, the high PME peak is attributed to an abundance of compounds for producing membrane phospholipids and myelin. In contrast, the lower PDE peak matches the less active phospholipid breakdown pathways [Buchli 1994]. Thus, the PME/PDE ratio change with brain maturation which is associated with myelinogenesis and the proliferation of glial cells.

2.1.3 PCr and Cr

Creatine (Cr) and its phosphorylated form, phosphocreatine (PCr), play essential roles in brain energy metabolism as an energy storage buffer for enzymatic activities in the cytoplasm. Indeed PCr is available at a relatively large concentration in tissue (about 4 mM in the brain) to regenerate locally and rapidly ATP from ADP. This reaction occurs through

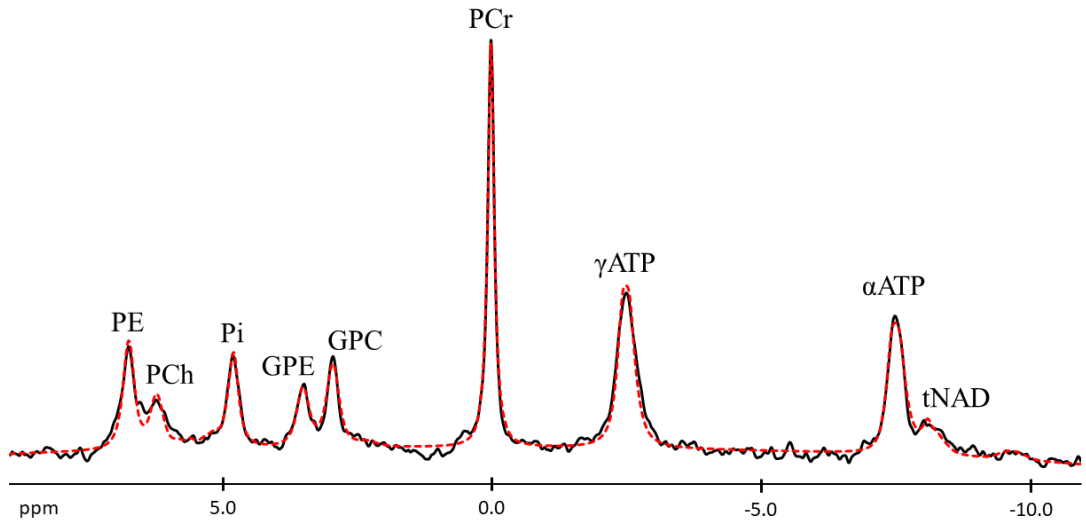

Figure 2.2 – Average human brain spectra of volunteers from study ENERGYSEP and its analysis by LCModel. PDE = GPE: glycerophosphoethanolamine; GPC: glycerophosphocholine; PME = PE: phosphoethanolamine; PC: phosphocholine. Courtesy of Fawzi Boumezbeur.

the creatine kinase (CK) enzyme (Figure 2.5). While PCr is consumed to regenerate ATP in the cytosol wherever it is needed, PCr is restored from ATP in mitochondria via the mitochondrial CK.

The good functioning of CK is essential because it enables the activities of all ATPases. One of the most critical ATPases for cell homeostasis is the Na^+/K^+ pump. This pump is responsible for maintaining the electrochemical potential of neuronal membranes, which is the basis for the generation and propagation of action potentials (Figure 2.4).

Phosphocreatine is more chemically stable than ATP and high PCr concentrations have been shown to downregulate mitochondrial ATP production [Walsh 2001].

The couple Cr/PCr is a good marker for cell energy metabolism [Forstner 1998, Snow 2001]. Those two metabolites are ubiquitous in all mammal cells, changes in their concentrations being linked to pathological phenomena such as inflammation or neurodegeneration.

In the muscle, the PCr/Cr ratio can be estimated by biopsy just after exercise at about 2.8 [Karatzaferi 1999, Smith 2004]. However, such approach is not nearly as acceptable in the brain, due to its invasive manner. In ^{1}H spectroscopy, Cr and PCr contents can be in theory examined separately via the slight chemical shift difference between their methylene resonances (Cr_{CH_2} at 3.91 and PCr_{CH_2} 3.93 ppm). It is nonetheless quite challenging unless the experiment is performed at UHF in ideal B_0 shimming conditions. Consequently, ^{1}H spectroscopy yields almost exclusively total creatine (=Cr+PCr) levels [Fountas 2000]. Even tough, from these few ambitious ^{1}H spectroscopy studies (mostly in animal models), it is known that the PCr/Cr ratio is closer to 1.2 in the brain [Xu 2005, Dorst 2022].

Thanks to the advent of chemical exchange saturation transfer (CEST) MRI two decades ago, recent studies demonstrated that Cr (shift 1.8-1.9 ppm left of the water peak) or PCr (shift 2.5-2.6 ppm) content can also be probed and mapped in the human muscle tissue at moderate filed strength such as B_0= 3T [Kogan 2014a] even it remain more efficient at B_0 = 7T and higher [Kogan 2014b]. Both studies showed that the increase of the Cr-CEST signal correlates with the decrease of the PCr signal intensity as seen directly using ^{31}P MRS.

However, the Cr-CEST signal can be compromised by relaxation and concomitant effects such as direct water saturation and semi-solid magnetization transfer (MT) effects that can be prevalent in the brain due to its lower Cr content. Recently, the polynomial lorentzian fitting (PLOT) method [Chen 2017] was developed to extract Cr/PCr CEST signal from tissue Z-spectrum based on *in vivo* validation results. This enabled us to optimize the Cr/PCr acquisition parameters on tissue directly. At higher fields, it is possible to separate Cr and PCr contributions using CEST techniques as demonstrated at 17T in rats [Bardin 2022, Lecis 2022].

It is important to note that CEST approaches are not exactly quantitative limiting the development of quantitative *in vivo* exploration of PCr/Cr equilibrium especially in clinical studies for which accounting or correcting for B_0 and B_1 inhomogeneities at UHF remain a challenge [Xu 2022].

2.1.4 Sodium and potassium

Even though sodium and potassium are ions, not metabolites, they are both crucial components of any cell's physiology. In the brain, sodium is present at different concentrations in distinct compartments. In the CSF, the extracellular and vascular spaces, sodium concentration is around 140-145 mM. The sodium concentration is approximately 10-15 mM in the intracellular compartment in healthy volunteers [Madelin 2015]. For potassium, those concentrations are more or less reversed with low concentrations of K^+ of about 4-5mM in the CSF, extracellular/vascular compartments, and high intracellular concentrations of around 140 mM. These concentration differences are significant factors in the transmembrane electrochemical potentials observed in excitable cells (neurons in particular) and maintained at a substantial cost (in terms of ATP) by the sodium-potassium pump (fig 2.3).

This pump consumes ATP to open and keep the action potential of the membrane. When a neuron is stimulated, one observes the sodium entering its interior through the sodium canal. It moves two potassium ions into the cell where potassium levels are high and pump three sodium ions out of the cell and into the extracellular fluid. In the case of a strong enough stimulus, this creates an action potential, allowing the transmission of the information from neuron to neuron. This scheme can be seen in figure 2.4.

A perturbation of this system can lead to severe consequences in the brain. Indeed, abnormal sodium accumulation in the intracellular compartment can be caused by a pump malfunction or if ATP is lacking due to mitochondrial dysfunction. This would upset

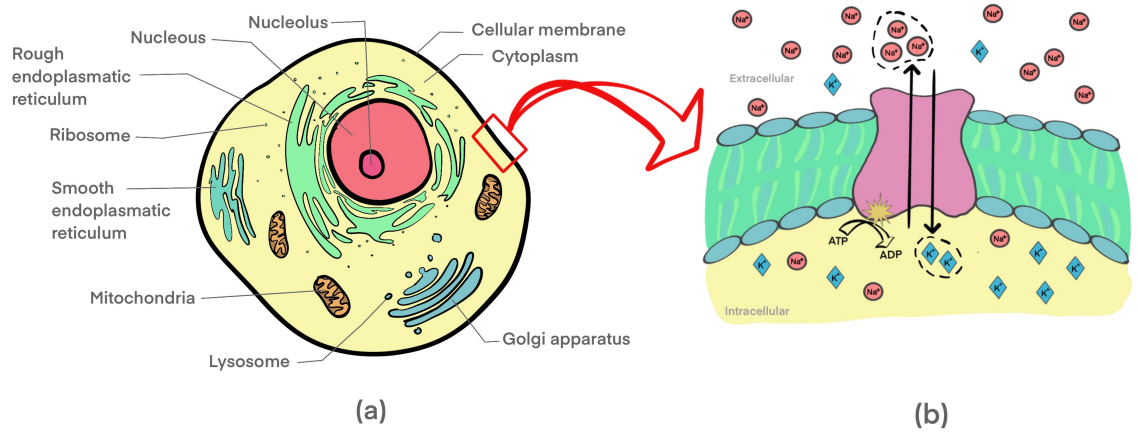

Figure 2.3 – (a) Schematic of a eukaryotic cell and a zoom-in on the transmembrane sodium-potassium pump. (b) Sodium ions bind to the pump, and phosphate groups from ATP attach to the pump, changing the shape of the pump. The pump emits three sodium ions in this new form and combines them with two potassium ions. When the potassium ion binds to the pump, the phosphate group separates. This causes the pump to release two potassium ions into the cytoplasm. Courtesy of Rebeca Araripe.

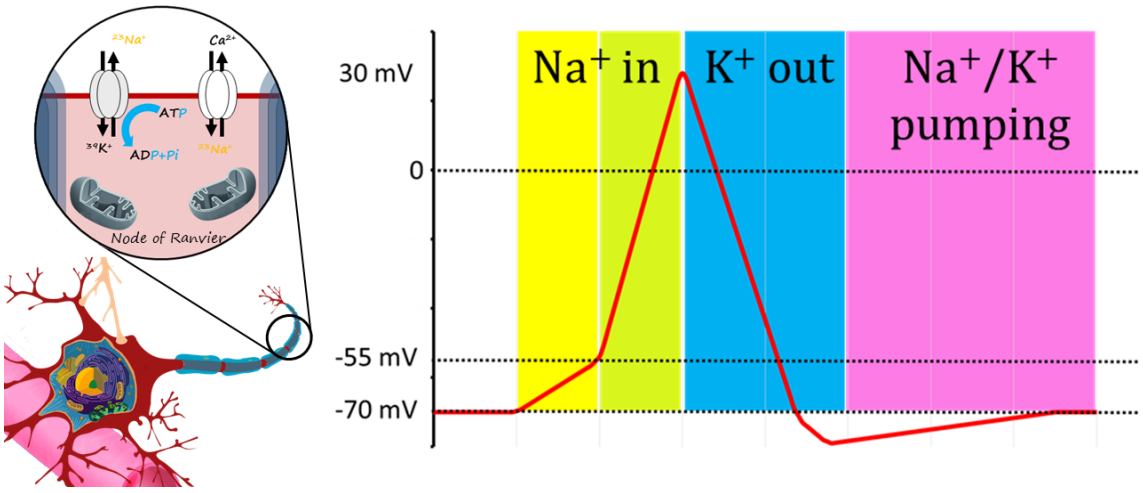

Figure 2.4 – Variations in potential through the sodium-potassium pump. Courtesy of Fawzi Boumezbeur.

the resting potential and overall function of the neurons leading to neurological/cognitive symptoms and ultimately neuronal cell death.

2.1.5 ATP and CK

ATP production is controlled mainly by the ATP synthase enzyme (at the end of the oxidative phosphorylation chain in mitochondria). The activities of the ATPases drive its consumption. In this picture, the creatine kinase (CK) reaction helps regulate cytosolic ATP distribution, sub-compartmentation (in organelles), and utilization (figure 2.5). These coupled reactions constitute a chemical exchange metabolic network of $PCr \leftrightarrow ATP \leftrightarrow Pi$ characterized by two forward and two reverse reaction fluxes, which can be studied non-

invasively by *in vivo* ^{31}P MRS combined with magnetization transfer (MT) preparation modules [Chen 2018].

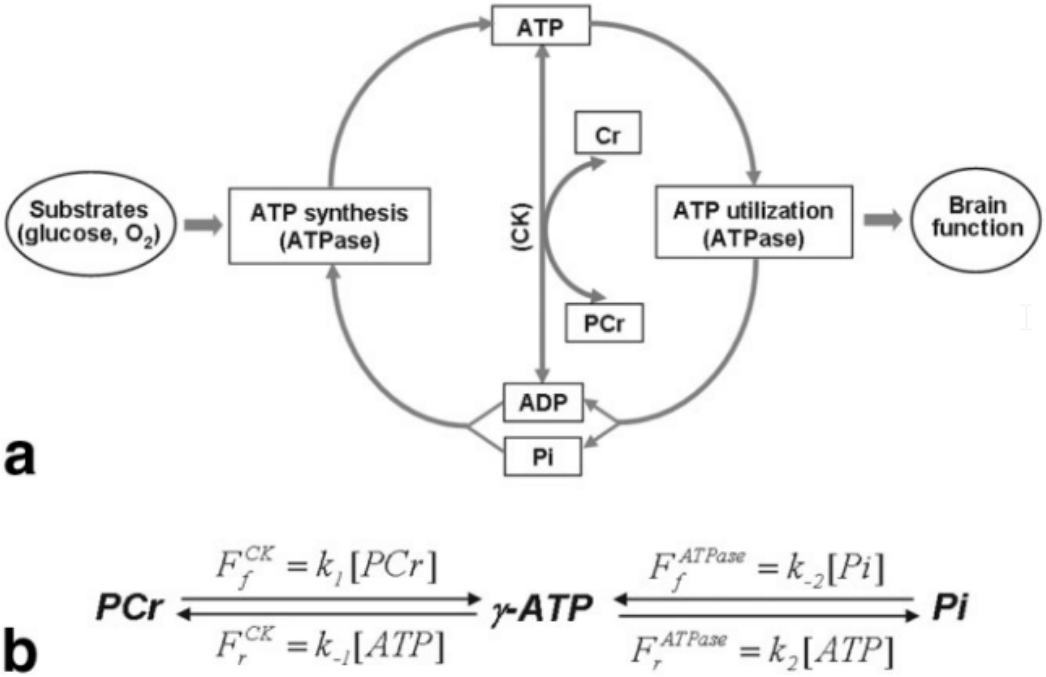

Figure 2.5 – a: Schematic diagram of the brain's metabolic network, including the metabolism of glucose, oxygen, and high-energy phosphate. These metabolic pathways control the production (i.e., ATP production) and consumption (i.e., utilization of ATP) of chemical energy and are tightly coupled to support brain function. b: A complete dynamic network illustrates the PCr ↔ ATP ↔ Pi chemical exchange system using the 3-spin exchange model (PCr, γ-ATP, and Pi). From [Du 2007].

2.2 Opportunities and challenges of X-nuclei Imaging

X-nuclei imaging aims to assess the underlying changes in physiological processes at the cellular level. There are various membrane proteins when we observe the metabolism at the cellular level. Those proteins are more or less permeable for specific ions. Sodium, potassium, and oxygen, for instance, partake in vital functions of the human body as homeostasis and respiration. They regulate cell volume, energy production, consumption, and excitation of the muscle or neuronal cells. In pathological conditions, microscopic changes affecting ionic homeostasis are expected to appear before macroscopic and structural modifications of the tissues. For that reason, X-nuclei imaging has the potential to become a tool for early preventive diagnostics as well as treatment evaluation.

Especially in recent years, most publications on clinical X-MRI applications have aimed at quantifying those signals, obtaining concentrations values that can be directly compared between X-MRI studies and with data obtained from other techniques. In theory, for sodium MRI, one should aim to assess its intracellular concentration because it is more directly linked to cell metabolism. However, differentiating this concentration in the MRI

signal is not trivial. And there is a debate in the X-MRI community about its feasibility. For ^{31}P MRI, this question is not explored in literature because phosphorylated metabolites such as ATP and PCr are known to be the intracellular reserve of energy, even though both have been found in extracellular spaces [Lee 1988], extracellular ATP being notably involved in cell signaling [El-Moatassim 1992].

Hardware improvements in B_0 strength, gradient performance, and sophisticated pulse sequences have allowed an influx of X-MRI publications using original [Utzschneider 2020, Sørensen 2022] quantification approaches. They have also permitted methods with lower SNR, such as multi-quantum filtering techniques [Hoesl 2022], which will be explained in the next section.

Recently, improvements in multi-nuclear coil design have led to increased clinical sodium MRI studies. Different setups have been reviewed for various applications, and multiple transmit-and-receive coils allowed an increase in SNR [Wiggins 2016, Lakshmanan 2018, Avdievich 2011]. Coil losses, rather than sample losses, prevail in X-MRI applications due to the lower tissue-coil coupling. Broadband or mode matching can reduce the SNR losses caused by coupling several receiver coil parts [Brown 2016].

As a challenge, one can cite low nuclear sensibility. As shown in the table 1.1, sodium has approximately a quarter of gyromagnetic moment and phosphorus roughly a third, impacting into the factor of (γ^2) their intrinsic sensitivity as explained in chapter one. Their concentrations are also several orders of magnitude lower than water, leading to thousand folds less signal (the reader may refer to chapter one for more details).

Besides, sodium possesses a rather large quadrupolar moment (I=3/2). Consequently, it exhibits rapid, bi-exponential T_1 and T_2 relaxation processes in complex media, which represent an additional difficulty for quantification and compartment modeling. Due to these short T_2/T_2^* decays, it is essential to use imaging sequences with fast and efficient excitation and acquisition. For imaging, UTE MRI sequences are often used for ^{23}Na, while for ^{31}P, MRS-based methods are still the most used, as we will explain later.

2.3 Phosphorus-31 MRS & MRI

After reviewing the relevant metabolites and reactions for this Ph.D. thesis in section2.1, we provide here an overview of the current status of ^{31}P-MRS and ^{31}P-MRI techniques. This should give the readership a better understanding of the context and interest of this work.

2.3.1 ^{31}P MRS and MRI Techniques

Phosphorus has a chemical shift range *in vivo* of about 30 ppm in contrast to the relatively narrow 10 ppm window for proton spectra (or even 5 ppm for conventional up-field spectra). Also, the number of metabolites of interest for *in vivo* ^{31}P NMR is much smaller than ^{1}H MRS. Indeed, as illustrated in the figure 2.2, there are about 10 main resonances or groups of resonances that can be investigated: Phosphocreatine ($\delta = 0.0$ ppm per convention), the

three α, β and γ resonances of ATP, inorganic phosphate, the two PME (PC and PE) and PDE (GPC and GPE) metabolites and the reduced and oxidized forms of Nicotinamide adenine dinucleotide resonances (NAD+NADH=tNAD). Consequently, most ^{31}P studies are conducted using NMR spectroscopy techniques.

Among those metabolites of interest, PCr is the most concentrated in the brain or muscles. In addition to estimating the (absolute or relative) concentrations of these phosphorylated metabolites, ^{31}P NMR spectra allow the estimation of the pH. Indeed, pH can be deduced from the chemical shifts of PCr and Pi using the modified Henderson-Hasselbach equation [Henderson 1908] as follow:

$$pH(i) = pK_a + \log\left[\frac{(\delta - \delta HA)}{\delta_A - \delta}\right] \tag{2.1}$$

where $pK_a = 6.75$ is the dissociation constant of Pi and $\delta_A = 5.63$ and $\delta_{HA} = 3.27$ are the chemical shifts of the mono-protonated (HPO_4^{2-}) and di-protonated ($H_2PO_4^-$) forms of Pi (i.e. phosphoric acid), respectively. The primary signal of Pi comes from the cytoplasm. Therefore, the equation 2.1 computes the intracellular pH.

Due to the low intrinsic SNR of ^{31}P-MRS, the most commonly used coils for those applications are surface coils arrays which yield better sensitivities at the cost of more inhomogenous B_1^+ radiofrequency fields (C.f. chapter one for more details).

Single Voxel localization

To acquire single voxel spectroscopy (SVS) datasets, single shot Point REsolved Spectroscopy (PRESS) [Paul A. Bottomley 1984] and STimulated Echo Acquisition Mode (STEAM) [Frahm 1985] are widely used in proton NMR experiments [Moonen 1989]. Due to the short T_2 relaxation times of ATP in particular, these techniques are not well suited for ^{31}P applications.

The Image Selected In vivo Spectroscopy (ISIS) sequence [Ordidge 1986] is one of the most appropriate SVS pulse-acquire-based localization methods for ^{31}P studies. It is a multi-shot approach combining eight acquisitions with three spatially selective inversion pulses to select a parallelepipedic volume along its three spatial dimensions.

However, due to its multi-shot nature, the ISIS sequence is prone to subtraction artifacts due to motion. Consequently, it is not recommended for experiments requiring a high temporal resolution, such as dynamic ^{31}P MRS study of exercising muscles. For such experiments, since the focus is on the PCr signal, the STEAM sequence [Frahm 1987] is satisfactory for dynamic ^{31}P MRS studies of a single muscle at 3T [Meyerspeer 2005]. However, its temporal resolution is worse than pulse-acquire approaches since it requires averaging to achieve similar SNR. Thus, a strategy using slice selective excitation with adiabatic selective refocusing (semi-LASER) has been proposed by Meyerspeer et al. at 7T [Meyerspeer 2011], this is a spin-echo-based sequence and offer a more accurate localization with a greater SNR for PCr (figure 2.6).

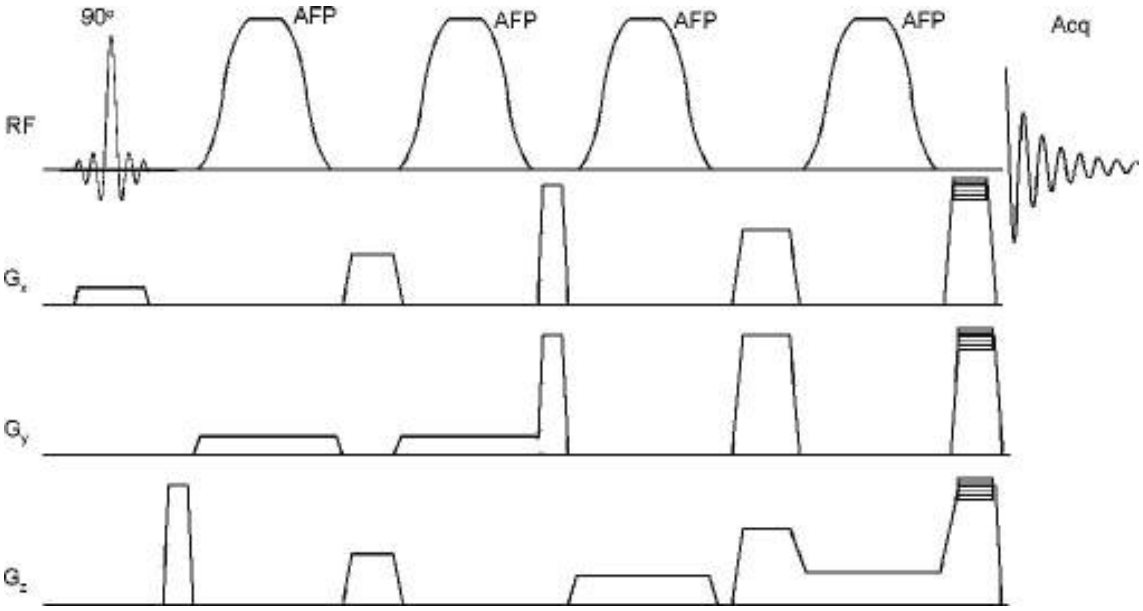

Figure 2.6 – Schematic of the semi-LASER spectroscopic imaging pulse sequence. Crusher gradients are positioned around every adiabatic full passage pulse. From [Scheenen 2008]

Multiple voxel localization

SVS techniques are not appropriate when one wants to investigate various targets simultaneously. Magnetic resonance spectroscopic imaging (MRSI) or Chemical Shift Imaging (CSI) approaches combine MRS sequences with spatial encoding schemes usually seen in MRI while preserving the spectral information content. One of the most common sequences for ^{31}P MRSI is the 2D or 3D CSI-FID sequence [Murphy-Boesch 1993, Hetherington 2001, Kan 2010]. This method presents the benefits of the pulse-acquire sequence (i.e., minimization of signal loss due to T_2^*-weighting, low SAR since only one RF pulse is needed per TR) with a 2D or 3D phase-encoding scheme. However, such PE scheme can be very time-consuming as at least one repetition is required for each point in k-space. A solution is using short TR with small excitation flip (Ernst) angles to accelerate the acquisition protocol. This way, 3D-CSI datasets were recently acquired at 7T within 29:00 minutes in very challenging conditions, precisely in lung carcinoma patients [Houtum 2021].

Some of the methods proposed for proton MRSI also have been translated to phosphorus. For instance, Echo Planar Spectroscopic Imaging (EPSI) [Posse 1994, Weiss 2012]. This method applies a rapidly oscillating gradient waveform encodes spatial and spectral information. This method can accelerate the acquisition by up to the number of encoding steps in one direction (figure 2.7). This technique has already been used for muscle [Wilhelm 2001] and brain ^{31}P MRSI studies [Ulrich 2007]. For these studies, a sinusoidal gradient waveform was used. This waveform is sensible to timing errors because it needs extra hardware to trigger the acquisition. Also, the required acquisition bandwidth for EPSI is a limiting factor for its application at UHF.

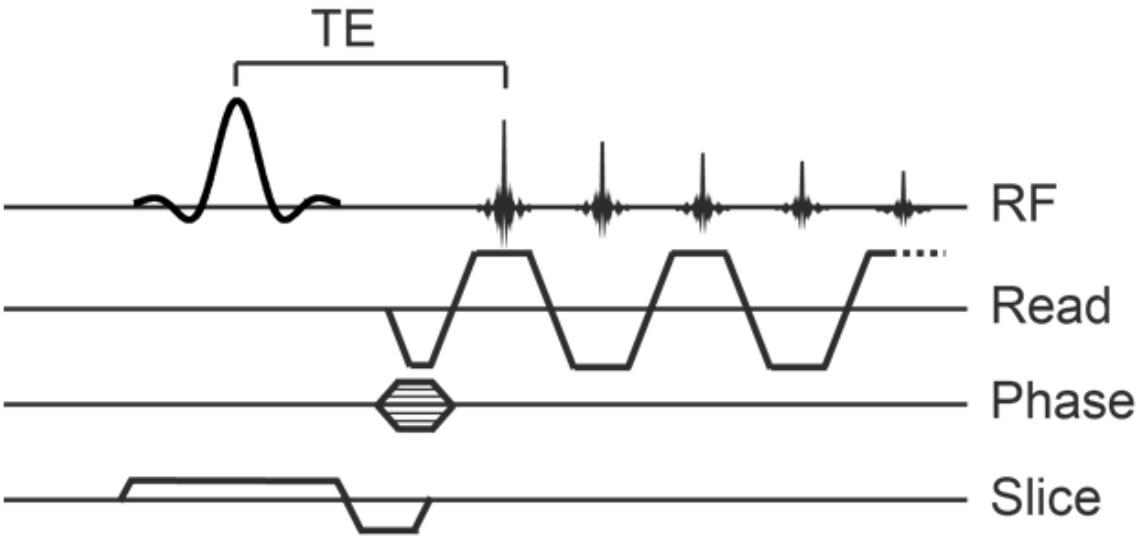

Figure 2.7 – Schematic of the EPSI pulse sequence. From [Weiss 2012].

^{31}P MRI: Frequency selective techniques

Spectrally selective ^{31}P-MRI is a more straightforward translation of proton MRI approaches to phosphorus metabolic imaging applications. These methods allow for acquisition maps of specific phosphorylated metabolites by using frequency selective RF pulses at the desired frequency, followed by standard MRI frequency and phase encoding techniques for spatial encoding, resulting in shorter acquisition times even at high spatial resolutions.

Multi-Dixon approaches have been used to quantify the PCr, Pi and ATP in human calf [Rink 2015]. The authors compared the approach against spectrally selective methods using a fully-balanced steady-state free precession (fbSSFP). They conclude that FS sequences should be preferred for measurements where only a single metabolite resonance is considered. MP-Dixon performs better in terms of SNR if a larger spectral width is of interest. The complexity of model signal combined with the lower SNR in the brain when compared to human calf, we decided to apply a frequency selective framework to avoid propagating errors of modelling.

Because of their role in energy metabolism and their relatively long T_2 relaxation times, most of these experiments focus on PCr and Pi mapping. For instance, the encoding methods have been considered as the T_2^*-weighted Turbo spin-echo [Parasoglou 2013] or RARE [Greenman 2011a] sequences. With an interleaved strategy, the RARE approach has demonstrated its ability to construct several metabolic maps simultaneously [Greenman 2011b].

Additional developments in the field with similar capabilities include using a gradient-echo sequence [Schmid 2016] non-Cartesian FLORET k-space trajectory [Khegai 2018] or a "compressed-sensing" acceleration strategy [Parasoglou 2012].

Saturation and magnetization transfer techniques

Dynamic *in vivo* ^{31}P-MRS is the only approach that can measure in-situ and non-invasively chemical exchange rates between phosphorylated metabolites thanks to Saturation (ST) or Magnetization Transfer (MT) methods [Forsén 1963] (figure 2.8). The MT presaturation module consists of a train of multiple RF pulses of constant amplitude and duration operating at the resonance frequency of a chosen metabolite.

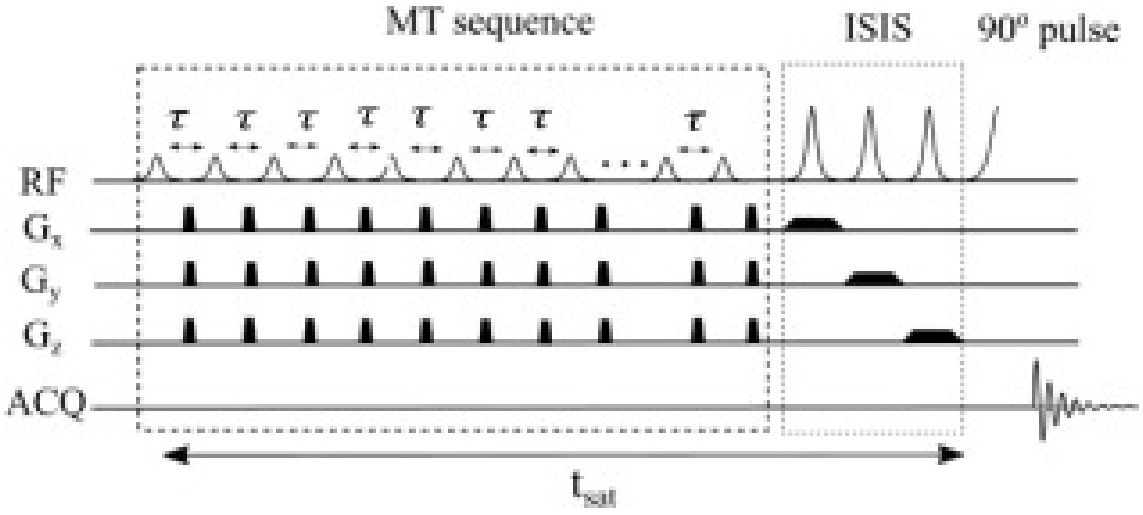

Figure 2.8 – Pulse sequence diagram of the MT sequence in combination with a 3D ISIS localization scheme. From [Chen 2018].

Several *in vivo* ^{31}P-MT methods have been developed. Conventional two-spin magnetization saturation transfer (CST), inversion-recovery transfer (IT), and two-dimensional chemical exchange spectroscopy (2DEXSY) [Macura 1981]. These methods have been applied to physiological studies of ATP metabolism in various organs, including the heart and brain. Of these methods, the CST method is probably the most widely used in biomedical research, probably because of the simplicity and efficiency of its methodology. This method is beneficial for measuring the forward rate constant, and flux of a PCr $\leftrightarrow$ ATP $\leftrightarrow$ Pi chemical exchange system when applying a frequency-selective radio frequency (RF) saturation pulse train to saturate the γ-ATP spins fully.

2.3.2 Clinical applications

The skeletal muscles and the brain are the most common organs explored using *in vivo* ^{31}P-NMR.

Muscle

Muscle ^{31}P explorations are probably the most numerous and widespread applications due to their relative simplicity, notably thanks to the high PCr concentration compared to other organs. These studies focus mainly on the analysis of resting and exercising legs. Studies have reported low PDEs in sedentary individuals [Valkovič 2016], while high levels

correlate with high-performance cyclists [Hug 2005, Hug 2006]. This shows the utility of PDE levels in skeletal muscle as a marker of training status.

In the brain, PME/PDE ratio is also of interest. For instance, Shi et al. acquired localized ^{31}P spectra at 3T in patients with bipolar disorder in either a euthymic state (n = 14) or a depressive state (n = 11). The spectra were compared with ones acquired in healthy subjects (n = 23). Metabolite ratios from a brain region that includes the frontal lobe, corpus callosum, thalamus, and occipital lobe were expressed as a percentage of the total phosphorus (TP) signal. Brain pH was also investigated. The authors observed a decrease in the PME/PDE ratio in patients with bipolar depression relative to healthy comparison subjects [Shi 2015]. In Krikken et al., a ^{31}P-MRSI study was conducted at 7 T to investigate phospholipid metabolism in breast cancer patients subjected to a neoadjuvant chemotherapy and correlate the eventual changes with treatment response. They demonstrated that detecting subtle changes in ^{31}P metabolites was possible after the first treatment cycle. Nonresponders showed different changes in metabolic ratios compared with partial and complete responders, particularly for PME/PDE [Krikken 2019].

In addition to "static" investigation (metabolic pool sizes or ratio corresponding to long-term equilibrium), ^{31}P MRS also allows the investigation of "dynamic" processes. These dynamic ^{31}P MRS studies are focused on intracellular pH homeostasis [Apps 2021] and ATP or PCr synthesis regulation during exercise [Heskamp 2021].

Brain

The brain is the seat of the most intense energy metabolism due to its ever-active neurons. It is no surprise that the neuron-rich gray matter has been found to have higher ratios of PCr/ATP and PCr compared to white matter in healthy volunteers [Mason 1998, Hetherington 2001, Ruhm 2021].

The brain is particularly reliant on (oxidative) energy production compared to other organs. As a result, it stands to reason that numerous brain illnesses are linked to imbalances in pH or abnormal levels of high-energy phosphates, ATP, or PCr. Many of these conditions have been studied with ^{31}P-MRS, including Alzheimer's disease [Rijpma 2018, Forlenza 2005] and Parkinson's disease [Hu 2000, Rango 2006], Multiple Sclerosis [Husted 1994, Guillevin 2019], migraine [Schulz 2007, Schulz 2009], epilepsy [Laxer 1992, Chu 1998], and cerebral ischemia [Levine 1992, Azzopardi 1989, Martin 1996]. ^{31}P-MRS also offers a tool to better determine the metabolic profile of brain cancers, with the primary findings indicating that meningiomas, glial tumors, lymphomas, and astrocytomas tend to alkalinize.

In 2021, a massive study [Rietzler 2021] was conducted on over 100 volunteers to investigate the influence of brain region, hemisphere, age, sex, and brain volume on phosphorylated metabolites concentrations in healthy adults. They focused on the supratentorial brain with a 3D ^{31}P-MRSI sequence at 3T, and the concentrations and ratios of PCr, inorganic phosphate (Pi), ATP were examined. From these data, significant regional differences were found, and sex differences were found in several regions. In some brain

regions and for some metabolites, hemispheric differences were detected. In addition, changes with (normal) aging were also found, which also differed between women and men.

To properly study a three-pool system, one needs to analyze the corresponding three metabolites (figure 2.9). In dynamic ^{31}P MRS, the 3-pool chemical exchange system requires studying ATP, PCr, and Pi signals to evaluate the flux through the creatine kinase reaction and the ATP synthesis/degradation flux.

Three-pool ^{31}P-spin chemical exchange kinetic network

$$\boxed{\text{PCr}} + \text{ADP}^- + \text{H}^+ \underset{F_f^{CK}=k_{-1}[\text{ATP}]}{\overset{F_f^{CK}=k_1[PCr]}{\rightleftharpoons}} \boxed{\text{ATP}} + \text{Cr} \qquad \boxed{\text{Pi}} + \text{ADP} \underset{F_r^{\text{ATPase}}=k_{-2}[\text{ATP}]}{\overset{F_f^{\text{ATPase}}=k_2[Pi]}{\leftrightharpoons}}$$

Two-pool ^{31}P-spin chemical exchange kinetic network

$$\boxed{\text{PCr}} + \text{ADP}^- + \text{H}^+ \underset{F_f^{CK}=k_{-1}[\text{ATP}]}{\overset{F_f^{CK}=k_1[PCr]}{\rightleftharpoons}} \boxed{\text{ATP}} + \text{Cr}$$

Figure 2.9 – Two and three pool models. Where k_1, k_{-1}, k_2, k_{-2} are the forward and reverse reaction rates; and [ATP], [PCr] and [Pi] are the concentrations of the three phosphate metabolites.

In this Ph.D. thesis, we adopted a simplified two-pool model for practical reasons. This focus on the creatine kinase activity and the PCr and γ-ATP resonances are justified because they are more sensitive to brain activation [Chen 1997, Chen 2018]. This suggests that V_{ck} is less tightly regulated than V_{ATP} which could translate into pathological states where energy imbalances occur. Recently, the flux through the creatine kinase enzyme was measured using spectroscopy [Ren 2015] and fingerprinting techniques [Wang 2017a]. These techniques focus on one brain region at a time using ^{31}P spectroscopy. However, it would be interesting to simultaneously measure that information on the whole brain. This is what will be explored in Part II.

2.4 Sodium-23 MRI

After introducing some basic knowledge on cerebral metabolism and the importance of sodium ions for neuronal cell homeostasis, in this section, we describe the leading techniques and clinical applications for sodium MRI to better understand the goals and interests of our research.

2.4.1 ^{23}Na MRI Techniques

Multi-quantum filtering imaging

Possessing a $\frac{3}{2}$ spin value, ^{23}Na nuclear magnetic moments can occupy four different energy levels. Consequently, three transitions are possible by a single quantum of energy ($\pm\gamma\hbar B_0$).

The correlation time describes the variations of electrostatic field close to the ^{23}Na nuclei. These electrostatic field gradients are generated by the electrons from the surrounding environment/molecules as lipids, proteins. Therefore, in a biological sample, there are varying quadrupolar interactions, which are combined to the Zeeman effect splitting acting as an additional relaxation mechanism leading to bi-exponential T_2 and T_1 relaxation processes with fast and slow components.

The coherence pathway is the sequence of coherence levels the NMR signal passes through between the first pulse and the time it is acquired. To measure and filter for different coherence pathways, in general, a 3-pulse sequence is needed along with RF phase cycling to select the coherence of interest. In an MQF sequence, the coherence pathway is manipulated by applying RF pulses, flipping the magnetization at angles θ and with phase shifts φ according to a predetermined phase cycling sequence. The coherence of interest is then selected by adding/subtracting the acquired signals, such as the signals of the other coherences cancel each other out [Bain 1984].

However, multiple quantum coherences (MQCs) can be sought after to investigate those interactions of the sodium ions with their environment (mainly from the slow-moving cell membranes and macromolecules). They can be separated using multiple quantum filtering (MQF) sequences [Jaccard 1986]. For sodium, Double Quantum Filtering (DQF) [Gast 2018] and Triple Quantum Filtering (TQF) [Worthoff 2019] sequences manipulate the NMR signal to select the double and triple coherence pathways that are thought to be more sensitive/specific to the intracellular compartment.

TQF (and even more so for DQF) methods suffer from a very low sensitivity of about 10% of SQ. This leads to longer acquisition times and worst spatial resolutions. In addition, the use of at least three 90-degree pulses that are repeated throughout the phase cycle leads to problematic SAR levels for clinical applications, especially at UHF.

Still, multiple quantum filtering methods may help sodium multi-compartment modeling and quantification.

In principle, the T_2 relaxation-based MQF allows the separation of sodium signals from different compartments due to the variably restricted mobility within each compartment [Worthoff 2019]. However, MQF is inclined to artifacts prompted via B_0 field-inhomogeneity, low SNR or long acquisition times, and its indirect calculation of sodium concentrations, similar to IR techniques [Gast 2018]. Recent quantitative multicompartment-multipulse methods exploit differences in T_1 and T_2 instances of different sodium compartments. This approach may also enable separating intracellular, extracellular, and cerebrospinal fluid signals but is hampered by low SNR [Gilles 2017].

These difficulties make the use of MQF sequences limited. Therefore, this is not the approach we explored in this thesis.

In a recent review on the potential and challenges of sodium MRI [Huhn 2019], it is recommended that the ^{23}Na MRI community focus on (1) improving SNR and resolution, (2) diminishing partial volume effects and scanning times, and (3) enabling precise differentiation of sodium compartmentalization as an ax of development. In this thesis, we worked on item (2) by developing and applying compressed sensing techniques

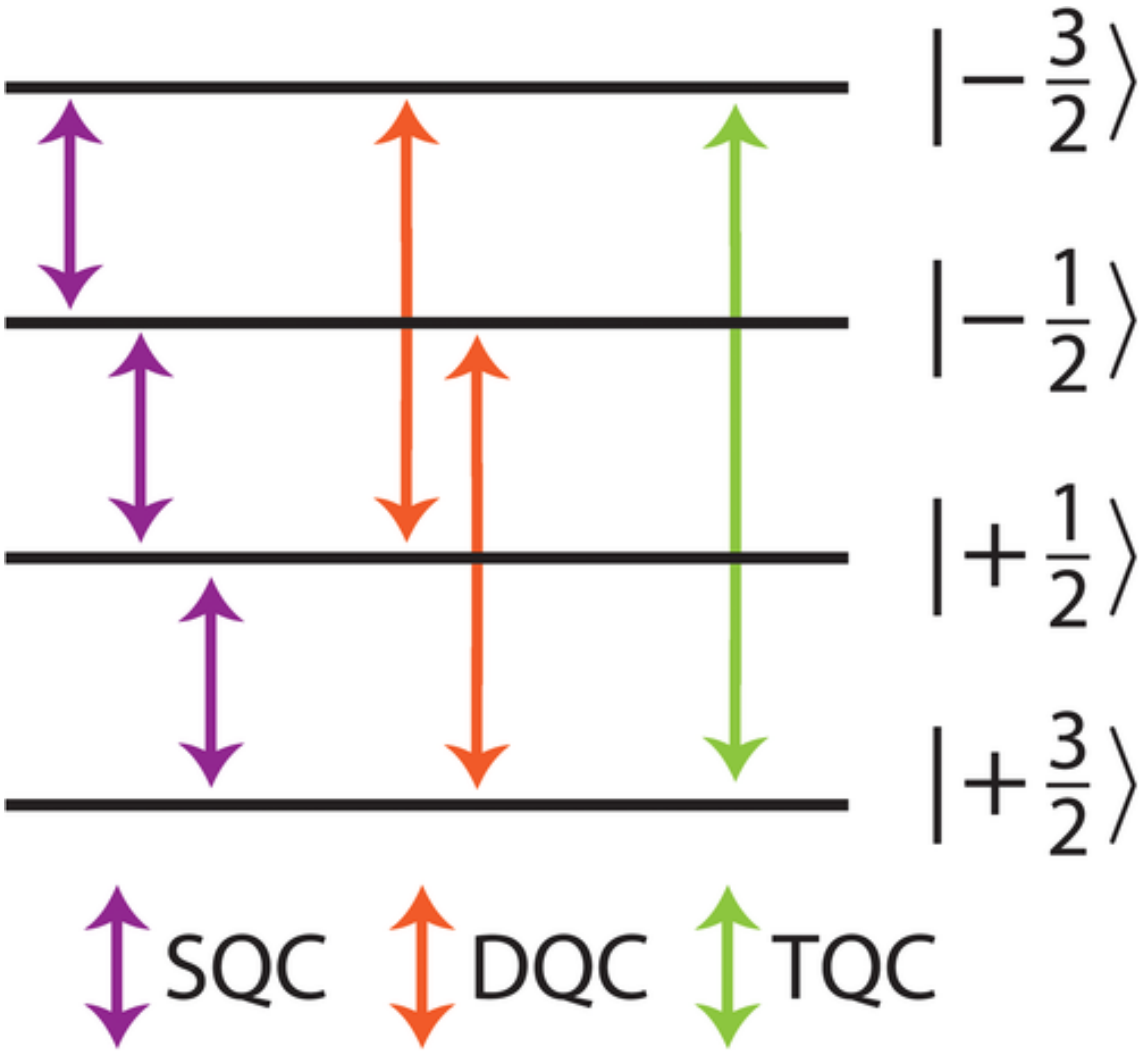

Figure 2.10 – Single-, double-, and triple-quantum coherences (SQC, DQC, and TQC, respectively) are illustrated as transitions between energy levels. Three single-quantum transitions are possible: one inner and two outer transitions. The TQ transition is threefold the frequency of the SQ transition. From [Hu 2020].

to quantitative ^{23}Na MRI as described in the following subsection.

Compressed sensing techniques

In sodium MRI, a movement to apply compressed sensing-based techniques started in 2012 [Madelin 2012]. A review [Chen 2021] summarizes all the compressed sensing studies published until 2021. These studies have in common different reconstruction techniques in addition to the standard l_1-norm and TV penalty (equation 1.34). Several innovative sparsity regularizations have been employed to apply CS to sodium MRI, such as second-order TV and dictionary-based learning [Behl 2016a, Lachner 2019, Kratzer 2020, Kratzer 2021].

Lachner et al. spearheaded the blend of multichannel imaging with CS sodium MRI in a study about breast cancer utilizing a multichannel dual-tuned sodium and proton

RF coil [Lachner 2019]. He found that using multiple sodium coils improved the results obtained using the proposed CS algorithm with higher picture quality [Lachner 2021]. As of late, Adlung et al. verified that convolutional brain networks could recreate 4-overlap undersampled sodium MRI images using regularization while keeping up with SNR and TSC measurement exactness for ischemic stroke patients [Adlung 2021]. Most studies investigating CS-based sodium MRI have involved data acquired at ultra-high field strengths, typically 7 T, with different types of non-Cartesian 3D spiral **k**-space sampling schemes with undersampling factors going from 2 to 10.

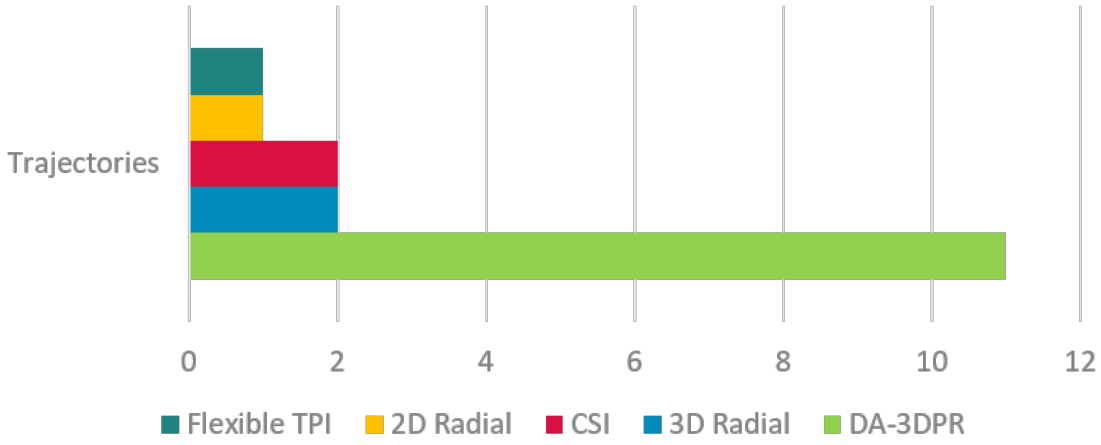

Figure 2.11 – Summary of compressed sensing sodium MRI studies compiled by [Chen 2021]. flexible TPI stands for flexible Twisted projection imaging [Lu 2010]. density-adapted three-dimensional radial projection reconstruction pulse sequence (DA-3DPR).

However, as shown in the figure 2.11, those studies did not explore original sampling schemes optimized with the goal of compressed sensing imaging. This could constitute a missing opportunity for ^{23}Na MRI as such optimized sampling schemes have been proposed successfully for CS-based proton MRI [Kumar Anand 2008, Vasanawala 2010, Lazarus 2019, Chaithya G R 2022, Chaithya 2022]. That is why one of this thesis' objectives was to develop such acquisition schemes for CS-based sodium MRI.

2.4.2 Clinical Applications

The first *in vivo* sodium image was acquired in 1985 [Hilal 1985]. Since then, sodium MRI has been continuously developed and applied to various organs (kidney, brain, heart, knee...) or pathological conditions (tumor, stroke, multiple sclerosis...) to gain an insight into (patho)physiology.

During ischemic stroke, blood flow in the brain is reduced or blocked due to artery constriction or occlusion. As a consequence of reduced oxygen inflow, oxidative ATP production is brutally limited, causing rapid neuronal dysfunction and a cascade of molecular events called apoptosis, leading ultimately to neurons' death. If possible, thrombolytic treatment needs to be applied in fewer than six hours. As it is difficult to place the onset

of the stroke, imaging biomarkers are required to determine this time, and TSC is one candidate for that [Thulborn 2018].

Tumors also affect TSC. Due to the rapidity of cell division rates in tumors, homeostasis is disturbed. Also, the pH value is altered. The fast disorganized growth of malignant cells leads to increased Na concentration due to larger interstitial spaces, even edema and necrotic tissues due to the lack of oxygen supply at the center of the tumor [Ouwerkerk 2003, Zaric 2021a]. For example, in one study, tissue sodium concentrations were measured within normal prostates and tumors in prostate cancer patients, using prostatectomy as a pathological criterion standard. Fifteen patients with biopsy-proven magnetic resonance imaging visible, intermediate- or high-risk prostate cancer underwent a sodium MRI examination before treatment with radical prostatectomy. Inversion-recovery sodium imaging acquisition time was 19 minutes. Results showed that peripheral zone tumors demonstrated a significantly increased TSC [Barrett 2018].

Inflammation is the initial cause of Multiple Sclerosis (MS). In the long term, the progressive demyelination of axons is coupled with overexpression of Na^+ channels. Therefore, ^{23}Na has been used to monitor the inflammatory process [Eisele 2016, Eisele 2019]. In one such study, 26 relapsing-remitting multiple scleroses (RRMS) patients were examined using sodium MRI using the DA-3DPR sampling scheme at 3T. The authors compared patients after a 5-year disease period with healthy controls [Zaaraoui 2012]. They examined TSCs in three different compartments: GM, normal-appearing white matter (NAWM), and T_2 lesions. In T_2 lesions in all MS patients, TSC was higher than control WM. In contrast, only the RRMS cohort with advanced disease duration exhibited significantly increased TSC for GM and NAWM. Both MS groups showed similar TSCs in T_2 lesions and NAWM. The GM TSC was higher in the RRMS cohort with advanced duration. Nonetheless, this study was able to detect sodium accumulation in the brain even in the early stages of RRMS. Analyzing the anatomical distribution of TSCs, the same research team found extensive brain regions with elevated TSCs in both MS cohorts. In advanced RRMS, increased TSC was scattered in the splenium of corpus callosum, thalamus, cingulate, and parietal lobe, frontal lobe, and prefrontal cortex.

* * *
* *
*

Part II

Estimation of cortical creatine kinase activity through dynamic ^{31}P MRI in healthy volunteers at 7T

Chapter 3

Introduction

I presented a preliminary version of our study on cortical creatine kinase activity at an international conference as:

R. Porciuncula Baptista, F. Mauconduit, A. Vignaud, C. Lerman-Rabrait and F. Boumezbeur. *Estimation of cortical creatine kinase activity by dynamic 31P brain MRI in healthy volunteers at 7T.* In Proceedings of the 38th European Society of Magnetic Resonance in Medicine, 2021.

A corresponding paper was submitted to NeuroImage and rejected earlier this year. It will be resubmitted once the necessary changes will be made.

Energy metabolism plays a fundamental role in cellular function. In the intensely active brain, neurons rely mainly on aerobic energy synthesis through cellular respiration, i.e., the oxidation of glucose (and a few other energy substrates such as Lactate) via the Krebs cycle and the oxidative phosphorylation chain. This process takes place in mitochondria and leads to the generation of a H^+ gradient across the inner mitochondrial membrane which is consumed to convert adenosine diphosphate (ADP) to Adenosine triphosphate (ATP) via the ATP-synthase activity. Moreover, the constant need for ATP (e.g., for ion homeostasis via Na^+/K^+ pump activity and other ATPases) is also sustained by the creatine kinase (CK). This enzyme catalyzes (reversibly) the conversion of ADP and phosphocreatine (PCr), an energy buffer, into ATP and creatine (Cr). The equations that describe this system were described at section 2.3.2.

Chronic energy deficits have been incriminated as critical factors in the physiopathology of many neurodegenerative diseases such as Multiple Sclerosis [Trapp 2009] or Alzheimer's Disease [Butterfield 2019]. The generic hypothesis is that mechanism implies a "virtual hypoxia state" in which energy demand in neurons fails to be met, leading to the disruption of the most energy-intensive processes such as neurotransmission, hence the development of impaired motor or cognitive dysfunctions.

It is hypothesized that at early, asymptomatic stages of these neurodegenerative diseases, (young) neurons would manage to increase their energy production rates, which would then cause up-regulated fluxes through the ATPsynthase and CK (with eventually augmented

ATP and PCr stores). In later, prodromal stages, the accumulated oxidative damage and declining mitochondrial function would lead to low ATP synthase and CK activities (possibly decreased ATP and PCr levels), unmet basic energy requirements, and ultimately cell death. It is thus believed that investigating in a quantitative manner brain energetics and high-energy phosphate (HEP) metabolites using dynamic *in vivo* Phosphorus-31 (^{31}P) NMR spectroscopy (^{31}P-MRS) could provide direct insight into the etiology and progression of such diseases [Zhu 2018a, Hoang 1998, Brown 1989].

Among the techniques one can use to probe energy metabolism non-invasively, *in vivo* ^{31}P-MRS is one of the most promising for clinical research since it allows several different results in clinical application [Zhu 2012]. Moreover, it does not require costly, exogenous ^{18}F, ^{13}C or ^{2}H labeled energy substrates or derivatives [Barros 2018]. While *in vivo* ^{31}P-MRS has been successfully applied in musculoskeletal system studies to investigate metabolic syndromes [Bogner 2009, Schmid 2016] thanks to the large PCr concentration in muscles (about 30-38 mmol/L), the application of ^{31}P-MRS to study neuroenergetics has often been limited by the relatively low concentrations of ATP and PCr in the brain. In recent years, ^{31}P-MRS has greatly benefited from the advent of clinical MRI scanners at UHF, which allowed the development of ^{31}P-magnetic resonance spectroscopy imaging (^{31}P-MRSI) approaches [Ruhm 2020].

Yet, the relevance of those ^{31}P-MRSI approaches to the study of neurodegenerative diseases is limited in two ways. First, those studies have relied on a relative quantification of the HEP concentrations assuming a homogeneous, stable concentration of γ-ATP in the brain [Ren 2015, Chen 2018, Ruhm 2020]. While this hypothesis is somewhat valid in healthy controls, such an assumption could mask the metabolic changes expected in patients suffering from those neurodegenerative diseases.

To achieve absolute quantification of HEP metabolites, one could use a synthetic signal generated by an external RF source, such as in the ERETIC method [Barantin 1997]. Yet, such a solution requires tampering with the MRI scanner electronics, which is seldom possible. Due to the low spatial resolution of ^{31}P applications, it is impossible to put an external and small phantom simultaneously on the human head. On the one hand, a phantom small enough to fit with the patient would have a few centimeters. Then the image with the resolution with a comparable size would suffer from a partial volume effect and therefore have few vowels available to measure concentration. On the other hand, phantoms big enough to have a sufficient number of voxels to do a linear regression would be too big to accommodate in the coil with the volunteer. Therefore, we adopted a phantom replacement approach using two references of signal, i.e., two phantoms with comparable load to the human brain [Stout 2017, Stout 2019]. Due to low spatial resolution, the acquisitions were made separately from the *in vivo* acquisitions.

To obtain absolute concentrations, the B_1^+ field heterogeneity of our ^{31}P radiofrequency coil was accounted for (details in method section) as well as the differential relaxation effects using previously measured T_1 relaxation times of ^{31}P metabolites in the human brain at 7T [Ren 2015] (Table 3.1).

HEP metabolites concentrations do not necessarily reflect the intensity of energy

Metabolite	Pi	Pi	PCr	α-ATP	β-ATP	γ-ATP
T_1[s]	5.80	3.70	3.39	1.35	1.13	1.70

Table 3.1 – Relaxation time T_1 of metabolites in resting human brain at 7T from [Ren 2015]

metabolism or mitochondrial function univocally. To offer an analogy, it is not enough to know how many vehicles per square meters (concentration of metabolites) are on the road to characterize the traffic conditions in a city [Hiller 2013]. To precisely determine whether the cars are stalled or moving freely, one must check how fast the cars are moving through the city streets (flux through the metabolic pathway). If there is traffic congestion, one can then interrogate how many people are driving on each road (abundance of transcripts or proteins) or wonder about the reasons why people would be driving at any given time (genetic events and environmental factors). Ideally, dynamic ^{31}P-MRS permits the estimation of production and degradation rates of ATP via the creatine kinase (CK) (V_{ck}) or ATPase/ATP-synthase activities. Those direct measures of energy metabolism can be obtained with the addition of a saturation transfer (ST) module with varying duration or saturation intensities [Zhu 2012, Chaumeil 2009].

Due to the modest concentrations of HEP in the brain and ^{31}P intrinsically low sensitivity (compared to ^{1}H), dynamic ^{31}P-MRS protocols using ST techniques to estimate V_{ck} have often required long acquisition time (TA) [Bottomley 2002]. These long TA are related to the choice of working in fully-relaxed conditions (TR»T_1). Since the T_1's of Pi and PCr are quite long, the standard magnetization transfer experiment is rather inefficient in generating sufficient contrast-to-noise ratio (CNR) per unit time. Consequently, those studies could only probe ATPase or CK activities in one region of interest (ROI) at a time [Zhu 2012].

Thanks to the improved spectral resolution and signal-to-noise ratio (SNR) achievable at UHF, three-dimensional (3D) multi-point Dixon [Dixon 1984] or frequency selective (FS) ^{31}P magnetic resonance imaging (MRI) sequences constitute attractive alternatives to ^{31}P-MRS or ^{31}P-MRSI approaches [Ren 2015]. Thus, we propose an frequency selective (FS) multiplex (alternate excitations of γ-ATP and PCr resonances) magnetic resonance imaging (MRI) sequence combined with a γ-ATP presaturation module to perform regional V_{ck} measurements in conditions compatible with a clinical research setting.

For this study, we used a ^{1}H/^{31}P dual resonance 8-elements transceiver phased array coil developed by N. Avdievich [Avdievich 2011]. While phased-array head volume coils outperform birdcage volume coil designs in terms of SNR, especially in cortical areas, one needs to manage their heterogeneous transmission profiles in return. Ideally, one would acquire a B_1^+ map for each subject as it is done for ^{1}H using the double-angle method (GRE-DA) [Insko 1993] or a single shot method using spectral selection like magnetization prepared turbo-FLASH (XFL) [Amadon 2010] or even adopt the Variable Flip Angle approach that we proposed for quantitative ^{23}Na MRI [Coste 2019]. Unfortunately, such acquisitions would be too long or too noisy to be compatible with our objective of proposing a clinically viable dynamic ^{31}P-MRI protocol. To tackle this problem, we developed an

original approach to correct those B_1^+ inhomogeneities based on a B_1^+ template calculated from a set of independent 3D B_1^+ maps acquired using a modified version of GRE-DA, which we call variable multiple flip angle (VMFA). The idea of using a B_1^+ template is in agreement with the one driving recent innovations for ^{1}H parallel-transmission such as the universal pulses [Gras 2017].

Overall, we aimed at demonstrating the feasibility of estimating absolute ATP and PCr concentrations as well as the flux through the CK reaction (V_{ck}) in various cortical ROI in a time frame acceptable for with clinical research applications at 7 Tesla. We used a FS multiplex sequence to achieve this goal while controlling for the effective excitation and saturation flip angles using a VMFA template.

Chapter 4

Methods

Chapter Outline

4.1 Data acquisition

This section describes the materials and methods needed for our ^{31}P MRI data acquisition.

4.1.1 Participants

This study was approved by local and French national ethics committees (CPP Sud Méditerranée 4, number 18 09 13, IDRCB: 2018-A011761-53), and written informed consent was obtained from all participants. This study was divided into two parts: (i) a dedicated VMFA mapping protocol to generate our 3D B_1^+ template and (ii) our dynamic ^{31}P-MRI protocol to estimate cortical ATP and PCr absolute concentrations and V_{ck} values.

For the first part, six volunteers were recruited (3M/3F, 29±6 years old). For the V_{ck} estimation, two groups of three volunteers were recruited: the first group allowed us to test the version of the sequence without saturation bands (2M/1F, 26±3 years old), and the second group allowed us to test the version of the sequence with saturation bands (2M/1F, 31± 18 years old). The three cohorts were disjointed. The reasoning for applying the saturation bands is explained in the section 4.1.4.

4.1.2 Test-objects

Two types of phantom were used in this project, one for the validation of the spectral selectivity of the sequence and the other to validate our quantification approach. They are described below. The solutions were mixtures of phosphate buffered saline (PBS) and tripolyphosphate (TPP). PBS is similar to Pi (a mixture of $H_2PO_4^-$ and HPO_4^{2-} with a pinch of NaCl in water) [Kogan 2014b, Thapa 2016, Valkovič 2021] and TPP is used as a practical alternative to ATP as it is less expensive and more stable over time [Chmelík 2008].

FS validation phantom

This phantom is composed of a cylinder containing 50 mmol/L of PBS. Inside four 50 mL tubes are placed containing respectively 12,5 mM, 25 mM, 50 mM, and 100 mM of TPP, the schematic can be seen in figure 1.1.

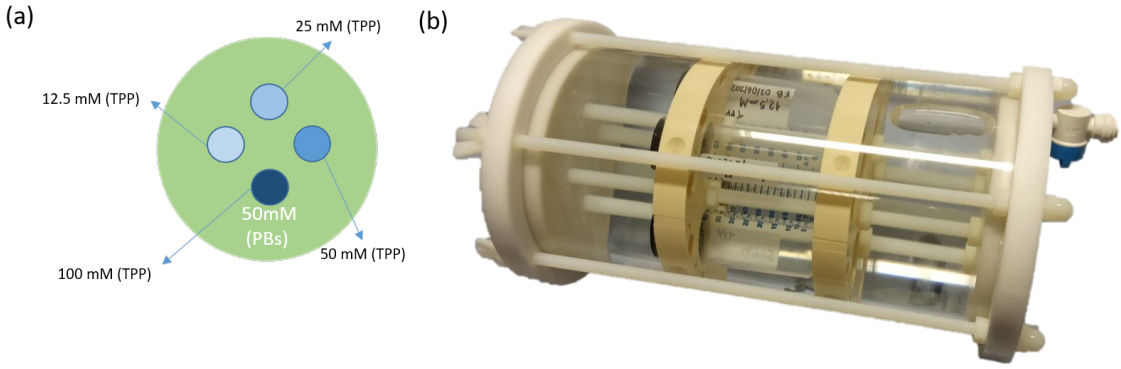

Figure 4.1 – Description of the validation phantom used for validation of the frequency selective excitation. (a) schematic of the frequency validation phantom (green represents PBS and blue TPP); (b) graphic of the frequency selection validation phantom. This phantom was machined in the mechanical workshop of NeuroSpin by Jeremy Bernard.

Quantification phantoms

Two identical 4.5L bottles containing either 25 or 50 mmol/L of PBS were used as external references of signal (figure 4.2). Their coil loading was judged comparable to a human head based on the allure of the experimental B_1^+ maps, voltage reference values and reception profiles. These phantoms were also used to validate our FA mapping method. I used the

top part of the bottle to simulate the head by positioning the bottle half outside the coil. I thus used the bottle part to simulate the load of the shoulders.

Figure 4.2 – Illustration of one of our quantification phantom

We recognize the limitations in the shape of these phantoms. Realistic phantoms have been studied in the literature [Collins 1998, Wood 2017, Marques 2021]. Later in the study, we 3Dprinted a realistic phantom based on the geometry proposed by Jona and all [Jona 2021]. Once a head-shape-like phantom was made available, we validated the FA maps with it. The phantom in figure 4.2 was then used to simulate the shoulder by coupling together.

This phantom was filled with 10 and 100 mM PBS solution for the outer and brain-like inner compartments respectively (see figure 4.3 for illustration).

4.1.3 MR System

MRI examinations were performed on a 7 Tesla Magnetom MRI scanner (Siemens Healthineers, Erlangen, Germany) using a whole-body gradient coil (G_{max}=100 mT/m, slew rate of 200 T/m/s) and a dual-resonance $^{1}H/^{31}P$ phased-array coil consisting in 8 transceiver elements for each nucleus. Each coil element is part of an inductively decoupled split elliptical transceiver-phased array with selectable geometry, which provides an easy and efficient way of compensating for changes in mutual inductive coupling associated with differences in loading due to variability in head shape and size (figure4.4) [Avdievich 2011]. The coil was manufactured by Resonance Research Inc. (Billerica, MA, USA) and used in circular polarization (CP) mode for transmission with eight receive channels (1Tx/8Rx).

4.1.4 Multiple Frequency Selective Sequence

All ^{31}P measurements were based on our MFS sequence with or without saturation transfer module, as represented in figure 4.5.

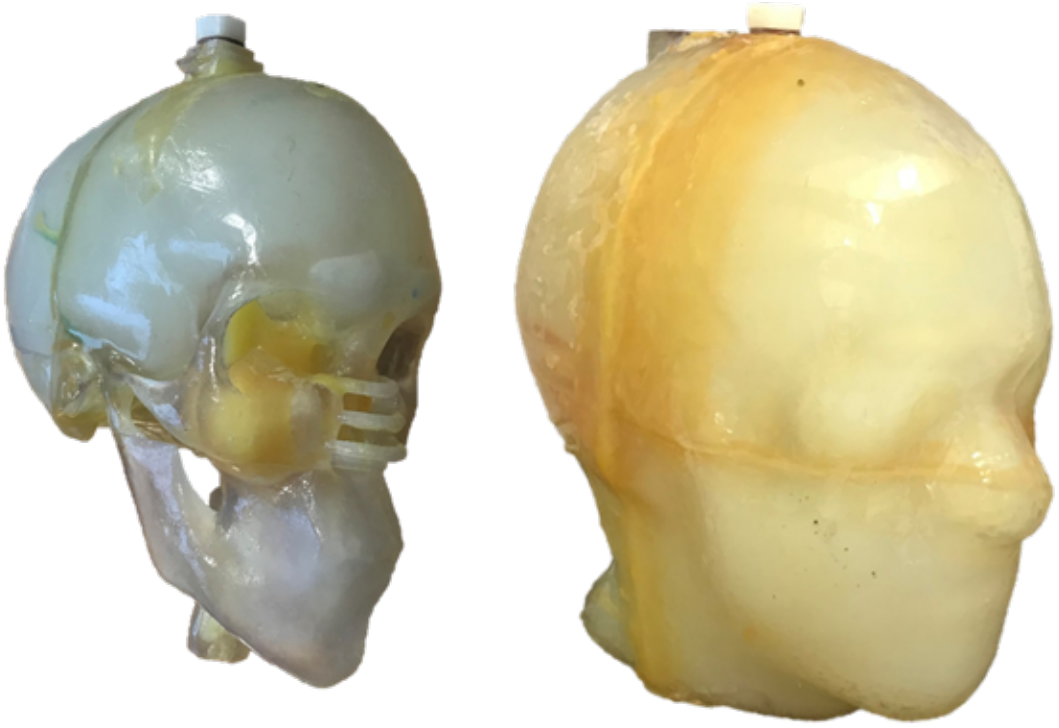

Figure 4.3 – Illustration of "Skully" phantom. The left side represents the inner compartment. The right side represents the outside compartment— a courtesy of Thaddée Delebarre (Ph.D. Student at NeuroSpin).

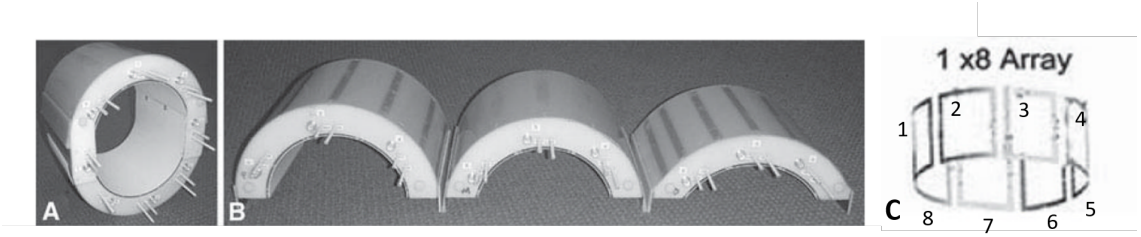

Figure 4.4 – An illustration of a dual-resonance RF coil similar to the one used for this study. (a) Back view of the elliptical 8-channel (1 × 8) split transceiver-phased array. The bottom part is shown assembled with the medium size top. (b) Three tops of the split array (c) Individual surface coils in the first (1 through 8). Adapted from [Avdievich 2011].

During this thesis, I developed this sequence from the canonical code for the FLASH (SPGR) sequence provided by Siemens as part of their IDEA toolkit. I modified it into a UTE sequence and added the alternating aspect and the saturation module. I developed a saturation module from zero to account for the variable saturation angles at different frequencies. I first developed this sequence for VB17 and later for VE12 in the Siemens IDEA development toolkit.

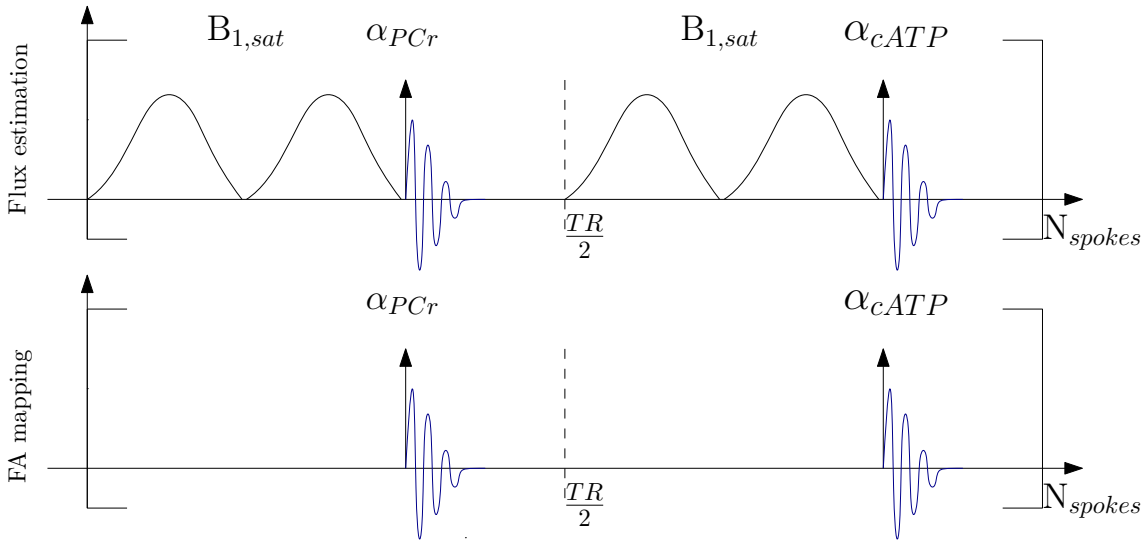

Figure 4.5 – Schematic of the MFS sequence. The core MFS sequence consisted in alternate frequency selective excitations of γ-ATP (at -2.5 ppm) and PCr (at 0 ppm) every TR. The main parameters are TE/TR=5/250 ms, number of spokes 3600, and TA=15 min. For the estimation of V_{ck}, FA was equal to 25°, and a saturation transfer module was applied every TR/2 consisting of two 40 ms Gaussian pulses selective for γ-ATP, the saturation intensity $B_{1,sat}$ being varied. No saturation were applied for the FA mapping protocol which focused on the acquisition of PCr images at increasing FA=(12,24,36,48)°.

Interface

The goal of this sequence was to allow for maximal flexibility. Therefore, several parameters of the sequence were kept adjustable in the "special card" accessible on the Siemens Syngo interface (figure 4.6). A non-exhaustive list of parameters is given below:

- **Gradient File Selection**: this parameter allows the user to change sampling scheme acquisition. Here we used TPI.
- **FreqSel Offset**: it defines the variation in the B_0 frequency (Δ_f) in (Hz) from the system frequency for the first and the second excitation pulse. This parameter is a list.
- **FreqSel Offset MT**: it defines the variation in the B_0 frequency (Δ_f) in (Hz) from the system frequency for the saturation transfer pulse.
- **Flip angle MT**: it defines the saturation pulses' intensity in degrees.
- **MT pulse duration**: duration of each saturation pulse in μs.
- **MT total duration**: duration of the overall saturation transfer module in μs, thus defining the intervals between pulses.
- **Number of pulses MT**: quantity of saturation pulses.

- **Readout OS factor**: it defines the factor by which the dwell time will be divided. For instance, if OS=5 while the data was acquired with a dwell time $\delta t = 2\mu s$ ($\Delta t = 10\mu s$) at the analog-to-digital converter level. For this study, value was set at default default = 1.

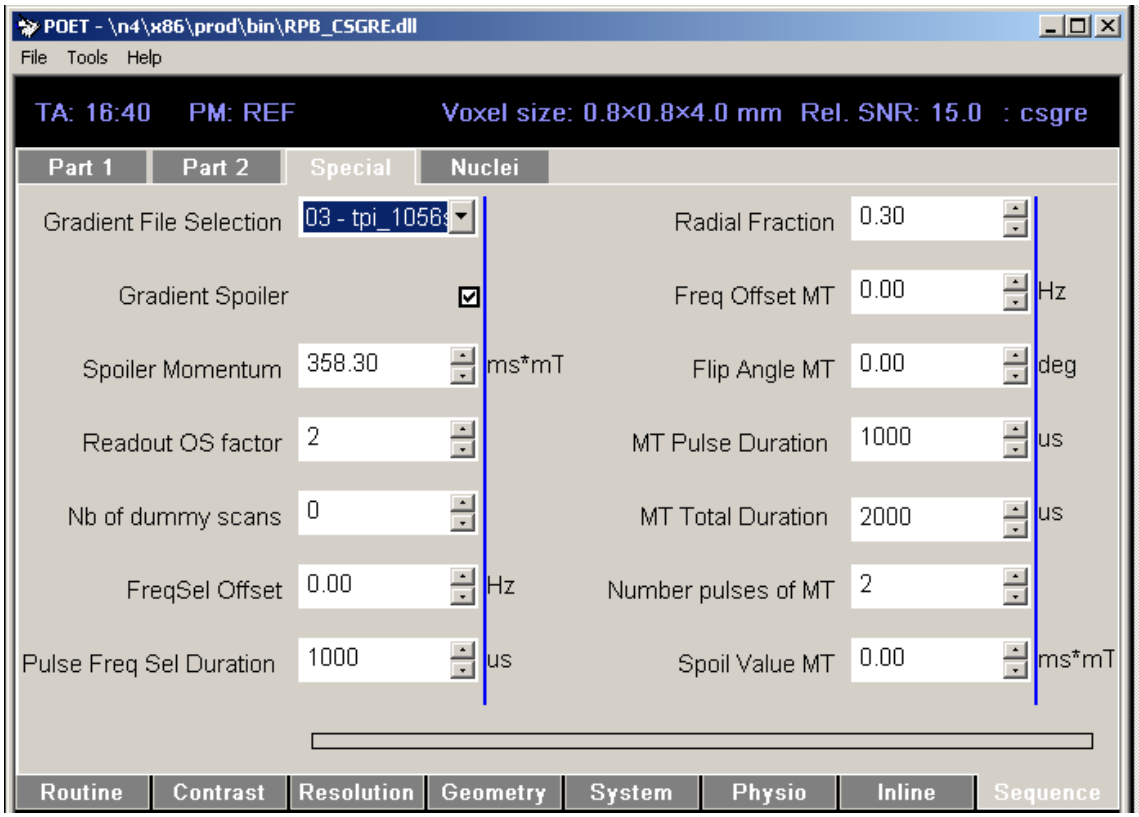

Figure 4.6 – Schematic of the MFS sequence "special card" on VB17.

Common parameters

To improve our point-spread function, a Twisted Projection Imaging (TPI) non-Cartesian k-space sampling scheme [Boada 1997] with radial fraction parameter (p) set at 0.3 was combined with a spoiled FID sequence. To limit T_2*-weighting and loss of signal, frequency selective 8 ms Gaussian pulses (FWHM = 2 σ = 328Hz from simulation) were used for alternate excitation of either PCr (at 0 ppm) and γ-ATP (at -2.5ppm), resulting in an effective TE of 5 ms.

The spectral selectivity was controlled *in vitro*. Ideally, we would test spectral selectivity with a phantom with two peaks that have the same spectral distance than γ-ATP and Pi. However, due to cost of obtaining a γ-ATP like peak, we fabricated a phantom with PBS and TPP instead. This two metabolite have a peak distance in order of 1300 Hz which is fourfold bigger than the Pi-γ-ATP pair. For this reason, we decided to observe spectral selectivity by shifting the excitation in one peak (PBS) and observe the signal acquire the peak without any shifts.

For this reason, we acquired in Skully with only PBS four images at different $\Delta_f = [0, 160, 320, 480]$ Hz based on value expected from simulations, and we observed that for $\Delta = 350$ Hz, we had a mitigation of 95 % of the signal intensity (figure 4.7).

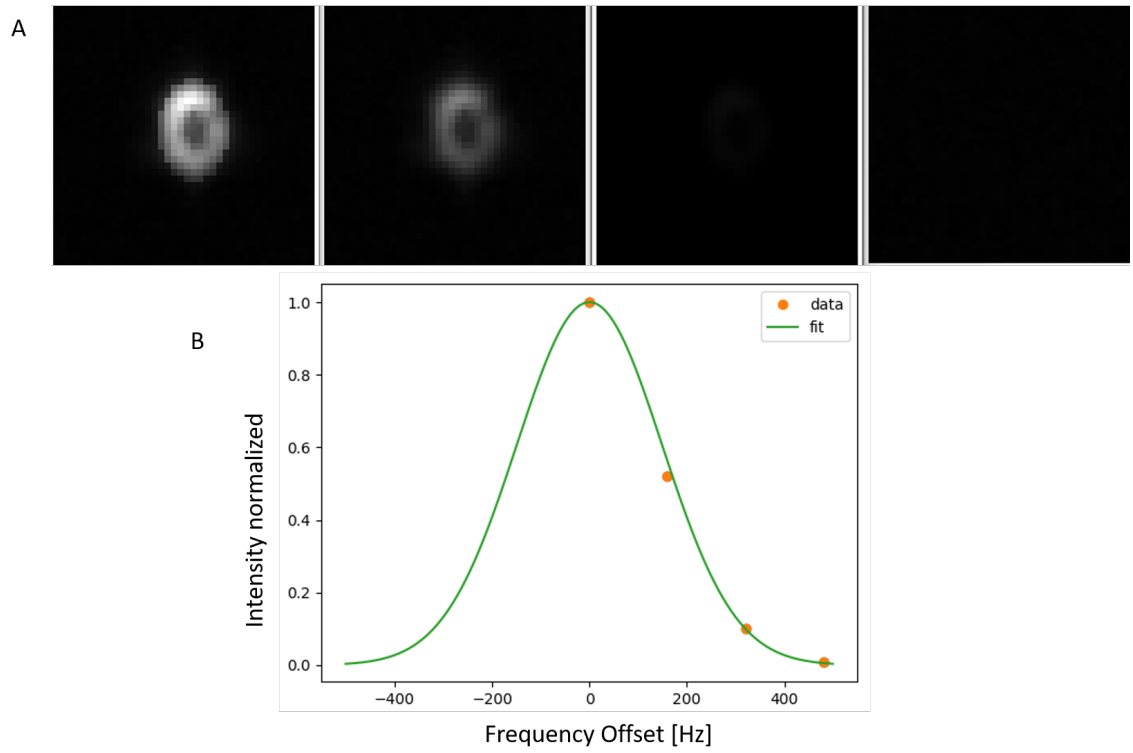

Figure 4.7 – Validation of FWHM of the Gaussian pulses of 8 ms. (A) Reconstructed images acquired at $\Delta_f = [0, 160, 320, 480]$. (B) Fit of the gaussian data

Short TR (250 ms) and small excitation flip angles (FA=25°) were used to improve our SNR per unit of time. Noise scans (FA=0°) were included for noise measurements, which were then used to prewhiten the data from each reception channel [Martens 2003].

The sequence was validated *in vitro* using a dedicated phantom with different concentrations of PBS and TPP. The schematic of the phantom and the results of the validation test can be seen in figure 4.8.

Version with saturation bands

The concentration of PCr in the muscle is about ten-fold higher than in the brain [Kemp 2007]. For this reason, signal contamination from the extracranial muscles can lead to a notable overestimation of the PCr concentration, especially in cortical areas. To investigate the possible impact of such contamination on our results, we repeated the measures of the flux estimation, but this time adding two outer volume saturation (OVS) bands over the maxillary muscles.

Two OVS bands were positioned as illustrated in figure 4.9. Saturation angles were limited due to SAR constraints. Therefore, the saturation flip angle had to be reduced

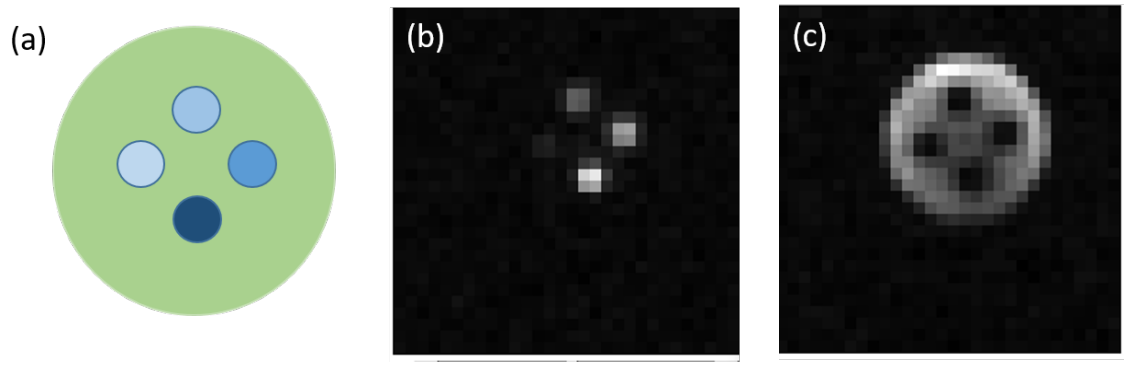

Figure 4.8 – Phantom is used to validate composed of PBS and TPP. (a) schematic of the phantom, 100 mM concentration of PBS, and four tubes of TPP with 12.5 , 25, 50, and 100 mM concentration. (b) Raw images reconstructed for TPP (c) raw images reconstructed for PBs.

from 90° to approximately 50°. Due to the short TR, this compromise was expected to only limit the efficiency of the saturation to 80% instead of 100% (for PCr after few TR).

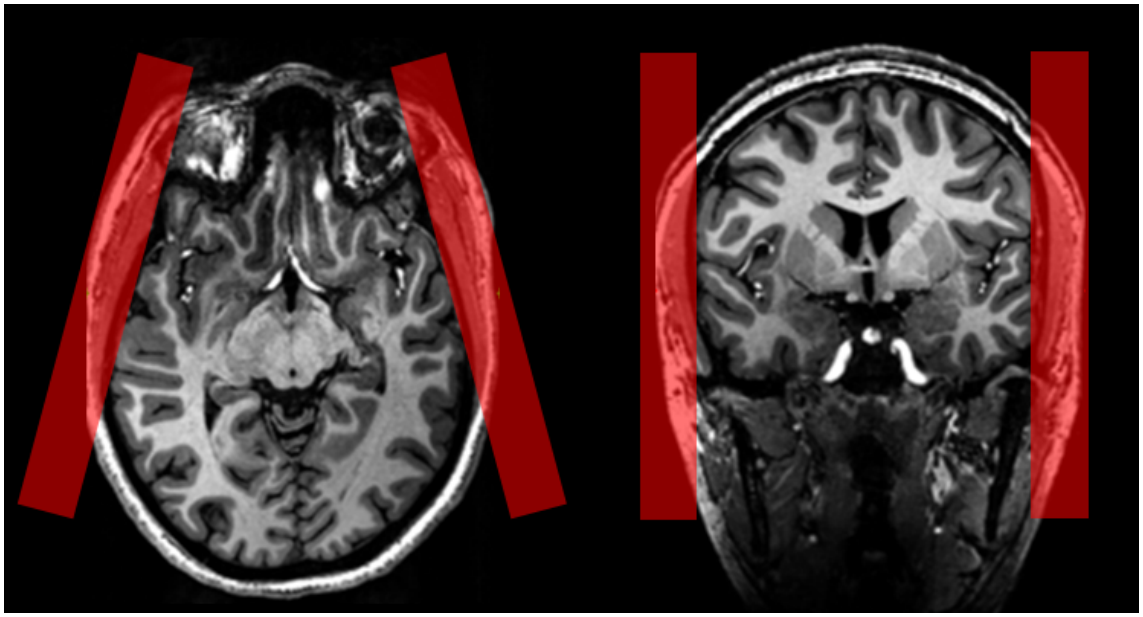

Figure 4.9 – Schema of the positioning of saturation bands. The head of the volunteer, and red, is the position of the saturation bands.

To confirm that this compromise was satisfactory to dampen external signals from the muscle to acceptable level minimizing their impact on HEP quantification in the brain, we performed a test in phantom.

4.1.5 *In vivo* MR Imaging protocols

Proton acquisitions

Each examination included the acquisition of a T_1-weighted image (MPRAGE, TE/TR/TI = 4/2600/1100 ms, FA= 9°, 2 mm isotropic resolution, TA=4:32 min) for anatomical

reference. An iterative second-order B_0 shimming procedure was performed, and a B_0 map was acquired (2 mm in-plane resolution, 2.5 mm slice thickness, FA=27°. TA=1:36 min).

VMFA acquisitions.

Due to the larger PCr signal when compared to γ-ATP, *in vivo* FA maps were estimated from the PCr images only, even though the same sequence was used in all protocols, and therefore both PCr and γ-ATP were acquired.

I determined the nominal flip angle value α for our variable multiple flip angle (VMFA) approach via Monte-Carlo (MC) simulations (figure A.0.1) considering our experimental noise level and expected SNR (SNR = $\frac{\mu_{signal}}{\sigma_{noise}}$).

Noise levels were estimated through *in vitro* acquisitions with FA=0°, with the bottle phantom in place. Then the noise was determined as the standard deviation of all voxels from the reconstructed image. The signal level measured in a phantom of known concentration was determined as the average signal in the phantom's mask. However, the concentration of the bottle phantom is superior to [PCr] in the brain. For this reason, we adjusted the signal value according to the ratio of those concentrations.

$$\mu_{\text{expected signal in vivo}} = \frac{\mu_{\text{signal phantom}}}{[\text{concentration phantom}]} \times [\text{concentration in vivo}] \tag{4.1}$$

Considering the duration of each MRI examination (total=1h15 adjustments included), we decided on acquiring four PCr images with FA=(12,24,36,48)°. Other acquisition parameters were: isotropic spatial resolution of 25x25x25 mm^3 (about 16 mL), number of spokes=3600, TA=15 min. More details are available in the appendixA.

Dynamic ^{31}P MRI acquisitions.

In order to estimate V_{ck}, γ-ATP and PCr images were acquired using our FSM sequence (fig. 4.5) with a saturation module consisting in two 40ms Gaussian pulses (FWHM=68Hz) at four increasing saturation intensities (FA_{sat} = (0,15,30,60)°). The largest saturation angle was set at a nominal value of 60° so that the γ-ATP signal level would remain just above the noise level of our acquisitions. Other acquisition parameters were: isotropic resolution 12.5x12.5x12.5 mm^3 (4 mL), number of spokes=3600, TA=15 min.

4.1.6 *In vitro* MR Imaging protocols

Phantom data were acquired from our two 4.5L phantoms using the two previously presented ^{31}P-MRI sequences at the frequency of phosphate buffered saline (PBS) without saturation. To validate our FA mapping approach, a 2D-XFL image of a central slice of our 50 mmol/L phantoms were acquired (nominal FA=60°, TR/TE=10000/3 ms, number of averages 96, in-plane resolution 25x25 mm^2, slice thickness 50 mm, TA=32 min).

4.2 Data processing

4.2.1 ^{31}P image reconstruction

Raw k-space data were tagged to separate PCr and γ-ATP signals; and both images were reconstructed offline using a homemade Matlab script (The MathWorks Inc., Natick, Massachusetts) using a non-uniform fast fourier transform (FFT) regridding algorithm consisting of a Kaiser-Bessel kernel interpolation as well as density compensation and Hamming filtering steps. The density compensation function we used was defined as:

Algorithm 1 Density compensation for TPI

Input p, coordinates
Output dcf
$N \leftarrow size(coordinate, 1) * size(coordinates, 2) * size(coordinates, 3)$
$wi \leftarrow zeros(N, 1)$
$temp \leftarrow reshape(coordinates, 3, [])$;
$w \leftarrow \sqrt{(temp(:,1)^2 + temp(:,2)^2 + temp(:,3)^2}$
$i \leftarrow 1$
for $i < N$ **do**
  if $w(i) < 0.5 * p$ **then**
    $wi(i) \leftarrow w(i)^2$
  else
    $wi(i) \leftarrow wi(i-1)$
  end if
  $i \leftarrow i + 1$
end for
$dcf \leftarrow reshape(wi, ro, 1, [])$;

Data were prewhittened [Martens 2003]. Magnitude images were combined using sum-of-squares.

4.2.2 FA correction

As previously explained in sub-section 1.2.3, surface coils have greater sensitivity but suffers from large B_1^+ (and B_1^-) inhomogeneities. To tackle this issue, we corrected our data for B_1^+ inhomogeneities. One would need an hour to acquire an individual map of B_1^+ at 3D, as we do not dispose of an extra hour with the volunteer. Here, we opted for a template approach. We also showed that it is a valid approach due to the similarity of FA maps between human subjects. We used the same sequence described above for the computation of FA maps. However, we only used the PCr images because they have greater SNR when compared to γ-ATP, thus giving more precise FA maps.

FA map calculation.

Once reconstructed each image of our VMFA protocol=was submitted to a non-local means denoising step (available from the scikit-learn image library [Pedregosa 2011]). The individual B_1^+ maps were then estimated from the numerical fit of the signal equation

(Equation 4.2) using a non-linear least squares minimization algorithm, assuming the previously reported T_1 relaxation time of PCr at 7T (Table 3.1):

$$S \propto M_0 \frac{\sin(\alpha)(1-\exp^{\frac{-TR}{T_1}})}{1-\exp^{\frac{-TR}{T_1}}\cos(\alpha)} \exp^{\frac{-TE}{T_{2*}}} \tag{4.2}$$

The initial FA maps were then regularized spatially by fitting the values to a 8^{th} degree polynomial 3D function.

FA map validation.

The validity of our VMFA protocol was evaluated *in vitro* by comparing our FA map to the reference map obtained using the XFL method using linear fitting and by computing the corresponding Pearson correlation factor.

FA Template.

All individual FA maps were over-sampled by a factor of two to match the resolution of the PCr and γ-ATP maps. Then it was co-registered to the MNI template space [Mazziotta 1995] with the help of their anatomical reference images (following a first rigid co-registration step). The FA template was then defined as the average FA map across all subjects. An overview of the pipeline can be seen in figure 4.10.

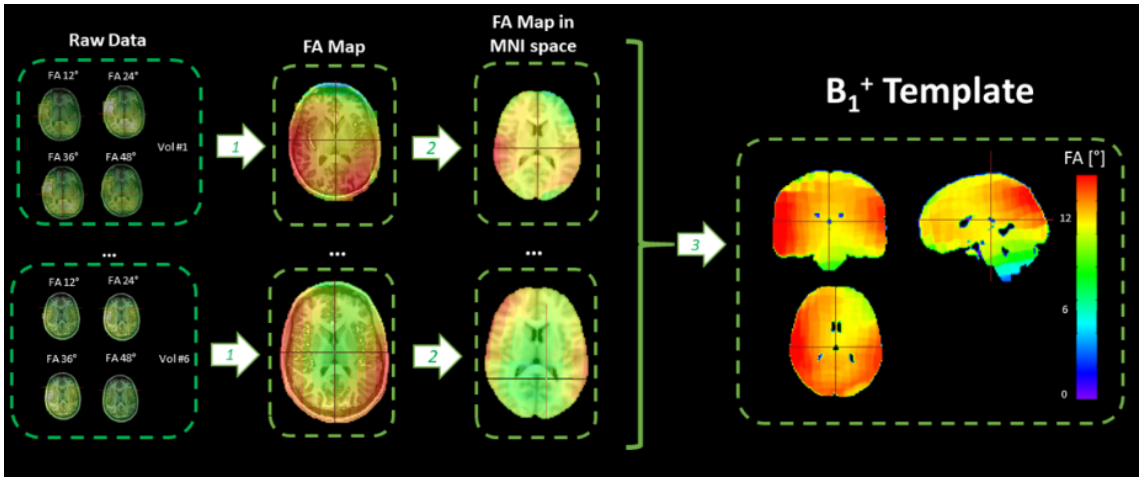

Figure 4.10 – Pipeline for FA map template computation. 1: Individual FA maps fit using the VFA approach. 2: Co-registration to the MNI template space via each anatomical reference. 3: Averaging in the MNI space of the individual FA maps.

Once I computed the template, a correction factor (CF) map could be determined as:

$$CF(x,y,z) = \frac{S(FA_{effective})(x,y,z)}{S(FA_{target})(x,y,z)} \tag{4.3}$$

Average CF values can then be calculated at the voxel level and applied in the individual space.

4.2.3 Definition of our cortical ROI

Masks for five large cortical ROI were defined from the Harvard-Oxford atlas [Frazier 2005, Makris 2006, Desikan 2006], avoiding areas exhibiting lower and more variable signal levels due to the phased-array coil geometry. The five ROI were constituted by aggregating smaller adjacent brain areas (see figure 5.6): frontal & anterior cingulate cortices (#1 in pink); frontal gyrus & opercular cortices (#2 in mustard); temporal, supramarginal & angular cortices (#3 in red); precuneus & posterior cingulate cortex (#4 in blue); occipital cortex (#5 in green).

4.2.4 Concentrations quantification

For each ROI, regional ATP and PCr concentrations were estimated from a two-point linear calibration step by comparing their average signal values to the signal from our two external references of concentration after correcting for the regional effective excitation flip angle (correction factor (CF)) and differential T_1 and T_2^* weightings. Experimental T_2^* were considered (estimated from the linewidths of our PCr, ATP, and PBS resonances). The previously reported [Ren 2015] T_1 relaxation times of PCr and γ-ATP at 7T were considered (Table 3.1). For PBS, we measured a T_1 of 5.8 s at room temperature. To compensate for the Rician noise, its non-zero average value was subtracted, estimated from acquisition with a FA=0°.

4.2.5 Flux Estimation

For each ROI, I estimated apparent ATP and PCr concentrations for each nominal saturation angle. The Bloch-McConnell equations [Lei 2003] for the two-pool model of chemical exchange between PCr and γ-ATP were considered as defined by Bottomley at al [Bottomley 2002]:

$$\mathrm{PCr} + \mathrm{ADP} \underset{\mathrm{k_r}}{\overset{\mathrm{k_f}}{\rightleftharpoons}} \mathrm{ATP} + \mathrm{Cr} \tag{4.4}$$

$$\frac{d}{dt}\mathbf{m} = \mathbf{A}\mathbf{m} + \mathbf{c}$$

Which has as for solution:

$$\mathbf{m} = \exp^{\mathbf{A}t}(\mathbf{m}(t=0) + \mathbf{A}^{-1}\mathbf{c})\mathbf{A}^{-1}\mathbf{c} \tag{4.5}$$

Where M represents the compounded PCr and ATP magnetization in a given state:

$$\mathbf{m} = \begin{bmatrix} M_x^{PCr} & M_y^{PCr} & M_z^{PCr} & M_x^{\gamma ATP} & M_y^{\gamma ATP} & M_z^{\gamma ATP} \end{bmatrix}^T$$

And $\mathbf{c}$ and $\mathbf{A}$ is defined as follows:

$$\mathbf{c} = \begin{bmatrix} 0 & 0 & \frac{M_0^{PCr}}{T_{1PCr}} & 0 & 0 & \frac{M_0^{\gamma ATP}}{T_{1\gamma ATP}} \end{bmatrix}^T$$

$$\mathbf{A} = \begin{bmatrix} \frac{-1}{T_{2PCr}} - k_f & \Delta w_0 & & & k_r & & \\ -\Delta w_0 & \frac{-1}{T_{2PCr}} - k_f & & & & k_r & \\ & & \frac{-1}{T_{1PCr}} - k_f & & & & k_r \\ k_f & & & \frac{-1}{T_{2\gamma ATP}} - k_r & \Delta w_0 & & \\ & k_f & & -\Delta w_0 & \frac{-1}{T_{2\gamma ATP}} - k_r & w_{\gamma ATP} & \\ & & k_f & & w_{\gamma ATP} & \frac{-1}{T_{1\gamma ATP}} - k_r \end{bmatrix}$$

With Δw_0 accounting for B_0 inhomogeneities. Through mass conservation in our two pool system, we can determine k_r as:

$$k_r = k_f [PCr]/[\gamma ATP] \tag{4.6}$$

[PCr] and [ATP] were estimated in mmol/L from their respective images without saturation.

For simplification and considering the relatively short TE, the influence of Δw_0 was considered negligible. Thanks to this hypothesis, the problem is reduced to the adjustment of the sole k_f value. Thus, for each ROI, k_f values were grid searched within the range (0.15-0.45) s^{-1} to minimize the mean-square-error between the apparent experimental concentrations and our model (equation 4.5).

Finally, V_{ck} was determined according to equation 4.7.

$$V_{ck} = [PCr] * k_f \tag{4.7}$$

An overview of the pipeline is shown in figure 4.11. V_{ck} values are converted in μmol/g/min after accounting for the brain tissue density of 1.1 g/mL.

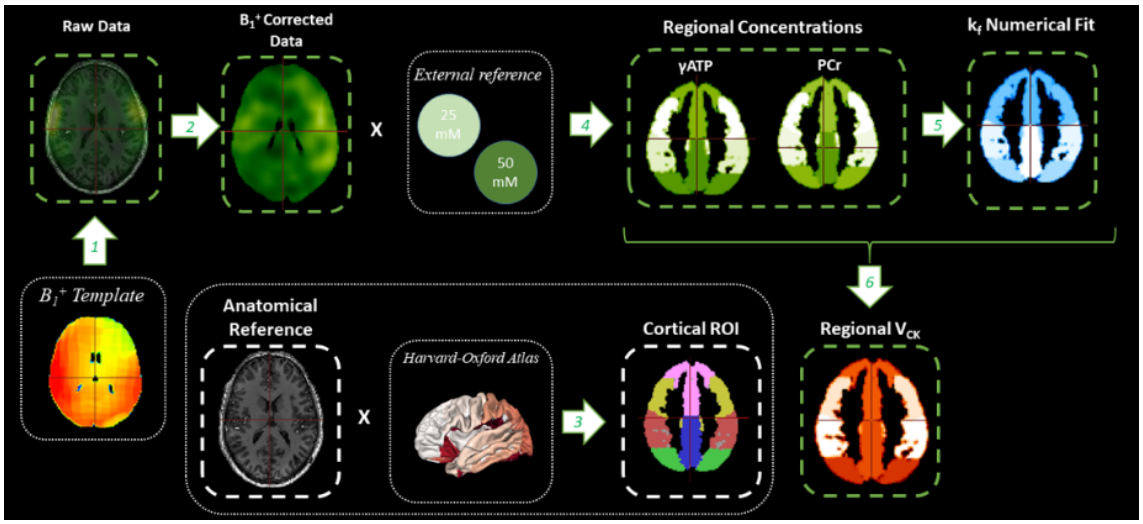

Figure 4.11 – V_{ck} flux estimation pipeline. Each set of ATP and PCr images is processed along the following steps: 1: Co-registration of the FA template to the individual space. 2. Application of the FA correction. 3: Brain segmentation and definition of our five ROI from the anatomical reference using the Harvard-Oxford atlas. 4: Quantification of the apparent ATP and PCr concentrations using the images of the two PBS phantoms for a two-point linear calibration. 5: Numerical fit of k_f using the Bloch-McConnell formalism. 6: Calculation of the regional V_{ck} values

.

Chapter 5

Results

Chapter Outline

5.1 *In vitro* validation of our B_1^+ mapping protocol

Figure 5.1 shows the agreement between our variable multiple flip angle (VMFA) mapping method and the reference method XFL for a central slice, because the XFL is a 2D sequence. The correlation factor between the two FA maps being R=0.95, we can consider the two methods to be equivalent.

The images have been normalized as follow:

$$FA_{normalized} = \frac{FA_{measured}}{FA_{target}}$$

This normalization was done to allow the comparison, because each sequence (VFMA and XFL) was optimized for different angles, i.e, their parameters were more robust to noise at different FA. VFMA target angle was FA=12° and target angle of XFL was FA=60 °.

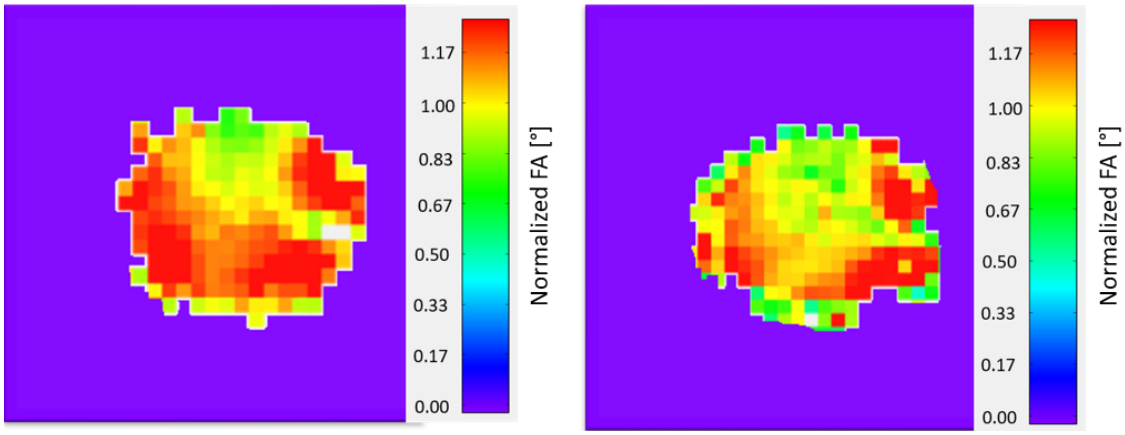

Figure 5.1 – Comparison between 2D XFL and the 3D adaptive multiple flip angle method. The scale shows the values obtained normalized to the target angle. Right, XFL method in a central slice of phantom, target FA=60°. Left, VFMA result in a central slice of a phantom, target FA=12°. Bottle phantom was used. The two FA are different because they are the values optimized by each protocol.

.

5.2 *In vivo* FA template construction

Figure 5.2 shows the B_1^+ template we obtained after averaging all individual maps in the MNI space. I computed the correlation matrices between all maps, yielding a mean R-value of 0.93 ± 0.02, the correlation factors ranging from 0.84 to 0.97, demonstrating the consistency of the B_1^+ fields between all our subjects (n=6).

5.3 *In vivo* ^{31}P MRI of ATP and PCr using our MFS sequence

5.3.1 Without outer volume saturation bands

The fig 5.3 shows a set of ATP and PCr images (for volunteer #1 of the first dataset) after reconstruction and co-registration to their anatomical reference. The effective resolution (FWHM) of the point-spread function was estimated at (25x25x25) mm^3 with a normalized SNR of about 1.2 per mmol/L per $\text{min}^{1/2}$ of acquisition time for γ-ATP.

5.3.2 With outer volume saturation bands

Figure 5.4 shows a set of ATP and PCr images (for volunteer #1 of the second dataset) acquired with two lateral OVS bands after reconstruction and co-registration to its anatomical reference.

The effective resolution (FWHM) of the point-spread function was estimated at (25x25x25) mm^3 isotropic with a normalized SNR of about 1.2 per mmol/L per $\text{min}^{1/2}$ of acquisition time for γ-ATP.

Thanks to the OVS bands, one can notice that we do not observe anymore the hyper-signal on the lateral sides in the second dataset.

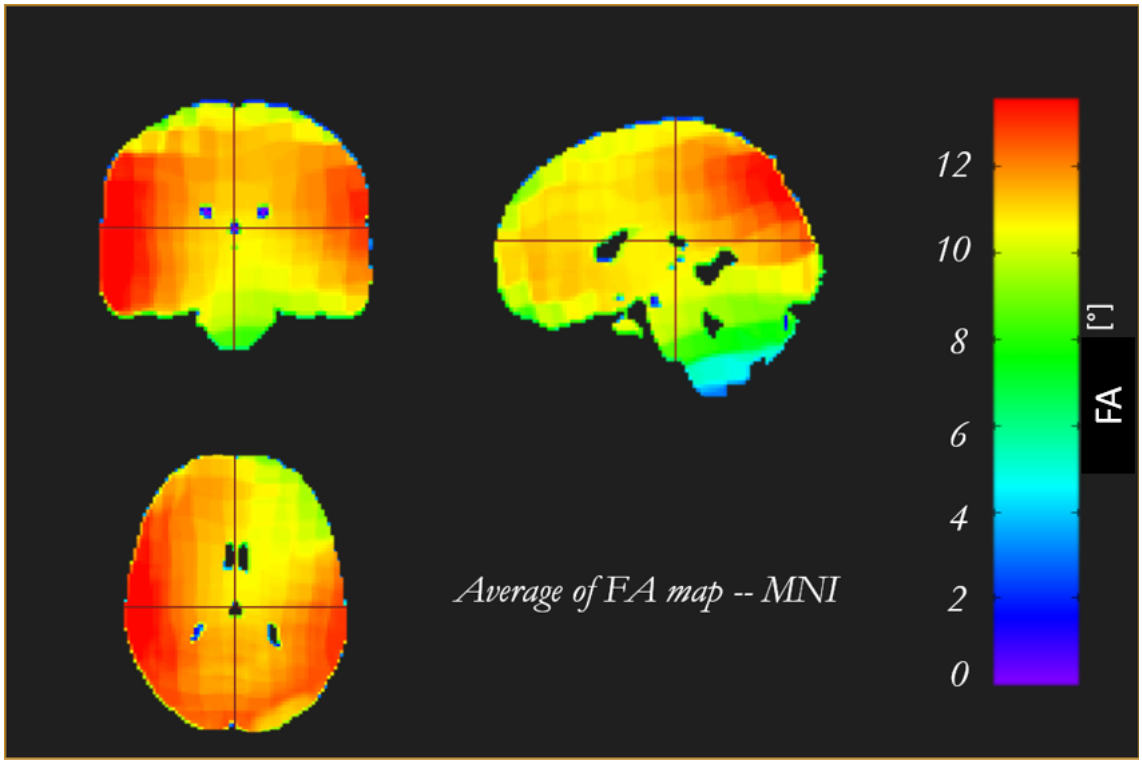

Figure 5.2 – Template FA map in MNI space averaged from six healthy volunteers. Average FA map in MNI space. The nominal excitation flip angle was 12°.

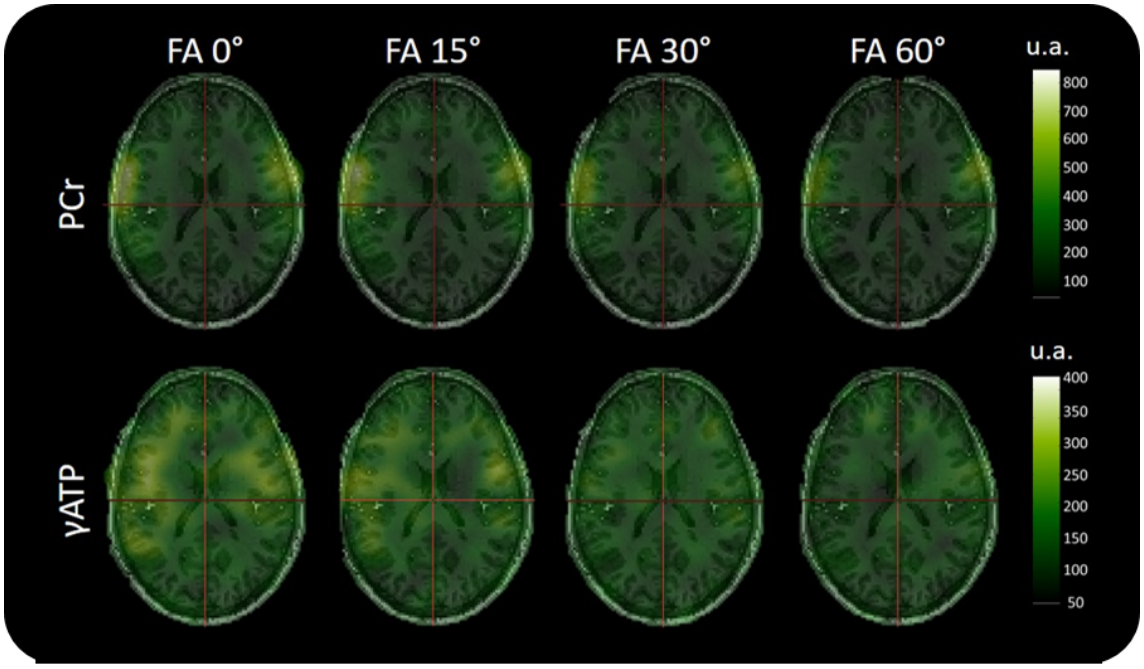

Figure 5.3 – After co-registration with their anatomical reference, a set of "raw" γ-ATP and PCr images is presented for increasing saturation pulse intensities. Coronal views for volunteer #1 (intensities in arbitrary unit). Acquisition parameters: TE/TR=5/250 ms, FA=25°, isotropic spatial resolution = 12.5 mm , TA=15 min, 3600 spokes, FA_{sat} = (0,15,30,60)°. T_1-weighted images at 2 mm isotropic resolution.

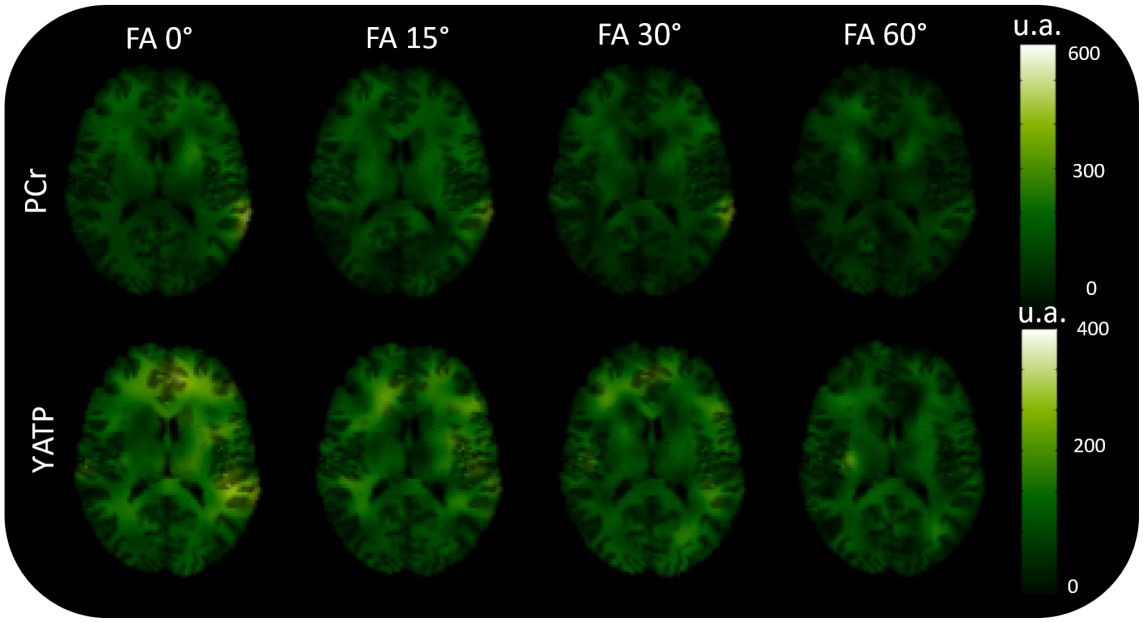

Figure 5.4 – After co-registration with their anatomical reference, one can appreciate the efficiency of the two lateral OVS bands on a set of "raw" γ-ATP and PCr images. Coronal views for volunteer #1 (intensities in arbitrary unit). Acquisition parameters: TE/TR=5/250 ms, FA=25°, spatial resolution=12.5 mm isotropic, TA=15 min, 3600 spokes, FA_{sat} = (0,15,30,60)° with two saturation bands. T_1-weighted images at 2 mm isotropic resolution.

5.4 B_1^+-corrected parametric maps

5.4.1 Without outer volume saturation bands

Cortical ATP and PCr concentrations values

Table 5.1 summarizes the results of our quantitative dynamic ^{31}P imaging protocol (mean ± standard deviation, N=3):= for [PCr], [ATP], forward CK kinetic rate k_f and corresponding V_{ck} flux rates for the five cortical ROI.

Region	[PCr] [mM]	γATP [mM]	k_f $[s^{-1}]$	V_{ck} [umol/g/min]
Frontal & Anterior cingulate Ctx	3.9 ± 0.7	2.6 ± 0.3	0.23 ± 0.02	57 ± 10
Frontal gyrus & opercular Ctx	4.8 ± 0.3	3.0 ± 0.3	0.32 ± 0.02	96 ± 12
Temporal, supramarginal & angular Ctx	5.2 ± 0.4	3.6 ± 0.5	0.33 ± 0.01	110 ± 15
Precuneus & posterior cingurate Ctx	3.8 ± 0.8	2.2 ± 0.3	0.31 ± 0.02	75 ± 10
Occipital Ctx	3.8 ± 0.5	2.5 ± 0.2	0.30 ± 0.01	71 ± 11

Table 5.1 – Concentration, kinetic constant k_f and V_{ck} values in resting human brain at 7T (N=3 subjects)

Values in the temporal ROI are superior when compared to other regions. This was the reason why we investigated the impact of extra-cranial PCr signal contamination from the maxillary muscle.

Regional k_f and V_{CK} maps

Figure 5.5 illustrates the 3D representation of those cortical V_{ck} values for our volunteers.

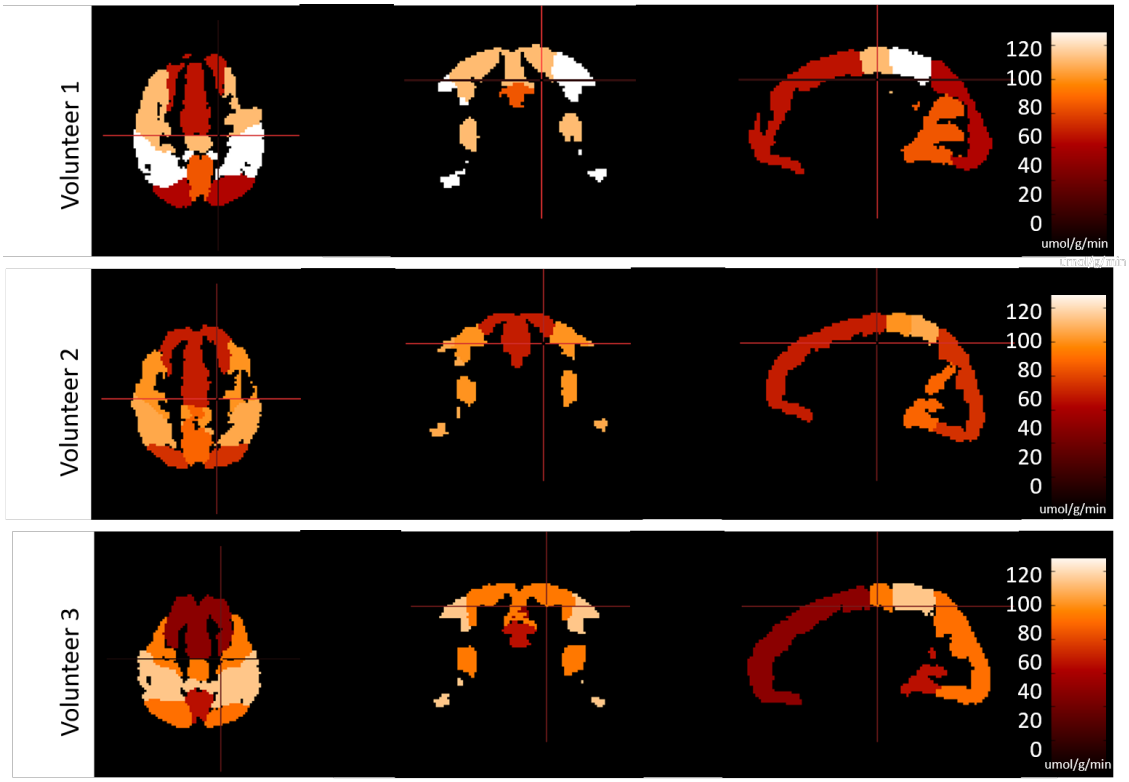

Figure 5.5 – Regional V_{ck} values for our three healthy individuals in the five considered ROI.

Coronal views of the average values of [ATP], [PCr], k_f, and V_{ck} in the five ROI we defined are shown in figure 5.6.

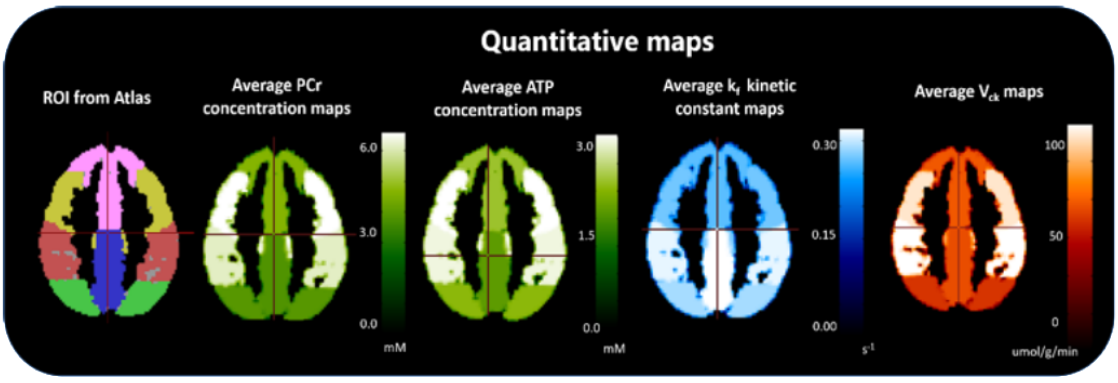

Figure 5.6 – Average B_1^+-corrected parametric maps. Our five cortical ROI (left) and average cortical for [PCr], [ATP], k_f and V_{ck} (from left to right). (pink): frontal & anterior cingulate cortices; (mustard): frontal gyrus & opercular cortices; (red): temporal, supramarginal & angular cortices ; (blue): precuneus & posterior cingulate cortex; #5 (green): occipital cortex.

5.4.2 With outer volume saturation bands

Cortical ATP and PCr concentration values

The table 5.2 summarizes the results of our quantitative dynamic ^{31}P imaging protocol (mean ± standard deviation, N=3) for [PCr], [ATP], forward CK kinetic rate k_f and corresponding V_{ck} flux rates for the five ROI.

Region	[PCr] [mM]	γATP [mM]	k_f $[s^{-1}]$	V_{ck} [umol/g/min]
Frontal & Anterior cingulate Ctx	5.8 ± 1.3	4.1 ± 0.9	0.23 ± 0.09	86 ± 10
Frontal gyrus & opercular Ctx	5.7 ± 0.08	3.3 ± 0.3	0.28 ± 0.11	100 ± 12
Temporal, supramarginal & angular Ctx	5.9 ± 0.1	3.3 ± 0.3	0.26 ± 0.01	98 ± 15
Precuneus & posterior cingurate Ctx	3.7 ± 0.5	2.4 ± 0.2	0.25 ± 0.02	61 ± 10
Occipital Ctx	3.5 ± 0.2	2.2 ± 0.2	0.30 ± 0.01	64 ± 11

Table 5.2 – Concentration, kinetic constant k_f and V_{ck} values in resting human brain at 7T (N=3 subjects)

Despite the obvious efficiency of the OVS bands to suppress extracranaial PCr signal, concentrations and fluxes values observed in the temporal cortex are not significantly different from those observed with the first version of the protocol.

Regional $k_f$and V_{CK}maps

Figure 5.7 illustrates the 3D representation of those cortical V_{ck} values for the second version of the protocol with OVS bands.

Coronal views of the average [ATP], [PCr], k_f and V_{ck} are shown in figure 5.8.

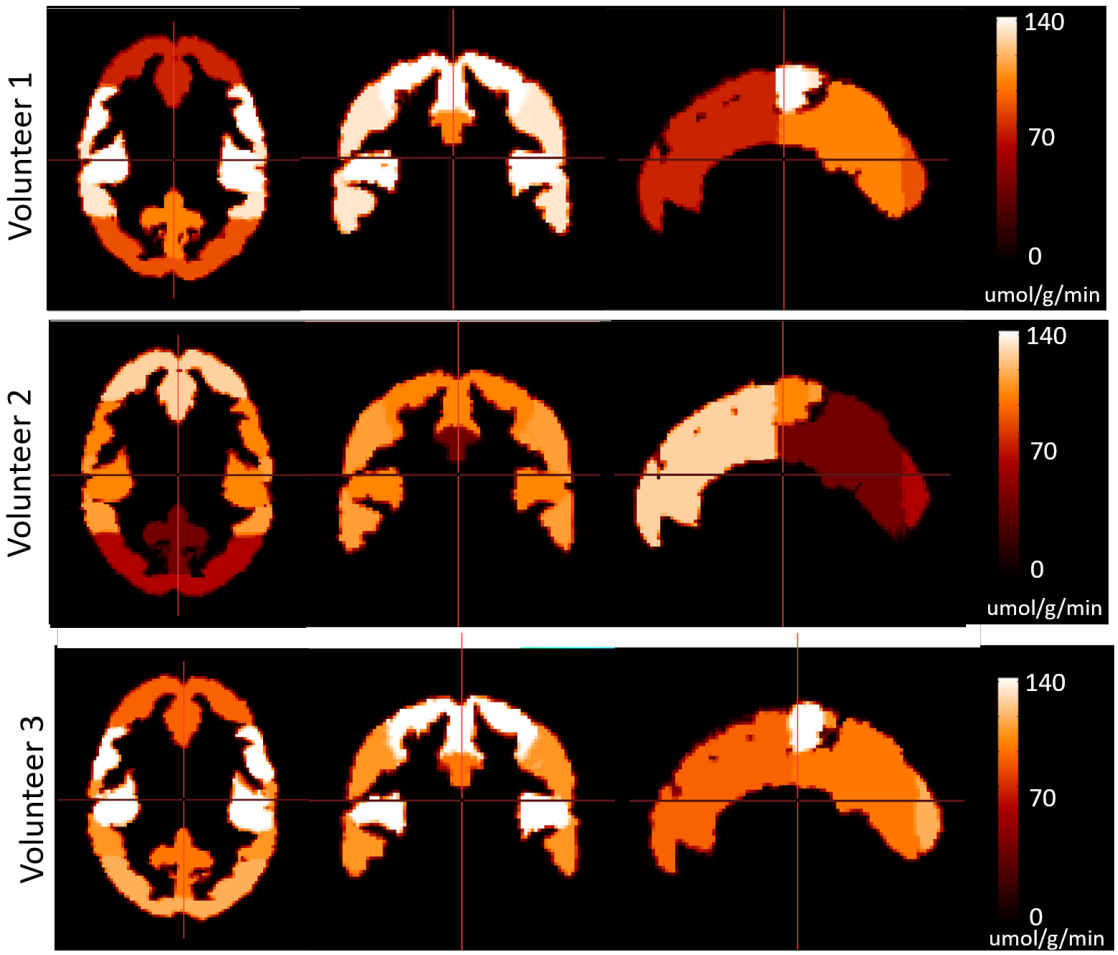

Figure 5.7 – Regional V_{ck} values for our three healthy individuals in the five considered ROI.

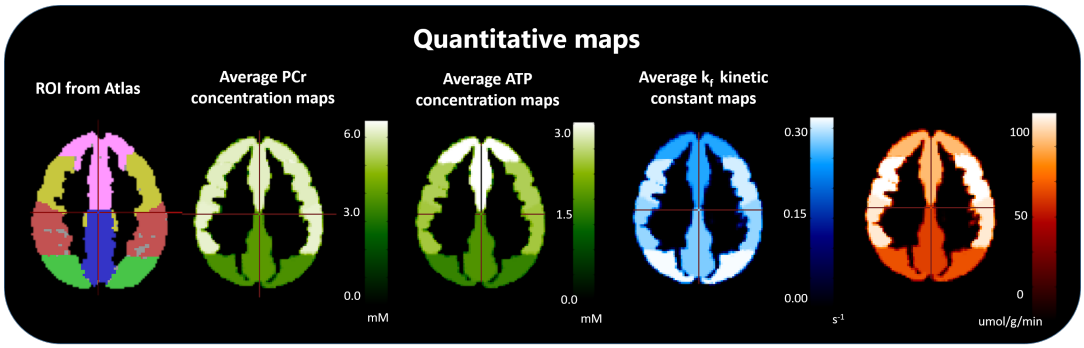

Figure 5.8 – Average B_1^+-corrected parametric maps. Our five cortical ROI (left) and average cortical for [PCr], [ATP], k_f and V_{ck} (from left to right). (pink): frontal & anterior cingulate cortices; (mustard): frontal gyrus & opercular cortices; (red): temporal, supramarginal & angular cortices ; (blue): precuneus & posterior cingulate cortex; #5 (green): occipital cortex

Chapter 6

Discussion

In this study, we set up a 3D dynamic ^{31}P imaging protocol. Specifically, we developed a sequence with multiple frequency selective excitation capabilities along with saturation/magnetization transfer and outer volume saturation modules. We developed a dedicated analysis pipeline to quantify the absolute adenosine triphosphate (ATP) and phosphocreatine (PCr) concentrations and the flux through the CK reaction in various cortical ROI. The acquisition protocol last about 1 hour which is a time frame compatible with clinical research applications (at least in research institutions such as NeuroSpin). All codes are available in a github repository.

We divided this study in three parts. In total with our three protocols, twelve volunteers participated in this study. An original variable multiple flip angle (VMFA) mapping approach was developed and validated *in vitro*, and a B_1^+ template was calculated using data from six volunteers and used to account for the effective excitation and saturation flip angles in our ROI-based analysis. We also investigated a variation of this protocol that applies two lateral outer volume saturation bands placed above the maxillary muscles.

The similarity between individual FA maps constitutes a strong argument in favor of the validity of our B_1^+ template approach. We believe a similar approach could be adopted for the ^{31}P MRS studies using surface coils. This idea is not new, the most comparable study being the one by Chmelik et al. [Chmelík 2014]. Comforted by these previous work, this approach is definitively of interest for future X-MRI studies for which individual B_1^+ maps can not be acquired. Another advantage of such B_1^+ template is that it would allow in theory the investigator to calculate the reference voltage needed to perform a targeted flip angle anywhere in the brain. Indeed voltage calibration procedures are rarely reliable in clinical and even preclinical settings for (transmitter) surface coils. This problem is bound to be more critical with the increasing number of coils (and their smaller sizes) used in X-MRI studies at UHF.

With the implementation of our OVS bands, we expected reduced PCr concentration compared to the data acquired without OVS particularly in the temporal region. Instead, we observed similar or slightly higher PCr concentrations. The OVS bands are obviously efficient in saturating the extracranial PCr signal from the maxillary muscles as it can be seen when comparing PCr images in Fig 5.4 with those shown in Fig 5.3. An explanation is

that the impact of these PCr contaminations is smaller than the inter-individual variabilities that are compounded in our acquisition protocol and quantification pipeline (FA estimation, co-registration and segmentation errors,...).

Our results are consistent without and with OVS bands, as shown by their moderate standard deviations and with the data reported in the literature. For instance, Ren et al. have reported a cerebral [PCr] of 4.4 ± 0.4 mM [Ren 2015] assuming a [ATP]=3.0 mM. For ATP, concentrations of 2.5 to 3.2 mmol/L were reported in healthy controls [Zhu 2021] in the occipital lobe, while [PCr] was estimated between 3.9 and 5.4 in the same study. Likewise, comparable k_f and V_{ck} values of 0.35 ± 0.03 s^{-1} and 94.3 ± 6.4 respectively were reported by Zhu et al. [Zhu 2021].

To obtain these values, Zhu et al. took 32 minutes to acquire spectra with and without γ-ATP resonance saturation from one region of interest. As a comparison, our study required 60 minutes (four sequences of 15 minutes) to investigate five ROIs.

This 3D dynamic ^{31}P imaging approach is also quite versatile. In particular, one could easily degrade its spatial resolution, or less intensive saturation bands could be investigated to accommodate shorter examination times while considering those same five large ROIs or others, depending on the clinical/scientific context.

We are aware that at this sample size, this study remains a proof-of-concept. Larger cohorts need to be recruited to evaluate the sensibility of this method and its ability to distinguish between for instance healthy young volunteers from aged ones, or between patients and aged-matched healthy controls, which at the end remains the goal of this technique. A reproductibility study is also an important next step for a final validation before clinical applications.

One of the main limitations of our protocol and analysis pipeline is its sensitivity to the potentially large B_0 inhomogeneities, especially at UHF. Indeed, the saturation transfer pulses were rather selective (FWHM=$68Hz$), the effective saturation flip angles values may have been slightly overestimated depending on the local γ-ATP resonance frequencies, especially in the occipital and frontal lobes for which the largest frequency offsets have been observed from the experimental B_0 maps. Also, one of our eight ^{31}P channels (placed on the frontal right side) seemed to perform sub-optimally (Figure B.0.1) probably depending on the head size. This led to the sensibly smaller k_f values and larger variabilities observed in those frontal areas.

Therefore, there is surely room for improvement regarding the design/choice of our saturation transfer or excitation pulses. In particular, optimized sinc RF pulses (asymmetric or SLR) could be considered in the near future to flatten their spectral selectivity profiles reducing their sensitivity to B_0 inhomogeneities while maintaining short effective TE and TR.

Notably, most issues that our B_1^+ template approach alleviates could be neglected if one was to use a volume coil, for instance a birdcage coil for transmission thanks to its largely homogeneous B_1^+ field. However, multiple reception-only channels would have been needed to maintain (or increase) the amount of signal we benefited from using our 8-channel phased array coil.

By relying on external references of concentrations for quantification, we assumed comparable load and reception profiles between our phantoms and volunteers. Ideally, a way to estimate correction terms for each reception channel would be needed to reach a more satisfactory quantification of our ATP or PCr concentration maps. Attempts were made in this direction by acquiring sensitivity profiles at low resolution (data not shown). However, the subsequent correction was unsatisfactory due to their low spatial resolution. Further developments could be considered in the future at even higher magnetic fields.

Chapter 7

Conclusion and perspectives

We aimed to assess the absolute concentration of γ-ATP and PCr in the brain and image the flux of creatine kinase reaction. These biomarkers are of great interest to neurologists, psychiatrists or neurobiologists because they directly assess the intensity of brain energy metabolism and the good health of its cells.

I developed a multiple frequency selective sequence from a FLASH sequence by transforming it into a UTE sequence, adding homemade saturation modules, and using a spectrally selective pulse. This sequence alternatively acquires images of PCr and γ-ATP. The corresponding signal is tagged in the raw Siemens files. I also adapted a reconstruction code in Matlab to read those tags, separate and organize them.

Due to the characteristics of the coil, a second protocol and cohort were needed to correct for B_1^+ inhomogeneities. This protocol was optimized through Monte-Carlo simulations to determine the set of FA values that were to be probed to acquire the most precise FA maps.

I developed two scripts in Python, one to co-register, quantify the concentration, model the saturation transfer via chemical exchange process, segment, and compute roi-based parametric maps. The second was to fit the data according to the SPGR signal equation, register the images into the MNI template space and compute a B_1^+ template map. I also evaluated the similarity between individual FA maps by computing their correlation matrix.

I also considered the limitations of our protocol in regards to the frequency selectivity of our pulses in the resulting parametric maps. Finally, I demonstrated the feasibility of determining [ATP], [PCr], k_f, and V_{ck} regional values in a sensitive, quantitative way and within a time compatible with clinical research (below 1h15) applications in several regions of interest at 7T simultaneously.

Some of these results were presented at the ESMRMB meeting in 2021. A full article was also submitted to NeuroImage. Unfortunately, it was rejected. The main concerns expressed by the reviewers were the small number of volunteers examined and the variability of the results obtained from the frontal areas which are possibly related to the instability or insufficient load of one of the coil element. Our team at NeuroSpin will continue this work using a new 32-channel ^{31}P coil that should solve these issues and the paper should

be resubmitted soon.

In the future, we will adopt this approach to investigate the V_{ck} and concentrations in neurodegenerative diseases. Also, we plan to adapt this protocol to investigate the PDE/PME ratio as it will be shown in the next section.

Chapter 8

^{31}P MRI: Contributions to clinical studies

Chapter Outline

8.1 Introduction

Several clinical research collaborations have been discussed during this PhD thesis. Among then, Prof. Rémy Guillevin from CHU Poitiers (figure 8.1) was especially interested in translating our sequence and the clinical protocol for studying Alzheimer's disease, glioblastoma or stroke patients.

As discussed in section 2.3, PME and PDE are metabolites linked to the regulation, synthesis and degradation of cell membrane-related phospholipids, PME are mobile membrane phospholipid precursors while PDE are related to their breakdown products. Both group of metabolites are reflecting membrane turnover. PME/PDE ratios are thus of interest to examine abnormal membrane metabolism [Daly 1987, Kemp 2000, Albers 2005]. The driving hypothesis is that changes in the PME/PDE ratio reflect either an abnormal cell proliferation (typically a decreased PDE/PME ratio is expected due to tumor growth)

or tissue necrosis or apoptosis (increased PDE/PME is expected following successful chemo/radiotherapy) [van der Kemp 2014, Sonkar 2019].

Figure 8.1 – CHU Poitiers Ultra High Magnetic Resonance Imaging Platform (from https://www.chu-poitiers.fr/specialites/irm7tesla/?lang=en)

8.2 Methods

For our sequence to be available to 7T Terra system, we transposed the sequence initially developed for VB17 to the VE12 version of Siemens MRI Scanner using IDEA Toolkit.

We executed some validation tests at NeuroSpin with the following protocol (see table 8.1). This protocol used the MFS sequence developed for ATP and PCr MRI (detailed in section 4.1.4). We chose to use the version without saturation bands since PME and PDE concentrations are not particularly prominent in muscles.

8.2.1 Data acquisition

One healthy volunteer was recruited at NeuroSpin to validate this protocol. Images were acquired on the 7T MRI Magnetom MRI scanner using the dual-resonance 8-channels ^{31}P/^{1}H phased-array coil (details in section 4.1.3). The sampling scheme was a non Cartesian TPI [Boada 1997], with p=0.3. The parameters used for this test were:

FA	Spokes	TE/TR [ms]	Res [mm^3]	F_1/F_2	TA
10 °	1500	4.5/250	20x20x20	860/320	6 min 15 s
20 °	1500	4.5/250	20x20x20	860/320	6 min 15 s
30 °	1500	4.5/250	20x20x20	860/320	6 min 15 s

Table 8.1 – Parameters of our validation protocol for the estimation of PDE/PME ratio in one first healthy volunteer

We chose to acquire images at three different FA, improving the robustness of the derived M_0 and T_1 maps compared to a minimalist estimation based on only two points.

8.2.2 Data processing

As done previously, tagged raw k-space data were separated and reorganized into PDE and PME specific k-space signals. Both images were reconstructed offline using a homemade Matlab script (The MathWorks Inc., Natick, Massachusetts) using a non-uniform fast fourier transform (FFT) regridding algorithm consisting of a Kaiser-Bessel one can find kernel interpolation density compensation and Hamming filtering steps as detailed in section4.2.1.

Since the aim is to derive PDE/PME ratio maps, corrections for B_1^+ heterogeneities are less relevant as they cancel out in the division. This makes this problem easier than the V_{ck} estimation presented in this thesis. Thus fewer parameters are be to estimated. Also the target resolution was lowered to get a suitable SNR. We took advantage of reducing the number of hypotheses fixed. Contrary to the previous work, T_1 can be estimated instead of considering values from the literature, which could be an advantage for clinical research studies.

To do so, we implemented a faster algorithm called NOn-linear VarIable Flip Angle data baSed T1 estimator (NOVIFAST) [Ramos-Llorden 2018]. Here is a short description of this approach: 1) VFA T_1 mapping is formulated as a non-linear least squares optimization problem that can be iteratively solved as a two-by-two linear system, constituting a fixed-point algorithm (NOVIFAST). Due to its formulation, NOVIFAST turns out to be very easy to implement and computationally highly efficient; 2) it also gives the precise solution for noiseless data.

This NOVIFAST permits the estimation of T_1 and K [Ramos-Llorden 2018] simultaneously. It is based on the equation:

$$\boldsymbol{A}(\boldsymbol{c}^k)\boldsymbol{c}^{k+1} = \boldsymbol{v}(\boldsymbol{c}^k). \tag{29}$$

with solution:

$$c_1^{k+1} = \frac{\begin{vmatrix} \langle \boldsymbol{z}, \boldsymbol{b} \rangle & \langle \boldsymbol{b}, \boldsymbol{a} \rangle \\ \langle \boldsymbol{z}, \tilde{\boldsymbol{a}} \rangle & \langle \boldsymbol{a}, \tilde{\boldsymbol{a}} \rangle \end{vmatrix}}{\begin{vmatrix} \langle \boldsymbol{b}, \boldsymbol{b} \rangle & \langle \boldsymbol{b}, \boldsymbol{a} \rangle \\ \langle \boldsymbol{b}, \tilde{\boldsymbol{a}} \rangle & \langle \boldsymbol{a}, \tilde{\boldsymbol{a}} \rangle \end{vmatrix}}, \quad c_2^{k+1} = \frac{\begin{vmatrix} \langle \boldsymbol{b}, \boldsymbol{b} \rangle & \langle \boldsymbol{z}, \boldsymbol{b} \rangle \\ \langle \boldsymbol{b}, \tilde{\boldsymbol{a}} \rangle & \langle \boldsymbol{z}, \tilde{\boldsymbol{a}} \rangle \end{vmatrix}}{\begin{vmatrix} \langle \boldsymbol{b}, \boldsymbol{b} \rangle & \langle \boldsymbol{b}, \boldsymbol{a} \rangle \\ \langle \boldsymbol{b}, \tilde{\boldsymbol{a}} \rangle & \langle \boldsymbol{a}, \tilde{\boldsymbol{a}} \rangle \end{vmatrix}}, \tag{30}$$

The algorithm can be implemented as in the algorithm 2.

After computing M_0 and T_1, images were masked using k-means algorithm with k=2 using M_0 as based image.

Algorithm 2 Pseudo-code of NOVIFAST

Given parameters: TR and flip angle $(\alpha_n)_{n=1}^N$
Initial values: K_{ini} and T_{ini}
$c_0^1 \leftarrow K_{ini}(1 - \exp(-TR/T_{ini})$
$c_0^2 \leftarrow \exp(-TR/T_{ini})$
$k \leftarrow 0$
$c^k \leftarrow (c_k^1, c_k^2)$
while convergence criterion is not met **do**
  Solve Eq. 29
  $k \leftarrow k + 1$
end while
return $\hat{K} = c_1^k/(1 - c_2^k)$ and $\hat{T}_1 = -TR/\log c_2^k$

I implemented this algorithm in Python3 and validated the results for noiseless data and MC simulations with increasing noises levels to match the cited paper [Ramos-Llorden 2018]. Code is available at https://github.com/rpbaptista/PMEPDE_ratio.

8.3 Results

8.3.1 Raw images

The reconstructed images for each excitation flip angles (10°/20°/30°) can be seen in fig8.2. Target spatial resolution was 20x20x20 mm^3 (8 mL).

We can see, as expected a stronger signal from PDE than PME, which is expected in the brain.

8.3.2 Quantitative maps

In figure 8.3, the T_1 maps for the two metabolites are shown for a central slice. The outside of the brain was masked. The T_1 for PME was found 6.5 ± 1.5. For PDE, T_1 was 6.8 ± 1.2.

The figure 8.4 shows the central slice of the PME/PDE ratio map. Spatial resolution was still 20x20x20 mm^3. The outside of the brain was masked.

The ratio for PME/PDE was found 0.68 ± 0.28.

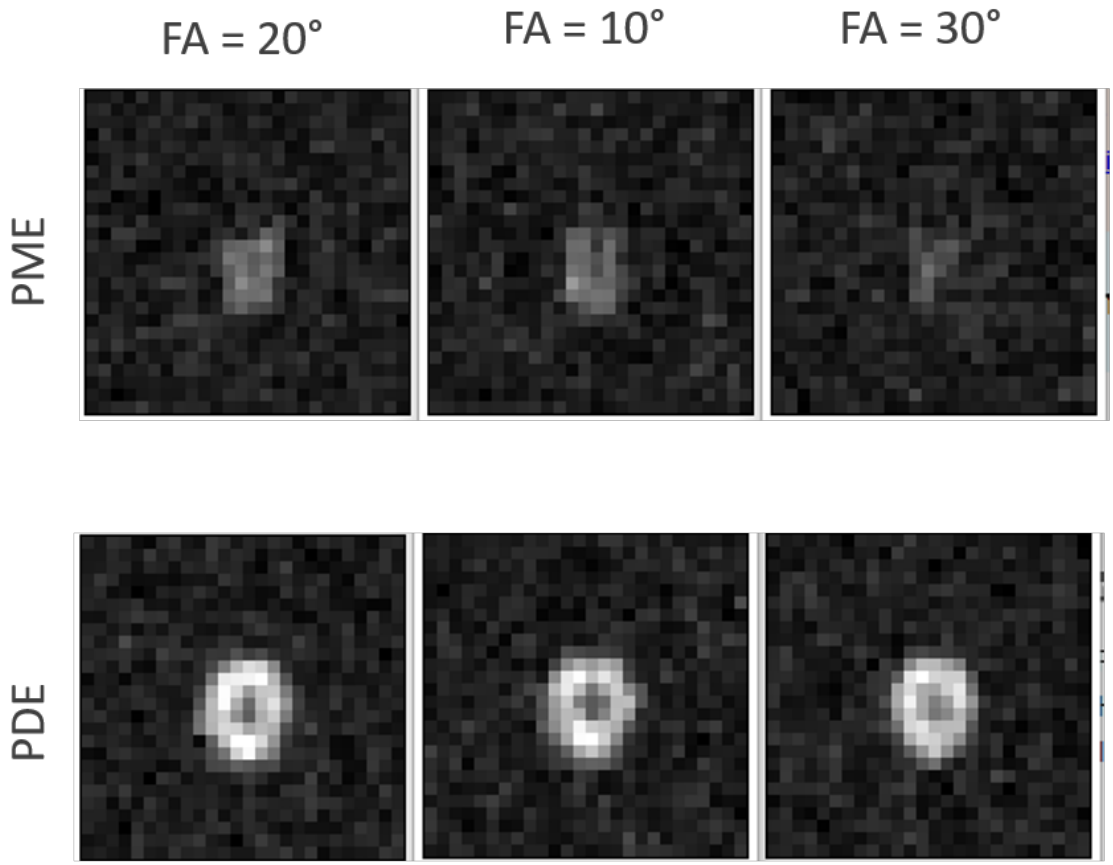

Figure 8.2 – A typical set of "raw" PDE and PME images, no co-registration with their anatomical reference was made for lack of acquisition.

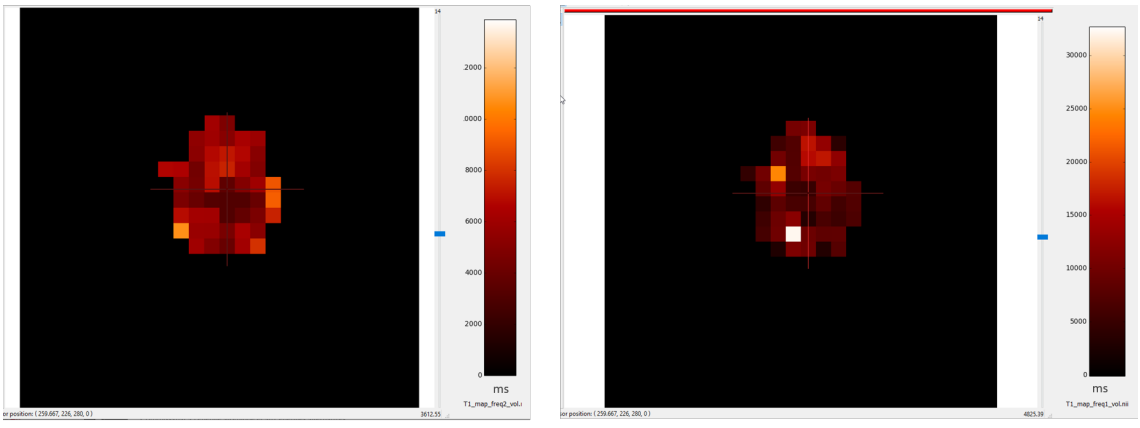

Figure 8.3 – Central slice of our T_1 maps for PDE and PME. Spatial resolution of 20x20x20 mm^3. The scale is given in milliseconds.

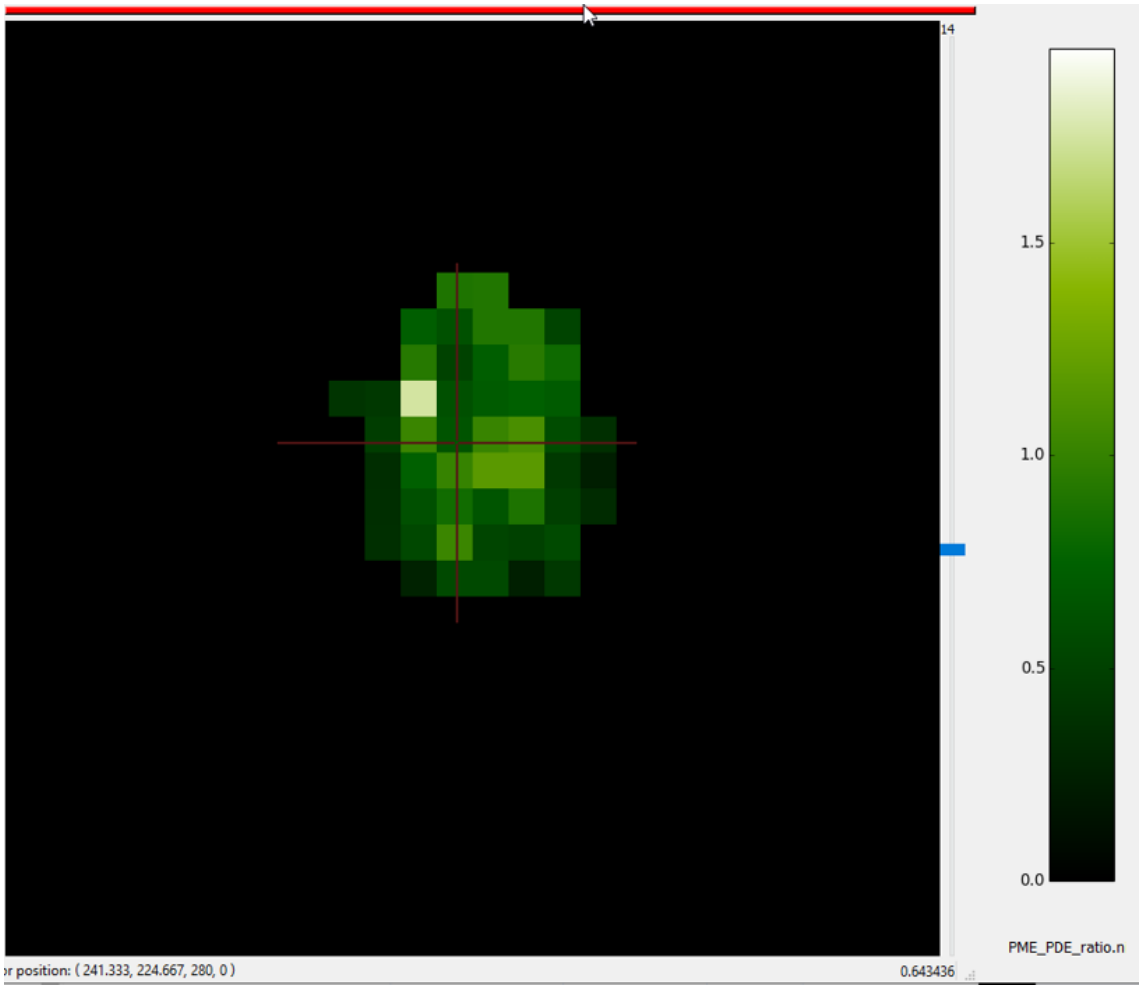

Figure 8.4 – Central slice of ratio PDE/PME map in a healthy volunteer. Spatial resolution of 20x20x20 mm^3.

8.4 Discussion

We managed to apply a simplified version of our pipeline to image PME/PDE in the brain at 7T. The values for the PME/DME ratio and T_1 are coherent with the literature. For instance, Shi et al. found PME/PDE to be 0.628±0.104 when evaluating 23 healthy volunteers and [Shi 2015]. For the T_1: PME = PE + PC, theirs respective T_1 are: 6.33 ± 1.10 and 4.31 ± 1.04. For PDE: GPE + GPC theirs respective T_1 are: 6.79 ± 0.95 and 5.82 ± 0.88. The concentration of PE is around eight folds PC in the brain [Ren 2015] and GPC is greater around 50% in concentration. This mean

This application is less disturbed by the three main limits of our technique. First, as we estimate a ratio, B_1^+ (nor B_1^-) inhomogeneities do not need to be corrected. Second, contamination due to partial volume effects is less of a problem because there are not higher concentrations of PDE or PME in the muscles compared to the brain. However, this approach remains sensible to B_0 inhomogeneites due to possible impact of Pi peak.

8.5 Conclusion and perspectives

The protocol is ready to be applied in a clinical study to a cohort of Alzheimer's Disease, glioblastoma or stroke patients versus age-matched controls. The next step we foresee is to validate this approach at the CHU of Poitiers, considering that the coil is not the same, which can lead to different levels of SNR. Consequently, a possible adjustment on the resolution is possible.

Also, the algorithm chosen is fast enough to allow online reconstruction and it can be easily implemented on ICE (Siemens reconstruction) or Gadgetron using the code available at the GitHub repository.

* * *
* *
*

Part III

Evaluation of 3D SPARKLING for undersampled ^{23}Na MRI at ultra-high magnetic fields

Chapter 9

Introduction

The SPARKLING algorithm has been developed in NeuroSpin for the parsimonious acquisition of high spatial resolution images. In this part of my Ph.D. thesis, I evaluate the application of SPARKLING to accelerate ^{23}Na imaging.

I presented a preliminary version of our study at an international conference as:

R. Porciuncula Baptista, A. Vignaud, Chaithya G R, G. Daval-Frérot, F. Mauconduit, M. Naudin, M. Lapert, R. Guillevan, P. Ciuciu, C. Lerman-Rabrait and F. Boumezbeur. *Evaluation of 3D SPARKLING for undersampled Sodium UTE MRI at ultra-high magnetic field.* In Proceedings of the 30th International Society of Magnetic Resonance in Medicine, 2022.

Cerebral sodium (^{23}Na) magnetic resonance imaging (MRI) provides unique information about brain tissue viability *in vivo*. Indeed, neurons rely on the energy-hungry sodium-potassium pump (Na^+K^+-ATPase) to regulate their transmembrane Na^+ and K^+ concentration gradients, which in turn determinate their resting membrane potential. In pathological conditions where the cell membranes are damaged or their energy synthesis capabilities are compromised, an increase in Intracellular Sodium Concentration is bound to occur, while Extracellular sodium concentration stays constant. This leads to an increase in tissue sodium concentration (TSC), neuronal dysfunction, and ultimately cell death [Mccarthy 2015].

Therefore changes in TSC are considered potential early biomarkers for many neurodegenerative diseases. Several studies confirmed the relevance of assessing tissue sodium concentration (TSC) in neurological disorders such as Alzheimer's [Haeger 2021], Multiple Sclerosis [Zaaraoui 2012, Eisele 2019], Huntington's, [Reetz 2012] and others [Zaric 2021b].

However, ^{23}Na-MRI faces several technical challenges, limiting its clinical use. This is mainly due to the moderate sodium concentration in the human brain (about 40 mM in the white matter (WM) and 140 mM in the cerebrospinal fluid (CSF)) and its low intrinsic nuclear magnetic resonance (NMR) sensitivity compared to proton MRI. In the healthy brain white matter, those differences can lead to up 5500 fold less signal-to-noise ratio

(SNR) [Ladd 2018]. Consequently, ^{23}Na images are acquired at lower spatial resolutions and require longer acquisition time (TA).

Another difficulty is the fast transverse relaxation time (T_2/T_2^*) of ^{23}Na NMR signal, which is typically less than 5 msec [Ridley 2018]. Consequently, ultra-short echo time (UTE) sequences combined with deterministic non-Cartesian k-space trajectories have been preferred [Konstandin 2014] by the ^{23}Na MRI community. Among the most commonly used non-Cartesian k-space sampling schemes, we can cite radial, density-adapted three-dimensional radial projection reconstruction pulse sequence (DA-3DPR) [Nagel 2009], Twisted Projection Imaging (TPI) [Boada 1997] or Fermat-looped orthogonally-encoded trajectories (FLORET) [Robison 2017].

These standard non-Cartesian readouts are flexible, as they are analytically and geometrically constrained, and, when combined with density-compensated reconstruction, they can provide good image quality. However, they can be sub-optimal in sampling the k-space, especially for higher $\mathbf{k}$ values which can lead to fast degrading spatial resolutions when the k-space is undersampled (as demonstrated by the computed point spread function (PSF) [Konstandin 2014]). In the recent years, to accelerate image acquisition while preserving spatial resolution, compressed sensing (CS) approaches have been proposed for proton MRI [Dale 2004, Mir 2004, Kumar Anand 2008, Vasanawala 2010].

In the past, proton MRI CS approaches were those which took advantage (i) of the sparse characteristic of MRI signals, (ii) incoherent sampling schemes, and (iii) nonlinear reconstruction with a sparsity promoting prior. Currently, the concept of an incoherence sampling scheme is considered sub-optimal, [Adcock 2017] and new CS techniques focus on (i) globally variable density sampling non-uniform between high and low frequencies but (ii) locally uniform coverage of k-space [Donoho 2006].

Recently, Chen et al. reviewed CS attempts in ^{23}Na MRI [Chen 2021]. Some of those articles also evaluate the impact of acceleration on TSC, as TSC is one of the main goals of ^{23}Na MRI. Twelve out of seventeen studies use radial or DA-3DPR as a sampling scheme, and only one used a version of TPI, even though it has a slightly better SNR [Nagel 2009].

All cited studies did not explore optimized sampling schemes. Their CS definition is based on the incoherence criteria. This criterion states that the measurement basis and the sparse representation basis must be uncorrelated so that the k-space undersampling artifacts add incoherently to the sparse signal coefficients. They assume the incoherence of density-adapted three-dimensional radial projection reconstruction pulse sequence (DA-3DPR) or TPI. No more specific CS trajectories have been studied. Several attempts have been made in proton MRI to improve the sampling scheme by using a series of second-order cone optimization sub-problems, ideas from the missile guidance field, or others [Kumar Anand 2008, Mir 2004, Dale 2004].

Here, we apply SPARKLING [Lazarus 2019] to ^{23}Na MRI. SPARKLING is inspired by CS approaches with a (i) global variable density sampling but (ii) locally uniform coverage of k-space. Compared to more classical approaches, this approach is an excellent candidate for shortening the TA while improving image quality in ^{23}Na MRI.

The application of CS techniques to sodium imaging presents its specific challenges

because the ability of CS to accelerate depends on the image size and available SNR: for both, the bigger it is, the better. Unfortunately for ^{23}Na MRI, both are limitings factors compared to ^{1}H MRI.

In this study, for the first time, we aimed at demonstrating that we can accelerate *in vivo* ^{23}Na acquisitions at 7T and perform valid TSC quantification using 3D SPARKLING. We compare to current state-of-the-art (TPI) with the same T_{obs}, bandwidth (BW), flip angle, and repetition time (TR). Our study design was divided in three parts (i) simulations to find the scenarios of SNR, spatial resolution, and density sampling parameters for which SPARKLING outperforms TPI (ii) *in vitro* measurements to assess the impact of the different AF on TSC quantification, (iii) *in vivo* experiments to analyze the resulting TSC maps quality in the healthy human brain.

Chapter 10

Methods

Chapter Outline

10.1 Determination of scenarios of interest using simulations

As stated before, the determination of scenarios of interest for CS ^{23}Na MRI is a non-trivial task due to its relatively low SNR and spatial resolution compared to ^{1}H MRI. To solve this problem, rather than relying on a fastidious experimental work on phantoms or healthy volunteers, we opted to develop a tool for synthesizing sodium images so as to investigate in a more systematic manner the impact of these factors and determine sets of acquisition parameters for which 3D SPARKLING may outperform TPI.

Please keep in mind that the generation of SPARKLING trajectories is time-consuming and an exhaustive simulation study of all possible acquisition parameters and corresponding SPARKLING trajectories was not possible.

The first step for retrospective studies is to have a database representing the reality of the target data. In proton MRI, several online databases are available as OpenNeuro (https://openneuro.org/) and FastMRI [Zbontar 2018]. For sodium MRI, it is less common. For that reason, we simulated synthetic images for retrospective studies taking into account a four-compartment method that will be detailed below, using MP2RAGE images we had acquired previously.

10.1.1 Creation of synthetic images

As proposed by Gilles et al. [Gilles 2017], the total ^{23}Na signal S in this model corresponds to the sum of the ^{23}Na signals from three tissue compartments (Fig. 10.1) with different sets of concentrations C_j, volume fractions α_j, and weighting factors λ_j (with j=1,2 and 3). The fourth compartment (solid) contribution to the signal is negligible.

For the creation of synthetic images, we used the following bi-exponential model with four compartments:

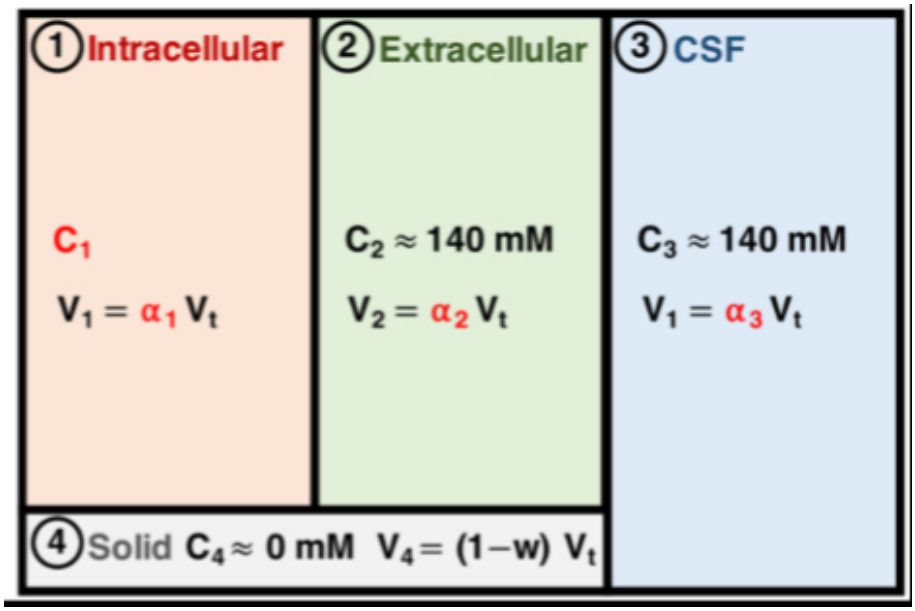

Figure 10.1 – Four-compartment model for brain tissue. ^{23}Na ions are present in the intracellular (1), extracellular (2), and CSF (3) compartments of the human brain. Sodium signal from the solid compartment (4) is negligible. Notations are, for j = 1 to 4: C_j = sodium concentrations, V_j = volumes, α_j = volume fractions, w = water fraction. Assumptions for this brain model: w = $\alpha_1 + \alpha_2 + \alpha_3$, with w = 0.8, total volume $V_t = V_1 + V_2 + V_3 + V_4$, and $C_2 = C_3 = 140$ mM. Unknown values of interest are in red: C_1, α_1, α_2, and α_3. From [Gilles 2017].

The volume fractions of each compartment are taken from [Fleysher 2009]. We used MP2RAGE at 0.75 mm isotropic as reference images. Images were segmented into CSF, WM, and GM using SPM12 [Penny 2011]. Once the masks were available, each compartment was multiplied by its corresponding weight.

For each compartment, the signal is computed as:

$$S_i = f * \exp\left(-\frac{TE}{T_{2i,s}}\right) + (1-f) * \exp\left(-\frac{TE}{T_{2i,l}}\right) \tag{10.1}$$

where f is the fraction corresponding to short $T_{2i,s}$.

The T_1 and T_2 values used in this model are from [Fleysher 2009].

	T_1 [ms]	T_{2s} [ms]	T_{2l} [ms]
Intracellular compartiment	24	2	12
Extracellular compartiment	46	3·5	30
CSF compartiment	64	56	56

Table 10.1 – Relaxation times on human brain sodium. From [Gilles 2017].

Then, signals maps were down-sampled to the target resolution. Based on the state-of-the-art of ^{23}Na MRI, we opted for the investigation of three targets resolutions: 2, 4 and 8 mm isotropic resolution. In the end, we obtained synthetic sodium images similar to those shown in figure 10.2.

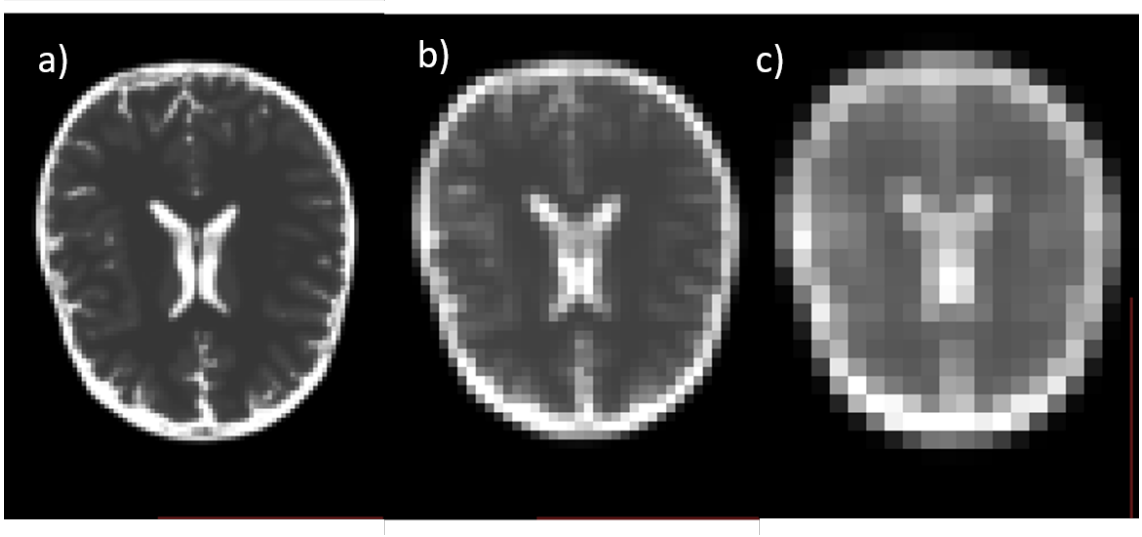

Figure 10.2 – Examples of synthetic ^{23}Na images: axial central slice for (a) spatial resolution 2 mm isotropic (b) spatial resolution 4 mm isotropic and (c) spatial resolution 8 mm isotropic using our fourcompartment model.

In figure10.2, we see images that are proportional to the signal MRI created with the model described above.

I coded the scripts to generate synthetic data in Python3. I developed a class for each compartment, and the user can choose the number of compartments and whether they are mono-exponential or bi-exponential. They are available in a public repository (https://github.com/rpbaptista/Quantification/).

I later added Gaussian noise in the **k**-space to match the input SNR of real acquisitions.

Input SNR was defined as the ratio of the maximum intensity of **k**-space for a given spoke divided by the standard deviation of a spoke where FA=0°. To do so, we needed

extra acquisition in order to model the noise. We did so for the higher acceleration factor we studied.

10.1.2 Creation of trajectories

TPI

Twisted projection trajectories (TPI) were introduced in 1997 by F. Boada et al. [Boada 1997]; at that time, the state-of-the-art sampling scheme acquisitions were radial. The premise behind TPI is that improvements in the sampling efficiency of three-dimensional projection imaging can be attained by removing the non-uniform sample density that results from uniform sampling in time along radial lines in **k**-space.

In three dimensions, the improvement in efficiency is made through a twist in the trajectories that preserves the sample density. In a thin spherical shell, the number of trajectories will be constant if the number of samples inside a thin spherical shell is proportional to the volume of the shell. This can be described through the equations [Boada 1997]:

$$\dot{k} = \frac{\alpha}{k^2} \tag{10.2}$$

and

$$\dot{k} + k^2(\dot{\theta} + \sin^2\theta\dot{\varphi}^2) = \gamma^2 G^2 \tag{10.3}$$

The solutions of those equations give the k-space trajectory. For more details, the reader may refer to the seminal article [Boada 1997]. The resulting trajectories can be seen in the figure10.3.

I implemented the algorithm for generating TPI trajectories in MATLAB and another sampling scheme (radial and density adaptive radial). The code gives an output of a .bin file containing the gradient values to be passed to the machine. This integrates with our sequence (one may refer to the chapter 4.1.4), giving flexibility to the experiments. If the user wants it, he can also retrieve the **k**-space vector to use in their sequence. This program is available in a public GitHub repository (https://github.com/rpbaptista/Trajectories/).

SPARKLING

The SPARKLING algorithm [Lazarus 2019] generates optimized k-space sampling patterns $\mathbf{K}[i] = (k_{x,i}, k_{y,i}, k_{z,i})$, where i represents a sample which comply to a target acquisition density. At the same time, SPARKLING respects MR hardware limitations such as maximum gradient amplitudes and slew rates. SPARKLING focuses on radially symmetric densities, which present the advantage of yielding results invariant to translation and rotation of the sample to the image. This target density is defined by two parameters: cutoff (C) and decay (D) (figure 10.4). They are defined as follows:

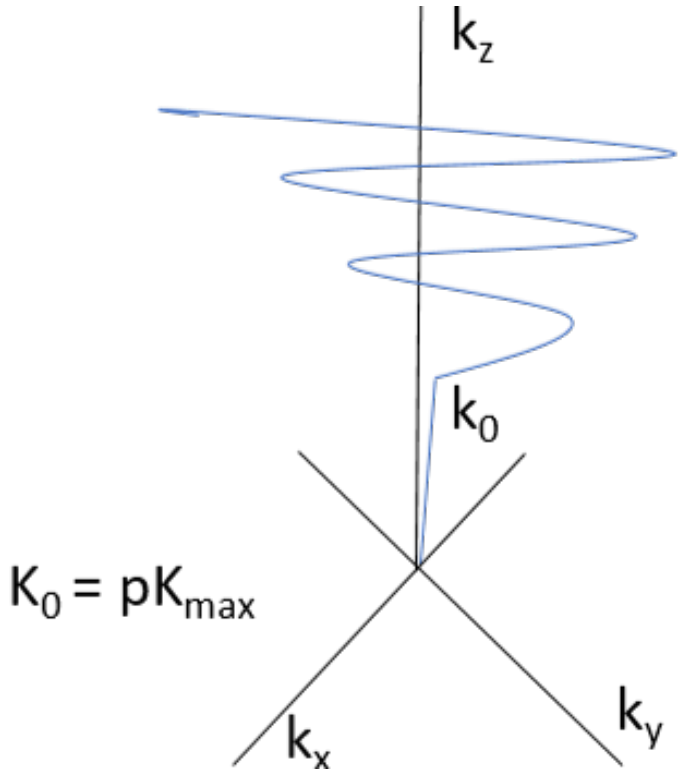

Figure 10.3 – Example of TPI "spoke": p represents the radial fraction.

$$\pi_{C,D}(x) = \begin{cases} K & |x| < C \\ K\left(\frac{C}{|x|}\right)^D & |x| > C \end{cases} \tag{10.4}$$

Where K is a constant obtained through normalization:

$$K = \frac{1-D}{2C(C^{D-1}-D)}$$

This algorithm has been extended to 3D and is described in detail elsewhere [Chaithya 2022]. 3D SPARKLING has a locally uniform coverage of k-space, differently from TPI or radial strategies. The trajectory $\hat{\mathbf{K}}$ is optimized as:

$$\hat{\mathbf{K}} = \arg\min_{\mathbf{K}} F_p(\mathbf{K}) = F_p^a(\mathbf{K}) - F_p^r(\mathbf{K}) \tag{10.5}$$

where $F_p^a(\mathbf{K})$ is the attraction term enforcing the sampling pattern $\mathbf{K}$ and $F_p^r(\mathbf{K})$ is the repulsion term which guarantees a good filling of the k-space. The repulsion term $F_p^r(\mathbf{K})$ and $F_p^a(\mathbf{K})$ are defined as:

$$F_p^r(\mathbf{K}) = \frac{1}{2p^2}\sum ||\mathbf{K}[i] - \mathbf{K}[j]||_2 \tag{10.6a}$$

$$F_p^a(\mathbf{K}) = \frac{1}{p}\sum \int_\omega ||(x - \mathbf{K}[i])||_2 \rho(x) dx \tag{10.6b}$$

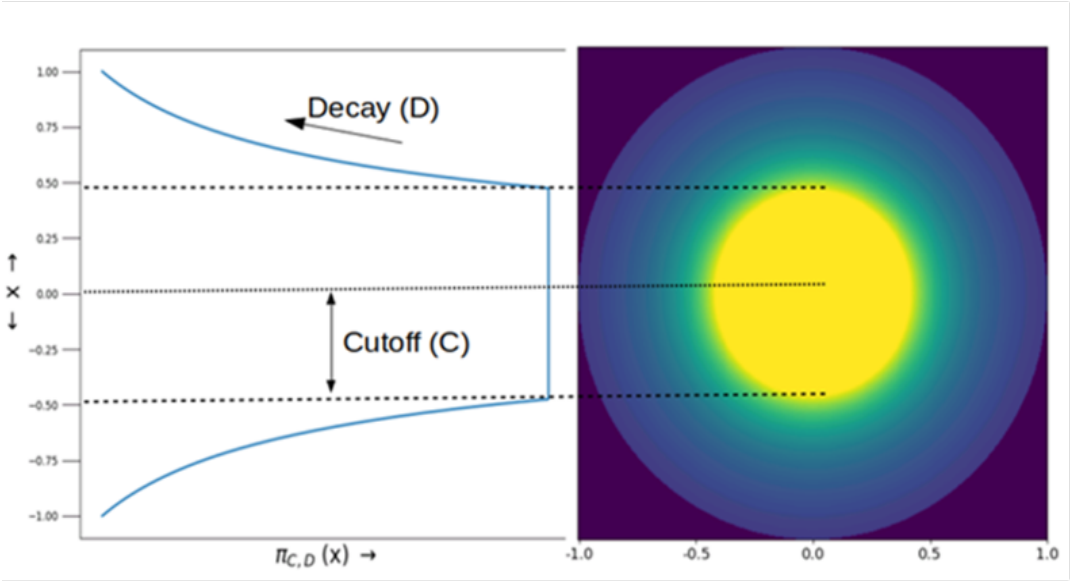

For an e

Figure 10.4 – Example of SPARKLING trajectory, parameters refer to the density function, cutt-off (C), and decay (D).

Here, we adopted a variation of SPARKLING, called MORE SPARKLING, [Chaithya G R 2022] to define sets of center-out spokes for ^{23}Na imaging. In this variation, the F_p^r factor incorporates a temporal weighting to enforce that the next point of the trajectory in the same spoke is further away from the center and is defined as:

$$F_p^r(\mathbf{K}) = \frac{1}{2p^2} \sum \exp^{|t_i - t_j|} ||\mathbf{K}[i] - \mathbf{K}[j]||_2 \tag{10.7a}$$

where t_i and t_j correspond to the times when the samples $\mathbf{K}[i]$ and $\mathbf{K}[j]$ are acquired.

This is important to reduce off-resonance artifacts and avoid signal loss due to averaging points in different observation times, which is especially important for the fast relaxing sodium nuclei.

The calculation of F_p^r and F_p^a is made through a gradient descent algorithm. All code has been optimized for GPU computing, [Chaithya 2022] and it is available on a python package called SPARKLING. Interested researchers are requested to contact the authors to obtain access to this package.

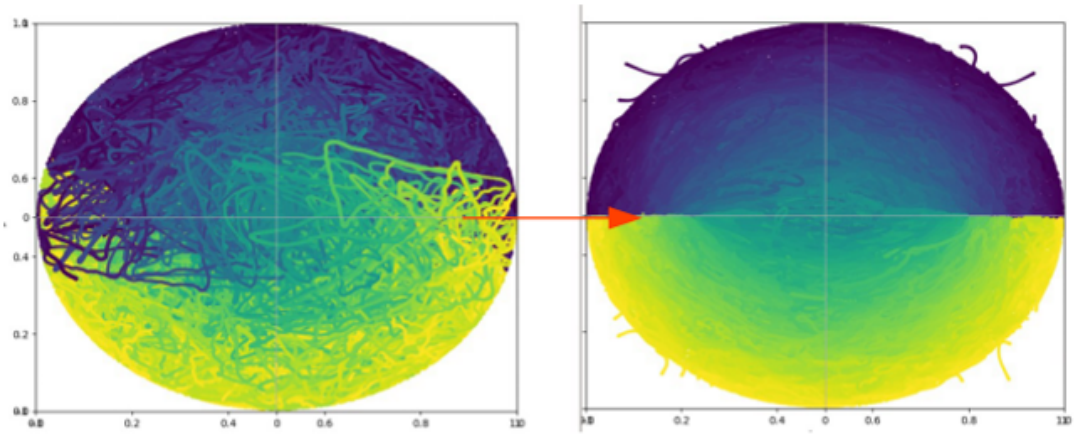

Figure 10.5 – SPARKLING and MORE-SPARKLING sampling schemes: In left, SPARKLING illustration trajectory. In the right, MORE-SPARKLING center-out trajectory. The color blue represents the beginning of the trajectory, and the color yellow is the end. From [Chaithya G R 2022].

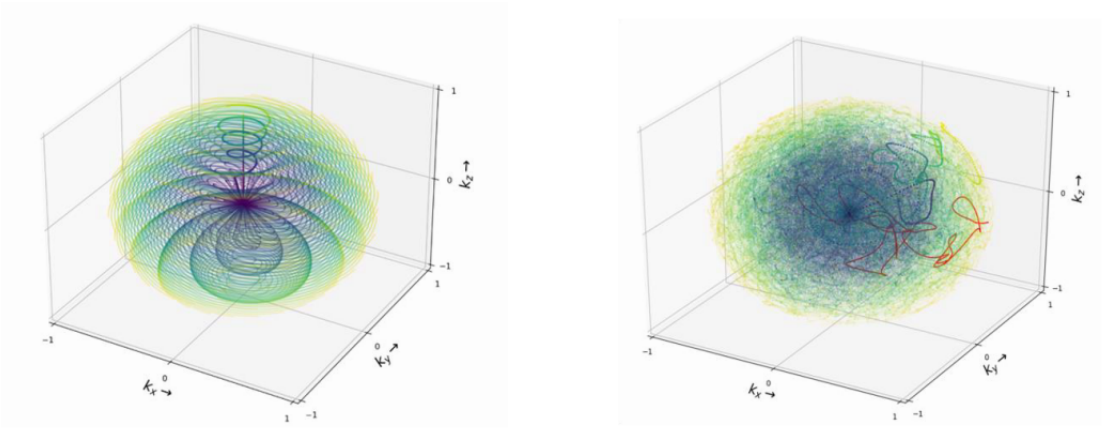

Figure 10.6 – TPI and SPARKLING sampling schemes: In left, TPI illustration trajectory. In the right, SPARKLING center out trajectory. The color blue represents the beginning of the trajectory and the color yellow the end. Each spoke on TPI and SPARKLING were acquired over the same $T_{obs} = 12.48$ ms.

10.1.3 Comparison between scenarios

Once I generated the trajectories and synthetic images, I examined which SNR level is needed for SPARKLING to outperforms TPI.

From the synthetic data in the image space, we transformed the data into **k**-space datasets by performing an IFFT. In this preliminary study, I resampled the data using density compensation [Pipe 2011] and NUFFT to avoid misleading the gain from the different trajectories with the reconstructions gain.

Once in the **k**-space, I re-sampled the data according to each trajectory. Due to time limitations, I set up our range of parameters in Table 10.3:

I added the noise directly in **k**-space to match the target SNR. The special case of infinity

AF	(2,8,32,64,128)
SNR	(2,5,10,15,20,50,∞)

Table 10.2 – Parameters studied for our scenario evaluation

SNR is where I applied no extra noise, and the SNR was the one from the MP2RAGE image. The SNR in MP2RAGE was at least 100. A NUFFT was applied to the new data set to retrieve the reconstructed image.

This procedure was done with the python package PySap-mri.

Finally, SSIM was calculated between the reference (initial) image and the reconstructed image for both scenarios (TPI vs SPARKLING).

10.2 Tuning of the trajectories parameters

10.2.1 TPI parameters

The TPI parameter p was set to $p = 0.3$ because it was already optimized in the literature [Romanzetti 2014].

10.2.2 SPARKLING parameters

The creation of trajectories can be time-consuming, even in GPU computing. For instance, computing a trajectory respecting the Nyquist criteria for a spatial resolution of 4 mm can take about 24 hours. For this reason, we had to limit the grid of trajectories evaluated in this study.

The cutoff values C were chosen around 30% because this parameter is related to the p value of the TPI trajectory that has been set at $p = 0.3$ [Romanzetti 2014]. For the spatial resolution, the target values were chosen to encompass the range of literature values. On one hand of the spectrum, in a recent study by Wilferth et al., a theoretical resolution of 2.5 mm isotropic was achieved using a 32 channel coil at 7T [Wilferth 2022]. On the other hand, multi-parametric sodium MRI has been implemented in our team using QUICS at a much lower resolution of 6 mm isotropic [Leroi 2018]. The resulting set of parameters grid-searched are summarized in Table 10.3.

Decay	(2,3)
Cutoff	(10,20,30,40,50)

Table 10.3 – Parameters studied for our evaluation of SPARKLING trajectories

The metric chosen to select the best set of parameters for cutoff and decay was the FWMH of the point spread function (PSF) of each trajectory: the lower being better. We chose this metric from the literature [Chaithya G R 2022]. We also avoided evaluating PSF after reconstruction because PSF in ^{23}Na data is known to be harder to estimate due to low SNR [Polak 2022].

10.3 Validation of our simulations

To evaluate if our simulations were valid, *in vitro* and *in vivo* ^{23}Na MRI datasets were acquired. The reference image was a 3D radial UTE at spatial resolution 8 mm isotropic with number of shots ($N_s 4\pi(k_{max}FOV)^2$) chosen to respect Nyquist criteria, [Bernstein 2004] and 32 number of averages (NA) were used as the reference image for our simulations.

At this resolution, the number of averages was chosen for validation because we could aim for a high SNR in a short acquisition time. For instance, the full Nyquist dataset with 32 averages takes about 30 min. Therefore, validating this protocol *in vivo* would be easier. If one has the time to do so, this validation can be done at any resolution as long as a sufficient SNR is achieved.

This test explored different acceleration factors and resolutions and focused on a fixed set of parameters: TR/TE=20/0.5 ms, FA=55°, FOV = (240 mm)^3, dwell time = 10 μs, 1248 points per spoke, which has previously been optimized for *in vivo* ^{23}Na acquisitions on our 7T set-up [Coste 2019].

MRI data were acquired on Magnetom or Terra 7T MR Siemens scanners (Siemens Healthineers, Erlangen, Germany) using respectively a dual-resonance ^{1}H/^{23}Na birdcage (Rapid Biomedical) or a 32-channel helmet coil (Rapid Biomedical).

The input SNR per spoke was measured from these experiments. I added Gaussian noise to the reference complex **k**-space data to simulate the performances of SPARKLING and TPI strategies at lower input SNR. For each considered input SNR, **k**-space was sub-sampled at various acceleration factors (AF=2, 4, 16, 32, 64, 128).

A reference radial image with full Nyquist **k**-space sampling was acquired and the metric chosen was SSIM. Images were reconstructed using the density compensated method [Pipe 1999] combined with CS reconstruction with density compensation using Pysap-MRI [Farrens 2020]. This package allows the management of large 3D non-Cartesian multichannel datasets. For each reconstruction, the regularization parameter (λ) was chosen visually in the 10^{-7} to 10^{-20} range (30 steps) to maximize "human-evaluated" image quality.

10.4 Impact of acceleration on TSC quantification

High-quality images are not the only goal of ^{23}Na MRI since, as discussed before, ^{23}Na MRI aims at being quantitative. It is known that CS techniques can affect the performance of quantification methods [Blunck 2020]. That is why we needed to study the impact of acceleration on the TSC quantification.

10.4.1 Theory

Our quantification method is based on our variable flip angle (VFA) approach [Coste 2019], which combines two images acquired at different FA to estimate M_0 and T_1 maps.

Two steady-state gradient sequences were used to perform the Variable Flip angle method:

$$\frac{S}{\sin(\alpha)} = a\frac{S}{\tan(\alpha)+b} \tag{10.8}$$

with

$$a = \exp^{\frac{-TR}{T_1}} \tag{10.9}$$

$$b = KM_0(1-\exp^{\frac{-TR}{T_1}}) \tag{10.10}$$

from which M_0 and T_1 can be extracted from:

$$KM_0 = \frac{b}{1-a} \tag{10.11}$$

$$T_1 = -\frac{TR}{\ln a} \tag{10.12}$$

M_0 images are then used for the calibration phase to compute TSC maps.

10.4.2 ^{23}Na MRI Acquisitions

MRI data were acquired on the Terra 7T MRI scanner (Siemens Healthineers, Erlangen, Germany) of the CHU of Poitiers equipped with a whole-body gradient coil (G_{max}=80mT/m, slew rate of 200 T/m/s) and a double-tune 1Tx/1Rx birdcage coil for ^{1}H and 1Tx/32Rx helmet coil for ^{23}Na (Rapid Biomedical GmbH, Rimpar, Germany).

^{23}Na MRI sequence parameters were those determined previously by our team [Coste 2019] to maximize SNR for *in vivo* ^{23}Na MRI: TE/TR=0.8/20 ms, FOV=296 mm isotropic, FA= 50°, dwell time = 10 μs of ADC, 1248 points per ADC, 32 averages. The oversampling factor, which indicates how many points are acquired per dwell time, was set to 5. The reason is that SPARKLING optimization generates better trajectories for this parameter. It does not affect the TPI trajectories generated.

One may notice a lengthening of the TE was needed from TE=0.5 ms to TE=0.8 ms due to the difference between the TERRA and MAGNETOM systems. Both were corresponding to the minimum TE possible for the sequence, the excitation pulse being a hard pulse with aduration of 860 μs in both cases.

MR Sequence

The sequence used for both trajectories I coded from a FLASH Siemens sequences and it has been described in detail in section 4.1.4. The only parameter changed between a TPI and a SPARKLING acquisitions was the file of trajectory, this guarantees the same RF pulses, spoiling and all other relevant parameters that allow this comparison to be fair.

10.4.3 Image reconstruction

Density compensation Pipe1999 using Pysap-MRI Gueddari2020 were performed in all the data. This package allows the management of large 3D non-Cartesian multi-channel datasets. The iterative method was the same for TPI and SPARKLING. The density compensation function depends only on the k-space trajectories, this keeps the comparison between TPI and SPARKLING fair. Density compensation is needed in non cartesian acquisitions in order to avoid degradation of PSF.

While iterative reconstruction is expected to be used and generate better results for CS acquisitions, only evaluating this reconstruction could make difficult to pinpoint the benefits of the trajectory versus reconstructions. That is the reason whe both iterative reconstruction using proximal optimized gradient method (POGM)Kim2021 and regridding were evaluated.

Raw k-space datasets of each acquisition block were processed offline. For each iterative reconstruction, the regularization parameter (λ) was chosen visually in the 10^{-7} to 10^{-20} range (30 steps) to maximize image quality. λ was constant between volunteers for a given acceleration factor and trajectory.

In this thesis, our nonlinear reconstruction reads as follows:

$$\hat{\mathbf{z}} = \arg\min_{\mathbf{z}} \frac{1}{2}||y - ||_2^2 + \lambda||z||_1$$

10.4.4 Data processing for TSC quantification

Reconstructed images obtained for each flip angle ($FA_1 = 25°$ and $FA_2 = 50°$) were rigid-body realigned, to compute M_0 and T_1.

One may notice the change from FA=55° to FA=50° from the optimized protocol of reference [Coste 2016]. This was needed thanks to the different coils, which led to an increase in SAR. To compensate, we had to slightly decrease the second flip angle.

To estimate TSC, four calibration tubes were used. They were placed on the exterior part of the coil (figure 10.7). The sodium concentrations in the four calibration tubes were: $T_1 = 51$ mmol/L (0.3% NaCl), $T_2 = 105$ mmol/L (0.6% NaCl), $T_3 = 155$ mmol/L (0.9% NaCl), and $T_4 = 209$ mmol/L (1.2% NaCl). The agarose gel was used to mimic the relaxation times of sodium in brain tissues at a concentration of 1.2%. The tubes were made at NeuroSpin chemical laboratory.

Image processing consisted in automatically segmenting the tubes on the images, the segmentation takes into account the fixed geometry tubes. For each tube a mask was generated, this allowed us to extract the M_0 voxels distribution, and performing a four-point linear regression of intra-tube intensity against tube concentrations.

The points used in the regression were a i-percentile of the concentration distribution in the tube. The percentile of concentration was calibrated to match the known concentration in the Skully phantom using a full Nyquist acquisition.

I developed these scripts for the analysis of our SPARKLING data in Python3. They are available in a public GitHub repository (https://github.com/rpbaptista/StudySparkling/).

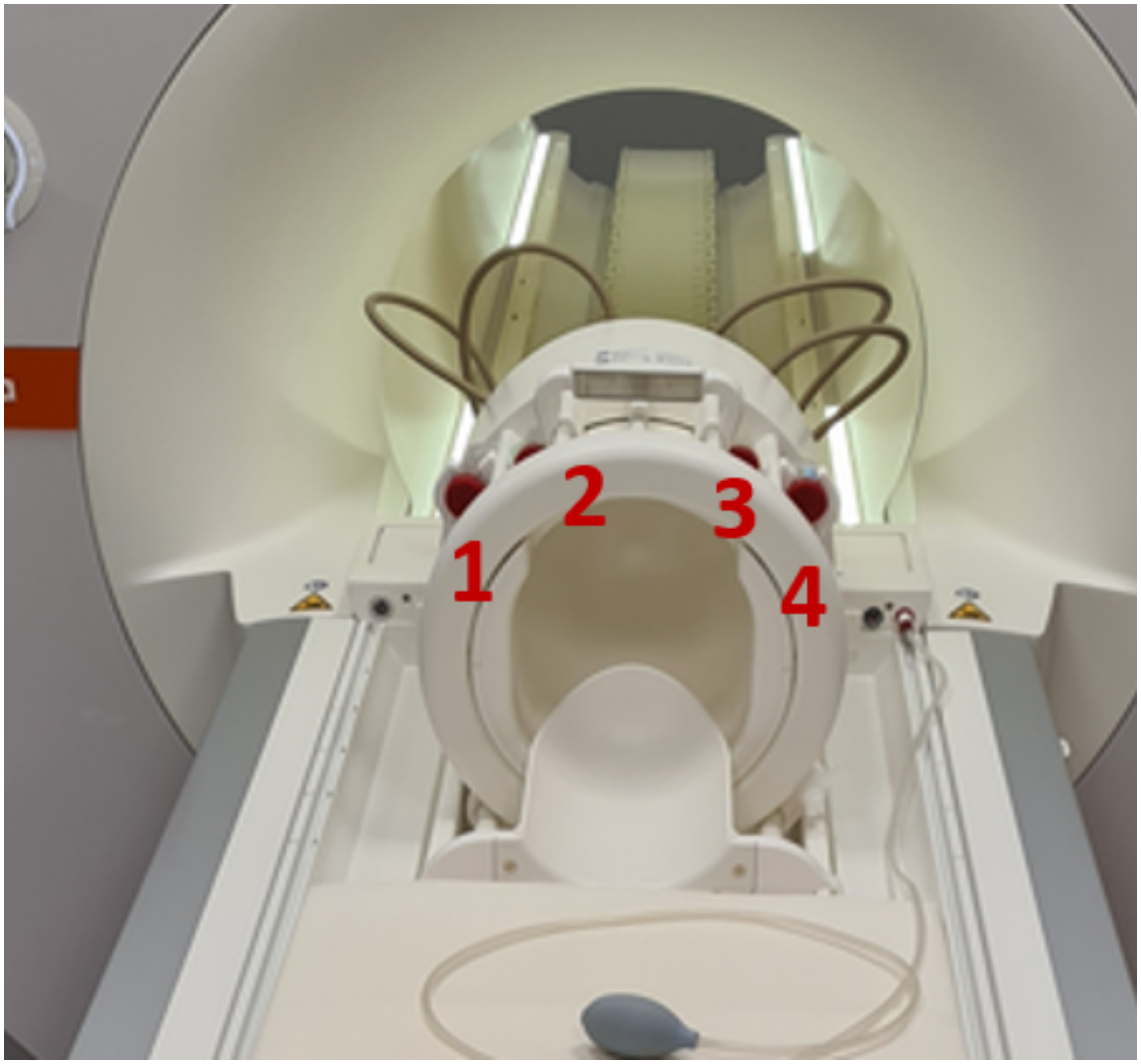

Figure 10.7 – Placement of tubes on the coil.

10.4.5 Evaluation Metrics

To evaluate the robustness of our quantification, we filled a realistic phantom (represented in fig. 10.8) with a known sodium concentration, and we measured the difference between the real concentration and the mean of the estimated concentration for each acceleration factor (AF=8,32,64,128). This phantom was 3D printed at NeuroSpin by J. Bernard, and is based on the geometry proposed by Jona and all [Jona 2021].

The relative errors in the obtained TSC values were compared between the accelerated datasets, the 4-point calibration method robustness being evaluated through the r^2 of the linear regression of the signal extracted from the reconstructed and segmented reference tubes.

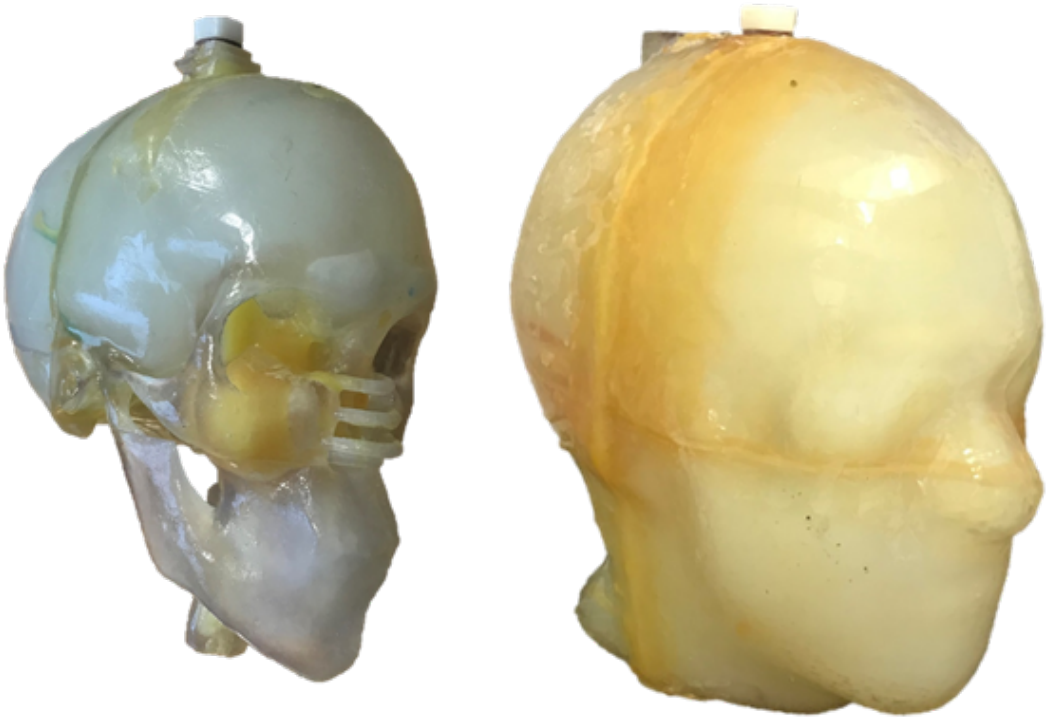

Figure 10.8 – Illustration of "skully" phantom. The left side represents the inner compartment. The right side represents the outside compartment. The photo is courtesy of Thaddée Delebarre (Ph.D. Student at NeuroSpin). The internal compartment is filled with 40 mM of NaCl, and the exterior is filled with 100 mM of NaCl. NaCl was chosen thanks to its stability over time.

Chapter 11

Results

Chapter Outline

11.1 Comparison of SPARKLING and TPI *in silico*

In this section, we present, for the considered scenarios of SNR and spatial resolution, the impact on SSIM of the different acceleration factors for both SPARKLING and TPI acquisitions.

For each considered spatial resolution, our simulations led us to a certain number of average to reach the target SNR.

In figure 11.1, one can see that high SNR levels are required for SPARKLING to outperforms TPI for a resolution of 3 mm isotropic. Unfortunately, obtaining these SNR levels at such resolution would require hundreds of averages which would make the acquisitions last hours. Consequently, we did not investigate further neither this 3 mm resolution nor the even more challenging resolution of 2 mm that we had examined through our simulations.

Figure 11.2 shows the SSIM for SPARKLING and TPI acquisitions at different SNR levels for a resolution of 4 mm isotropic.

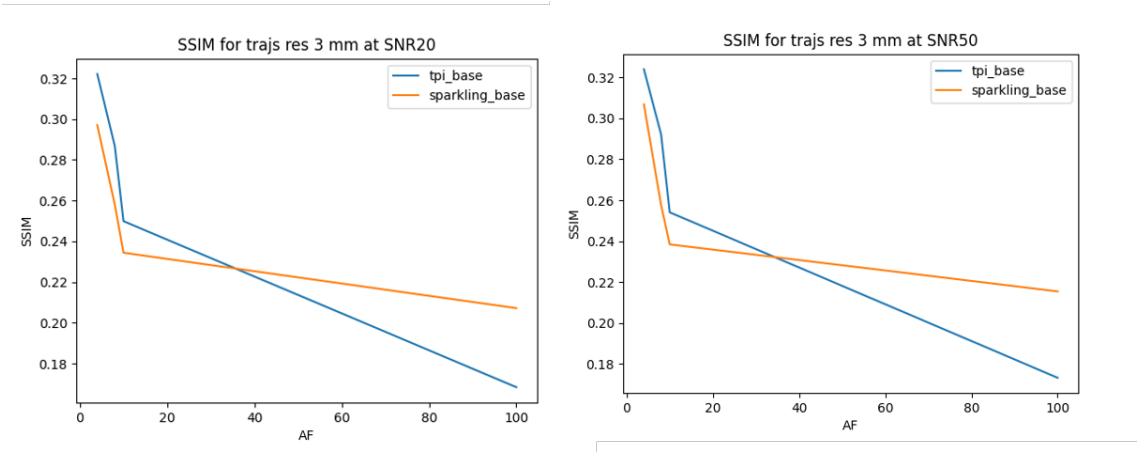

Figure 11.1 – Different evolution of SSIM computed for different SNR and acceleration factors for a simulated acquisition at resolution 3 mm isotropic. SNR=(20,50) are shown here.

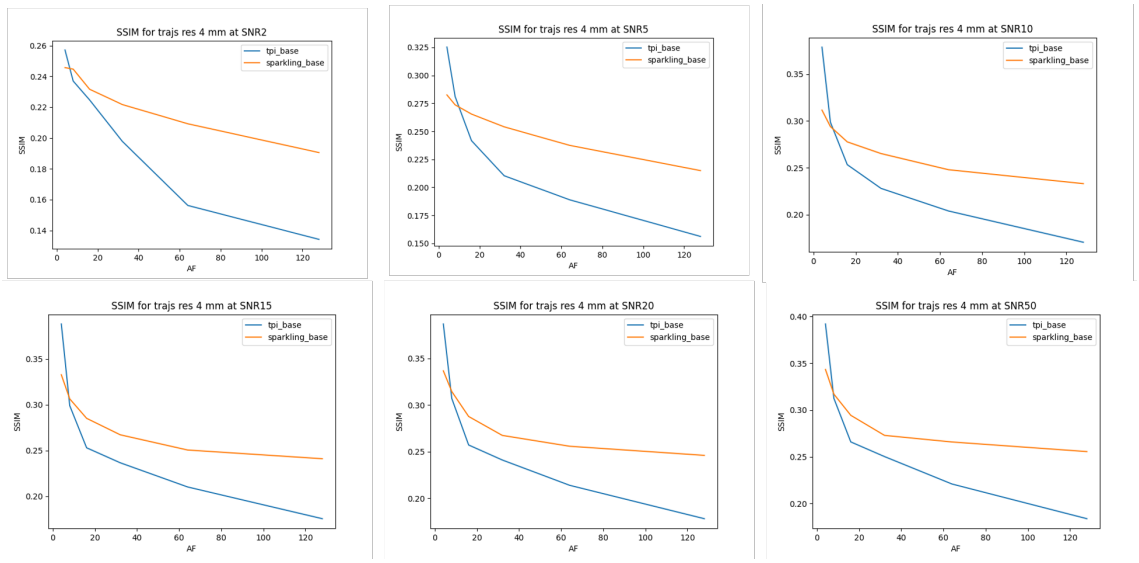

Figure 11.2 – Different evolution of SSIM computed for different SNR and acceleration factors simulated acquisitions at resolution of 4 mm isotropic. SNR=(2,5,10,15,20,50) were explored.

At SNR = 2, we can already see the interest of using SPARKLING. One can notice that the levels of SSIM are somewhat low (0.2-0.4). Figure shows the central slice of the images for a resolution of 4 mm. One can appreciate that for a SSIM of 0.22 (TPI/AF=64) the image quality is quite degraded (bottom right of the grid). Comparatively, SSIM values above 0.30 correspond to rather neat images.

From this analysis, we concluded that a minimal SNR level of 10 was required to observe an advantage of SPARKLING over TPI for high accelerations factors, i.e. to achieve SSIM > 0.3 . To reach this level of SNR in our experimental set-up for a 4 mm resolution, 32 averages are deemed necessary.

Overall, the SSIM were found to be lower than what an observer would score the images. This shows the limits of SSIM, which will be discussed in the next chapter.

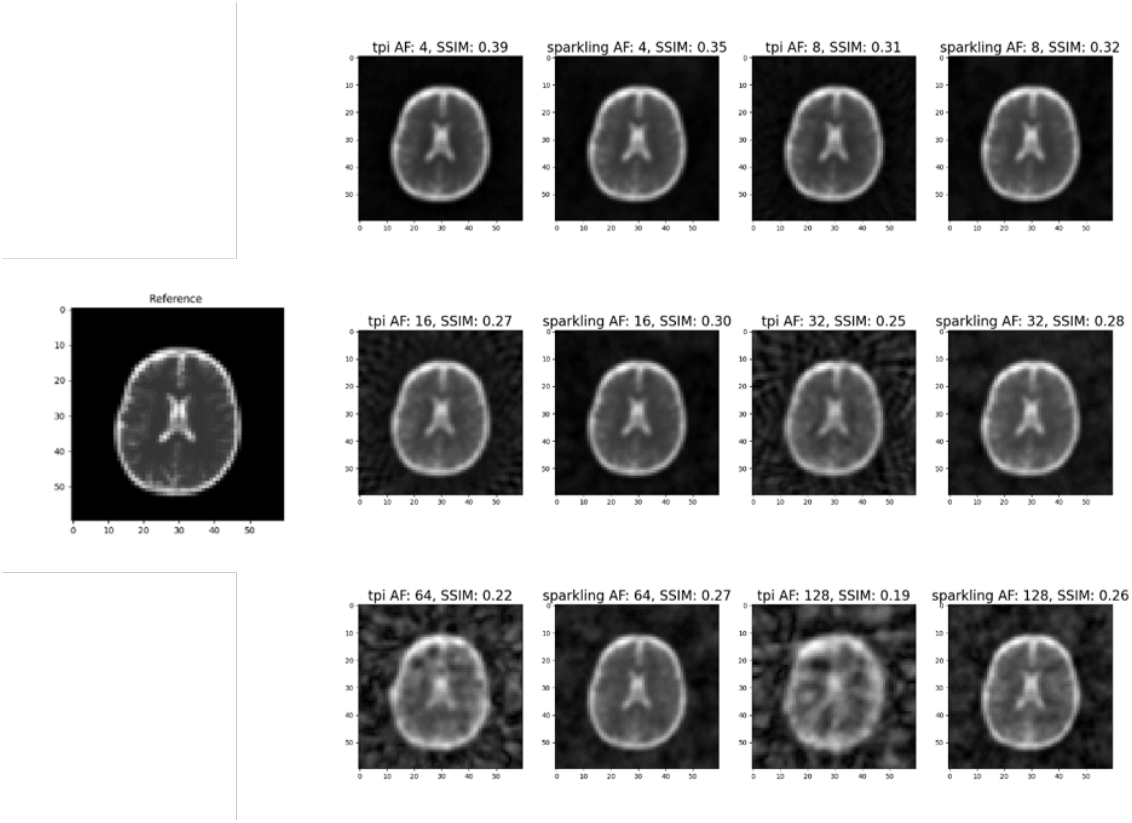

Figure 11.3 – Central slice of reconstructed simulated image at resolution for and SSIM for different SNR. Reference image synthetic sodium image from MP2RAGE. SNR=∞.

Considered all-together, these simulation data summarized in figure **??** show that SPARKLING should outperform TPI for high acceleration factors such as AF=64 (for any SNR) or even at lower AF=8 as long as a high enough SNR is achieved.

11.2 Tuning of SPARKLING parameters

Table 11.1 summarizes the FWHM of the PSF for SPARKLING acquisitions with different parameters. Based on this table, we chose parameters C=30 and D=2 to continue this work.

	FWHM				
Decay \ Cutoff	10	20	30	40	50
2	(2.2,2.2,2.2)	(2.2,2.2,2.2)	**(2.0,2.0,2.0)**	(2.2,2.2,2.2)	(2.2,2.2,2.2)
3	(2.2,2.2,2.2)	(2.2,2.2,2.2)	(2.2,2.2,2.2)	(2.2,2.2,2.2)	(2.2,2.2,2.2)

Table 11.1 – FWHM for different parameters at AF = 1. Unit is voxels.

Figure 11.4 shows the central slice of the log of PSF for the investigated TPI and SPARKLING trajectories. Parameters for SPARKLING were C=30 and D=2.

We chose a log scale to better visualize the ripples surrounding the central lobe of the PSF (to enhance smaller values).

One can notice that the peak of the PSF for SPARKLING trajectories is thinner than for TPI trajectories.

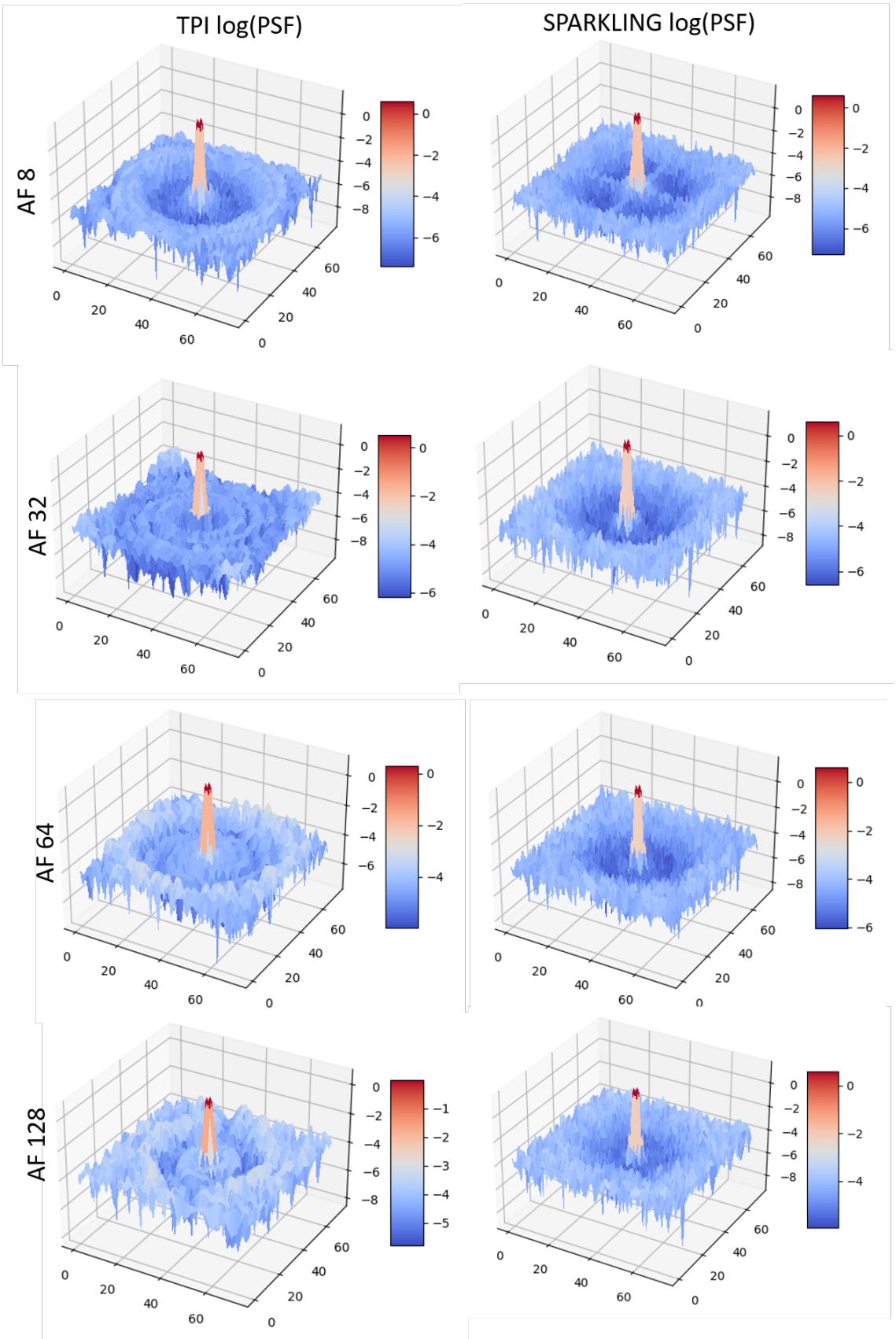

Figure 11.4 – Log of PSF of the central slice in Z for different accelerations for SPARKLING and TPI

11.3 Comparison between experimental data

11.3.1 *In vitro*

Figures 11.5 and 11.6 show the results between *in vitro* and simulation at 8 mm spatial resolutions. Good compatibility between SSIM simulated, and SSIM acquired. Even at AF=128, the object can still be discerned even at a lower quality for the SPARKLING sampling scheme. For TPI, at AF=64, the image becomes completely blurred.

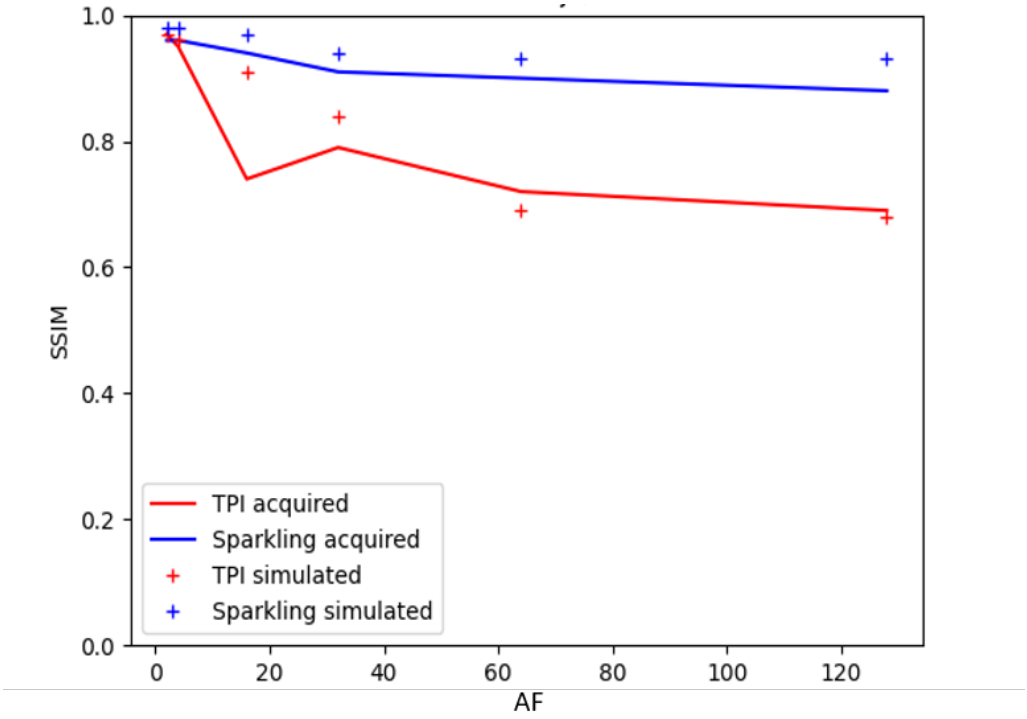

Figure 11.5 – Comparison between TPI and SPARKLING SSIM scores for *in vitro* acquisition and simulation data with acceleration factors of 2, 4, 16, 32, 64, and 128, images acquired and simulated with a spatial resolution of 8 mm isotropic.

In figure 11.6, one can see that at AF=16, TPI images become significantly blurred, and the contours of the tubes can barely be differentiated. At the same time, this happens only at AF=64 for SPARKLING.

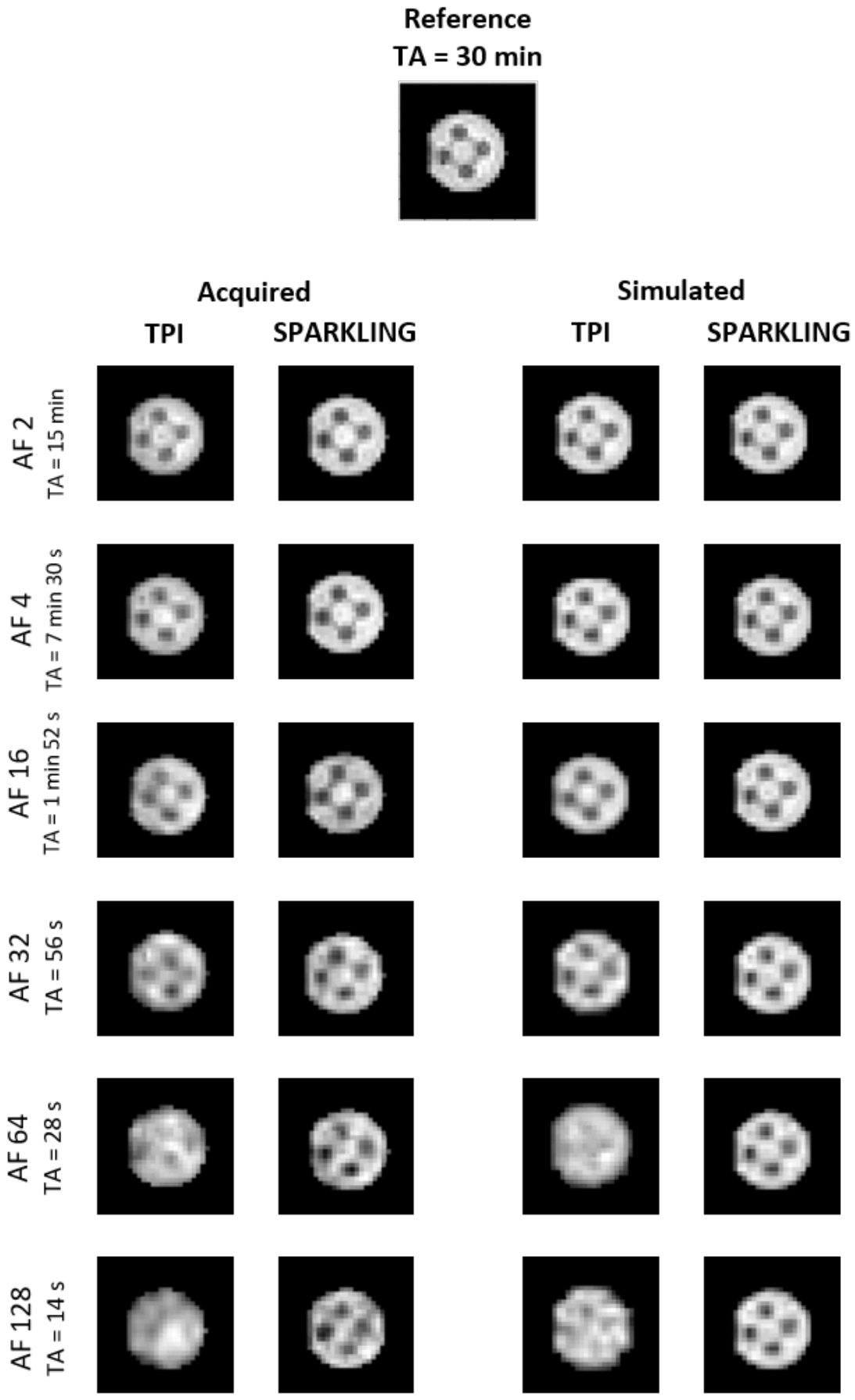

Figure 11.6 – Central slice of 3D reconstruction for TPI acquired and Sparkling acquired and their correspondent simulation for different accelerations factors of 2, 4, 16, 32, 64, and 128 at constant input SNR per spoke and spatial resolution of $(8\ \text{mm})^3$ on a phantom.

11.3.2 *In vivo*

Figures 11.7 and 11.8 show the results between *in vivo* and simulation at 8 mm resolutions. Values of SSIM for SPARKLING remain close to 1 in simulation for all acceleration factors. In reality, this value is closer to 0.90, but it also remains constant for all acceleration factors. This shows the stability and robustness of SPARKLING.

It also shows the interest in averaging images. We see here with NA=32. We can accelerate over 32 because we achieved a threshold SNR of interest, for TPI simulation show a decrease in SSIM, which is also seen in acquisitions. SSIM closes to one was not obtained in acquisitions for *in vivo* data.

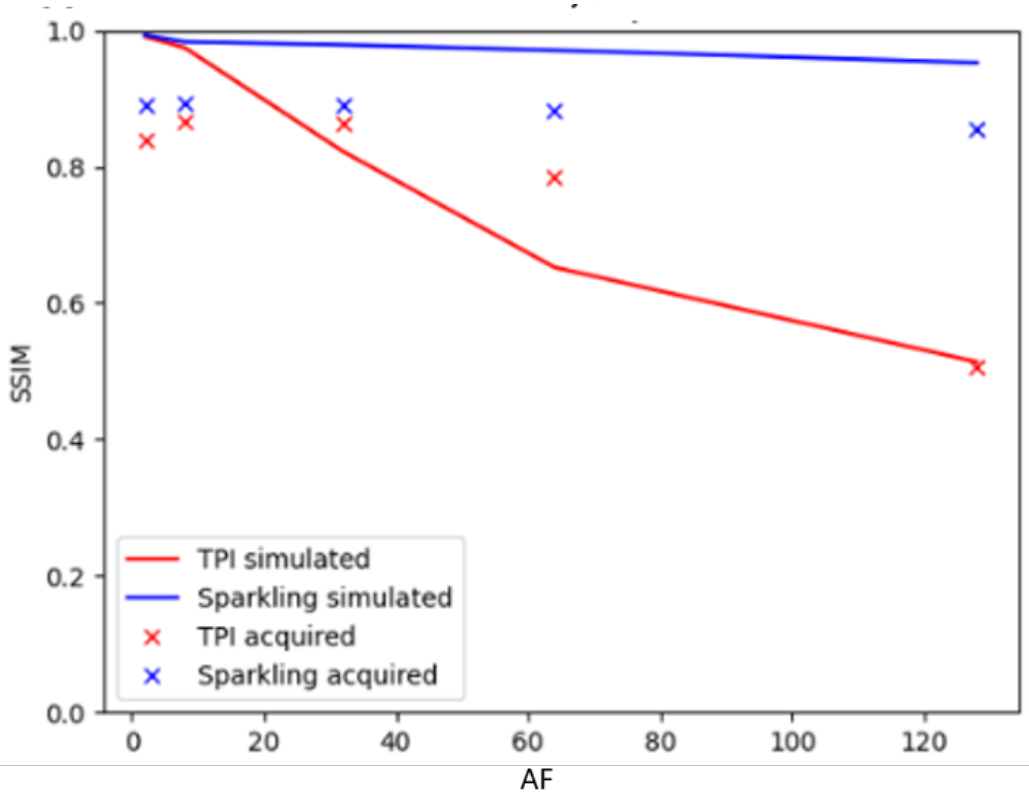

Figure 11.7 – Comparison between TPI and SPARKLING SSIM scores for *in vivo* acquisition and simulation with acceleration factors of 2, 4, 16, 32, 64, and 128, images acquired and simulated with a spatial resolution of 8 mm isotropic.

Figure 11.8 shows, one of the main results of this thesis, that at AF=32, TPI images become significantly blurred, and the contours of the CSF can barely be differentiated. At the same time, this happens only at AF=128 for SPARKLING. So even though the values of SSIM do not align precisely with the simulation, experimental data agree with simulations regarding the differences between the impact of acceleration on TPI a SPARKLING, thus validating (at least partially) our simulation tool.

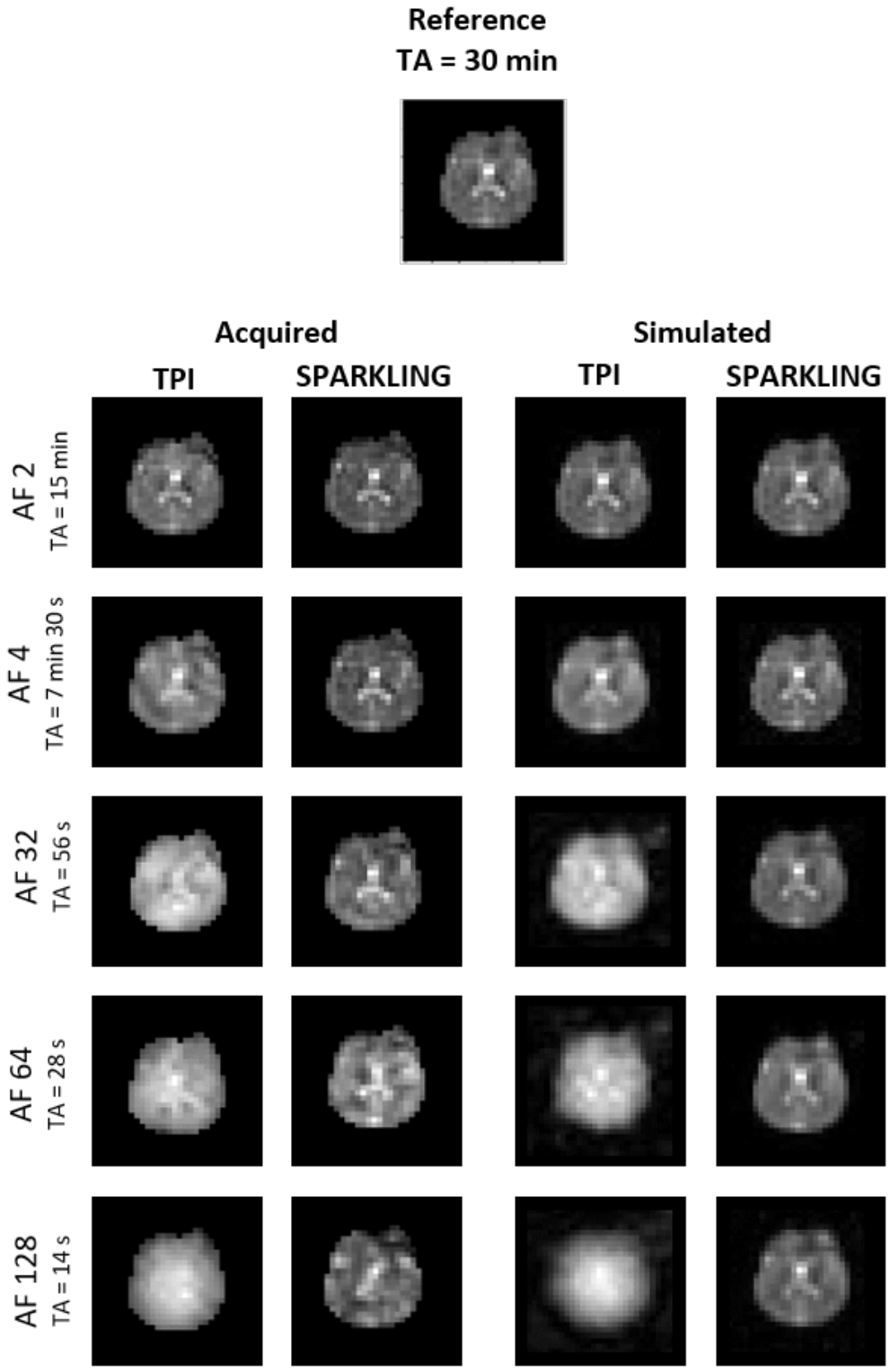

Figure 11.8 – Central slice of 3D TPI and Sparkling experimental images and their corresponding simulation for different accelerations factors (AF= 2, 4, 16, 32, 64, and 128) for a constant input SNR per spoke and a target spatial resolution of $(8\ \text{mm})^3$ in a healthy volunteer at 7T.

11.4 Impact of acceleration on TSC quantification

11.4.1 PSF and accelerated trajectories

The FWHM of the PSF corresponding to each trajectory examined in our *in vivo* and *in vitro* tests were evaluated and are summarized in the table below:

	FWHM (in pixels)			
	AF=8	AF=32	AF=64	AF=128
TPI	(2.4,2.4,2.4)	(2.6,2.6,2.6)	(2.6,2.6,2.6)	(2.6,2.6,2.6)
SPARKLING	(2.2,2.2,2.2)	(2.2,2.2,2.2)	(2.4,2.4,2.4)	(2.4,2.4,2.4)

Table 11.2 – FWHM for trajectories at 4 mm and cutoff of 30 and decay of 2 for SPARKLING and p=0.3 for TPI

11.4.2 *In vitro*

For all our linear regressions performed across different accelerations factors for calibration, R^2 values were systematically superior to 0.96, showing good robustness with the low variance of the calibration method. An example of linear calibration regression is shown in figure 11.9 for illustration.

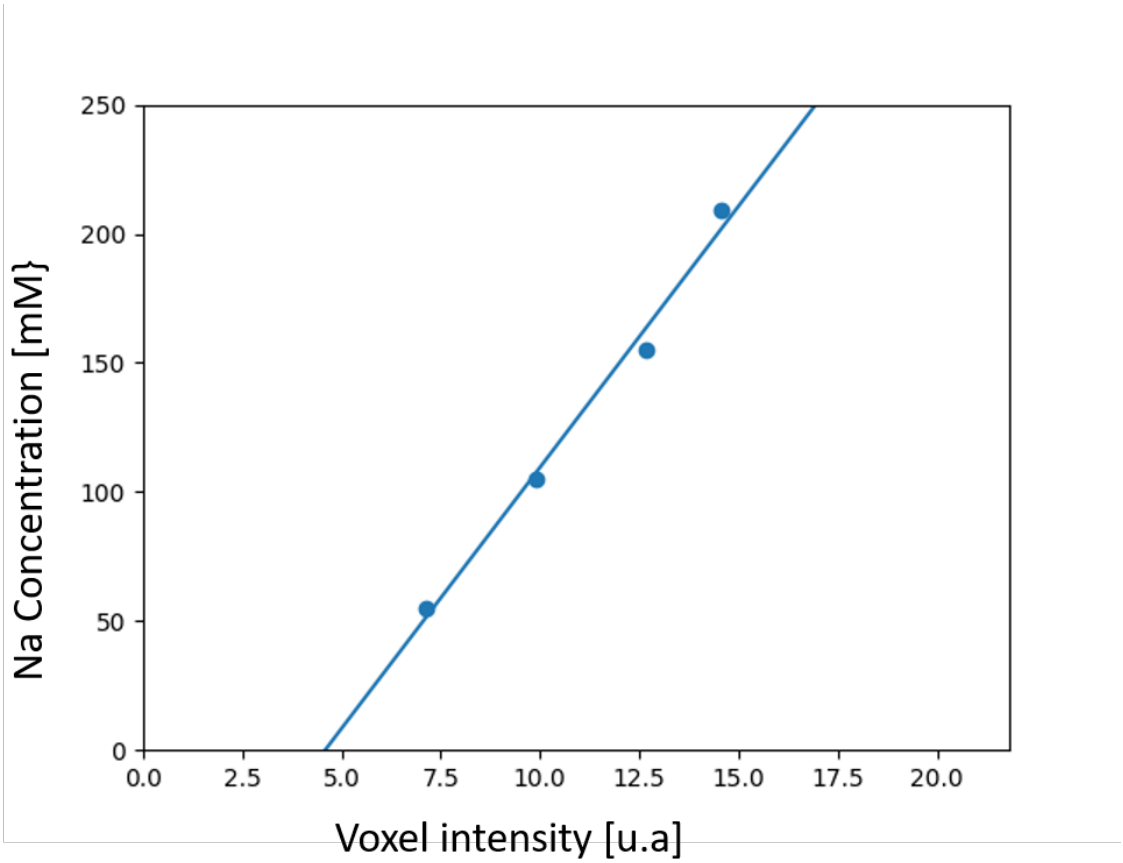

Figure 11.9 – Calibration curve for AF=128, SPARKLING *in vitro*.

The line does not cross at (0,0) due to the background noise with a non-zero mean due to its Rician nature.

The table 11.3 shows the concentration across different acceleration factors for images reconstructed with NUFFT. The true concentration is 40 mM in the inner compartment.

	NUFFT reconstruction: Concentration [mM]			
AF / Trajectory	AF=8	AF=32	AF=64	AF=128
TPI	40 ± 4	42 ± 2	56 ± 4	74 ± 5
SPARKLING	42 ± 3	41 ± 2	55 ± 3	67 ± 4

Table 11.3 – Average concentration in inner compartment of skully for different acceleration factors for NUFFT reconstruction.

One can notice that TPI displays slightly worst results at higher acceleration factor than SPARKLING which is consistent with its worse PSF. For AF=32, the relative quantification error was about 2.5% for SPARKLING and 5% in NUFFT.

These results show that AF=128 generates 85% for TPI and 67.5% for SPARKLING of bias in the quantification. This is why AF=128 should probably not be considered as a viable acceleration factor for quantitative ^{23}Na MRI.

Table 11.4 shows the concentrations across different acceleration factors for images reconstructed with iterative reconstruction.

	Iterative reconstruction: Concentration [mM]			
AF / Trajectory	AF=8	AF=32	AF=64	AF=128
TPI	42 ± 2	51 ± 3	70 ± 5	110 ± 7
SPARKLING	44 ± 2	39 ± 2	65 ± 5	103 ± 6

Table 11.4 – Average concentration in inner compartment of skully for different acceleration factors for reconstruction iterative.

As for the concentrations obtained from the iterative reconstruction, quantification errors were worst for TPI, especially at higher acceleration. For AF=32, the relative quantification error was about 2.5% for SPARKLING and 27.5% for TPI.

These results show that AF=128 generates 175% for TPI and 153% for SPARKLING of bias in the quantification. This is why AF=128 should probably not be considered as a viable acceleration factor for quantitative ^{23}Na MRI.

11.4.3 *In vivo* Sodium MRI images

Figures 11.10 show the reconstructed images for the NUFFT algorithm for two healthy volunteers. One can see that cortical details are better preserved for the SPARKLING acquisition reconstructed with NUFFT.

For AF=32, one can barely see any cortical details for TPI, while they are still visible for SPARKLING at AF=64. From only an image quality point-of-view, SPARKLING at AF=128 is still a decent representation of the brain. NUFFT reconstruction has the

advantage of being fast, and it could be available on the console, even though this was not the case in our work.

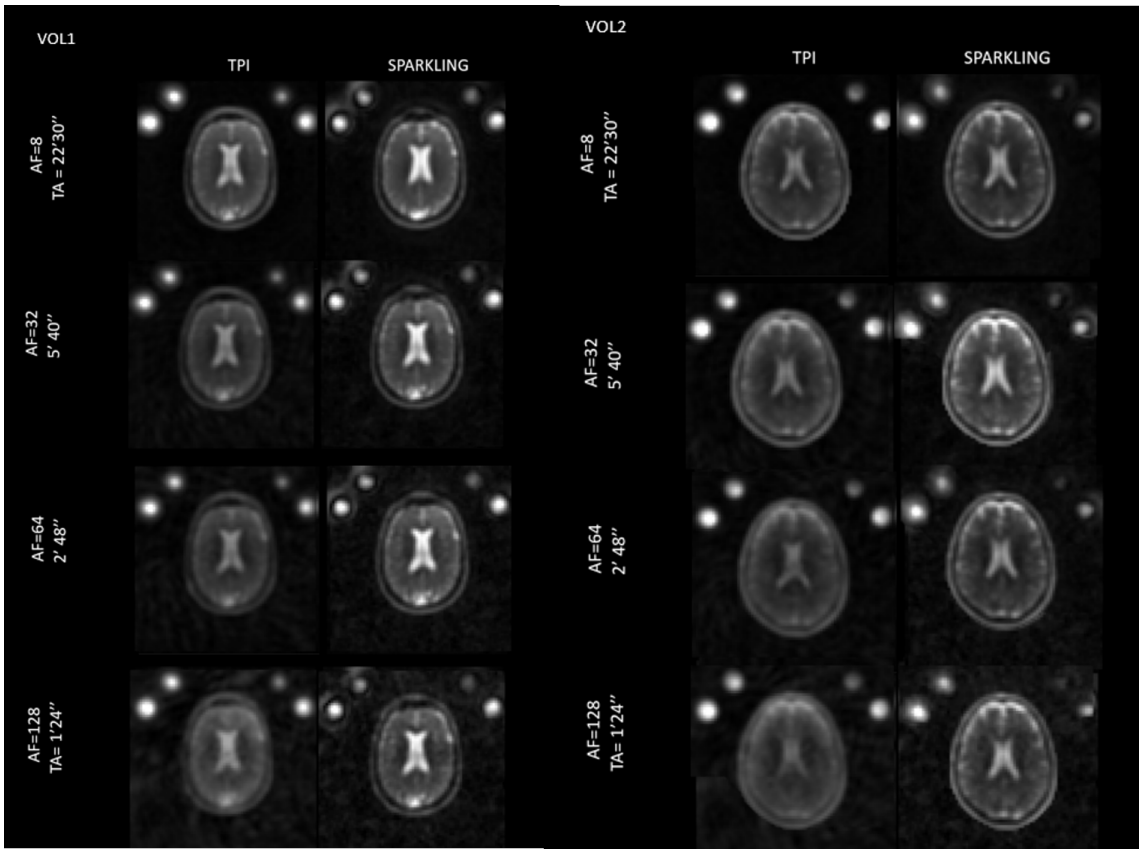

Figure 11.10 – Reconstructions for volunteers: TPI and SPARKLING reconstruction for volunteers 1 & 2 with NUFFT with density compensation.

Figures 11.11 show the same data reconstructed using the POGM algorithm.

Overall the same observations can be made when comparing SPARKLING to TPI. However, when comparing NUFFT and POGM algorithm, images reconstructed using POGM looks better as expected from the regularization.

The examination of the tubes used for calibration can be a good indicator to compare the effective resolutions. One can see that for TPI images, the tubes appear larger than they are. Image quality seems similar between both subjects for all reconstructions.

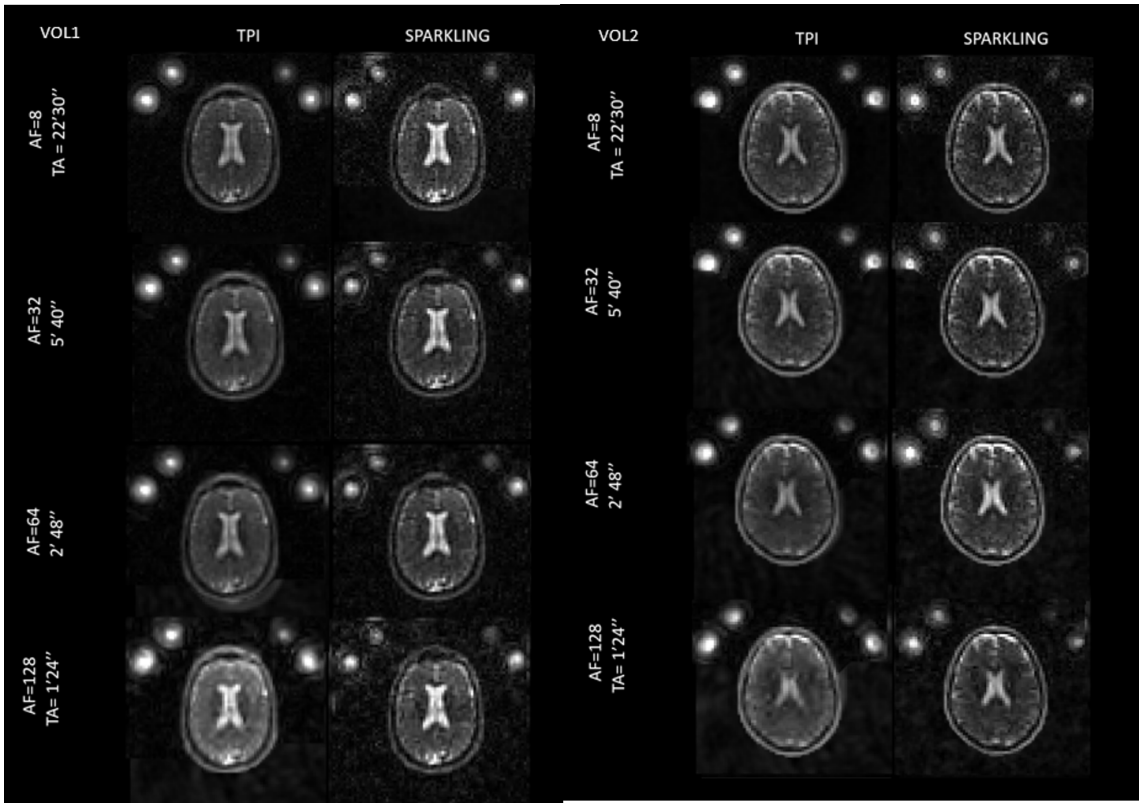

Figure 11.11 – Reconstructions for volunteers: TPI and SPARKLING reconstruction for volunteers 1 & 2 with POGM iterative reconstruction with density compensation.

11.4.4 TSC Maps *in vivo*

For all our linear regressions performed across our cohort for calibration, R^2 values were systematically superior to 0.95, showing good robustness with a low variance of the calibration method. An example of linear calibration regression is shown in figure 11.12 for illustration.

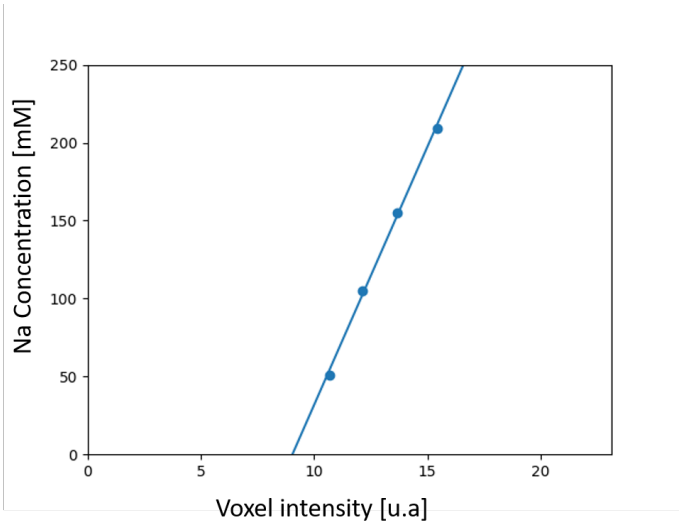

Figure 11.12 – Calibration curve for AF=128, SPARKLING *in vivo*.

The line does not cross at (0,0) due to the background noise with a non-zero mean due to its Rician nature.

Figure 11.13 shows the concentration maps for our volunteers for both TPI and SPARKLING acquisitions with an acceleration factor of 32 (acquisition time = 5'40").

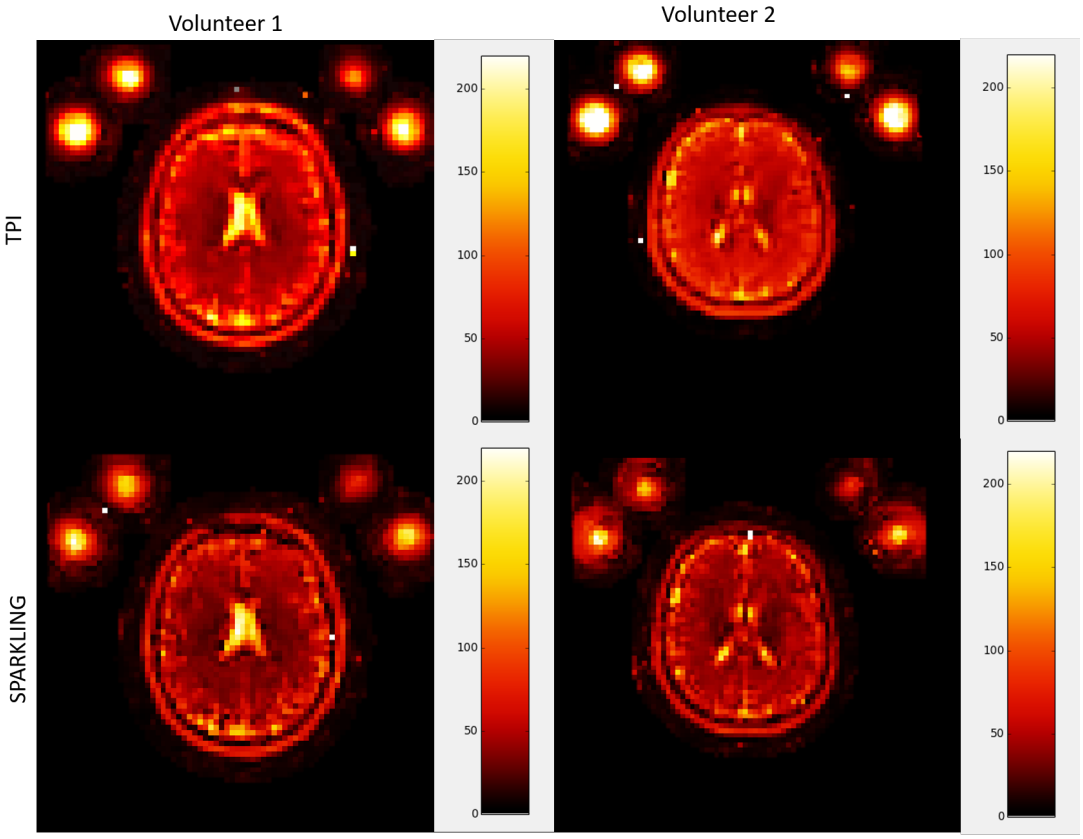

Figure 11.13 – Central slice of concentration maps of sodium using POGM reconstruction.

As observed for our *in vitro* data, TSC values were found slightly higher for TPI compared to SPARKLING the average difference is 11 ± 2 mM .

Chapter 12

Discussion

This study compared sub-sampled SPARKLING and TPI acquisitions for quantitative ^{23}Na MRI at 7T. TPI is one of the state-of-the-art sampling schemes in X-nuclei MRI. SPARKLING is an optimization-based sampling scheme that uses CS techniques to accelerate acquisitions. To the best of our knowledge, this is the first optimization-based sampling scheme to be applied to ^{23}Na MRI.

We set up a simulation tool to study different SNR and spatial resolution scenarios and tune SPARKLING parameters. This tool describes reality well enough, as illustrated by our *in vitro* and *in vivo* acquisitions. We quantified image quality in phantom through structural similarity index measure (SSIM) using a reference full Nyquist radial acquisition. High SSIM scores between simulations and *in vitro* data were also found. Our *in vivo* data showed that SSIM displayed a bias compared to our simulations. We attribute this difference to the difference in PSF between the radial reference (full Nyquist acquisitions) and the accelerated SPARKLING/TPI data. SSIM is known to be weakly sensitive to blurring [Punga 2014]. For this reason, and due to time limitations to acquire a full Nyquist reference, we did not evaluate/compare SSIM across our *in vivo* data [Wang 2015].

To simulate our scenarios, we used a database of synthetic images created from MP2RAGE, we noticed that SSIM values were lower than expected when compared to radial references. This can be attributed to the fact we did not model realistically the T_2^* decay in our simulation. While this can be negligible for simulated proton images, T_2^* decay is much faster for ^{23}Na MRI and different points in k-space do not exhibit a stable signal intensity, impacting the PSF of ^{23}Na MRI.

We showed that SPARKLING trajectories have a better PSF than TPI for the same number of spokes. This was evaluated by comparing the full width at half maximum of their PSF for different trajectories. The evaluation of PSF after reconstruction is not trivial for CS reconstruction, which was not explored in this work.

We also showed that SPARKLING offers similar image quality for TPI/AF=8 and SPARKLING/AF=32 at 4 mm isotropic with a 32 channel coil. We also showed that this level of acceleration (AF=32) for SPARKLING leads to negligible 2,5% or 5% quantification errors when reconstruction is realized using NUFFT or POGM algorithms respectively. The difference in PSF can explain this difference. More blurred is the image, more overestimated

the TSC should be. Another difference is that in the iterative reconstruction, B_1^- mitigation is already included, while it is not in NUFFT. Considering the positioning of the calibration tubes at the rim of the birdcage, this correction could be significant and an independent B_1^--correction step could be needed for NUFFT reconstructions. Notably, for AF=64 or higher, the quantification errors observed in our *in vitro* data are higher than the TSC differences found between healthy and Alzheimer's patients, for instance by Haeger et al. [Haeger 2021]. For this reason, we consider that *in vivo* quantitative ^{23}Na MRI should probably not be under-sampled beyond an acceleration factor of 32.

Recent studies [Gnahm 2014, Blunck 2020] explored CS techniques for 3 mm isotropic at 7T using DA-3DPR. Here, we targeted a spatial resolution of 4 mm isotropic. The extrapolation of these results for different resolutions and nuclei depends on the previous evaluation of SNR and image sizes, which was the first part of this work. This means that are in most scenarios, TPI (and other deterministic k-space sampling schemes) remains highly relevant.

Determination of scenarios of interest for SPARKLING is not trivial because CS performance depends on SNR and image sizes [Lazarus 2019]. One may wonder the theoretical limíts of this application when compared to TPI. As input SNR depends on so many factors such as coil perfomance, magnetic field strength, resolution etc..., we could not establish such scenarios in an universal manner.

A reproducibility study is on-going with the recruitment of more volunteers. Unfortunately, those data were not available to be presented in this manuscript.

Another limit of this strategy is that as we change from deterministic and parametric sampling schemes to non-deterministic sampling scheme such as SPARKLING, we lose flexibility at the console. Indeed the computing time necessary to calculate SPARKLING trajectories is not compatible for rapid adjustment of the resolution, number of spokes or points per spoke. For now, SPARKLING trajectories must be computed offline or available in a library. However, we believe that improving image quality is worth investigating faster optimization techniques that would increase flexibility.

Future results could be further improved by exploring the reconstruction side. For instance, modeling the different averages acquired as samples of the same distribution instead of only averaging them. This way, we would reinforce that all the acquisitions represent the same object and that the average variability between each of the samples comes from the noise. It would also be possible to add anatomical priors/constraints or use dictionary learning techniques [Behl 2016b].

Chapter 13

Conclusion and perspectives

We managed to set up a simulation tool for TPI and SPARKLING ^{23}Na acquisitions that match well with reality. This was verified visually *in vivo* and *in vitro*. We also quantified the resulting image quality through the SSIM metric.

With this simulation tool, we searched for an optimal SNR and spatial resolution scenario in which SPARKLING is beneficial to accelerate ^{23}Na acquisitions, and we tuned the parameters of SPARKLING according to this scenario. SPARKLING is a new sampling scheme driven by numerical optimization. This is the first time, to our knowledge, that such type of **k**-space sampling scheme has been used for ^{23}Na MRI or any other X-nuclei MRI application.

We also studied the impact of different reconstruction methods and accelerations factors on quantifying total sodium concentration. We showed that TSC estimated by SPARKLING was slightly less biased when compared to TPI. This can be attributed to the difference between their PSF. We also showed that the iterative reconstruction POGM is more biased compared to NUFFT. This could be explained by the B_1^- correction implemented within the iterative reconstruction.

We showed that at 7T with a 32-channel coil for 4 mm isotropic resolution, we can obtain similar results for TPI/AF= 8 and SPARKLING/AF=32 in terms of image quality and total sodium quantification accuracy. This represents a huge gain in acquisition time that could be harnessed for the future application of SPARKLING for clinical research.

As discussed, sodium MRI can potentially become a biomarker for neurodegenerative diseases. Also, dynamic sodium MRI could become a complementary technique to fMRI thanks to its ability to assess indirectly metabolism and neurotransmission, contrary to the BOLD effect, which evaluates neurovascular coupling. The level of acceleration found in this study, combined with even bigger magnetic fields such as 11.7T, could be of interest to revisit sodium changes observed during neuronal activation as proposed [Bydder 2019].

Chapter 14

^{23}Na MRI: Contributions to clinical studies

Chapter Outline

14.1 Alzheimer's Study

A full version of this study was published in:

A. Haeger, M. Bottlaender, J. Lagarde, **R. Porciuncula Baptista**, C. Rabrait-Lerman, V. Luecken, J. B. Schulz, A. Vignaud, M. Sarazin, K. Reetz, S. Romanzetti and F. Boumezbeur. What can 7T sodium MRI tell us about cellular energy depletion and neurotransmission in Alzheimer's disease? Alzheimer's and Dementia, vol. 39, no. 33, pages 3:65–3:76, 4243

An Alzheimer's Disease study was set up at NeuroSpin to answer the question: "What can 7T sodium MRI tell us about cellular energy depletion and neurotransmission in Alzheimer's Disease?" This study was a collaboration between Aachen University (Aachen, Germany) , Sainte-Anne Hospital (Paris, France), and NeuroSpin, and it was led by Dr. Alexa Haeger under the joint supervision of Drs. Sandro Romanzetti et Fawzi Boumezbeur (figure 14.1).

Before this study at NeuroSpin, only two ^{23}Na MRI preliminary studies in AD had been published in the literature. One was with a small cohort of five patients with mild

Figure 14.1 – At left, Aachen University, Aachen, Germany (from https://www.easyuni.com/germany/rwth-aachen-university-10431/). Right, Sainte-Anne Hospital, Paris, France (from https://commons.wikimedia.org/wiki/User:LPLT).

AD [Mellon 2009], limiting their findings' statistical power. And a more recent one at 3 Tesla [Mohamed 2021] has limited spatial resolution (4 mm isotropic). They both showed an increase in intensity from ^{23}Na MRI in areas of the brain usually affected by AD, such as the hippocampus.

Thanks to the favorable conditions available at NeuroSpin and Service Hospitalier Frédéric Joliot (SHFJ, Joliot Institute for Life Sciences, CEA, Orsay, France), i.e. the availability of a 7T MRI scanner and radiochemistry and PET facilities respectively, there was an opportunity to conduct an ambitious study to investigate for the first time in the same cohort of AD patients correlations between TSC changes using quantitative ^{23}Na MRI (with an improved 3 mm resolution), morphometric changes using high-resolution ^{1}H MRI (0.75 mm resolution), amyloid-β and Tau loads, and clinical scores.

In this analysis, the SENIOR cohort was used as matched-aged control [Haeger 2020]. The SENIOR study is a longitudinal study that has taken place at NeuroSpin/CEA since March of 2012. This study recruited a cohort of 100 healthy volunteers (50F/50M) between 50 and 70 years old. Each volunteer participates in a day-long protocol of several exams every year for ten years. The goal of this study is to look for biomarkers of brain aging. Each year, identical base sequences are acquired, which allows the tracing along the years. Also, new sequences are added for other studies. I participated in specific exploitation of this ongoing study, which consisted in acquiring ^{23}Na MRI datasets and computing the TSC maps.

In this work, seventeen patients with AD (10 female, mean age 71.6 $\pm$ 7.9 years) recruited from the memory clinic of Sainte-Anne Hospital in Paris (France) participated willingly, their imaging and clinical results were compared to 22 age-matched control subjects from the SENIOR cohort.

All subjects received a cognitive assessment, including cognitive screening tests with the Mini-Mental State Examination (MMSE) [Folstein 1975] and the MoCA, [Nasreddine 2005]; Clinical Dementia Rating (CDR), verbal and visual episodic memory (Free and Cued Selective Reminding Test [FCSRT] [Grober 1987] and the Rey Complex Figure Test

[RCFT] [Shin 2006]). Executive and Visio-constructive function, working memory, and gesture praxis were further assessed.

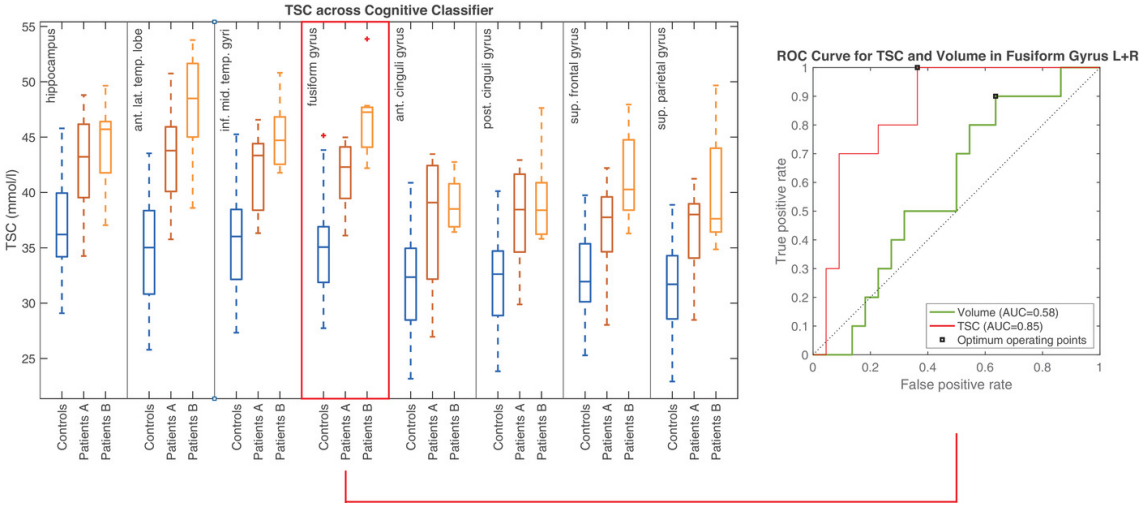

Figure 14.2 – Stage-dependent tissue sodium concentration (TSC) results and predictive power of TSC. Left, Boxplots representing the median regional TSC values across eight selected regions of interest (ROIs; i.e., hippocampus, anterior lateral temporal lobe, inferior middle temporal gyri, fusiform gyrus, anterior cingulate gyri, posterior cingulate gyri, superior frontal, and superior parietal gyri) for controls (blue) and the patients' group divided according to k-means classification in cognitively better (Patients A, n = 10) and worse (Patients B, n = 7) subgroups. Right, Receiver operating characteristic (ROC) analysis for TSC and volume in the fusiform gyrus for the effectiveness of discrimination between controls and cognitively less affected patients (Patients A). The marker illustrates the optimal operating point at a threshold of 36.1 mmol/L (True positive rate: 1.0; False positive rate: 0.36). Area under the ROC curve (AUC) for TSC = 0.85; AUC for volume = 0.58. From [Haeger 2021].

Among my contributions to the study, we can include participation in the 7T MRI acquisitions and discussions. I have also been at the origin of the split between Patients A and Patient B clusters. In reality, there were several clinical criteria to be considered, and I proposed a clustering approach technique that considered all of them. The approach was k-means and integrated Moca, MMSE, FCSRT, and ReyMemory. This generated a homogeneous split between all the criteria. Therefore, it allowed a uniform comparison between patients across criteria. Consequently, as illustrated by figure,14.2 we found a statistically significant correlation between disease progression via the worsening of clinical scores and TSC increases.

14.2 ENERGYSEP Study

Multiple sclerosis (MS) is related to an irreversible neuro-axonal degeneration, leading to debilitating symptoms. However, the sequence of the events that leads to this irreversible damage is still poorly understood [Ontaneda 2015]. This study is a collaboration with Pr. Benedetta Bodini's team at Institut du Cerveau et de la Moëlle (ICM, Paris, France - figure 14.3).

Figure 14.3 – Institut du Cerveau et de la Moëlle, CHU de la Pitié-Salpétrière. © Didier Boy de la Tour

The ENERGYSEP study aims at answering two critical questions regarding the relationship between early energy deregulation and neurodegeneration in MS: i) whether the brain energy dysfunction measured at a given time point can predict the subsequent occurrence of neurodegeneration; ii) to what extent and for how long neurons can bear this virtual hypoxia before undergoing structural damage.

This study wants to tackle these questions by combining multiple *in vivo* imaging techniques at 3 and 7 Tesla: ^{23}Na MRI, ^{31}P MRSI, diffusion-weighted MR spectroscopy and imaging, high resolution T_1 and T_2 weighted imaging. ^{23}Na MRI has shown its interest when studying patients with MS. TSC in the brain was correlated with clinical disabilities [Zaaraoui 2012,Paling 2013]. ^{31}P MRSI has been used by several research groups to measure the concentration of *in vivo* key energy products from the brain [Deelchand 2015].

My role in this study was setting up the ^{23}Na MRI sequence, reconstruction. The analysis pipeline was setup by our collaborator Sandro Romanzetti. I also trained the intern MD Juliette DUFOUR (ICM, Paris) to perform the analysis independently. The pipeline includes segmentation, B_1^+ correction, quantification, and partial volume correction. The study is still ongoing, but preliminary results can be found in figure 14.4.

Briefly, TSC differences were found between age-matched healthy volunteers and MS patients. The largest was found in the Caudate region, at almost ten mM. In all regions (caudate, hippocampus, inferior parietal, pallidum, parahippocampus, superior frontal, and superior temporal cortex), MS patients exhibit higher TSC values than controls. The

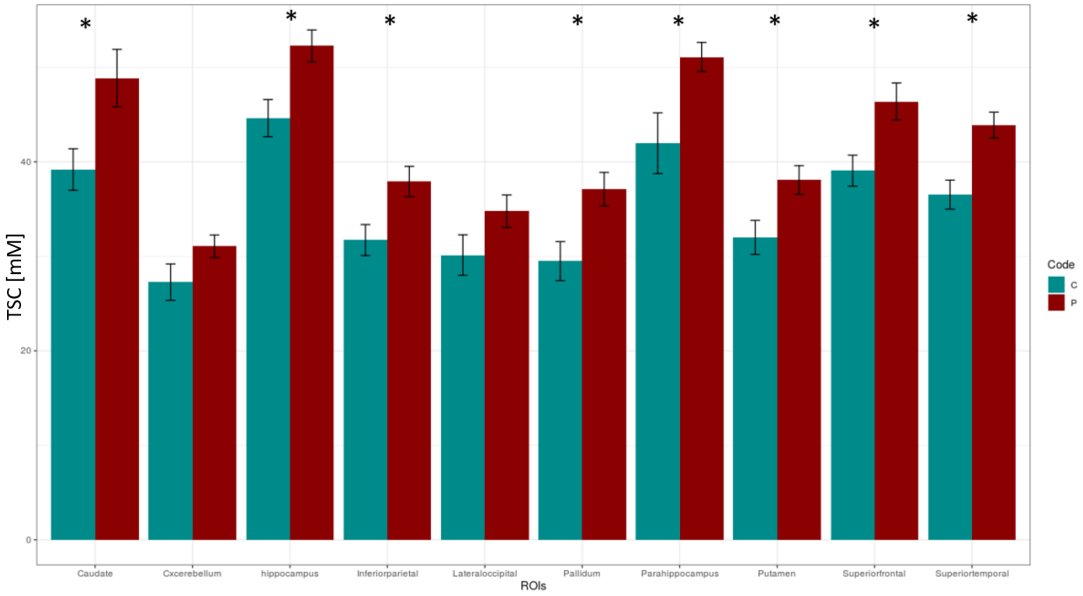

Figure 14.4 – Comparison of TSC between patients (n=17) and controls (n=11) in different ROIs in the brain. The symbol (*) indicates where $p < 0.05$ statistical difference between the two groups is found. C stands for control. P stands for patients. Courtesy from Dr Juliette DUFOUR (ICM, Paris).

smallest difference was observed in the cerebellum and was not statistically significant.

14.3 CHU Poitiers collaboration

The ENERGYSEP and Alzheimer's studies used TPI acquisition following the protocol developed by A. Coste, [Coste 2018] which takes around 30 minutes to acquire enough images to enable quantification and B_1^+ correction at 3 mm isotropic of theoretical resolution. When considering the PSF of the chosen trajectories, the actual resolution is about 6 mm. We believe that it should be possible to realize shorter ^{23}Na MRI acquisitions with similar resolution, image quality and TSC quantification accuracy using SPARKLING for a broader scope of clinical applications at 7T.

Based on my work on CS sodium MRI using SPARKLING, and rich from the experiences provided by these two first clinical studies, our team is planning to set up in collaboration with Pr. Remy Guillevin and Dr. Mathieu Naudin (Dactim Mis, LMA, UMR CNRS 7348, Poitiers, Vienne, France) a ^{23}Na MRI SPARKLING protocol at CHU Poitiers on their 7T Terra system.

Indeed, several clinical research studies are in the works to investigate MS (group size 250 patients) and other neurological diseases at CHU Poitiers using undersampled SPARKLING instead of TPI to take advantage of its better PSF and acceleration factor, enabling ^{23}Na MRI in a real clinical setting. Those projects would start in early 2023.

* * *
* *
*

General Conclusions and Perspectives

Conclusions

This thesis aimed at exploring new acquisition, reconstruction, and quantification schemes for ^{23}Na and ^{31}P MRI at 7 T and higher, accelerating the access of their respective metabolic information to better investigate neuroenergetics, in particular in patients suffering from neurodegenerative diseases.

Our ^{31}P MRI contribution consisted in developing and evaluating a novel protocol and sequence capable of measuring the absolute concentration of γ-ATP and PCr, as well as the creatine kinase flux in the whole brain simultaneously. We studied two variations of this sequence, with and without saturation bands, to mitigate the contamination from the extra-cranial PCr signal. I also developed a variation of this sequence and protocol to study the PME/PDE ratio in the context of our clinical collaboration with the research team of Pr. Guillevin at CHU Poitiers.

There are still many limitation or axis of improvement for this technique, the most obvious is its sensitivity to B_0 inhomogeneities, which could limit its applicability, especially in challenging areas such as the hippocampus or the frontal and occipital cortices.

Our ^{23}Na MRI contribution involved studying, modeling, and applying a compressed sensing method called SPARKLING for 3D ^{23}Na MRI. The goal was to speed up acquisitions. Based on our results, we believe that a fourfold reduction in acquisition time could be achieved at 7 T with a 32-channel coil with a relatively minor impact on quantification accuracy.

The limitation of this technique is that its efficiency is dependent on the SNR available. Therefore, its reproducibility and robustness could be questionable. Thus, depending on the target resolution and acquisition time, traditional (deterministic) k-space sampling schemes could still perform better. However, at ultra high magnetic fields, thanks to the ever increasing SNR, SPARKLING should certainly constitute the better strategy.

In agreement with open-source philosophy and keeping in mind the reproducibility of science, everytime it was possible, my code has been made available in open-source GitHub repository. Due to ethical/regulatory constraints, the same could not be done with the data.

Perspectives

Regarding ^{31}P MRI, a next step would be to apply this technique to examine old and young healthy volunteers to investigate the regional variations of ATP, PCr and V_{CK} in normal brain aging. One could move on by comparing multiple sclerosis patients to age-matched controls.

For ^{23}Na MRI, aside from the aforementioned optimization and application of SPARKLING to future clinical investigations at CHU Poitiers, we would like next to revisit the exciting work from Bydder et al. [Bydder 2019] using under-sampled SPARKLING ^{23}Na MRI. This would help in shortening ^{23}Na acquisitions so as to match with the time resolution of conventional fMRI and its various activation paradigms.

Another interesting perspective of both works concerns their extension to other X-nuclei MRI techniques in particular around the new 11.7T Iseult scanner of NeuroSpin. Indeed, while ^{23}Na and ^{31}P are two of the most concentrated (and endogenous) NMR-visible nuclei *in vivo*, other, even less concentrated or sensitive nuclei (^{7}Li, ^{39}K, ^{35}Cl, ^{2}H, ^{13}C, ^{17}O...) could benefit from SPARKLING optimized trajectories or frequency selective excitation thanks to respectively the additional signal [Le Ster 2022] and spectral resolution available at such high magnetic field.

The first study on healthy volunteers on the 11.7 T clinical scanner is scheduled for 2023. Hopefully, this work shall be soon applied to this unique MRI scanner.

* * *
* *
*

Appendices

Appendix A

Protocol Optimization

For tackling the difficulty of FA estimation in ^{31}P, we performed a Monte-Carlo simulation to optimize flip angles for FA mapping. For doing so, we considered the signal:

$$y = K_0 P(\alpha_i) \tag{A.1}$$

where,

$$P(\alpha_i) = \frac{\sin(\alpha_i)(1 - e^{\frac{-TR}{T_1}})}{1 - e^{\frac{-\mathrm{TR}}{T_1}} \cos(\alpha)} \tag{A.2}$$

.

Therefore, we can define the mean square error (MSE) ε as:

$$\begin{aligned} \varepsilon &= \sum (K_0 P(\alpha_i) - y_i)^2 \\ &= \sum K_0^2 P_{\alpha_i}^2 - 2 \sum K_0 P(\alpha_i) y_i + \sum y_i^2 \end{aligned} \tag{A.3}$$

Taking the partial derivate of equation A.3 in relation to α:

$$\frac{\partial \varepsilon}{\partial \alpha} = 2 \sum K_0 P^2(\alpha_i) - 2 \sum P(\alpha_i) y_i$$

Now, we can compute the minimum mean square error (MMSE) by making $\frac{\partial \varepsilon}{\partial \alpha} = 0$, which gives us:

$$K_0 = \frac{\sum P(\alpha_i) y_i}{\sum P^2(\alpha_i)}$$

With this mathematical frame, we performed simulations N=1000 for different noise levels considering a giving T_1 and TR.

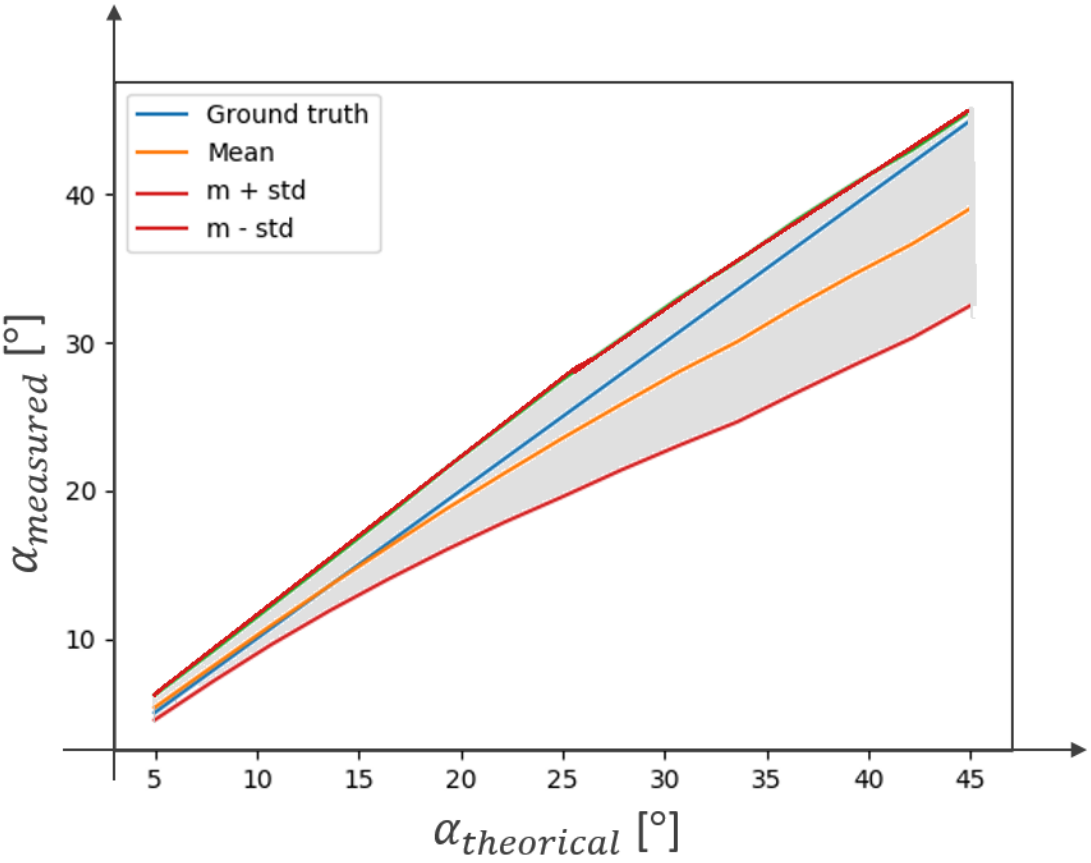

Figure A.0.1 – Monte Carlo for optimization of FA for $B_1{}^+$ mapping using VMFA. Blue curve represents the ground truth, gray area represents ranges of values between mean $\pm\sigma$. Finally, value adopted was 12° because its presents no bias and it was a compromise between low standard deviation and bias. Level of SNR was estimated from experimental *in vivo* data. Number of repetitions was 1000.

Appendix B

Reception profile

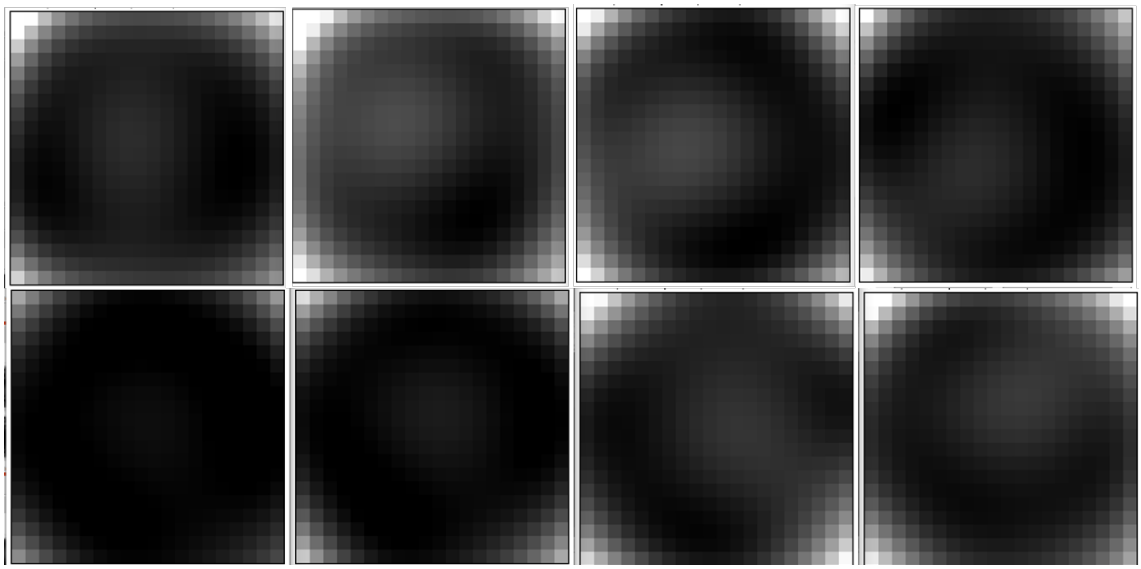

Figure B.0.1 – Sensitivity profile

Appendix C

Résumé en français

Abstract in French

Sujet : Imagerie Métabolique Cérébrale Quantitative par Résonance Magnétique Nucléaire du Sodium et du Phosphore à 7 Tesla

Les différents aspects abordés dans cette thèse sont résumés ici. On commence par introduire le contexte et l'état de l'art, pour ensuite décrire les nouvelles méthodologies et instrumentation développés dans ce travail pour s'attaquer aux défis de l'imagerie par résonance magnétique nucléaire du Phosphore et du Sodium à très hauts champs magnétiques.

C.1 Contexte et état de l'art

Au début des années 1980, l'Imagerie par Résonance Magnétique (IRM) a été introduite dans le domaine clinique. Grâce à son caractère non-invasif et à son innocuité, cette technique d'imagerie est devenue de plus en plus populaire. Le noyau d'hydrogène (ou proton) est utilisé à des fins d'imagerie en raison de son abondance dans l'eau et les graisses du corps humain et de son excellente sensibilité intrinsèque (seul le noyau de tritium possède une meilleure sensibilité RMN). Depuis, l'IRM du proton (^1H) a permis aux professionnels de santé et aux chercheurs d'exploiter les différents contrastes disponibles et de diversifier ses champs d'application : de la routine clinique aux neurosciences cognitives.

Un scanner IRM clinique est usuellement constitué d'une bobine supraconductrice d'approximativement un mètre de diamètre générant un champ magnétique statique intense (B_0). Au fil des années, les évolutions technologiques ont permis d'augmenter l'intensité du champ B_0 de moins de 0,1 Tesla (T) jusqu'à 11,7 T aujourd'hui pour l'Homme [Quettier 2020, Allard 2022] et jusqu'à 21 T pour les rongeurs [Schepkin 2010]. En IRM, le rapport signal-à-bruit (SNR) augmente avec l'intensité du champ magnétique B_0 selon une loi de puissance quadratique (β 1,96) [Le Ster 2022]. Cette augmentation du SNR disponible permet d'améliorer les résolutions temporelles, spatiales et les seuils de

sensibilité en IRM. En IRM du ^{1}H, on peut ainsi atteindre une résolution spatiale nominale aussi fine que 0,2 mm isotrope pour l'imagerie du cerveau humain [Stucht 2015].

Grâce à la démocratisation récente des scanners IRM cliniques à 7T et à la mise à disposition d'images anatomiques du cerveau à résolutions submillimétriques, les médecins peuvent d'ores et déjà diagnostiquer et suivre plus précisément les lésions épileptiques focales, qui étaient à peine visibles dans des champs magnétiques plus faibles [Feldman 2019, Opheim 2021]. Outre les données anatomiques, l'IRM du ^{1}H permet d'accéder à de nombreuses autres informations. L'IRM fonctionnelle (IRMf), par exemple, a contribué au développement des neurosciences, en permettant une meilleure compréhension, plus objective, du fonctionnement du cerveau. Comme pour la plupart des modalités d'IRM du ^{1}H, grâce à l'augmentation du champ B_0, l'IRMf a gagné en sensibilité et en spécificité [Beisteiner 2011, Worthoff 2019].

L'IRM des noyaux exotiques (autres que le proton), également désignée par le terme d'IRM des noyaux X (IRM-X), apporte un tout nouvel ensemble d'informations. L'IRM du sodium-23 (^{23}Na) et du phosphore-31 (^{31}P), en particulier, a le potentiel d'évaluer le métabolisme cellulaire et le métabolisme énergétique, car l'activité de la pompe sodium-potassium (Na^+K^+-ATPase) est essentielle au maintien de l'homéostasie cellulaire, notamment dans les neurones. Si la membrane cellulaire est endommagée ou s'il y a un déficit aigu ou chronique du métabolisme énergétique, cela peut conduire à un dysfonctionnement cellulaire et, finalement, à la mort cellulaire [Mccarthy 2015].

Plusieurs études ont démontré la pertinence de l'IRM-X pour étudier les maladies neurodégénératives telles que la maladie d'Alzheimer [Haeger 2021], la maladie de Parkinson, [Grimaldi 2021] ou la sclérose en plaques [Eisele 2019, Huhn 2019]. Cependant, l'IRM-X présente des difficultés, principalement en raison des sensibilités RMN intrinsèques relativement faibles de ces noyaux exotiques par rapport au proton et des concentrations in vivo beaucoup plus faibles de ces espèces chimiques par rapport à l'eau. Il en résulte des signaux de l'ordre de 10^3 à 10^5 fois plus faibles que celui de l'IRM du ^{1}H, selon les applications. Les chercheurs doivent trouver des compromis spécifiques en termes de résolutions spatiale et temporelle pour résoudre ce problème tout en maintenant des seuils de détection satisfaisants. Dans cette bataille, les développements continus de logiciels et de matériels sont cruciaux pour faire avancer le domaine et réaliser les promesses de l'imagerie métabolique par IRM-X.

NeuroSpin est un département du CEA (Commissariat à l'Energie Atomique et aux Energies Alternatives). C'est un centre de recherche dédié au développement de la neuroimagerie par IRM à ultra-hauts champs magnétiques. Il est équipé de trois scanners IRM précliniques (7T, 11.7T et 17T) et de trois scanners IRM cliniques à 3T, 7T et 11.7T (figure C.1.1), le dernier étant le scanner IRM le plus grand et le plus puissant au Monde (C.1.2). A ce titre, il ne pourrait y avoir de meilleur endroit que NeuroSpin pour développer l'IRM des noyaux exotiques et ses applications.

Bien qu'il existe de nombreuses méthodes de spectroscopie (SRM) ou d'imagerie RMN permettant d'étudier les potentiels biomarqueurs du métabolisme cérébrale [Cadoux-Hudson 1989, Wang 2017b], leur sensibilités, résolutions (ou couverture) spatiales et tempo-

FIGURE C.1.1 – Iseult 11.7 MRI Scanner : ©F.Rhodes - CEA

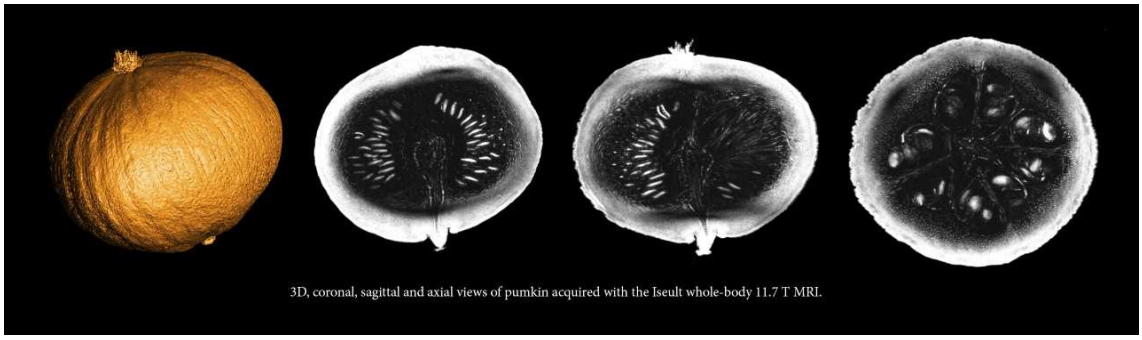

FIGURE C.1.2 – Des images de potiron. De [Allard 2022]

relles (temps d'acquisition) constituent souvent un obstacle à leur application en recherche clinique. Cette thèse de doctorat vise à réaliser des développements méthodologiques en IRM du ^{23}Na et du ^{31}P afin de faire un pas en avant vers leur plus large utilisation en recherche clinique en particulier pour l'étude des maladies neurodégénératives en accélérant leurs acquisitions sans compromettre la qualité et la quantitativité des images. Ainsi, à l'avenir, les professionnels de santé pourraient intégrer ces techniques dans leur routine clinique et, par conséquent, être en mesure d'accéder à des informations inaccessibles autrement sur le métabolisme cellulaire et de mieux comprendre les maladies neurodégénératives et leurs progressions.

C.2 Estimation de l'activité corticale de la créatine kinase par IRM dynamique du ^{31}P chez des volontaires sains à 7T

C.2.1 Introduction

Le métabolisme énergétique joue un rôle fondamental dans la fonction cérébrale et des déficits chroniques ont été associés à de nombreuses maladies neurodégénératives [Zhu 2018b]. Grace aux des approches de transfert de saturation (ST) [Zhu 2012], la spectroscopie RMN du phosphore-31 (^{31}P) in vivo permet d'estimer les activités des enzymes responsables de la synthèse et de la dégradation de l'adénosine triphosphate (ATP), unité d'énergie de la cellule eucaryote et de la Phosphocréatine (PCr), un métabolite phosphaté de hautes énergies servant de tampon énergétique. Ces enzymes sont d'une part l'ATP synthase présente dans les mitochondries en bout de la chaine de phosphorylation oxydative et d'autre part les ATPases comme la pompe Na^+K^+ auxquelles s'ajoute la créatine kinase (CK) qui convertie (de façon réversible) l'ADP (adénosine diphosphate) en ATP.

Cependant, les longs temps d'acquisition (TA) limitent son utilisation à quelques régions d'intérêt (ROI). Ici, nous proposons et évaluons un protocole d'imagerie 3D sélectif en fréquence (FS) entrelacé pour quantifier les concentrations de γ-adénosine triphosphate (γ-ATP) et de phosphocréatine (PCr) et estimer simultanément le flux réactionnel à travers la CK (V_{ck}) dans plusieurs ROI corticales dans un délai compatible avec les applications de recherche clinique.

C.2.2 Méthodes

Des volontaires sains (2M/1F, 26±3 ans) ont été scannés sur une IRM 7T corps entier (Siemens Healthineers, Erlangen, Allemagne) en utilisant une antenne volumique à réseau phasé ^{1}H/^{31}P 8Tx/8Rx [Avdievich 2011] en mode CP. Quatre images de PCr et γ-ATP ont été acquises en utilisant une séquence FS SPGR combinée à un module de ST γ-ATP C.2.1. Des références anatomiques ont également été acquises. Pour contrôler les FA effectifs appliqués pour l'excitation et la saturation, une carte B_1^+ in vivo modèle a été calculée à partir d'une cohorte dédiée (3M/3F, 29±6 ans, Fig. C.2.2). Les deux cohortes étaient disjointes.

Les images ont été corrigées des inhomogénéités de champ B_1^+ après leur recalage à l'espace modèle et leur segmentation à l'aide de nipype [Gorgolewski 2011]. Cinq ROIs corticales ont été définies à partir de l'Atlas Harvard-Oxford (Fig. 3) et les signaux γ-ATP et de PCr ont été moyennés dans chaque ROI. L'étalonnage des concentrations a été effectué à l'aide de deux références externes (PBS à 25 et 50 mM) [Soher 1996], les pondérations de relaxation T_1 et T_2^* différentielles étant pris en compte, à l'aide de données expérimentales ou de la littérature [Ren 2015]. Afin d'estimer, pour chaque volontaire et ROI, la constante cinétique k_f de la réaction CK (PCr+ADP $\Longleftrightarrow$ γ-ATP +Cr) et donc le flux V_{ck} (V_{CK}=[PCr] k_f), le processus de transfert de saturation sur les aimantations de la PCr et de γ-ATP pour les différentes valeurs effectives de saturation fut simulé en utilisant les équations de Bloch-McConnell [Lei 2003, Ren 2015]. Pour compenser le bruit

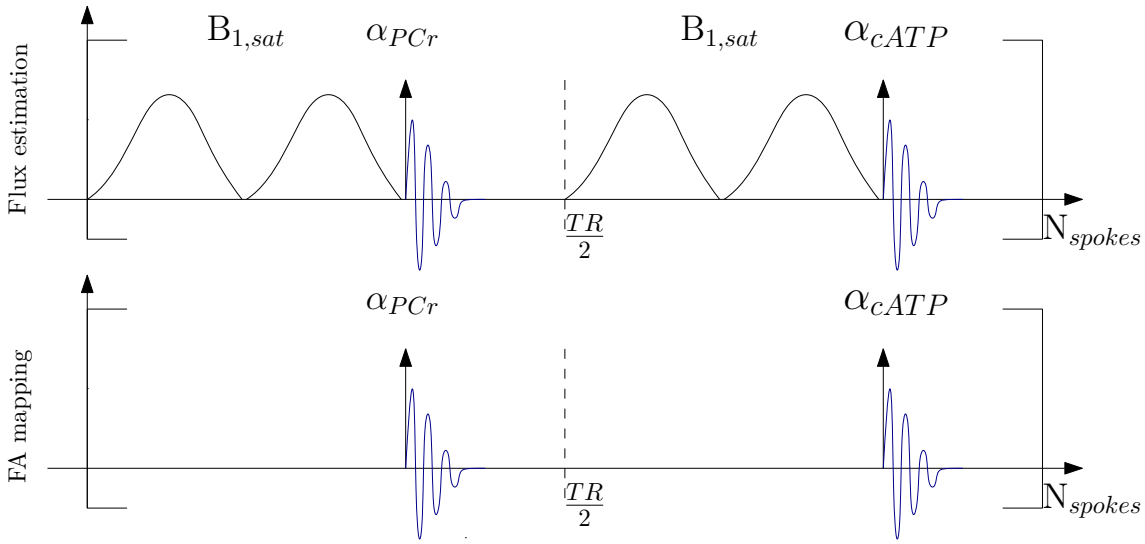

FIGURE C.2.1 – Schéma des séquences MFS. La séquence MRS de base consistait en des excitations sélectives alternées à la fréquence de l'γ-ATP (à -2,5 ppm) et du PCr (fixée à 0 ppm par convention) à chaque TR. Paramètres TE/TR=5/250 ms, nombre de rayons 3600 et TA=15 min pour chaque paire d'images. Pour l'estimation de V_{ck}, FA ciblé était égal à 25° et un module de transfert de saturation était appliqué tous les TR/2 consistant en deux impulsions gaussiennes de 40 ms sélectives pour γ-ATP, l'intensité nominale des impulsions de saturation $B_{1,sat}$ étant croissante FA=(12,24,36,48)°. Pour le protocole de cartographie du champ B_1^+, aucune saturation n'a été appliquée et seules les images de PCr ont été considérés en raison de leur SNR plus élevés.

Ricien, nous avons soustrait sa valeur moyenne non nulle, estimée à partir d'une acquisition avec un FA=0°. Ensuite, k_f a été déterminé en utilisant l'algorithme de minimisation des moindres carrés.

C.2.3 Résultats et discussion

La figure C.2.3 illustre nos résultats. Les concentrations d'ATP, de PCr, les valeurs de k_f et de V_{CK} sont toutes conformes à la littérature [Zhu 2012] pour les ROIs frontal, occipital et posterior.

Cette methode montre la possibilité d'examiner les V_{ck} et concentrations absolues. Cependant, il est sensible aux inhomogeinties de B_0. Et l'optimisation des pulses est une prochaine voie à être étudiée.

C.2.4 Conclusion

En conclusion, nous avons réussi à mettre en place un protocole d'IRM 3D dynamique du ^{31}P sensible et dont le temps d'acquisition est compatible avec les contraintes de la recherche clinique, présentant une résolution relativement élevée (résolution isotropique théorique de 12,5 mm).

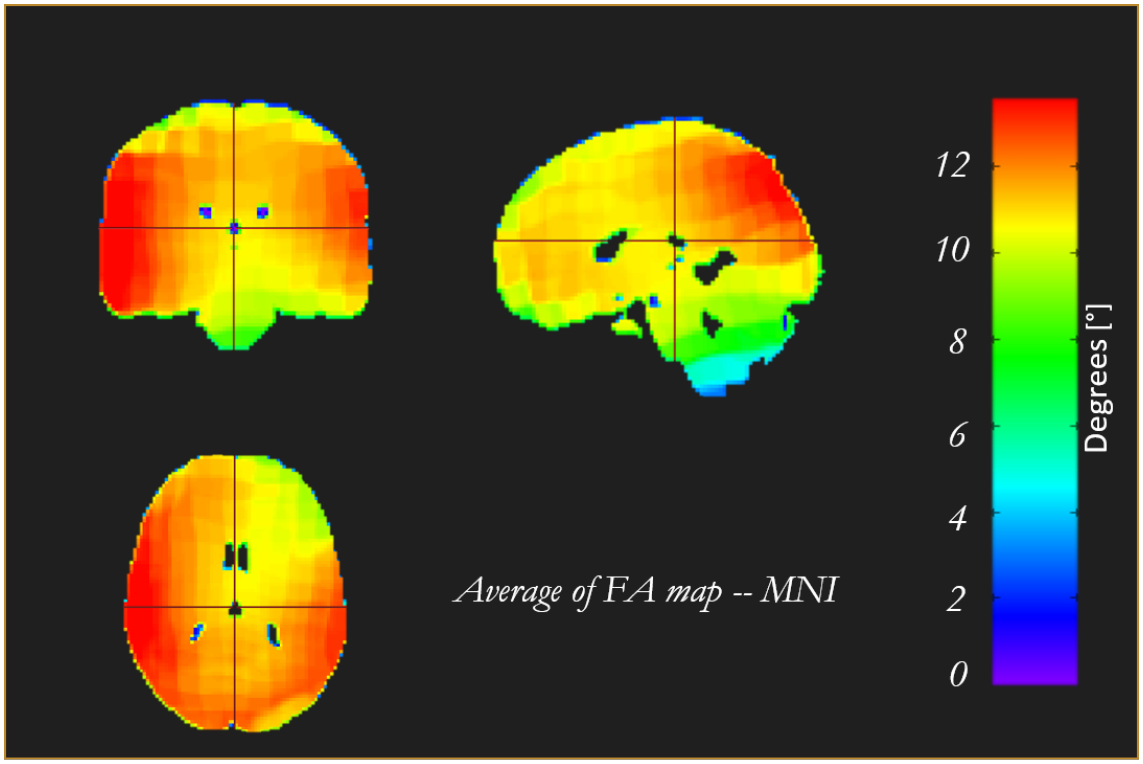

FIGURE C.2.2 – Carte FA moyenne dans l'espace MNI à travers notre cohorte de six volontaires sains. L'angle de bascule nominal de l'excitation était de 12°.

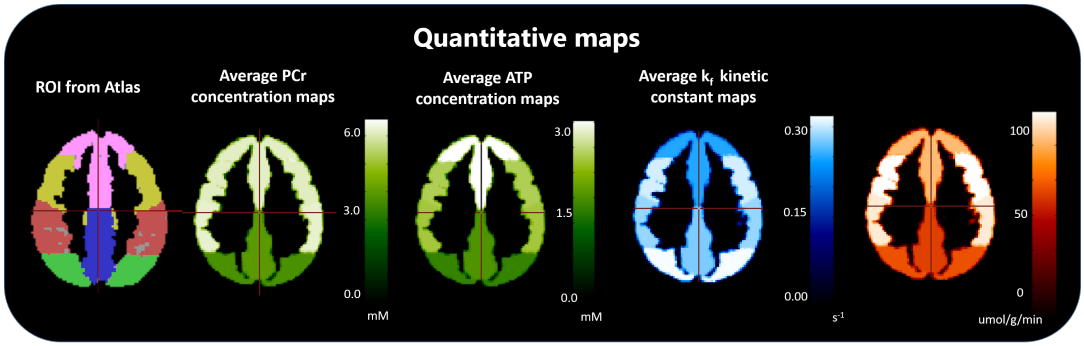

FIGURE C.2.3 – Cartes parametriques moyennes corrigées pour les inhomogénéités de champ B_1^+. Définition de nos cinq ROI corticales (à gauche) suivie des cartes des valeurs régionales moyennes pour [PCr], [ATP], k_f et V_{ck} (de gauche à droite). (rose) : cortex frontal et cingulaire antérieur ; (moutarde) : gyrus frontal et cortex operculaire ; (rouge) : cortex temporal, supramarginal et angulaire ; (bleu) : cortex précunéen et cingulaire postérieur ; (vert) : cortex occipital.

.

C.3 Évaluation de SPARKLING pour l'IRM du ^{23}Na 3D sous-échantillonnée à trés haut champ magnétique

C.3.1 Introduction

L'IRM cérébrale du sodium (^{23}Na) fournit des informations uniques sur la physiologie du tissu cérébral in vivo. Plusieurs études ont confirmé la pertinence de l'évaluation de la concentration tissulaire de sodium (TSC) dans différentes maladies neurologiques telles que la maladie d'Alzheimer [Haeger 2021] ou la sclérose en plaques [Eisele 2016]. Les études actuelles utilisent des séquences à temps d'écho ultra-court (UTE) combinées à des trajectoires déterministes non-cartésiennes de l'espace k (espace des phases ou encore espace des fréquences spatiales) telles que les trajectoires radiale, TPI (pour Twisted Projection Imaging) [Boada 1997] ou FLORET (pour Fermat Looped, Orthogonally Encoded Trajectories) [Robison 2017]. Pourtant, les temps d'acquisition (TA) restent relativement longs, même à haut champ magnétique, en raison de la sensibilité intrinsèque RMN modérée du sodium et de sa faible concentration (par rapport à l'eau). Bien que plus efficaces que les trajectoires cartésiennes, ces trajectoires non cartésiennes "standards" ne couvrent pas entièrement l'espace k car elles sont contraintes analytiquement et donc géométriquement. Par conséquent, nous supposons que l'IRM des noyaux X en général et les acquisitions d'IRM du ^{23}Na en particulier pourraient bénéficier d'approches de détection comprimée (CS) axées sur des algorithmes d'optimisation numérique [Lustig 2007] comme SPARKLING [Lazarus 2019, Chaithya G R 2022] qui aboutissent à (i) un échantillonnage global à densité variable ainsi qu'à (ii) une couverture localement uniforme de l'espace k. Comme l'a montré une étude préliminaire en IRM de susceptibilité (Susceptibility Weighted imaging - SWI), cette approche est un bon candidat pour raccourcir le TA sans dégrader la qualité de l'image en IRM du ^{23}Na. Toutefois, la détermination de scénarios d'intérêt pour l'IRM du ^{23}Na n'est pas triviale car les performances du CS dépendent du rapport signal-à-bruit disponible (SNR) et de la taille des images ([Lazarus 2019]). Dans cette étude, notre objectif est d'identifier la meilleure combinaison de sous-échantillonnage et de SNR d'entrée (dépendant de la densité de spin et de la taille du voxel) pour laquelle SPARKLING surpasse la TPI.

C.3.2 Méthodes

Tant pour nos tests in vivo qu'in vitro, des acquisitions 3D selon les trajectoires TPI et radiale à une résolution nominale isotrope de $(8mm)^3$ et un nombre de rayons (spokes en anglais) ($N_s = 4\pi(k_{max}FOV)^2$) nécessaires pour répondre au critère de Nyquist [Bernstein 2004] ont été réalisées avec 32 acquisitions (NA) moyennées afin de servir d'images de référence pour nos simulations.

Cette étude explore différents facteurs d'accélération ($AF = (\frac{N_{sradialfullnyquist})}{(N_{scurrentacquisition}}$)) et adopte un ensemble prédéterminé de paramètres : TR/TE=20/0.5 ms, FA=50°, FOV = (240 mm)^3, temps de séjour = 10 μs, 1248 points, qui ont été précédemment optimisé pour

l'acquisition d'IRM du ^{23}Na in vivo à NeuroSpin [Coste 2016].

Les données IRM ont été acquises sur des scanners Magnetom ou Terra 7T MR Siemens (Siemens Healthineers) en utilisant respectivement une cage d'oiseau $^{1}H/^{23}$Na à double résonance ou une bobine à 32 canaux (Rapid Biomedical).

Le SNR d'entrée par rayon a été mesuré à partir des données de référence. Un bruit gaussien a été ajouté aux données complexes de l'espace k de référence pour simuler les performances des stratégies SPARKLING et TPI (Fig. C.3.1) pour diverse valeurs de SNR d'entrée plus ou moins faibles. Pour chaque SNR d'entrée considéré, l'espace k a été sous-échantillonné à différents AF (2, 4, 16, 32, 64, 128).

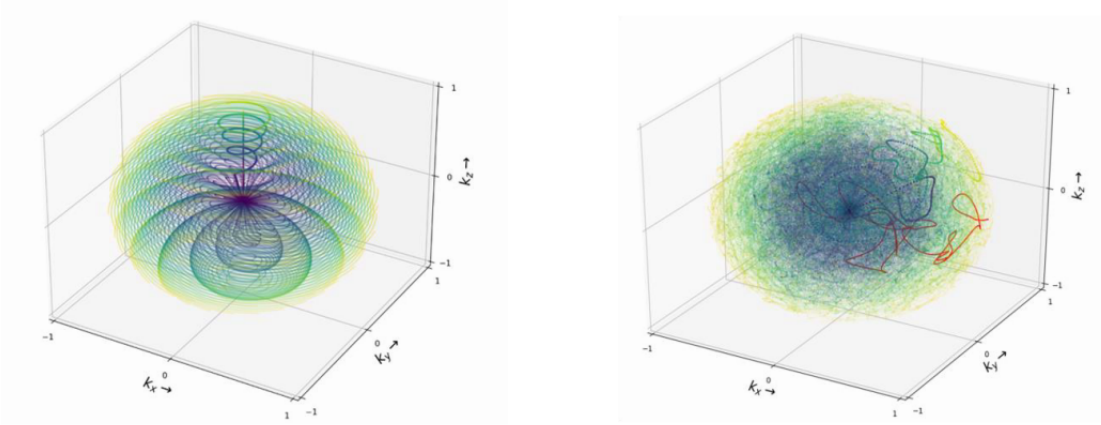

FIGURE C.3.1 – Schémas d'échantillonnage TPI et SPARKLING : A gauche, trajectoire d'illustration TPI. A droite, trajectoire centrée par SPARKLING. La couleur bleue représente le début de la trajectoire et la couleur jaune la fin. Chaque rayon, à la fois sur TPI et SPARKLING ont été acquis sur la même $T_{obs} = 12.48$ ms

Les images ont été reconstruites par CS avec compensation de densité [Pipe 2011] à l'aide de Pysap-MRI [Farrens 2020], qui traite de grands ensembles de données multicanaux 3D non-cartésiens. Pour chaque reconstruction, le paramètre de régularisation [Lazarus 2019] (lambda) a été choisi visuellement dans la plage de 10^{-7} à 10^{-20} (30 pas) pour maximiser la qualité de l'image.

La métrique choisie pour la comparaison était le score SSIM qui [Wang 2004] tente de modéliser et d'imiter le système visuel humain. Afin de valider nos simulations, des images de sodium in vitro d'un fantôme fait maison ont été acquises à l'aide des schémas d'échantillonnage TPI et SPARKLING en utilisant les mêmes paramètres d'acquisition pour une résolution de 8 mm isotrope et NA=32. Des ensembles de données distincts ont été acquis à AF=2, 4, 16, 32, 64, 128.

Une fois nos simulations validées in vitro (Fig. C.3.2), des jeux de données d'IRM du ^{23}Na in vivo ont été acquis chez un volontaire humain à AF=2, 4, 32, 64, 128. La résolution et la NA ont été réglées pour correspondre au SNR utilisé avec succès dans les simulations tout en maintenant la durée totale de l'examen en dessous de 60 minutes.

Les images ^{23}Na in vivo acquises avec l'antenne 32 canaux présentaient un meilleur SNR que l'antenne cage d'oiseau (birdcage en anglais) disponible à NeuroSpin. Les SNR d'entrée

attendus à 9,4 et 11,7T ont été extrapolés en considérant la relation quasi-quadratique observée experimentalement pour le ^{1}H [Pohmann 2016]. $\frac{SNR_{Target}}{SNR_{7T}} = \frac{B_{0,Target}}{7}^{1.65}$.

C.3.3 Résultats

La figure C.3.2 représente les scores SSIM obtenus pour chaque FA et montre un bon accord entre les simulations et les données du fantôme.

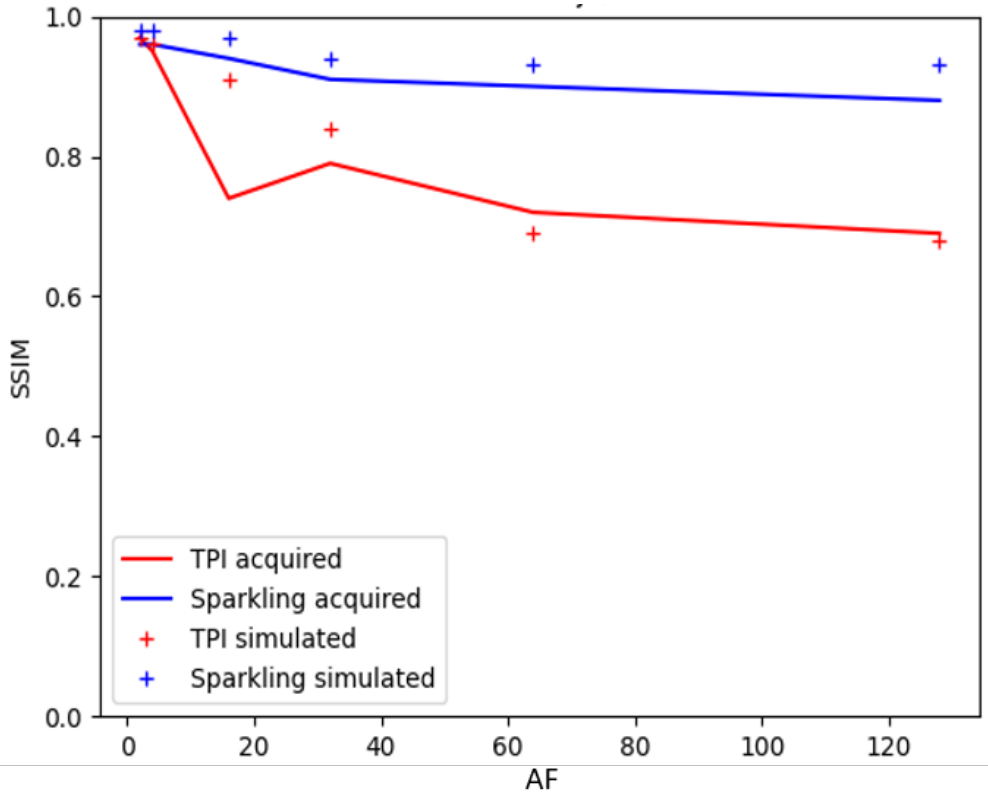

FIGURE C.3.2 – Comparaison entre les scores TPI et SPARKLING SSIM avec des facteurs d'accélération de 2, 4, 16, 32, 64 et 128 sur un fantôme, avec une résolution spatiale de 8 mm isotrope.

La figure C.3.3 illustre la comparaison entre trajectoires TPI et SPARKLING à une résolution nominale de $(4mm)^3$ réalisée sur le scanner IRM Terra 7T du CHU de Poitiers et leur antenne sodium 32 canaux démontrant des performances similaires pour l'IRM du ^{23}Na sous-échantillonnée avec TPI à AF=8 et SPARKLING à AF=32.

C.3.4 Discussion

Comme illustré par nos images, nous avons obtenu un bon accord global entre nos résultats expérimentaux et simulés. Les différences résiduelles peuvent être attribuées à de légères différences dans les fonctions d'étalement du point, en particulier en raison de la pondération T_2^*. Le SSIM est connu pour être faiblement sensible au flou. Dans les résultats in vitro et in vivo, les résultats de SPARKLING résistent à des facteurs d'accélération plus élevés par rapport aux images TPI. Cependant, une valeur minimale de SNR d'entrée doit être

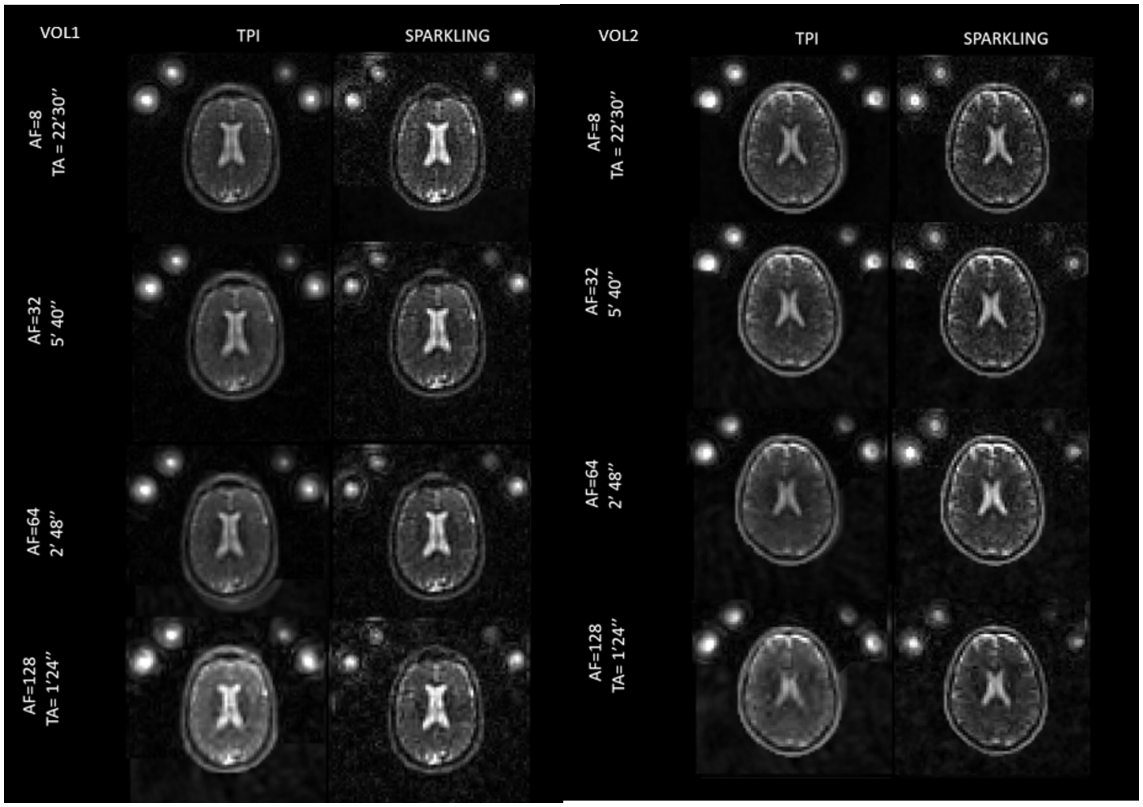

FIGURE C.3.3 – TPI et SPARKLING reconstructions pour volontaires 1 & 2 avec reconstruction iterative POGM avec compensation de densité.

atteinte pour voir cet avantage se manifester. Pour des champs magnétiques ou des antennes moins sensibles, la TPI ainsi que d'autres trajectoires déterministes non-cartésiennes de l'espace k restent pertinentes.

C.3.5 Conclusion

À 7T avec une antenne volumique à cage d'oiseau, le schéma de sous-échantillonnage SPARKLING 3D centré est plus performant que le TPI pour l'IRM du ^{23}Na à une résolution de $(8mm)^3$. Cet avantage est particulièrement prédominant pour les AF>8. Toujours à 7T mais avec une antenne plus sensible à 32 canaux, cet superiorité du SPARKLING se manifeste pour une résolution de $(4\ \text{mm})^3$, le SPARKLING accéléré 32 fois donnant des résultats similaires au TPI accéléré 8 fois. Sur la base de nos simulations extrapolant le SNR d'entrée pour l'IRM du ^{23}Na à 11,7T, nous envisageons l'acquisition d'IRM dynamique du sodium en 90 secondes avec une résolution de $(3\ \text{mm})^3$, ce qui pourrait être intéressant pour revisiter les changements de TSC pendant l'activation neuronale comme proposé par Bydder et al. [Bydder 2019].

C.4 Conclusion Générale

Le but de cette thèse était d'explorer de nouveaux schémas d'acquisitions, de reconstructions et de quantification pour l'IRM du ^{23}Na et du ^{31}P à 7 T et ainsi d'accélérer la translation

de ces méthodes d'exploration du métabolisme cérébral vers la recherche clinique. En particulier, ces mesures métaboliques pourraient constituer des biomarqueurs objectifs et quantitatifs pour l'étude des maladies neurodégénératives et de leur progression dès le stage précoce/prodromal.

Notre contribution à l'IRM du ^{31}P a consisté à développer et à évaluer un nouveau protocole et une nouvelle séquence capables de mesurer simultanément les concentrations absolus d'ATP et de PCr ainsi que le flux à travers la créatine kinase dans le cerveau entier. Nous avons étudié deux variantes de cette séquence, avec et sans bandes de saturation pour atténuer le signal musculaire de la PCr. Nous avons également développé une variation de cette séquence et un protocole pour étudier le rapport PME/PDE dans une collaboration clinique avec le CHU de Poitiers.

Cette technique présente néanmoins des limitations en particulier une sensibilité aux inhomogénéités du champ B_0 qui pourrait etre minimiser par une optimisation des impulsions radiofréquences sélectives en fréquence que ce soit pour l'excitation ou la saturation.

Notre contribution à l'IRM du ^{23}Na a consisté à étudier, modéliser et appliquer une stratégie d'acquisition 3D comprimée/parcimonieuse dénommée SPARKLING. L'objectif était d'accélérer les acquisitions ^{23}Na, ce que nous avons démontré possible, avec des facteurs d'accélération de 8 à 32 résultant en des cartes de TSC acceptables en terme de résolution effective et de quantitativité.

Cette technique est toutefois limitée dans son applicabilité par sa forte dépendance au SNR disponible. En conséquence, pour une résolution et un temps d'acquisition visés, les schémas d'échantillonnage traditionnels restent pertinents. Enfin, à l'horizon de l'aimant Iseult à 11.7T, il sera intéressant d'explorer les bénéfices de l'approche SPARKLING pour d'autres noyaux exotiques que le sodium.

* * *
* *
*

Publications

Articles in Peer-Reviewed Journals

Renata Porciuncula Baptista, Alexandre Vignaud, Chaithya G R, Guillaume Daval-Frérot, Franck Mauconduit, Mathieu Naudin, Marc Lapert, Remy Guillevan, Philippe Ciuciu, Cécile Rabrait-Lerman and Fawzi Boumezbeur, *Evaluation of 3D SPARKLING for undersampled tissue sodium concentration UTE MRI at 7T*. Magnetic Resonance in Medicine, 2022.(To be submitted).

Renata Porciuncula Baptista, Franck Mauconduit, Alexandre Vignaud, Cécile Rabrait-Lerman, Fawzi Boumezbeur. *Estimation of cortical creatine kinase activity by dynamic 31P brain MRI in healthy volunteers at 7T*. NeuroImage, 2022.(Submitted to NeuroImage, rejected, to be resubmitted).

Alexa Haeger, Michel Bottlaender, Julien Lagarde, **Renata Porciuncula Baptista**, Cécile Rabrait-Lerman, Volker Luecken, Joerg B. Schulz, Alexandre Vignaud, Marie Sarazin, Kathrin Reetz, Sandro Romanzetti and Fawzi Boumezbeur. *What can 7T sodium MRI tell us about cellular energy depletion and neurotransmission in Alzheimer's Disease?*.Alzheimer's & Dementia: The Journal of the Alzheimer's Association, vol. 17, no. 11, pp. 1843, Dec. 2021.

Abstracts at International Conferences with Reading Committee and Proceedings

Renata Porciuncula Baptista, Alexandre Vignaud, Chaithya G R, Guillaume Daval-Frérot, Franck Mauconduit, Mathieu Naudin, Marc Lapert, Remy Guillevan, Philippe Ciuciu, Cécile Rabrait-Lerman and Fawzi Boumezbeur. *Evaluation of 3D SPARKLING for undersampled Sodium UTE MRI at ultra-high magnetic field.* Proceedings of the 31th Annual Meeting of the International Society for Magnetic Resonance in Medicine, London, 2022. Digital Poster.

Renata Porciuncula Baptista, Franck Mauconduit, Alexandre Vignaud, Cécile Rabrait-Lerman, Fawzi Boumezbeur. *Estimation of cortical creatine kinase activity by dynamic 31P brain MRI in healthy volunteers at 7T.* Proceedings of the 38th Annual Meeting of the European Society for Magnetic Resonance in Medicine and Biology, Virtual, 2021. Oral.

Alexa Haeger, Michel Bottlaender, Julien Lagarde, **Renata Porciuncula Baptista**, Cécile Rabrait-Lerman, Volker Luecken, Joerg B. Schulz, Alexandre Vignaud, Marie Sarazin, Kathrin Reetz, Sandro Romanzetti and Fawzi Boumezbeur. *Ultra-High Field Sodium MRI in Alzheimer's Disease Reveals Stage-dependent Metabolic Alterations Associated with Tau-pathology.*Proceedings of the 30th Annual Meeting of the International Society for Magnetic Resonance in Medicine, Digital Poster, Dec. 2021.

* * *
* *
*

Bibliography

[Adcock 2017] B. Adcock, A. C. Hansen, C. Poon and B. Roman. *Breaking the coherence barrier: A new theory for compressed sensing.* Forum of Mathematics, Sigma, vol. 5, no. May 2022, 2017. (Cited on page 98.)

[Adlung 2021] A. Adlung, N. K. Paschke, A. K. Golla, D. Bauer, S. A. Mohamed, M. Samartzi, M. Fatar, E. Neumaier-Probst, F. G. Zöllner and L. R. Schad. *23Na MRI in ischemic stroke: Acquisition time reduction using postprocessing with convolutional neural networks.* NMR in Biomedicine, vol. 34, no. 4, pages 1–13, 2021. (Cited on page 51.)

[Albers 2005] M. J. Albers, M. D. Krieger, I. Gonzalez-Gomez, F. H. Gilles, J. G. McComb, M. D. Nelson and S. Blüml. *Proton-decoupled 31 P MRS in untreated pediatric brain tumors.* Magnetic Resonance in Medicine, vol. 53, no. 1, pages 22–29, jan 2005. (Cited on page 87.)

[Albers 2009] M. J. Albers, T. N. Butler, I. Rahwa, N. Bao, K. R. Keshari, M. G. Swanson and J. Kurhanewicz. *Evaluation of the ERETIC method as an improved quantitative reference for 1 H HR-MAS spectroscopy of prostate tissue.* Magnetic Resonance in Medicine, vol. 61, no. 3, pages 525–532, mar 2009. (Cited on pages xvi and 31.)

[Allard 2022] J. Allard, A. Amadon, G. Aubert, J. Belorgey, C. Berriaud, C. Bonnelye, N. Boulant, F. Boumezbeur, P. Brédy, P. Dietz, G. Dilasser, O. Dubois, V. Gras, I. Gonzalez Insua, Q. Guihard, V. Jannot, F-P. Juster, F. Koeber, B. Koestel, D. Le Bihan, C. Lerman, F. Leprêtre, F. Nunio, L. Quettier, H. Landes, H. Lannou, A. Massire, F. Mauconduit, F. Molinié, L. Renou, A. Roger, P. Rouffiat, W. Ruth, T. Schild, P. Sieber, M. Santin, M. Schroeder, L. Scola, A. Sinanna, V. Stepanov, M. Szmigiel, R. Touzery, P. Védrine, A. Vignaud and K. Wicklow. *Progress on the commissioning of the Iseult 11.7T whole-body MRI: first images.* In Proceedings of the 30th International Society of Magnetic Resonance in Medicine, 2022. (Cited on pages xv, xxi, 1, 3, 147, and 149.)

[Amadon 2010] A. Amadon, M.A. Cloos, N. Boulant, M. Hang, C. J. Wiggings and H. Fautz. *Validation of a very fast B1-mapping sequence for parallel transmission on*

a human brain at 7T. In Proceedings of the 18th International Society of Magnetic Resonance in Medicine, 2010. (Cited on page 57.)

[Apps 2021] A. Apps, L. Valkovič, M. Peterzan, J. Y. C. Lau, M. Hundertmark, W. Clarke, E. M. Tunnicliffe, J. Ellis, D. J. Tyler, S. Neubauer, O. J. Rider, C. T. Rodgers and A. I. Schmid. *Quantifying the effect of dobutamine stress on myocardial Pi and pH in healthy volunteers: A 31 P MRS study at 7T.* Magnetic Resonance in Medicine, vol. 85, no. 3, pages 1147–1159, mar 2021. (Cited on page 47.)

[Avdievich 2011] N. I. Avdievich. *Transceiver-Phased Arrays for Human Brain Studies at 7 T.* Applied Magnetic Resonance, vol. 41, no. 2-4, pages 483–506, dec 2011. (Cited on pages xvii, 42, 57, 61, 62, and 150.)

[Azzopardi 1989] D. Azzopardi, J. S. Wyatt, E. B. Cady, D. T. Delpy, J. Baudin, A. L. Stewart, P. L. Hope, P. A. Hamilton and E. O. R. Reynolds. *Prognosis of Newborn Infants with Hypoxic-Ischemic Brain Injury Assessed by Phosphorus Magnetic Resonance Spectroscopy.* Pediatric Research, vol. 25, no. 5, pages 445–451, may 1989. (Cited on page 47.)

[Bain 1984] A. D. Bain. *Coherence levels and coherence pathways in NMR. A simple way to design phase cycling procedures.* Journal of Magnetic Resonance (1969), vol. 56, no. 3, pages 418–427, feb 1984. (Cited on page 49.)

[Barantin 1997] L. Barantin, A. Le Pape and S. Akoka. *A new method for absolute quantitation of MRS metabolites.* Magnetic Resonance in Medicine, vol. 38, no. 2, pages 179–182, 1997. (Cited on pages 30 and 56.)

[Bardin 2022] S. Bardin, M. Lecis, D. Boido, C. Boutin, G. Baron, G. Aldini, P. Berthault, F. Boumezbeur and L. Ciobanu. *In vivo detection of carnosine and its derivatives using chemical exchange saturation transfer.* Magnetic Resonance in Medicine, vol. 88, no. 3, pages 1314–1323, sep 2022. (Cited on page 39.)

[Barrett 2018] T. Barrett, F. Riemer, M. A. McLean, J. Kaggie, F. Robb, J. S. Tropp, A. Warren, O. Bratt, N. Shah, V. J. Gnanapragasam, F. J. Gilbert, M. J. Graves and F. A. Gallagher. *Quantification of Total and Intracellular Sodium Concentration in Primary Prostate Cancer and Adjacent Normal Prostate Tissue With Magnetic Resonance Imaging.* Investigative Radiology, vol. 53, no. 8, pages 450–456, aug 2018. (Cited on page 52.)

[Barros 2018] L. F. Barros, J. P. Bolaños, G. Bonvento, A.-K. Bouzier-Sore, A. Brown, J. Hirrlinger, S. Kasparov, F. Kirchhoff, A. N. Murphy, L. Pellerin, M. B. Robinson and B. Weber. *Current technical approaches to brain energy metabolism.* Glia, vol. 66, no. 6, pages 1138–1159, jun 2018. (Cited on page 56.)

[Beatty 2005] P. Beatty, D. Nishimura and J. Pauly. *Rapid gridding reconstruction with a minimal oversampling ratio.* IEEE Transactions on Medical Imaging, vol. 24, no. 6, pages 799–808, 2005. (Cited on page 27.)

[Behl 2016a] N. G. Behl, C. Gnahm, P. Bachert, M. E. Ladd and A. M. Nagel. *Three-dimensional dictionary-learning reconstruction of 23 Na MRI data.* Magnetic Resonance in Medicine, vol. 75, no. 4, pages 1605–1616, apr 2016. (Cited on page 50.)

[Behl 2016b] N. G. Behl, C. Gnahm, P. Bachert, M. E. Ladd and A. M. Nagel. *Three-dimensional dictionary-learning reconstruction of 23 Na MRI data.* Magnetic Resonance in Medicine, vol. 75, no. 4, pages 1605–1616, apr 2016. (Cited on page 130.)

[Beisteiner 2011] R. Beisteiner, S. Robinson, M. Wurnig, M. Hilbert, K. Merksa, J. Rath, I. Höllinger, N. Klinger, C. Marosi, S. Trattnig and A. Geißler. *Clinical fMRI: Evidence for a 7T benefit over 3T.* NeuroImage, vol. 57, no. 3, pages 1015–1021, 2011. (Cited on pages 1 and 148.)

[Bernstein 2004] M. Bernstein, K. King and X. Zhou. Handbook of mri pulse sequences. Elsevier Science, 2004. (Cited on pages xvi, 8, 16, 23, 109, and 153.)

[Block 2007] K. T. Block, M. Uecker and J. Frahm. *Undersampled radial MRI with multiple coils. Iterative image reconstruction using a total variation constraint.* Magnetic Resonance in Medicine, vol. 57, no. 6, pages 1086–1098, jun 2007. (Cited on page 24.)

[Blunck 2020] Y. Blunck, S. C. Kolbe, B. A. Moffat, R. J. Ordidge, J. O. Cleary and L. A. Johnston. *Compressed sensing effects on quantitative analysis of undersampled human brain sodium MRI.* Magnetic Resonance in Medicine, vol. 83, no. 3, pages 1025–1033, 2020. (Cited on pages 109 and 130.)

[Boada 1997] F. E. Boada, J. S. Gillen, G. X. Shen, S. Y. Chang and K. R. Thulborn. *Fast three dimensional sodium imaging.* Magnetic Resonance in Medicine, vol. 37, no. 5, pages 706–715, 1997. (Cited on pages 24, 64, 88, 98, 104, and 153.)

[Bogner 2009] W. Bogner, M. Chmelik, A. I. Schmid, E. Moser, S. Trattnig and S. Gruber. *Assessment of 31P relaxation times in the human calf muscle: A comparison between 3 T and 7 T in vivo.* Magnetic Resonance in Medicine, vol. 62, no. 3, pages 574–582, 2009. (Cited on page 56.)

[Bottomley 2002] P. A. Bottomley, R. Ouwerkerk, R. F. Lee and R. G. Weiss. *Four-angle saturation transfer (FAST) method for measuring creatine kinase reaction rates in vivo.* Magnetic Resonance in Medicine, vol. 47, no. 5, pages 850–863, 2002. (Cited on pages 57 and 70.)

[Brown 1989] G. G. Brown, S. R. Levine, J. M. Gorell, J. W. Pettegrew, J. W. Gdowski, J. A. Bueri, J. A. Helpern and K. Welch. *In vivo 31P NMR profiles of Alzheimer's disease and multiple subcortical infarct dementia.* Neurology, vol. 39, no. 11, pages 1423–1423, 1989. (Cited on page 56.)

[Brown 2014] R. W. Brown, Y.-C. N. Cheng, E. M. Haacke, M. R. Thompson and R. Venkatesan. Magnetic ressonance imaging: Physical Principles ans Sequence Design. John Wiley Sons, second édition, 2014. (Cited on page 8.)

[Brown 2016] R. Brown, K. Lakshmanan, G. Madelin, L. Alon, G. Chang, D. K. Sodickson, R. R. Regatte and G. C. Wiggins. *A flexible nested sodium and proton coil array with wideband matching for knee cartilage MRI at 3T.* Magnetic Resonance in Medicine, vol. 76, no. 4, pages 1325–1334, oct 2016. (Cited on page 42.)

[Buchli 1994] R. Buchli, E. Martin, P. Boesiger and H. Rumpel. *Developmental Changes of Phosphorus Metabolite Concentrations in the Human Brain: A 31P Magnetic Resonance Spectroscopy Study In Vivo.* Pediatric Research, vol. 35, no. 4, pages 431–435, apr 1994. (Cited on pages 8 and 37.)

[Butterfield 2019] D. A. Butterfield and B. Halliwell. *Oxidative stress, dysfunctional glucose metabolism and Alzheimer disease.* Nature Reviews Neuroscience, vol. 20, no. 3, pages 148–160, 2019. (Cited on page 55.)

[Bydder 2019] M. Bydder, W. Zaaraoui, B. Ridley, M. Soubrier, M. Bertinetti, S. Confort-Gouny, L. Schad, M. Guye and J. P. Ranjeva. *Dynamic 23Na MRI - A non-invasive window on neuroglial-vascular mechanisms underlying brain function.* NeuroImage, vol. 184, no. May 2018, pages 771–780, 2019. (Cited on pages 131, 140, and 156.)

[Cadoux-Hudson 1989] T. A. Cadoux-Hudson, M. J. Blackledge and G. K. Radda. *Imaging of human brain creatine kinase activity in vivo.* The FASEB Journal, vol. 3, no. 14, pages 2660–2666, 1989. (Cited on pages 2 and 148.)

[Chaithya G R 2022] Chaithya G R, Guillaume Daval-Frérot, Aurélien Massire, Boris Mailhe, Mariappan Naddar, Alexandre Vignaud and Philippe Ciuciu. *MORE-SPARKLING: Non-Cartesian trajectories with Minimized Off-Resonance Effects.* In Proceedings of the 30th International Society of Magnetic Resonance in Medicine, 2022. (Cited on pages 24, 51, 106, 107, 108, and 153.)

[Chaithya 2022] G. Chaithya, P. Weiss, G. Daval-Frérot, A. Massire, A. Vignaud and P. Ciuciu. *Optimizing full 3D SPARKLING trajectories for high-resolution Magnetic Resonance Imaging.* IEEE Transactions on Medical Imaging, pages 1–1, 2022. (Cited on pages 51, 105, and 106.)

[Chandarana 2011] H. Chandarana, T. K. Block, A. B. Rosenkrantz, R. P. Lim, D. Kim, D. J. Mossa, J. S. Babb, B. Kiefer and V. S. Lee. *Free-Breathing Radial 3D Fat-Suppressed T1-Weighted Gradient Echo Sequence.* Investigative Radiology, vol. 46, no. 10, pages 648–653, oct 2011. (Cited on page 24.)

[Chaumeil 2009] M. M. Chaumeil, J. Valette, M. Guillermier, E. Brouillet, F. Boumezbeur, A. S. Herard, G. Bloch, P. Hantraye and V. Lebon. *Multimodal neuroimaging provides a highly consistent picture of energy metabolism, validating 31P MRS for*

measuring brain ATP synthesis. Proceedings of the National Academy of Sciences of the United States of America, vol. 106, no. 10, pages 3988–3993, 2009. (Cited on page 57.)

[Chen 1997] W. Chen, X.-H. Zhu, G. Adriany and K. U??urbil. *Increase of creatine kinase activity in the visual cortex of human brain during visual stimulation: A31p NMR magnetization transfer study.* Magnetic Resonance in Medicine, vol. 38, no. 4, pages 551–557, oct 1997. (Cited on page 48.)

[Chen 2017] L. Chen, H. Zeng, X. Xu, N. N. Yadav, S. Cai, N. A. Puts, P. B. Barker, T. Li, R. G. Weiss, P. C. van Zijl and J. Xu. *Investigation of the contribution of total creatine to the CEST Z -spectrum of brain using a knockout mouse model.* NMR in Biomedicine, vol. 30, no. 12, page e3834, dec 2017. (Cited on page 39.)

[Chen 2018] C. Chen, M. C. Stephenson, A. Peters, P. G. Morris, S. T. Francis and P. A. Gowland. *31 P magnetization transfer magnetic resonance spectroscopy: Assessing the activation induced change in cerebral ATP metabolic rates at 3 T.* Magnetic Resonance in Medicine, vol. 79, no. 1, pages 22–30, jan 2018. (Cited on pages xvii, 41, 46, 48, and 56.)

[Chen 2021] Q. Chen, N. J. Shah and W. A. Worthoff. *Compressed Sensing in Sodium Magnetic Resonance Imaging: Techniques, Applications, and Future Prospects.* Journal of Magnetic Resonance Imaging, pages 1–17, 2021. (Cited on pages xvii, 50, 51, and 98.)

[Chmelík 2008] M. Chmelík, A. I. Schmid, S. Gruber, J. Szendroedi, M. Krssák, S. Trattnig, E. Moser and M. Roden. *Three-dimensional high-resolution magnetic resonance spectroscopic imaging for absolute quantification of 31 P metabolites in human liver.* Magnetic Resonance in Medicine, vol. 60, no. 4, pages 796–802, oct 2008. (Cited on page 60.)

[Chmelík 2014] M. Chmelík, M. Považan, F. Jírru, I. J. Kukurová, M. Dezortová, M. Krššák, W. Bogner, M. Hájek, S. Trattnig and L. Valkovič. *Flip-angle mapping of 31 P coils by steady-state MR spectroscopic imaging.* Journal of Magnetic Resonance Imaging, vol. 40, no. 2, pages 391–397, aug 2014. (Cited on page 81.)

[Chu 1998] W.-J. Chu, H. P. Hetherington, R. I. Kuzniecky, T. Simor, G. F. Mason and G. A. Elgavish. *Lateralization of human temporal lobe epilepsy by 31 P NMR spectroscopic imaging at 4.1 T.* Neurology, vol. 51, no. 2, pages 472–479, aug 1998. (Cited on page 47.)

[Clarke 1999] D. Clarke and L. Sokoloff. *Basic neurochemistry: molecular, cellular and medical aspects.* Lippincott-Raven, Philadelphia, 1999. (Cited on page 36.)

[Clarke 2018] G. D. Clarke, R. J. Corbett, C. E. Mize and J. C. Chan. *Magnetic resonance in the investigation of intracellular phosphate.* Phosphate in Paediatric Health and Disease, page 127, 2018. (Cited on page 37.)

[Collins 1998] D. Collins, A. Zijdenbos, V. Kollokian, J. Sled, N. Kabani, C. Holmes and A. Evans. *Design and construction of a realistic digital brain phantom.* IEEE Transactions on Medical Imaging, vol. 17, no. 3, pages 463–468, jun 1998. (Cited on page 61.)

[Coste 2016] A. Coste, A. E. Commission, A. Vignaud, A. E. Commission, P. Ciuciu, A. E. Commission, F. Boumezbeur and A. E. Commission. *31P MR Imaging and Concentration Measurements.* no. May, pages 1–3, 2016. (Cited on pages 111 and 154.)

[Coste 2018] A. Coste, S. Romanzetti, D. Le Bihan, C. Rabrait-Lerman and F. Boumezbeur. *In vivo 31P MRI at 7 Tesla in humans using a 3D spectrally selective SSFP sequence and TPI k-space sampling.* In ISMRM, 2018. (Cited on page 138.)

[Coste 2019] A. Coste, F. Boumezbeur, A. Vignaud, G. Madelin, K. Reetz, D. Le Bihan, C. Rabrait-Lerman and S. Romanzetti. *Tissue sodium concentration and sodium T1 mapping of the human brain at 3 T using a Variable Flip Angle method.* Magnetic Resonance Imaging, vol. 58, pages 116–124, may 2019. (Cited on pages 57, 109, and 110.)

[Dale 2004] B. M. Dale, J. S. Lewin and J. L. Duerk. *Optimal design ofk-space trajectories using a multi-objective genetic algorithm.* Magnetic Resonance in Medicine, vol. 52, no. 4, pages 831–841, oct 2004. (Cited on pages 24 and 98.)

[Daly 1987] P. F. Daly, R. C. Lyon, P. J. Faustino and J. S. Cohen. *Phospholipid metabolism in cancer cells monitored by 31P NMR spectroscopy.* Journal of Biological Chemistry, vol. 262, no. 31, pages 14875–14878, nov 1987. (Cited on page 87.)

[de Graaf 2007] R. A. de Graaf. In Vivo NMR Spectroscopy: Principles and Techniques: 2nd Edition. 2007. (Cited on pages 8, 12, 13, and 17.)

[Deelchand 2015] D. K. Deelchand, T.-M. Nguyen, X.-H. Zhu, F. Mochel and P.-G. Henry. *Quantification of in vivo 31 P NMR brain spectra using LCModel.* NMR in Biomedicine, vol. 28, no. 6, pages 633–641, jun 2015. (Cited on page 136.)

[Desikan 2006] R. S. Desikan, F. Ségonne, B. Fischl, B. T. Quinn, B. C. Dickerson, D. Blacker, R. L. Buckner, A. M. Dale, R. P. Maguire, B. T. Hyman, M. S. Albert and R. J. Killiany. *An automated labeling system for subdividing the human cerebral cortex on MRI scans into gyral based regions of interest.* NeuroImage, vol. 31, no. 3, pages 968–980, jul 2006. (Cited on page 70.)

[Dhamala 2019] E. Dhamala, I. Abdelkefi, M. Nguyen, T. J. Hennessy, H. Nadeau and J. Near. *Validation of in vivo MRS measures of metabolite concentrations in the human brain.* NMR in Biomedicine, vol. 32, no. 3, page e4058, mar 2019. (Cited on page 30.)

[Dixon 1984] W. T. Dixon. *Simple proton spectroscopic imaging.* Radiology, vol. 153, no. 1, pages 189–194, oct 1984. (Cited on page 57.)

[Donoho 2006] D. L. Donoho. *Compressed sensing.* IEEE Transactions on Information Theory, vol. 52, no. 4, pages 1289–1306, 2006. (Cited on page 98.)

[Dorst 2022] J. Dorst, T. Borbath, K. Landheer, N. Avdievich and A. Henning. *Simultaneous detection of metabolite concentration changes, water BOLD signal and pH changes during visual stimulation in the human brain at 9.4T.* Journal of Cerebral Blood Flow Metabolism, vol. 42, no. 6, pages 1104–1119, jun 2022. (Cited on page 38.)

[Du 2007] F. Du, X. H. Zhu, H. Qiao, X. Zhang and W. Chen. *Efficient in vivo 31P magnetization transfer approach for noninvasively determining multiple kinetic parameters and metabolic fluxes of ATP metabolism in the human brain.* Magnetic Resonance in Medicine, vol. 57, no. 1, pages 103–114, 2007. (Cited on pages xvii and 41.)

[Du 2008] J. Du, M. Bydder, A. M. Takahashi and C. B. Chung. *Two-dimensional ultrashort echo time imaging using a spiral trajectory.* Magnetic resonance imaging, vol. 26, no. 3, pages 304–312, 2008. (Cited on page 20.)

[DUTT 1993] A. DUTT and V. ROKHLIN. *FAST FOURIER-TRANSFORMS FOR NONEQUISPACED DATA.* SIAM JOURNAL ON SCIENTIFIC COMPUTING, vol. 14, no. 6, pages 1368–1393, NOV 1993. (Cited on page 27.)

[Eisele 2016] P. Eisele, S. Konstandin, M. Griebe, K. Szabo, M. E. Wolf, A. Alonso, A. Ebert, J. Serwane, C. Rossmanith, M. G. Hennerici, L. R. Schad and A. Gass. *Heterogeneity of acute multiple sclerosis lesions on sodium (23 Na) MRI.* Multiple Sclerosis Journal, vol. 22, no. 8, pages 1040–1047, jul 2016. (Cited on pages 52 and 153.)

[Eisele 2019] P. Eisele, S. Konstandin, K. Szabo, A. Ebert, C. Roßmanith, N. Paschke, M. Kerschensteiner, M. Platten, S. O. Schoenberg, L. R. Schad and A. Gass. *Temporal evolution of acute multiple sclerosis lesions on serial sodium (23 Na) MRI.* Multiple Sclerosis and Related Disorders, vol. 29, no. September 2018, pages 48–54, 2019. (Cited on pages 1, 52, 97, and 148.)

[El-Moatassim 1992] C. El-Moatassim, J. Dornand and J.-C. Mani. *Extracellular ATP and cell signalling.* Biochimica et Biophysica Acta (BBA) - Molecular Cell Research, vol. 1134, no. 1, pages 31–45, feb 1992. (Cited on page 42.)

[Ernst 1966] R. R. Ernst and W. A. Anderson. *Application of Fourier Transform Spectroscopy to Magnetic Resonance.* Review of Scientific Instruments, vol. 37, no. 1, pages 93–102, jan 1966. (Cited on page 19.)

[Ernst 1993] T. Ernst, R. Kreis and B. Ross. *Absolute Quantitation of Water and Metabolites in the Human Brain. I. Compartments and Water.* Journal of Magnetic Resonance, Series B, vol. 102, no. 1, pages 1–8, aug 1993. (Cited on page 30.)

[Farrens 2020] S. Farrens, A. Grigis, L. El Gueddari, Z. Ramzi, C. G.R., S. Starck, B. Sarthou, H. Cherkaoui, P. Ciuciu and J.-L. Starck. *PySAP: Python Sparse Data Analysis Package for multidisciplinary image processing.* Astronomy and Computing, vol. 32, page 100402, jul 2020. (Cited on pages 109 and 154.)

[Feldman 2019] R. E. Feldman, B. N. Delman, P. S. Pawha, H. Dyvorne, J. W. Rutland, J. Yoo, M. C. Fields, L. V. Marcuse and P. Balchandani. *7T MRI in epilepsy patients with previously normal clinical MRI exams compared against healthy controls.* PLOS ONE, vol. 14, no. 3, pages 1–24, 03 2019. (Cited on pages 1 and 148.)

[Fessler 2007] J. A. Fessler. *On NUFFT-based gridding for non-Cartesian MRI.* Journal of Magnetic Resonance, vol. 188, no. 2, pages 191–195, 2007. (Cited on page 27.)

[Fessler 2020] J. A. Fessler. *Optimization Methods for Magnetic Resonance Image Reconstruction: Key Models and Optimization Algorithms.* IEEE Signal Processing Magazine, vol. 37, no. 1, pages 33–40, 2020. (Cited on page 29.)

[Fleysher 2009] L. Fleysher, N. Oesingmann, B. Stoeckel, R. I. Grossman and M. Inglese. *Sodium long-component T 2* mapping in human brain at 7 Tesla.* Magnetic Resonance in Medicine, vol. 62, no. 5, pages 1338–1341, nov 2009. (Cited on pages 102 and 103.)

[Folstein 1975] M. F. Folstein, S. E. Folstein and P. R. McHugh. *"Mini-mental state": a practical method for grading the cognitive state of patients for the clinician.* Journal of psychiatric research, vol. 12, no. 3, pages 189–198, 1975. (Cited on page 134.)

[Forlenza 2005] O. V. Forlenza, P. Wacker, P. V. Nunes, J. Yacubian, C. C. Castro, M. C. G. Otaduy and W. F. Gattaz. *Reduced phospholipid breakdown in Alzheimer's brains: a 31P spectroscopy study.* Psychopharmacology, vol. 180, no. 2, pages 359–365, jul 2005. (Cited on page 47.)

[Forsén 1963] S. Forsén and R. A. Hoffman. *Study of moderately rapid chemical exchange reactions by means of nuclear magnetic double resonance.* The Journal of Chemical Physics, vol. 39, no. 11, pages 2892–2901, 1963. (Cited on page 46.)

[Forstner 1998] M. Forstner, M. Kriechbaum, P. Laggner and T. Wallimann. *Structural Changes of Creatine Kinase upon Substrate Binding.* Biophysical Journal, vol. 75, no. 2, pages 1016–1023, aug 1998. (Cited on page 38.)

[Fountas 2000] K. N. Fountas, E. Z. Kapsalaki, S. D. Gotsis, J. Z. Kapsalakis, H. F. Smisson III, K. W. Johnston, J. S. Robinson Jr. and N. Papadakis. *In vivo Proton Magnetic Resonance Spectroscopy of Brain Tumors.* Stereotactic and Functional Neurosurgery, vol. 74, no. 2, pages 83–94, 2000. (Cited on page 38.)

[Frahm 1985] J. Frahm, K. Merboldt, W. Hänicke and A. Haase. *Stimulated echo imaging.* Journal of Magnetic Resonance (1969), vol. 64, no. 1, pages 81–93, 1985. (Cited on page 43.)

[Frahm 1987] J. Frahm, K.-D. Merboldt and W. Hänicke. *Localized proton spectroscopy using stimulated echoes.* Journal of Magnetic Resonance (1969), vol. 72, no. 3, pages 502–508, may 1987. (Cited on page 43.)

[Frazier 2005] J. A. Frazier, S. Chiu, J. L. Breeze, N. Makris, N. Lange, D. N. Kennedy, M. R. Herbert, E. K. Bent, V. K. Koneru, M. E. Dieterich, S. M. Hodge, S. L. Rauch, P. E. Grant, B. M. Cohen, L. J. Seidman, V. S. Caviness and J. Biederman. *Structural Brain Magnetic Resonance Imaging of Limbic and Thalamic Volumes in Pediatric Bipolar Disorder.* American Journal of Psychiatry, vol. 162, no. 7, pages 1256–1265, jul 2005. (Cited on page 70.)

[Gast 2018] L. V. Gast, T. Gerhalter, B. Hensel, M. Uder and A. M. Nagel. *Double quantum filtered 23 Na MRI with magic angle excitation of human skeletal muscle in the presence of B 0 and B 1 inhomogeneities.* NMR in Biomedicine, vol. 31, no. 12, page e4010, dec 2018. (Cited on page 49.)

[Gentleman 1966] W. M. Gentleman and G. Sande. *Fast Fourier Transforms: For Fun and Profit.* In Proceedings of the November 7-10, 1966, Fall Joint Computer Conference, AFIPS '66 (Fall), page 563–578, New York, NY, USA, 1966. Association for Computing Machinery. (Cited on page 26.)

[Gilles 2017] A. Gilles, A. M. Nagel and G. Madelin. *Multipulse sodium magnetic resonance imaging for multicompartment quantification: Proof-of-concept.* Scientific Reports, vol. 7, no. 1, pages 1–19, 2017. (Cited on pages xix, xxiii, 49, 102, and 103.)

[Gnahm 2014] C. Gnahm, M. Bock, P. Bachert, W. Semmler, N. G. Behl and A. M. Nagel. *Iterative 3D projection reconstruction of 23Na data with an 1H MRI constraint.* Magnetic Resonance in Medicine, vol. 71, no. 5, pages 1720–1732, 2014. (Cited on page 130.)

[Gorgolewski 2011] K. Gorgolewski, C. D. Burns, C. Madison, D. Clark, Y. O. Halchenko, M. L. Waskom and S. S. Ghosh. *Nipype: A flexible, lightweight and extensible neuroimaging data processing framework in Python.* Frontiers in Neuroinformatics, vol. 5, no. August, 2011. (Cited on page 150.)

[Gras 2017] V. Gras, A. Vignaud, A. Amadon, D. Le Bihan and N. Boulant. *Universal pulses: A new concept for calibration-free parallel transmission.* Magnetic Resonance in Medicine, vol. 77, no. 2, pages 635–643, 2017. (Cited on page 58.)

[Greenman 2011a] R. L. Greenman and H. A. Smithline. *The Feasibility of Measuring Phosphocreatine Recovery Kinetics in Muscle Using a Single-shot 31P RARE MRI Sequence.* Academic Radiology, vol. 18, no. 7, pages 917–923, jul 2011. (Cited on page 45.)

[Greenman 2011b] R. L. Greenman, X. Wang and H. A. Smithline. *Simultaneous acquisition of phosphocreatine and inorganic phosphate images for Pi:PCr ratio mapping using a RARE sequence with chemically selective interleaving.* Magnetic Resonance Imaging, vol. 29, no. 8, pages 1138–1144, oct 2011. (Cited on page 45.)

[Grimaldi 2021] S. Grimaldi, M. M. El Mendili, W. Zaaraoui, J.-P. Ranjeva, J.-P. Azulay, A. Eusebio and M. Guye. *Increased Sodium Concentration in Substantia Nigra in Early Parkinson's Disease: A Preliminary Study With Ultra-High Field (7T) MRI.* Frontiers in Neurology, vol. 12, sep 2021. (Cited on pages 1 and 148.)

[Grober 1987] E. Grober and H. Buschke. *Genuine memory deficits in dementia.* Developmental neuropsychology, vol. 3, no. 1, pages 13–36, 1987. (Cited on page 134.)

[Guillevin 2019] C. Guillevin, P. Agius, M. Naudin, G. Herpe, S. Ragot, N. Maubeuge, J. Philippe Neau and R. Guillevin. *1 H- 31 P magnetic resonance spectroscopy: effect of biotin in multiple sclerosis.* Annals of Clinical and Translational Neurology, vol. 6, no. 7, pages 1332–1337, jul 2019. (Cited on page 47.)

[Haeger 2020] A. Haeger, J.-F. Mangin, A. Vignaud, C. Poupon, A. Grigis, F. Boumezbeur, V. Frouin, J.-R. Deverre, M. Sarazin, L. Hertz-Pannier, M. Bottlaender, C. Baron, V. Berland, N. Blancho, S. Desmidt, C. Doublé, C. Ginisty, V. Joly-Testault, L. Laurier, Y. Lecomte, C. Leroy, C. Manciot, S. Marchand, G. Mediouni, X. Millot, L. Monassier, S. Roger and C. Vuillemard. *Imaging the aging brain: study design and baseline findings of the SENIOR cohort.* Alzheimer's Research Therapy, vol. 12, no. 1, page 77, dec 2020. (Cited on page 134.)

[Haeger 2021] A. Haeger, M. Bottlaender, J. Lagarde, R. Porciuncula Baptista, C. Rabrait-Lerman, V. Luecken, J. B. Schulz, A. Vignaud, M. Sarazin, K. Reetz, S. Romanzetti and F. Boumezbeur. *What can 7T sodium MRI tell us about cellular energy depletion and neurotransmission in Alzheimer's disease?* Alzheimer's and Dementia, vol. 17, no. 11, pages 1843–1854, 2021. (Cited on pages xxi, 1, 4, 97, 130, 135, 148, and 153.)

[Hahn 1950] E. L. Hahn. *Spin Echoes.* Phys. Rev., vol. 80, pages 580–594, Nov 1950. (Cited on page 10.)

[Henderson 1908] L. J. Henderson. *CONCERNING THE RELATIONSHIP BETWEEN THE STRENGTH OF ACIDS AND THEIR CAPACITY TO PRESERVE NEUTRALITY.* American Journal of Physiology-Legacy Content, vol. 21, no. 2, pages 173–179, mar 1908. (Cited on page 43.)

[Hennig 1986] J. Hennig, A. Nauerth and H. Friedburg. *RARE imaging: A fast imaging method for clinical MR.* Magnetic Resonance in Medicine, vol. 3, no. 6, pages 823–833, dec 1986. (Cited on page 11.)

[Hernandez 2020] D. Hernandez and K.-N. Kim. *A Review on the RF Coil Designs and Trends for Ultra High Field Magnetic Resonance Imaging.* Investigative Magnetic Resonance Imaging, vol. 24, no. 3, page 95, 2020. (Cited on page 9.)

[Heskamp 2021] L. Heskamp, F. Lebbink, M. J. Uden, M. C. Maas, J. A. H. R. Claassen, M. Froeling, G. J. Kemp, A. Boss and A. Heerschap. *Post-exercise intramuscular O 2 supply is tightly coupled with a higher proximal-to-distal ATP synthesis rate in human tibialis anterior.* The Journal of Physiology, vol. 599, no. 5, pages 1533–1550, mar 2021. (Cited on page 47.)

[Hetherington 2001] H. P. Hetherington, D. D. Spencer, J. T. Vaughan and J. W. Pan. *Quantitative 31P spectroscopic imaging of human brain at 4 Tesla: Assessment of gray and white matter differences of phosphocreatine and ATP.* Magnetic Resonance in Medicine, vol. 45, no. 1, pages 46–52, 2001. (Cited on pages 44 and 47.)

[Hilal 1985] S. K. Hilal, A. A. Maudsley, J. B. Ra, H. E. Simon, P. Roschmann, S. Wittekoek, Z. H. Cho and S. K. Mun. *In Vivo NMR Imaging of Sodium-23 in the Human Head.* Journal of Computer Assisted Tomography, vol. 9, no. 1, pages 1–7, jan 1985. (Cited on page 51.)

[Hiller 2013] K. Hiller and C. M. Metallo. *Profiling metabolic networks to study cancer metabolism.* Current Opinion in Biotechnology, vol. 24, no. 1, pages 60–68, feb 2013. (Cited on page 57.)

[Hoang 1998] T. Q. Hoang, S. Bluml, D. J. Dubowitz, R. Moats, O. Kopyov, D. Jacques and B. D. Ross. *Quantitative proton-decoupled 31P MRS and 1H MRS in the evaluation of Huntington's and Parkinson's diseases.* Neurology, vol. 50, no. 4, pages 1033–1040, 1998. (Cited on page 56.)

[Hoesl 2022] M. A. Hoesl, L. R. Schad and S. Rapacchi. *Volumetric 23Na Single and Triple-Quantum Imaging at 7T: 3D-CRISTINA.* Zeitschrift für Medizinische Physik, vol. 32, no. 2, pages 199–208, may 2022. (Cited on page 42.)

[Hoge 1997] R. D. Hoge, R. K. S. Kwan and G. Bruce Pike. *Density compensation functions for spiral MRI.* Magnetic Resonance in Medicine, vol. 38, no. 1, pages 117–128, jul 1997. (Cited on page 24.)

[Hoult 2000] D. I. Hoult. *The principle of reciprocity in signal strength calculations - A mathematical guide.* Concepts in Magnetic Resonance, vol. 12, no. 4, pages 173–187, 2000. (Cited on page 17.)

[Houtum 2021] Q. Q. Houtum, F. F. Mohamed Hoesein, J. J. Verhoeff, P. P. Rossum, A. A. Lindert, T. T. Velden, W. W. Kemp, D. D. Klomp and C. C. Arteaga de Castro. *Feasibility of 31 P spectroscopic imaging at 7 T in lung carcinoma patients.* NMR in Biomedicine, vol. 34, no. 5, may 2021. (Cited on page 44.)

[Hu 2000] M. T. M. Hu, S. D. Taylor-Robinson, K. R. Chaudhuri, J. D. Bell, C. Labbe, V. J. Cunningham, M. J. Koepp, A. Hammers, R. G. Morris, N. Turjanski and D. J. Brooks. *Cortical dysfunction in non-demented Parkinson's disease patients: A combined 31P-MRS and 18FDG-PET study.* Brain, vol. 123, no. 2, pages 340–352, feb 2000. (Cited on page 47.)

[Hu 2020] R. Hu, D. Kleimaier, M. Malzacher, M. A. Hoesl, N. K. Paschke and L. R. Schad. *X-nuclei imaging: Current state, technical challenges, and future directions.* Journal of Magnetic Resonance Imaging, vol. 51, no. 2, pages 355–376, 2020. (Cited on pages xvii and 50.)

[Hug 2005] F. Hug, D. Bendahan, Y. L. Fur, P. J. Cozzone and L. Grelot. *Metabolic Recovery in Professional Road Cyclists: A 31P-MRS Study.* Medicine and Science in Sports and Exercise, vol. 37, no. 5, pages 846–852, may 2005. (Cited on page 47.)

[Hug 2006] F. Hug, T. Marqueste, Y. Le Fur, P. J. Cozzone, L. Grélot and D. Bendahan. *Selective training-induced thigh muscles hypertrophy in professional road cyclists.* European Journal of Applied Physiology, vol. 97, no. 5, pages 591–597, jul 2006. (Cited on page 47.)

[Huhn 2019] K. Huhn, T. Engelhorn, R. A. Linker and A. M. Nagel. *Potential of sodium MRI as a biomarker for neurodegeneration and neuroinflammation in multiple sclerosis.* Frontiers in Neurology, vol. 10, no. FEB, pages 1–12, 2019. (Cited on pages 1, 49, and 148.)

[Husted 1994] C. A. Husted, G. B. Matson, D. A. Adams, D. S. Goodin and M. W. Weiner. *In vivo detection of myelin phospholipids in multiple sclerosis with phosphorus magnetic resonance spectroscopic imaging.* Annals of Neurology, vol. 36, no. 2, pages 239–241, aug 1994. (Cited on page 47.)

[Insko 1993] E. Insko and L. Bolinger. *Mapping of the Radiofrequency Field.* Journal of Magnetic Resonance, Series A, vol. 103, no. 1, pages 82–85, jun 1993. (Cited on page 57.)

[Insko 2002] E. K. Insko, D. B. Clayton and M. A. Elliott. *In Vivo Sodium MR Imaging of the Intervertebral Disk at 4 T.* Academic Radiology, vol. 9, no. 7, pages 800–804, jul 2002. (Cited on page 31.)

[Irarrazabal 1995] P. Irarrazabal and D. G. Nishimura. *Fast Three Dimensional Magnetic Resonance Imaging.* Magnetic Resonance in Medicine, vol. 33, no. 5, pages 656–662, may 1995. (Cited on page 24.)

[Jaccard 1986] G. Jaccard, S. Wimperis and G. Bodenhausen. *Multiple-quantum NMR spectroscopy of S =3/2 spins in isotropic phase: A new probe for multiexponential relaxation.* The Journal of Chemical Physics, vol. 85, no. 11, pages 6282–6293, dec 1986. (Cited on page 49.)

[Jackson 1991] J. Jackson, C. Meyer, D. Nishimura and A. Macovski. *Selection of a convolution function for Fourier inversion using gridding (computerised tomography application).* IEEE Transactions on Medical Imaging, vol. 10, no. 3, pages 473–478, 1991. (Cited on page 27.)

[Jona 2021] G. Jona, E. Furman-Haran and R. Schmidt. *Realistic head-shaped phantom with brain-mimicking metabolites for 7 T spectroscopy and spectroscopic imaging.* NMR in Biomedicine, vol. 34, no. 1, jan 2021. (Cited on pages 61 and 112.)

[Kan 2010] H. E. Kan, D. W. J. Klomp, C. S. Wong, V. O. Boer, A. G. Webb, P. R. Luijten and J. A. Jeneson. *In vivo31P MRS detection of an alkaline inorganic phosphate pool with short T1 in human resting skeletal muscle.* NMR in Biomedicine, vol. 23, no. 8, pages 995–1000, oct 2010. (Cited on page 44.)

[Karatzaferi 1999] C. Karatzaferi, A. De Haan, C. Offringa and A. Sargeant. *Improved high-performance liquid chromatographic assay for the determination of "high-energy" phosphates in mammalian skeletal muscle: application to a single-fibre study in man.* Journal of Chromatography B: Biomedical Sciences and Applications, vol. 730, no. 2, pages 183–191, 1999. (Cited on page 38.)

[Kemp 2000] G. Kemp. *Non-Invasive Methods for Studying Brain Energy Metabolism: What They Show and What It Means.* Developmental Neuroscience, vol. 22, no. 5-6, pages 418–428, 2000. (Cited on page 87.)

[Kemp 2007] G. J. Kemp, M. Meyerspeer and E. Moser. *Absolute quantification of phosphorus metabolite concentrations in human musclein vivo by31P MRS: a quantitative review.* NMR in Biomedicine, vol. 20, no. 6, pages 555–565, oct 2007. (Cited on page 65.)

[Khegai 2018] O. Khegai, G. Madelin, R. Brown and P. Parasoglou. *Dynamic phosphocreatine imaging with unlocalized pH assessment of the human lower leg muscle following exercise at 3T.* Magnetic Resonance in Medicine, vol. 79, no. 2, pages 974–980, feb 2018. (Cited on page 45.)

[Kogan 2014a] F. Kogan, M. Haris, C. Debrosse, A. Singh, R. P. Nanga, K. Cai, H. Hariharan and R. Reddy. *In vivo chemical exchange saturation transfer imaging of creatine (CrCEST) in skeletal muscle at 3T.* Journal of Magnetic Resonance Imaging, vol. 40, no. 3, pages 596–602, sep 2014. (Cited on page 39.)

[Kogan 2014b] F. Kogan, M. Haris, A. Singh, K. Cai, C. Debrosse, R. P. R. Nanga, H. Hariharan and R. Reddy. *Method for high-resolution imaging of creatine in vivo using chemical exchange saturation transfer.* Magnetic Resonance in Medicine, vol. 71, no. 1, pages 164–172, jan 2014. (Cited on pages 39 and 60.)

[Konstandin 2014] S. Konstandin and A. M. Nagel. *Measurement techniques for magnetic resonance imaging of fast relaxing nuclei.* Magnetic Resonance Materials in Physics, Biology and Medicine, vol. 27, no. 1, pages 5–19, feb 2014. (Cited on pages 23 and 98.)

[Kratzer 2020] F. J. Kratzer, S. Flassbeck, A. M. Nagel, N. G. Behl, B. R. Knowles, P. Bachert, M. E. Ladd and S. Schmitter. *Sodium relaxometry using 23 Na MR*

fingerprinting: A proof of concept. Magnetic Resonance in Medicine, vol. 84, no. 5, pages 2577–2591, nov 2020. (Cited on page 50.)

[Kratzer 2021] F. J. Kratzer, S. Flassbeck, S. Schmitter, T. Wilferth, A. W. Magill, B. R. Knowles, T. Platt, P. Bachert, M. E. Ladd and A. M. Nagel. *3D sodium (23 Na) magnetic resonance fingerprinting for time-efficient relaxometric mapping.* Magnetic Resonance in Medicine, vol. 86, no. 5, pages 2412–2425, nov 2021. (Cited on page 50.)

[Kreis 1993] R. Kreis, T. Ernst and B. Ross. *Absolute Quantitation of Water and Metabolites in the Human Brain. II. Metabolite Concentrations.* Journal of Magnetic Resonance, Series B, vol. 102, no. 1, pages 9–19, aug 1993. (Cited on page 30.)

[Krikken 2019] E. Krikken, W. J. Kemp, P. J. Diest, T. Dalen, H. W. Laarhoven, P. R. Luijten, D. W. Klomp and J. P. Wijnen. *Early detection of changes in phospholipid metabolism during neoadjuvant chemotherapy in breast cancer patients using phosphorus magnetic resonance spectroscopy at 7T.* NMR in Biomedicine, vol. 32, no. 6, page e4086, jun 2019. (Cited on page 47.)

[Kumar Anand 2008] C. Kumar Anand, A. Thomas Curtis and R. Kumar. *Durga: A heuristically-optimized data collection strategy for volumetric magnetic resonance imaging.* Engineering Optimization, vol. 40, no. 2, pages 117–136, feb 2008. (Cited on pages 24, 51, and 98.)

[Lachner 2019] S. Lachner, O. Zaric, M. Utzschneider, L. Minarikova, Š. Zbýň, B. Hensel, S. Trattnig, M. Uder and A. M. Nagel. *Compressed sensing reconstruction of 7 Tesla 23Na multi-channel breast data using 1H MRI constraint.* Magnetic Resonance Imaging, vol. 60, pages 145–156, jul 2019. (Cited on pages 50 and 51.)

[Lachner 2021] S. Lachner, M. Utzschneider, O. Zaric, L. Minarikova, L. Ruck, Š. Zbýň, B. Hensel, S. Trattnig, M. Uder and A. M. Nagel. *Compressed sensing and the use of phased array coils in 23Na MRI: a comparison of a SENSE-based and an individually combined multi-channel reconstruction.* Zeitschrift für Medizinische Physik, vol. 31, no. 1, pages 48–57, feb 2021. (Cited on page 51.)

[Ladd 2018] M. E. Ladd, P. Bachert, M. Meyerspeer, E. Moser, A. M. Nagel, D. G. Norris, S. Schmitter, O. Speck, S. Straub and M. Zaiss. *Pros and cons of ultra-high-field MRI/MRS for human application.* Progress in Nuclear Magnetic Resonance Spectroscopy, vol. 109, pages 1–50, 2018. (Cited on pages 8 and 98.)

[Lakshmanan 2018] K. Lakshmanan, R. Brown, G. Madelin, Y. Qian, F. Boada and G. C. Wiggins. *An eight-channel sodium/proton coil for brain MRI at 3 T.* NMR in Biomedicine, vol. 31, no. 2, page e3867, feb 2018. (Cited on page 42.)

[LAUTERBUR 1973] P. C. LAUTERBUR. *Image Formation by Induced Local Interactions: Examples Employing Nuclear Magnetic Resonance.* Nature, vol. 242, no. 5394, pages 190–191, mar 1973. (Cited on page 15.)

[Laxer 1992] K. D. Laxer, B. Hubesch, D. Sappey-Marinier and M. W. Weiner. *Increased pH and Seizure Foci Inorganic Phosphate in Temporal Demonstrated by [31P]MRS.* Epilepsia, vol. 33, no. 4, pages 618–623, jul 1992. (Cited on page 47.)

[Lazarus 2019] C. Lazarus. *Compressed Sensing in MRI : optimization-based design of k-space filling curves for accelerated MRI To cite this version : L ' echantillonnage compressif en IRM : conception optimis ee trajectoires d ' echantillonnage ´ erer pour acc el l ' IRM.* PhD thesis, 2019. (Cited on pages 24, 51, 98, 104, 130, 153, and 154.)

[Le Ster 2022] C. Le Ster, A. Grant, P. Van de Moortele, A. Monreal-Madrigal, G. Adriany, A. Vignaud, F. Mauconduit, C. Rabrait-Lerman, B. A. Poser, K. Uğurbil and N. Boulant. *Magnetic field strength dependent SNR gain at the center of a spherical phantom and up to 11 T.* Magnetic Resonance in Medicine, jul 2022. (Cited on pages 23, 140, and 147.)

[Lecis 2022] M. Lecis, S. Bardin, C. I. Ciobanu and L. Ciobanu. *PEAKIT: A Gaussian Process regression analysis tool for chemical exchange saturation transfer spectra.* Journal of Magnetic Resonance, vol. 334, page 107122, jan 2022. (Cited on page 39.)

[Lee 1988] H. J. Lee, W. S. Fillers and M. R. Iyengar. *Phosphocreatine, an intracellular high-energy compound, is found in the extracellular fluid of the seminal vesicles in mice and rats.* Proceedings of the National Academy of Sciences, vol. 85, no. 19, pages 7265–7269, oct 1988. (Cited on page 42.)

[Lei 2003] H. Lei, K. Ugurbil and W. Chen. *Measurement of unidirectional Pi to ATP flux in human visual cortex at 7 T by using in vivo 31P magnetic resonance spectroscopy.* Proceedings of the National Academy of Sciences of the United States of America, vol. 100, no. SUPPL. 2, pages 14409–14414, 2003. (Cited on pages 70 and 150.)

[Leroi 2018] L. Leroi, A. Coste, L. de Rochefort, M. D. Santin, R. Valabregue, F. Mauconduit, E. Giacomini, M. Luong, E. Chazel, J. Valette, D. Le Bihan, C. Poupon, F. Boumezbeur, C. Rabrait-Lerman and A. Vignaud. *Simultaneous multi-parametric mapping of total sodium concentration, T1, T2 and ADC at 7 T using a multi-contrast unbalanced SSFP.* Magnetic Resonance Imaging, vol. 53, pages 156–163, nov 2018. (Cited on page 108.)

[Levine 1992] S. R. Levine, J. A. Helpern, K. M. Welch, A. M. Vande Linde, K. L. Sawaya, E. E. Brown, N. M. Ramadan, R. K. Deveshwar and R. J. Ordidge. *Human focal cerebral ischemia: evaluation of brain pH and energy metabolism with P-31 NMR spectroscopy.* Radiology, vol. 185, no. 2, pages 537–544, nov 1992. (Cited on page 47.)

[Lin 2019] C. Y. Lin and J. A. Fessler. *Efficient Dynamic Parallel MRI Reconstruction for the Low-Rank Plus Sparse Model.* IEEE Transactions on Computational Imaging, vol. 5, no. 1, pages 17–26, mar 2019. (Cited on page 29.)

[Ljunggren 1983] S. Ljunggren. *A simple graphical representation of fourier-based imaging methods.* Journal of Magnetic Resonance (1969), vol. 54, no. 2, pages 338–343, sep 1983. (Cited on page 21.)

[Lu 2010] A. Lu, I. C. Atkinson, T. C. Claiborne, F. C. Damen and K. R. Thulborn. *Quantitative sodium imaging with a flexible twisted projection pulse sequence.* Magnetic Resonance in Medicine, vol. 63, no. 6, pages 1583–1593, jun 2010. (Cited on pages xvii and 51.)

[Lustig 2007] M. Lustig, D. Donoho and J. M. Pauly. *Sparse MRI: The application of compressed sensing for rapid MR imaging.* Magnetic Resonance in Medicine, vol. 58, no. 6, pages 1182–1195, 2007. (Cited on pages 24, 28, and 153.)

[Macura 1981] S. Macura, Y. Huang, D. Suter and R. Ernst. *Two-dimensional chemical exchange and cross-relaxation spectroscopy of coupled nuclear spins.* Journal of Magnetic Resonance (1969), vol. 43, no. 2, pages 259–281, may 1981. (Cited on page 46.)

[Madelin 2012] G. Madelin, G. Chang, R. Otazo, A. Jerschow and R. R. Regatte. *Compressed sensing sodium MRI of cartilage at 7T: Preliminary study.* Journal of Magnetic Resonance, vol. 214, pages 360–365, 2012. (Cited on pages xvi, 25, and 50.)

[Madelin 2015] G. Madelin, R. Kline, R. Walvick and R. R. Regatte. *A method for estimating intracellular sodium concentration and extracellular volume fraction in brain in vivo using sodium magnetic resonance imaging.* Scientific Reports, vol. 4, no. 1, page 4763, may 2015. (Cited on page 39.)

[Makris 2006] N. Makris, J. M. Goldstein, D. Kennedy, S. M. Hodge, V. S. Caviness, S. V. Faraone, M. T. Tsuang and L. J. Seidman. *Decreased volume of left and total anterior insular lobule in schizophrenia.* Schizophrenia Research, vol. 83, no. 2-3, pages 155–171, apr 2006. (Cited on page 70.)

[Marques 2021] J. P. Marques, J. Meineke, C. Milovic, B. Bilgic, K. Chan, R. Hedouin, W. Zwaag, C. Langkammer and F. Schweser. *QSM reconstruction challenge 2.0: A realistic in silico head phantom for MRI data simulation and evaluation of susceptibility mapping procedures.* Magnetic Resonance in Medicine, vol. 86, no. 1, pages 526–542, jul 2021. (Cited on page 61.)

[Martens 2003] H. Martens, M. Høy, B. M. Wise, R. Bro and P. B. Brockhoff. *Pre-whitening of data by covariance-weighted pre-processing.* Journal of Chemometrics, vol. 17, no. 3, pages 153–165, 2003. (Cited on pages 65 and 68.)

[Martin 1996] E. Martin, R. Buchli, S. Ritter, R. Schmid, R. H. Largo, E. Boltshauser, S. Fanconi, G. Duc and H. Rumpel. *Diagnostic and Prognostic Value of Cerebral 31P Magnetic Resonance Spectroscopy in Neonates with Perinatal Asphyxia.* Pediatric Research, vol. 40, no. 5, pages 749–758, nov 1996. (Cited on page 47.)

[Mason 1998] G. F. Mason, W.-J. Chu, J. T. Vaughan, S. L. Ponder, D. B. Twieg, D. Adams and H. P. Hetherington. *Evaluation of31P metabolite differences in human cerebral gray and white matter*. Magnetic Resonance in Medicine, vol. 39, no. 3, pages 346–353, mar 1998. (Cited on page 47.)

[Mazziotta 1995] J. C. Mazziotta, A. W. Toga, A. Evans, P. Fox and J. Lancaster. *A Probabilistic Atlas of the Human Brain: Theory and Rationale for Its Development*. NeuroImage, vol. 2, no. 2, pages 89–101, jun 1995. (Cited on page 69.)

[Mccarthy 2015] J. V. Mccarthy, J. V. Mccarthy and T. G. Cotter. *Cell shrinkage and apoptosis : a role for potassium and sodium ion efflux Cell shrinkage and apoptosis : a role for potassium and sodium ion efflux*. Cell Death and Differentiation (1997), vol. i, no. January 1998, pages 756–770, 2015. (Cited on pages 1, 97, and 148.)

[Mellon 2009] E. A. Mellon, D. Pilkinton, C. Clark, M. Elliott, W. Witschey, A. Borthakur and R. Reddy. *Sodium MR imaging detection of mild Alzheimer disease: preliminary study*. American Journal of Neuroradiology, vol. 30, no. 5, pages 978–984, 2009. (Cited on page 134.)

[Meyerspeer 2005] M. Meyerspeer, M. Krššák, G. J. Kemp, M. Roden and E. Moser. *Dynamic interleaved 1H/31P STEAM MRS at 3 Tesla using a pneumatic force-controlled plantar flexion exercise rig*. Magnetic Resonance Materials in Physics, Biology and Medicine, vol. 18, no. 5, pages 257–262, oct 2005. (Cited on page 43.)

[Meyerspeer 2011] M. Meyerspeer, T. Scheenen, A. I. Schmid, T. Mandl, E. Unger and E. Moser. *Semi-LASER localized dynamic 31 P magnetic resonance spectroscopy in exercising muscle at ultra-high magnetic field*. Magnetic Resonance in Medicine, vol. 65, no. 5, pages 1207–1215, may 2011. (Cited on page 43.)

[Mir 2004] R. Mir, A. Guesalaga, J. Spiniak, M. Guarini and P. Irarrazaval. *Fast three-dimensionalk-space trajectory design using missile guidance ideas*. Magnetic Resonance in Medicine, vol. 52, no. 2, pages 329–336, aug 2004. (Cited on pages 24 and 98.)

[Mohamed 2021] S. A. Mohamed, K. Herrmann, A. Adlung, N. Paschke, L. Hausner, L. FrÖlich, L. Schad, C. Groden and H. U. Kerl. *Evaluation of Sodium (23Na) MR-imaging as a Biomarker and Predictor for Neurodegenerative Changes in Patients With Alzheimer's Disease*. in vivo, vol. 35, no. 1, pages 429–435, 2021. (Cited on page 134.)

[Moonen 1989] C. T. W. Moonen, M. V. Kienlin, P. C. M. Van Zijl, J. Cohen, J. Gillen, P. Daly and G. Wolf. *Comparison of single-shot localization methods (steam and press) for In vivo proton NMR spectroscopy*. NMR in Biomedicine, vol. 2, no. 5-6, pages 201–208, dec 1989. (Cited on page 43.)

[Müller-Gärtner 1992] H. W. Müller-Gärtner, J. M. Links, J. L. Prince, R. N. Bryan, E. McVeigh, J. P. Leal, C. Davatzikos and J. J. Frost. *Measurement of Radiotracer Concentration in Brain Gray Matter Using Positron Emission Tomography: MRI-Based Correction for Partial Volume Effects.* Journal of Cerebral Blood Flow and Metabolism, vol. 12, no. 4, pages 571–583, jul 1992. (Cited on page 32.)

[Murphy-Boesch 1993] J. Murphy-Boesch, R. Stoyanova, R. Srinivasan, T. Willard, D. Vigneron, S. Nelson, J. S. Taylor and T. R. Brown. *Proton-decoupled31P chemical shift imaging of the human brain in normal volunteers.* NMR in Biomedicine, vol. 6, no. 3, pages 173–180, may 1993. (Cited on page 44.)

[Nagel 2009] A. M. Nagel, F. B. Laun, M. A. Weber, C. Matthies, W. Semmler and L. R. Schad. *Sodium MRI using a density-adapted 3D radial acquisition technique.* Magnetic Resonance in Medicine, vol. 62, no. 6, pages 1565–1573, 2009. (Cited on pages 24 and 98.)

[Nasreddine 2005] Z. S. Nasreddine, N. A. Phillips, V. Bédirian, S. Charbonneau, V. Whitehead, I. Collin, J. L. Cummings and H. Chertkow. *The Montreal Cognitive Assessment, MoCA: a brief screening tool for mild cognitive impairment.* Journal of the American Geriatrics Society, vol. 53, no. 4, pages 695–699, 2005. (Cited on page 134.)

[Niesporek 2015] S. C. Niesporek, S. H. Hoffmann, M. C. Berger, N. Benkhedah, A. Kujawa, P. Bachert and A. M. Nagel. *Partial volume correction for in vivo 23 Na-MRI data of the human brain.* NeuroImage, vol. 112, pages 353–363, may 2015. (Cited on page 32.)

[Ontaneda 2015] D. Ontaneda, R. J. Fox and J. Chataway. *Clinical trials in progressive multiple sclerosis: lessons learned and future perspectives.* The Lancet Neurology, vol. 14, no. 2, pages 208–223, feb 2015. (Cited on page 135.)

[Opheim 2021] G. Opheim, A. van der Kolk, K. M. Bloch, A. J. Colon, K. A. Davis, T. R. Henry, J. F. Jansen, S. E. Jones, J. W. Pan, K. Rössler, J. M. Stein, M. C. Strandberg, S. Trattnig, P.-F. Van de Moortele, M. I. Vargas, I. Wang, F. Bartolomei, N. Bernasconi, A. Bernasconi, B. Bernhardt, I. Björkman-Burtscher, M. Cosottini, S. R. Das, L. Hertz-Pannier, S. Inati, M. T. Jurkiewicz, A. R. Khan, S. Liang, R. E. Ma, S. Mukundan, H. Pardoe, L. H. Pinborg, J. R. Polimeni, J.-P. Ranjeva, E. Steijvers, S. Stufflebeam, T. J. Veersema, A. Vignaud, N. Voets, S. Vulliemoz, C. J. Wiggins, R. Xue, R. Guerrini and M. Guye. *7T Epilepsy Task Force Consensus Recommendations on the Use of 7T MRI in Clinical Practice.* Neurology, vol. 96, no. 7, pages 327–341, 2021. (Cited on pages 1 and 148.)

[Ordidge 1986] R. Ordidge, A. Connelly and J. Lohman. *Image-selected in Vivo spectroscopy (ISIS). A new technique for spatially selective nmr spectroscopy.* Journal of Magnetic Resonance (1969), vol. 66, no. 2, pages 283–294, 1986. (Cited on page 43.)

[Ouwerkerk 2003] R. Ouwerkerk, K. B. Bleich, J. S. Gillen, M. G. Pomper and P. A. Bottomley. *Tissue Sodium Concentration in Human Brain Tumors as Measured with 23 Na MR Imaging.* Radiology, vol. 227, no. 2, pages 529–537, may 2003. (Cited on page 52.)

[Pabst 2001] T. Pabst, J. Sandstede, M. Beer, W. Kenn, A. Greiser, M. von Kienlin, S. Neubauer and D. Hahn. *Optimization of ECG-triggered 3D23Na MRI of the human heart.* Magnetic Resonance in Medicine, vol. 45, no. 1, pages 164–166, jan 2001. (Cited on page 31.)

[Paling 2013] D. Paling, B. S. Solanky, F. Riemer, D. J. Tozer, C. A. M. Wheeler-Kingshott, R. Kapoor, X. Golay and D. H. Miller. *Sodium accumulation is associated with disability and a progressive course in multiple sclerosis.* Brain, vol. 136, no. 7, pages 2305–2317, jul 2013. (Cited on page 136.)

[Parasoglou 2012] P. Parasoglou, L. Feng, D. Xia, R. Otazo and R. R. Regatte. *Rapid 3D-imaging of phosphocreatine recovery kinetics in the human lower leg muscles with compressed sensing.* Magnetic Resonance in Medicine, vol. 68, no. 6, pages 1738–1746, dec 2012. (Cited on page 45.)

[Parasoglou 2013] P. Parasoglou, D. Xia and R. R. Regatte. *Spectrally selective 3D TSE imaging of phosphocreatine in the human calf muscle at 3 T.* Magnetic Resonance in Medicine, vol. 69, no. 3, pages 812–817, mar 2013. (Cited on page 45.)

[Paul A. Bottomley 1984] Paul A. Bottomley. *Selective volume method for performing localized NMR spectroscopy*, 1984. (Cited on page 43.)

[Pauly 1991a] J. Pauly, P. Le Roux, D. Nishimura and A. Macovski. *Parameter relations for the Shinnar-Le Roux selective excitation pulse design algorithm (NMR imaging).* IEEE Transactions on Medical Imaging, vol. 10, no. 1, pages 53–65, mar 1991. (Cited on page 13.)

[Pauly 1991b] J. Pauly, P. Le Roux, D. Nishimura and A. Macovski. *Parameter relations for the Shinnar-Le Roux selective excitation pulse design algorithm (NMR imaging).* IEEE Transactions on Medical Imaging, vol. 10, no. 1, pages 53–65, 1991. (Cited on page 15.)

[Pedregosa 2011] F. Pedregosa, G. Varaquaux, A. Gramfort, V. Michel, B. Thirion, O. Grisel, M. Blondel, P. Prettenhofer, R. Weiss, V. Dubourg, J. Vanderplas, A. Passos, D. Cournapeau, M. Brucher, M. Perrot and E. Duchesnay. *Scikit-learn: Machine Learning in Python.* Journal ofMachine Learning Research, vol. 12, no. 9, pages 2825–2830, 2011. (Cited on page 68.)

[Penny 2011] W. D. Penny, K. J. Friston, J. T. Ashburner, S. J. Kiebel and T. E. Nichols. Statistical parametric mapping: the analysis of functional brain images. Elsevier, 2011. (Cited on page 102.)

[Pipe 1999] J. G. Pipe and P. Menon. *Sampling density compensation in MRI: Rationale and an iterative numerical solution.* Magnetic Resonance in Medicine, vol. 41, no. 1, pages 179–186, 1999. (Cited on pages 27 and 109.)

[Pipe 2011] J. G. Pipe, N. R. Zwart, E. A. Aboussouan, R. K. Robison, A. Devaraj and K. O. Johnson. *A new design and rationale for 3D orthogonally oversampled k-space trajectories.* Magnetic Resonance in Medicine, vol. 66, no. 5, pages 1303–1311, 2011. (Cited on pages 107 and 154.)

[Pohmann 2016] R. Pohmann, O. Speck and K. Scheffler. *Signal-to-noise ratio and MR tissue parameters in human brain imaging at 3, 7, and 9.4 tesla using current receive coil arrays.* Magnetic Resonance in Medicine, vol. 75, no. 2, pages 801–809, feb 2016. (Cited on pages 1 and 155.)

[Polak 2022] P. Polak, R. F. Schulte and M. D. Noseworthy. *An approach to evaluation of the point-spread function for 23 Na magnetic resonance imaging.* NMR in Biomedicine, vol. 35, no. 2, feb 2022. (Cited on page 108.)

[Porciuncula Baptista 2021] R. Porciuncula Baptista, F. Mauconduit, A. Vignaud, C. Lerman-Rabrait and F. Boumezbeur. *Estimation of cortical creatine kinase activity by dynamic 31P brain MRI in healthy volunteers at 7T.* In Proceedings of the 38th European Society of Magnetic Resonance in Medicine, 2021. (Cited on page 55.)

[Porciuncula Baptista 2022] R. Porciuncula Baptista, A. Vignaud, Chaithya G R, G. Daval-Frérot, F. Mauconduit, M. Naudin, M. Lapert, R. Guillevan, P. Ciuciu, C. Lerman-Rabrait and F. Boumezbeur. *Evaluation of 3D SPARKLING for undersampled Sodium UTE MRI at ultra-high magnetic field.* In Proceedings of the 30th International Society of Magnetic Resonance in Medicine, 2022. (Cited on page 97.)

[Posse 1994] S. Posse, C. DeCarli and D. Le Bihan. *Three-dimensional echo-planar MR spectroscopic imaging at short echo times in the human brain.* Radiology, vol. 192, no. 3, pages 733–738, sep 1994. (Cited on page 44.)

[Punga 2014] M. V. Punga, S. Moldovanu and L. Moraru. *Structural similarity analysis for brain MR image quality assessment.* pages 137–143, 2014. (Cited on page 129.)

[Quettier 2020] L. Quettier, G. Aubert, J. Belorgey, C. Berriaud, P. Bredy, G. Dilasser, O. Dubois, G. Gilgrass, Q. Guihard, V. Jannot, F.-P. Juster, H. Lannou, F. Molinie, F. Nunio, A. Roger, T. Schild, L. Scola, A. Sinanna, V. Stepanov and P. Vedrine. *Commissioning Completion of the Iseult Whole Body 11.7 T MRI System.* IEEE Transactions on Applied Superconductivity, vol. 30, no. 4, pages 1–5, jun 2020. (Cited on pages 1 and 147.)

[Rabi 1938] I. I. Rabi. *A new method of measuring intensities of magnetization.* Physica, vol. 6, no. 2, pages 137–144, 1938. (Cited on page 8.)

[Ramos-Llorden 2018] G. Ramos-Llorden, G. Vegas-Sanchez-Ferrero, M. Bjork, F. Vanhevel, P. M. Parizel, R. San Jose Estepar, A. J. den Dekker and J. Sijbers. *NOVI-FAST: A Fast Algorithm for Accurate and Precise VFA MRI.* IEEE Transactions on Medical Imaging, vol. 37, no. 11, pages 2414–2427, nov 2018. (Cited on pages 89 and 90.)

[Rango 2006] M. Rango, C. Bonifati and N. Bresolin. *Parkinson's Disease and Brain Mitochondrial Dysfunction: A Functional Phosphorus Magnetic Resonance Spectroscopy Study.* Journal of Cerebral Blood Flow Metabolism, vol. 26, no. 2, pages 283–290, feb 2006. (Cited on page 47.)

[Reetz 2012] K. Reetz, S. Romanzetti, I. Dogan, C. Saß, C. J. Werner, J. Schiefer, J. B. Schulz and N. J. Shah. *Increased brain tissue sodium concentration in Huntington's Disease - A sodium imaging study at 4T.* NeuroImage, vol. 63, no. 1, pages 517–524, 2012. (Cited on page 97.)

[Ren 2015] J. Ren, A. D. Sherry and C. R. Malloy. *31P-MRS of healthy human brain: ATP synthesis, metabolite concentrations, pH, and T1 relaxation times.* NMR in Biomedicine, vol. 28, no. 11, pages 1455–1462, 2015. (Cited on pages xxiii, 48, 56, 57, 70, 82, 93, and 150.)

[Renieblas 2017] G. P. Renieblas, A. T. Nogués, A. M. González, N. Gómez-Leon and E. G. del Castillo. *Structural similarity index family for image quality assessment in radiological images.* Journal of Medical Imaging, vol. 4, no. 3, page 035501, jul 2017. (Cited on page 29.)

[Ridley 2018] B. Ridley, A. M. Nagel, M. Bydder, A. Maarouf, J. P. Stellmann, S. Gherib, J. Verneuil, P. Viout, M. Guye, J. P. Ranjeva and W. Zaaraoui. *Distribution of brain sodium long and short relaxation times and concentrations: a multi-echo ultra-high field 23Na MRI study.* Scientific Reports, vol. 8, no. 1, pages 1–12, 2018. (Cited on page 98.)

[Rietzler 2021] A. Rietzler, R. Steiger, S. Mangesius, L.-M. Walchhofer, R. M. Gothe, M. Schocke, E. R. Gizewski and A. E. Grams. *Energy metabolism measured by 31P magnetic resonance spectroscopy in the healthy human brain.* Journal of Neuroradiology, dec 2021. (Cited on page 47.)

[Rijpma 2018] A. Rijpma, M. van der Graaf, O. Meulenbroek, M. G. Olde Rikkert and A. Heerschap. *Altered brain high-energy phosphate metabolism in mild Alzheimer's disease: A 3-dimensional 31P MR spectroscopic imaging study.* NeuroImage: Clinical, vol. 18, pages 254–261, 2018. (Cited on page 47.)

[Rink 2015] K. Rink, M. C. Berger, A. Korzowski, M. Breithaupt, A. Biller, P. Bachert and A. M. Nagel. *Nuclear-Overhauser-enhanced MR imaging of 31P-containing metabolites: multipoint-Dixon vs. frequency-selective excitation.* Magnetic Resonance Imaging, vol. 33, no. 10, pages 1281–1289, dec 2015. (Cited on page 45.)

[Robison 2017] R. K. Robison, A. G. Anderson and J. G. Pipe. *Three-dimensional ultrashort echo-time imaging using a FLORET trajectory.* Magnetic Resonance in Medicine, vol. 78, no. 3, pages 1038–1049, sep 2017. (Cited on pages 24, 98, and 153.)

[Robson 2003] M. D. Robson, P. D. Gatehouse, M. Bydder and G. M. Bydder. *Magnetic resonance: an introduction to ultrashort TE (UTE) imaging.* Journal of computer assisted tomography, vol. 27, no. 6, pages 825–846, 2003. (Cited on page 20.)

[Romanzetti 2014] S. Romanzetti, C. C. Mirkes, D. P. Fiege, A. Celik, J. Felder and N. J. Shah. *Mapping tissue sodium concentration in the human brain: A comparison of MR sequences at 9.4 Tesla.* NeuroImage, vol. 96, pages 44–53, aug 2014. (Cited on pages 31 and 108.)

[Rudin 1992] L. I. Rudin, S. Osher and E. Fatemi. *Nonlinear total variation based noise removal algorithms.* Physica D: Nonlinear Phenomena, vol. 60, no. 1-4, pages 259–268, nov 1992. (Cited on page 29.)

[Ruhm 2020] L. Ruhm, J. Dorst, N. Avdievich and A. Henning. *Phosphorus metabolic images of the human brain at 9.4 T using Chemical Shift Imaging: Investigation of differences in grey and white matter tissue.* Proceedings of the 28th Annual Meeting of ISMRM, page 0478, 2020. (Cited on page 56.)

[Ruhm 2021] L. Ruhm, J. Dorst, N. Avdievitch, A. M. Wright and A. Henning. *3D 31 P MRSI of the human brain at 9 . 4 Tesla : Optimization and quantitative analysis of metabolic images.* no. May, pages 1–16, 2021. (Cited on page 47.)

[Saint-Jalmes 2014] H. Saint-Jalmes, P.-A. Eliat, J. Bezy-Wendling, A. Bordelois and G. Gambarota. *ViP MRI: virtual phantom magnetic resonance imaging.* Magnetic Resonance Materials in Physics, Biology and Medicine, vol. 27, no. 5, pages 419–424, oct 2014. (Cited on page 30.)

[Salvati 2016] R. Salvati, E. Hitti, J.-J. Bellanger, H. Saint-Jalmes and G. Gambarota. *Fat ViP MRI: Virtual Phantom Magnetic Resonance Imaging of water–fat systems.* Magnetic Resonance Imaging, vol. 34, no. 5, pages 617–623, jun 2016. (Cited on page 30.)

[Sarty 2001] G. E. Sarty, R. Bennett and R. W. Cox. *Direct reconstruction of non-Cartesiank-space data using a nonuniform fast Fourier transform.* Magnetic Resonance in Medicine, vol. 45, no. 5, pages 908–915, may 2001. (Cited on page 27.)

[Scheenen 2008] T. W. J. Scheenen, A. Heerschap and D. W. J. Klomp. *Towards 1H-MRSI of the human brain at 7T with slice-selective adiabatic refocusing pulses.* Magnetic

Resonance Materials in Physics, Biology and Medicine, vol. 21, no. 1-2, pages 95–101, mar 2008. (Cited on pages xvii and 44.)

[Schepkin 2010] V. D. Schepkin, W. W. Brey, P. L. Gor'kov and S. C. Grant. *Initial in vivo rodent sodium and proton MR imaging at 21.1 T.* Magnetic Resonance Imaging, vol. 28, no. 3, pages 400–407, apr 2010. (Cited on pages 1 and 147.)

[Schmid 2016] A. I. Schmid, M. Meyerspeer, S. D. Robinson, S. Goluch, M. Wolzt, G. B. Fiedler, W. Bogner, E. Laistler, M. Kršňák, E. Moser, S. Trattnig and L. Valkovič. *Dynamic PCr and pH imaging of human calf muscles during exercise and recovery using 31 P gradient-Echo MRI at 7 Tesla.* Magnetic Resonance in Medicine, vol. 75, no. 6, pages 2324–2331, jun 2016. (Cited on pages 45 and 56.)

[Schomberg 1995] H. Schomberg and J. Timmer. *The gridding method for image reconstruction by Fourier transformation.* IEEE Transactions on Medical Imaging, vol. 14, no. 3, pages 596–607, 1995. (Cited on page 27.)

[Schulz 2007] U. G. Schulz, A. M. Blamire, R. G. Corkill, P. Davies, P. Styles and P. M. Rothwell. *Association between cortical metabolite levels and clinical manifestations of migrainous aura: an MR-spectroscopy study.* Brain, vol. 130, no. 12, pages 3102–3110, may 2007. (Cited on page 47.)

[Schulz 2009] U. G. Schulz, A. M. Blamire, P. Davies, P. Styles and P. M. Rothwell. *Normal Cortical Energy Metabolism in Migrainous Stroke.* Stroke, vol. 40, no. 12, pages 3740–3744, dec 2009. (Cited on page 47.)

[Shannon 1949] C. Shannon. *Communication in the Presence of Noise.* Proceedings of the IRE, vol. 37, no. 1, pages 10–21, 1949. (Cited on page 21.)

[Shi 2015] X.-F. Shi, P. J. Carlson, Y.-H. Sung, K. K. Fiedler, L. N. Forrest, T. L. Hellem, R. S. Huber, S.-E. Kim, C. Zuo, E.-K. Jeong, P. F. Renshaw and D. G. Kondo. *Decreased brain PME/PDE ratio in bipolar disorder: a preliminary 31 P magnetic resonance spectroscopy study.* Bipolar Disorders, vol. 17, no. 7, pages 743–752, nov 2015. (Cited on pages 47 and 93.)

[Shin 2006] M.-S. Shin, S.-Y. Park, S.-R. Park, S.-H. Seol and J. S. Kwon. *Clinical and empirical applications of the Rey–Osterrieth complex figure test.* Nature protocols, vol. 1, no. 2, pages 892–899, 2006. (Cited on page 135.)

[Smith 2004] S. A. Smith, S. J. Montain, G. P. Zientara and R. A. Fielding. *Use of phosphocreatine kinetics to determine the influence of creatine on muscle mitochondrial respiration: an in vivo 31 P-MRS study of oral creatine ingestion.* Journal of Applied Physiology, vol. 96, no. 6, pages 2288–2292, jun 2004. (Cited on page 38.)

[Snow 2001] R. J. Snow and R. M. Murphy. *Creatine and the creatine transporter: a review.* Molecular and cellular biochemistry, vol. 224, no. 1-2, pages 169–81, aug 2001. (Cited on page 38.)

[Soher 1996] B. J. Soher, P. C. M. van Zijl, J. H. Duyn and P. B. Barker. *Quantitative proton MR spectroscopic imaging of the human brain.* Magnetic Resonance in Medicine, vol. 35, no. 3, pages 356–363, mar 1996. (Cited on page 150.)

[Song 2004] H. K. Song and L. Dougherty. *Dynamic MRI with projection reconstruction and KWIC processing for simultaneous high spatial and temporal resolution.* Magnetic Resonance in Medicine, vol. 52, no. 4, pages 815–824, oct 2004. (Cited on page 24.)

[Sonkar 2019] K. Sonkar, V. Ayyappan, C. M. Tressler, O. Adelaja, R. Cai, M. Cheng and K. Glunde. *Focus on the glycerophosphocholine pathway in choline phospholipid metabolism of cancer.* NMR in Biomedicine, vol. 32, no. 10, oct 2019. (Cited on page 88.)

[Sørensen 2022] M. K. Sørensen, M. Beyer, O. N. Jensen and N. C. Nielsen. *Quantification of protein and phosphorus in livestock feed using mobile NMR sensor technology.* Biosystems Engineering, vol. 216, pages 93–97, apr 2022. (Cited on page 42.)

[Soret 2007] M. Soret, S. L. Bacharach and I. Buvat. *Partial-Volume Effect in PET Tumor Imaging.* Journal of Nuclear Medicine, vol. 48, no. 6, pages 932–945, jun 2007. (Cited on pages xvi and 32.)

[Starcuk 1993] Z. Starcuk, K. Bartusek and Z. Starcuk. *Asymmetric Amplitude-Modulated Radiofrequency Pulses and Their Application to Band-Selective Decoupling.* Journal of Magnetic Resonance, Series A, vol. 104, no. 3, pages 340–344, oct 1993. (Cited on page 15.)

[Stobbe 2008] R. Stobbe and C. Beaulieu. *Advantage of sampling density weighted apodization over postacquisition filtering apodization for sodium MRI of the human brain.* Magnetic Resonance in Medicine, vol. 60, no. 4, pages 981–986, oct 2008. (Cited on page 24.)

[Stout 2017] J. Stout, A.-S. Hanak, L. Chevillard, B. Djemaï, P. Risède, E. Giacomini, J. Poupon, D. A. Barrière, F. Bellivier, B. Mégarbane and F. Boumezbeur. *Investigation of lithium distribution in the rat brain ex vivo using lithium-7 magnetic resonance spectroscopy and imaging at 17.2 T.* NMR in Biomedicine, vol. 30, no. 11, page e3770, nov 2017. (Cited on page 56.)

[Stout 2019] J. Stout. *Spectroscopie et Imagerie RMN multi-noyaux à très haut champ magnétique.* PhD thesis, 2019. (Cited on page 56.)

[Stucht 2015] D. Stucht, K. A. Danishad, P. Schulze, F. Godenschweger, M. Zaitsev and O. Speck. *Highest Resolution In Vivo Human Brain MRI Using Prospective Motion Correction.* PLOS ONE, vol. 10, no. 7, pages 1–17, 07 2015. (Cited on pages 1 and 148.)

[Thapa 2016] B. Thapa, J. Kaggie, N. Sapkota, D. Frank and E.-K. Jeong. *Design and Development of a General-Purpose Transmit/Receive (T/R) Switch for 3T MRI, Compatible for a Linear, Quadrature and Double-Tuned RF Coil.* Concepts in Magnetic Resonance Part B: Magnetic Resonance Engineering, vol. 46B, no. 2, pages 56–65, apr 2016. (Cited on page 60.)

[Thedens 1999] D. R. Thedens, P. Irarrazaval, T. S. Sachs, C. H. Meyer and D. G. Nishimura. *Fast magnetic resonance coronary angiography with a three-dimensional stack of spirals trajectory.* Magnetic Resonance in Medicine, vol. 41, no. 6, pages 1170–1179, jun 1999. (Cited on page 24.)

[Thulborn 2018] K. R. Thulborn. *Quantitative sodium MR imaging: A review of its evolving role in medicine.* NeuroImage, vol. 168, no. November 2016, pages 250–268, 2018. (Cited on pages 2 and 52.)

[Tofts 1988] P. S. Tofts and S. Wray. *A critical assessment of methods of measuring metabolite concentrations by NMR spectroscopy.* NMR in Biomedicine, vol. 1, no. 1, pages 1–10, feb 1988. (Cited on page 30.)

[Tomi-Tricot 2018] R. Tomi-Tricot. *Clinical applications of the kT-points method to homogenise spin excitation in 3T MRI.* Theses, Université Paris Saclay (COmUE), September 2018. (Cited on pages xv and 14.)

[Trapp 2009] B. D. Trapp and P. K. Stys. *Virtual hypoxia and chronic necrosis of demyelinated axons in multiple sclerosis.* The Lancet Neurology, vol. 8, no. 3, pages 280–291, 2009. (Cited on page 55.)

[Twieg 1983] D. B. Twieg. *The k -trajectory formulation of the NMR imaging process with applications in analysis and synthesis of imaging methods.* Medical Physics, vol. 10, no. 5, pages 610–621, sep 1983. (Cited on page 21.)

[Ulrich 2007] M. Ulrich, T. Wokrina, G. Ende, M. Lang and P. Bachert. *31P-1H echo-planar spectroscopic imaging of the human brain in vivo.* Magnetic Resonance in Medicine, vol. 57, no. 4, pages 784–790, apr 2007. (Cited on page 44.)

[Utzschneider 2020] M. Utzschneider, N. G. R. Behl, S. Lachner, L. V. Gast, A. Maier, M. Uder and A. M. Nagel. *Accelerated quantification of tissue sodium concentration in skeletal muscle tissue: quantitative capability of dictionary learning compressed sensing.* Magnetic Resonance Materials in Physics, Biology and Medicine, vol. 33, no. 4, pages 495–505, aug 2020. (Cited on page 42.)

[Valkovič 2016] L. Valkovič, M. Chmelík, B. Ukropcová, T. Heckmann, W. Bogner, I. Frollo, H. Tschan, M. Krebs, N. Bachl, J. Ukropec, S. Trattnig and M. Kršňák. *Skeletal muscle alkaline Pi pool is decreased in overweight-to-obese sedentary subjects and relates to mitochondrial capacity and phosphodiester content.* Scientific Reports, vol. 6, no. 1, page 20087, apr 2016. (Cited on page 46.)

[Valkovič 2021] L. Valkovič, J. Y. C. Lau, I. Abdesselam, O. J. Rider, I. Frollo, D. J. Tyler, C. T. Rodgers and J. J. J. Miller. *Effects of contrast agents on relaxation properties of 31 P metabolites.* Magnetic Resonance in Medicine, vol. 85, no. 4, pages 1805–1813, apr 2021. (Cited on page 60.)

[van der Kemp 2014] W. J. van der Kemp, B. L. Stehouwer, P. R. Luijten, M. A. van den Bosch and D. W. Klomp. *Detection of alterations in membrane metabolism during neoadjuvant chemotherapy in patients with breast cancer using phosphorus magnetic resonance spectroscopy at 7 Tesla.* SpringerPlus, vol. 3, no. 1, page 634, dec 2014. (Cited on page 88.)

[Vasanawala 2010] S. S. Vasanawala, M. T. Alley, B. a. Hargreaves, R. a. Barth, J. M. Pauly and M. Lustig. *Improved Pediatric MR Imaging with Compressed Sensing.* Radiology, vol. 256, no. 2, pages 607–616, aug 2010. (Cited on pages 51 and 98.)

[Walsh 2001] B. Walsh, M. Tonkonogi, K. Soderlund, E. Hultman, V. Saks and K. Sahlin. *The role of phosphorylcreatine and creatine in the regulation of mitochondrial respiration in human skeletal muscle.* The Journal of Physiology, vol. 537, no. 3, pages 971–978, dec 2001. (Cited on page 38.)

[Wang 2004] Z. Wang, A. C. Bovik, H. R. Sheikh and E. P. Simoncelli. *Image quality assessment: From error visibility to structural similarity.* IEEE Transactions on Image Processing, vol. 13, no. 4, pages 600–612, 2004. (Cited on pages 29 and 154.)

[Wang 2015] H. Wang, D. Hristov, J. Qin, L. Tian and K. Willmann, Jürgen. *Three-dimensional Dynamic Contrast-enhanced US Imaging for Early Antiangiogenic.* Radiology, vol. 277, no. 2, pages 424–434, 2015. (Cited on page 129.)

[Wang 2017a] C. Y. Wang, Y. Liu, S. Huang, M. A. Griswold, N. Seiberlich and X. Yu. *31P magnetic resonance fingerprinting for rapid quantification of creatine kinase reaction rate in vivo.* NMR in Biomedicine, vol. 30, no. 12, pages 1–27, 2017. (Cited on page 48.)

[Wang 2017b] H. Wang, A. M. Lutz, D. Hristov, L. Tian and J. K. Willmann. *Intra-animal comparison between three-dimensional molecularly targeted us and three-dimensional dynamic contrast-enhanced us for early antiangiogenic treatment assessment in colon cancer.* Radiology, vol. 282, no. 2, pages 443–452, 2017. (Cited on pages 2 and 148.)

[Wang 2019] Z. J. Wang, M. A. Ohliger, P. E. Z. Larson, J. W. Gordon, R. A. Bok, J. Slater, J. E. Villanueva-Meyer, C. P. Hess, J. Kurhanewicz and D. B. Vigneron. *Hyperpolarized 13 C MRI: State of the Art and Future Directions.* Radiology, vol. 291, no. 2, pages 273–284, may 2019. (Cited on page 9.)

[Warnking 2004] J. M. Warnking and G. B. Pike. *Bandwidth-modulated adiabatic RF pulses for uniform selective saturation and inversion.* Magnetic Resonance in Medicine, vol. 52, no. 5, pages 1190–1199, nov 2004. (Cited on page 17.)

[Weiss 2012] K. Weiss. *Magnetic Resonance Imaging of Cardiac Metabolism*. PhD thesis, 12 2012. (Cited on pages xvii, 44, and 45.)

[Wiggins 2016] G. C. Wiggins, R. Brown and K. Lakshmanan. *High-performance radiofrequency coils for 23 Na MRI: brain and musculoskeletal applications*. NMR in Biomedicine, vol. 29, no. 2, pages 96–106, feb 2016. (Cited on page 42.)

[Wilferth 2022] T. Wilferth, A. Mennecke, L. V. Gast, S. Lachner, M. Müller, V. Rothhammer, K. Huhn, M. Uder, A. Doerfler, A. M. Nagel and M. Schmidt. *Quantitative 7 Tesla 23 Na MRI of the Human Brain Using a 32-Channel Phased-Array Head Coil: Application to Patients with Secondary Progressive Multiple Sclerosis*. NMR in Biomedicine, jul 2022. (Cited on page 108.)

[Wilhelm 2001] T. Wilhelm and P. Bachert. *In Vivo 31P Echo-Planar Spectroscopic Imaging of Human Calf Muscle*. Journal of Magnetic Resonance, vol. 149, no. 1, pages 126–130, mar 2001. (Cited on page 44.)

[Wood 2017] S. Wood, N. Krishnamurthy, T. Santini, S. Raval, N. Farhat, J. A. Holmes and T. S. Ibrahim. *Design and fabrication of a realistic anthropomorphic heterogeneous head phantom for MR purposes*. PLOS ONE, vol. 12, no. 8, page e0183168, aug 2017. (Cited on page 61.)

[Worthoff 2019] W. A. Worthoff, A. Shymanskaya and N. J. Shah. *Relaxometry and quantification in simultaneously acquired single and triple quantum filtered sodium MRI*. Magnetic Resonance in Medicine, vol. 81, no. 1, pages 303–315, jan 2019. (Cited on pages 1, 49, and 148.)

[Xu 2005] S. Xu, J. Yang, C. Q. Li, W. Zhu and J. Shen. *Metabolic alterations in focally activated primary somatosensory cortex of α-chloralose-anesthetized rats measured by 1H MRS at 11.7 T*. NeuroImage, vol. 28, no. 2, pages 401–409, nov 2005. (Cited on page 38.)

[Xu 2022] J. Xu, J. J. Chung and T. Jin. *Chemical exchange saturation transfer imaging of creatine, phosphocreatine, and protein arginine residue in tissues*. NMR in Biomedicine, jan 2022. (Cited on page 39.)

[Yang 2009] Z. Yang and M. Jacob. *Efficient NUFFT algorithm for non-Cartesian MRI reconstruction*. In 2009 IEEE International Symposium on Biomedical Imaging: From Nano to Macro, pages 117–120, 2009. (Cited on page 27.)

[Zaaraoui 2012] W. Zaaraoui, S. Konstandin, B. Audoin, A. M. Nagel, A. Rico, I. Malikova, E. Soulier, P. Viout, S. Confort-Gouny, P. J. Cozzone, J. Pelletier, L. R. Schad and J.-P. Ranjeva. *Distribution of Brain Sodium Accumulation Correlates with Disability in Multiple Sclerosis : A cross-sectional 23Na MR Imaging Study*. Radiology, vol. 264, no. 3, pages 859–867, 2012. (Cited on pages 52, 97, and 136.)

[Zaric 2021a] O. Zaric, A. Farr, L. Minarikova, S. Lachner, E. Asseryanis, A. M. Nagel, M. Weber, C. F. Singer and S. Trattnig. *Tissue Sodium Concentration Quantification at 7.0-T MRI as an Early Marker for Chemotherapy Response in Breast Cancer: A Feasibility Study.* Radiology, vol. 299, no. 1, pages 63–72, apr 2021. (Cited on page 52.)

[Zaric 2021b] O. Zaric, V. Juras, P. Szomolanyi, M. Schreiner, M. Raudner, C. Giraudo and S. Trattnig. *Frontiers of sodium MRI revisited: From cartilage to brain imaging.* Journal of Magnetic Resonance Imaging, vol. 54, no. 1, pages 58–75, 2021. (Cited on page 97.)

[Zbontar 2018] J. Zbontar, F. Knoll, A. Sriram, T. Murrell, Z. Huang, M. J. Muckley, A. Defazio, R. Stern, P. Johnson, M. Bruno, M. Parente, K. J. Geras, J. Katsnelson, H. Chandarana, Z. Zhang, M. Drozdzal, A. Romero, M. Rabbat, P. Vincent, N. Yakubova, J. Pinkerton, D. Wang, E. Owens, C. L. Zitnick, M. P. Recht, D. K. Sodickson and Y. W. Lui. *fastMRI: An Open Dataset and Benchmarks for Accelerated MRI.* nov 2018. (Cited on page 102.)

[Zeng 2013] G. L. Zeng, Y. Li and E. V. R. DiBella. *Non-iterative reconstruction with a prior for undersampled radial MRI data.* International Journal of Imaging Systems and Technology, vol. 23, no. 1, pages 53–58, mar 2013. (Cited on page 24.)

[Zhu 2012] X. H. Zhu, H. Qiao, F. Du, Q. Xiong, X. Liu, X. Zhang, K. Ugurbil and W. Chen. *Quantitative imaging of energy expenditure in human brain.* NeuroImage, vol. 60, no. 4, pages 2107–2117, 2012. (Cited on pages 56, 57, 150, and 151.)

[Zhu 2018a] X.-H. Zhu and W. Chen. *In vivo X-Nuclear MRS Imaging Methods for Quantitative Assessment of Neuroenergetic Biomarkers in Studying Brain Function and Aging.* Frontiers in Aging Neuroscience, vol. 10, no. November, pages 1–16, 2018. (Cited on page 56.)

[Zhu 2018b] X. H. Zhu, B. Y. Lee and W. Chen. *Functional energetic responses and individual variance of the human brain revealed by quantitative imaging of adenosine triphosphate production rates.* Journal of Cerebral Blood Flow and Metabolism, vol. 38, no. 6, pages 959–972, 2018. (Cited on page 150.)

[Zhu 2021] X.-H. Zhu, B.-Y. Lee, P. Tuite, L. Coles, A. G. Sathe, C. Chen, J. Cloyd, W. C. Low, C. J. Steer and W. Chen. *Quantitative Assessment of Occipital Metabolic and Energetic Changes in Parkinson's Patients, Using In Vivo 31P MRS-Based Metabolic Imaging at 7T.* Metabolites, vol. 11, no. 3, page 145, 2021. (Cited on page 82.)

[Ziarelli 2006] F. Ziarelli and S. Caldarelli. *Solid-state NMR as an analytical tool: Quantitative aspects.* Solid State Nuclear Magnetic Resonance, vol. 29, no. 1-3, pages 214–218, feb 2006. (Cited on page 30.)

[Zur 1991] Y. Zur, M. L. Wood and L. J. Neuringer. *Spoiling of transverse magnetization in steady-state sequences.* Magnetic Resonance in Medicine, vol. 21, no. 2, pages 251–263, oct 1991. (Cited on page 19.)

* * *
* *
*

Abbreviations and Acronyms

2D	two-dimensional
3D	three-dimensional
AD	Alzheimer's Diseases
AF	acceleration factor
ATP	Adenosine triphosphate
BASSI	bandwidth-modulated adiabatic selective saturation and inversion
BOLD	blood-oxygenation-level dependent
BW	bandwidth
CEA	Commisariat à l'énergie atomique et aux énergies alternatives
CEST	chemical exchange saturation transfer
CF	correction factor
CK	creatine kinase
cNR	contrast-to-noise ratio
CP	circular polarization
CS	compressed sensing
CSF	cerebrospinal fluid
CSI	Chemical Shift Imaging
DA-3DPR	density-adapted three-dimensional radial projection reconstruction pulse sequence
DAM	double angle method
DFT	discrete fourier transform
DQC	double-quantum coherence
DWI	Diffusion-weighted magnetic resonance imaging
DWT	discrete wavelet transform

EPSI	Echo Planar Spectroscopic Imaging
ERETIC	Electronic REference To access In vivo Concentrations
FA	flip angle
FFT	fast fourier transform
FID	free induction decay
FISTA	fast iterative shrinkage-thresholding algorithm
FLASH	fast low angle shot
fMRI	functional MRI
FOV	field of view
FS	frequency selective
FWHM	full width at half-maximum
GPC	glycerophosphocholine
GPE	glycerophosphoethanolamine
GRE	gradient-recalled-echo
HEP	high-energy phosphate
ISIS	Image Selected In vivo Spectroscopy
IT	inversion recovery transfer
MC	Monte-Carlo
MMSE	minimum mean square error
MP-RAGE	magnetisation-prepared rapid gradient echo
MRI	magnetic resonance imaging
MRSI	magnetic resonance spectroscopic imaging
MSE	mean square error
MT	magnetization transfer
NAD	nicotinamide adenine dinucleotide
NMR	nuclear magnetic resonance
NOVIFAST	NOn-linear VarIable Flip Angle data baSed T1 estimator
NUFFT	non uniform fast fourier transform
OVS	outer volume saturation
PA	programmable attenuator
PBS	phosphate buffered saline

PC	phosphocoline
PCr	phosphocreatine
PD	proton density
PDE	phosphodiesters
PE	phosphoethanolamine
PI	Phosphore inorganic
PLOT	polynomial lorentzian fitting
PME	Phosphomonoesters
POGM	proximal optimized gradient method
ppm	parts per million
PRESS	single shot Point REsolved Spectroscopy
PSF	point spread function
RARE	Rapid Acquisition with Relaxation Enhancement
RF	radiofrequency
ROI	region of interest
SAR	specific absorption rate
SD	sample standard deviation
SLR	Shinnar-Le Roux
SNR	signal-to-noise ratio
SPGR	spoiled gradient sequence
SPSP	spatial-spectral pulses
SQC	single-quantum coherence
SSIM	structural similarity index measure
STEAM	STimulated Echo Acquisition Mode
SVS	single voxel spectroscopy
TA	acquisition time
TCA	tricarboxylic acid
TE	echo time
TI	inversion time
TP	total phosphorus
TPI	Twisted Projection Imaging
TPP	triphenylphosphate
TQC	triple-quantum coherence
TR	repetition time
TSC	tissue sodium concentration
TV	total variation

UHF	ultra-high field
UTE	ultra-short echo time
VFA	variable flip angle
ViP MRI	Virtual Phantom Magnetic Resonance Imaging
VMFA	variable multiple flip angle
WG	waveform generator
WM	white matter
XFL	magnetization prepared turbo-FLASH

* * *
* *
*